Axial Crush Performance of Hot Stamped Tailor Welded Blanks

Experiments and Numerical Simulations

by

Cale Peister

A thesis

presented to the University of Waterloo

in fulfillment of the

thesis requirement for the degree of

Master of Applied Science

in

Mechanical and Mechatronics Engineering

Waterloo, Ontario, Canada, 2019

Author's Declaration

I hereby declare that I am the sole author of this thesis. This is a true copy of the thesis, including any required final revisions, as accepted by my examiners.

I understand that my thesis may be made electronically available to the public.

Abstract

This thesis investigates the axial crush performance of hot stamped tailor-welded blanks (TWBs) and their potential for weight reduction in the front crush structure of a vehicle. A baseline demonstrator structure, fabricated from the mass-production front side frame of a large sport utility vehicle (SUV), was subjected to a dynamic crush test performed at a speed of 50-56 km/h. The collapse mode and load-displacement history were characterized to establish the baseline performance when using conventional high strength steels.

TWBs comprising ultra-high strength Usibor® 1500-AS and more ductile Ductibor® 500-AS were studied. Five configurations of top-hat channels were formed: non-tailored monolithic Ductibor® 500-AS in 1.2 mm and 1.6 mm thicknesses, common-gauge Usibor® 1500-AS welded to Ductibor® 500-AS TWBs in 1.2 mm and 1.6 mm thicknesses, and a multi-gauge TWB comprising 1.2 mm Ductibor® 500-AS and 1.6 mm Usibor® 1500-AS. After forming, the monolithic and common-gauge parts had relatively uniform hardnesses in each material, with the Usibor® 1500-AS and Ductibor® 500-AS achieving 490 HV and 230 HV, respectively, and the hardness transition across the laser weld line was just 2 mm wide. The multi-gauge TWBs were formed in a new die that could accommodate the step in thickness. These reached hardnesses of 540 HV and 250 HV respectively due to increased quench rates in the new die.

Formed monolithic Ductibor® 500-AS channels were spot welded to flat backing plates of ferritic/bainitic JAC590R steel with a 590 MPa strength to form three point bend specimens, and were tested under dynamic and quasi-static conditions. The high ductility of this material allowed these rails to fold tightly without any fracture. In dynamic tests of 1.2 mm specimens, the specimens exhibited two distinct deformation modes: wrapping and folding. In the wrapping mode, sufficient friction between the impactor and specimen prevents sliding so the specimen wraps around the impactor, whereas in the folding mode the specimen slides across the surface of the impactor and forms a tight fold. The results were very repeatable and displayed positive rate sensitivity. The thicker 1.6 mm specimens sustained more load and absorbed more energy than the 1.2 mm specimens.

Formed channels in all five configurations were spot welded together in pairs to form axial crush rails, and were tested under dynamic and quasi-static loading. The monolithic Ductibor® 500-AS specimens had a tendency towards global buckling, especially in the 1.2 mm thickness. The TWB

specimens were stabilized by the hard section clamped in the fixed end of the rail, preventing buckling and promoting progressive axial folding. The Ductibor® 500-AS formed very tight folds without fracture or cracking. Once this soft zone fully consolidated, the hard Usibor® 1500-AS begin to crush and fracture as it increased the crush load to resist intrusion. The 1.6 mm common-gauge TWB absorbed the most energy in the dynamic (31.8 kJ) and quasi-static (29.8 kJ) tests. This 1.6 mm TWB configuration also had the least amount of fracture because the majority of the test energy was absorbed by the thicker 1.6 mm Ductibor® 500-AS.

Numerical models of the three point bend and axial crush experiments were developed in LS-DYNA to simulate the crash behaviour. The models of axial crush had very good agreement with the experimental results. The models of three point bends also matched very closely with the experimental results, with the exception of the 1.6 mm quasi-static condition in which the curves match initially but diverge partway through the experiment.

After showing that Ductibor® 500-AS performs well in an energy absorbing crush application, its performance in the crush tip of the baseline demonstrator structure was predicted. The constitutive and fracture properties of Ductibor® 500-AS were substituted for the JAC590R in a crash model of the crush tip region of this structure. The folding modes and load-displacement response predicted for the hot stamped Ductibor® 500-AS crush tip were very similar to the predictions for the baseline condition with JAC590R. In addition, the baseline model was validated by performing crush experiments on the baseline crush tips with very good agreement between the experiment and model.

The results of this research demonstrate that Ductibor® 500-AS has significant potential for direct substitution of 590 MPa strength conventionally stamped in crush applications. This outcome supports the use of a hot stamped TWB frontal crush structures comprising Ductibor® 500-AS in the energy absorbing zone to absorb energy, and Usibor® 1500-AS in the rear section to resist intrusion into the passenger compartment. The use of ultra-high strength Usibor® 1500-AS will allow for weight reduction through use of thinner gauge sheet. The use of a laser welded blank consolidates multiple parts into one, eliminating numerous spot welds and other joining processes from the final assembly. In future work, the suitability of higher strength Ductibor® 1000-AS for crush structures should be investigated for further weight reduction potential.

Acknowledgements

I would like to thank my supervisor, Dr. Michael Worswick, for the opportunity to work with his group of highly skilled researchers on this interesting and fulfilling project. His support and guidance throughout my studies have been invaluable and it has been an excellent learning experience. I would also like to acknowledge Dr. Clifford Butcher for his direction in material modelling for my research, and for the opportunity to work as a teaching assistant. Thanks to Dr. José Imbert for all of his support of crash testing, as well as Ryan George, Dr. Michael Nemcko, and Dr. Armin Abedini for all of their support and guidance with hot stamping, design, and material characterization.

Assistance and guidance in the lab from Eckhard Budziarek, Andy Barber, Tom Gawel and Jeff Wemp enabled me to complete experiments safely and successfully. Support from Mark Kuntz and the Engineering Machine Shop allowed us to quickly solve issues in the lab and avoid delays.

Support for this project from sponsors Honda R&D Americas, the Promatek Research Centre (Cosma International), and ArcelorMittal, as well as additional support from the Natural Sciences and Engineering Research Council, the Canada Research Chair Secretariat, the Canadian Foundation for Innovation, the Ontario Advanced Manufacturing Consortium, the Ontario Research Fund, and the Ontario Centres of Excellence is gratefully acknowledged. In particular, I would like to thank Skye Malcolm and Jim Dykeman from Honda for their constant support and guidance on numerical simulation and material testing, as well as the fabrication group at Honda R&D Americas for fabrication of the side frame demonstrator structures. I also thank Cyrus Yau and Pavlo Penner at the Promatek Research Centre for their support in tooling development and spot welding of the hot stamped test specimens. Finally, I thank ArcelorMittal for their support of this project, in particular Ron Soldaat and Willie Bernert for provision of the hot stamped materials and support in material characterization, as well as Eric Famchon for performing the laser welding of the TWB samples.

I would also like to acknowledge all of those working in the Waterloo Forming and Crash Lab during my tenure who made this experience enjoyable in the office, in the lab, at conferences, and outside of work. Thanks to Cameron O'Keeffe for being a great crash test partner, and for your friendship throughout the challenges of grad school; and Sante DiCecco for organizing nights of BBQ, pho, and other shenanigans with Massimo DiCiano and Chi-Hsiang Liao. Thanks also to

Matt Tummers, Cameron Tolton, Pedram Samadian, Alireza Mohamadizadeh, and Steven Lee for being on “Team Steel” with me. Encouragement from Amir Zhumagulov, Kenneth Cheong, Kyu Bin Han, Sam Kim, Jacqueline Noder, and Kaab Omer was also very much appreciated.

Lastly, I would like to thank my parents, Bill and Susan, and my sister, Erin, for their unwavering support and encouragement during my time as a grad student.

Dedication

Dedicated to my parents

Table of Contents

List of Figures

List of Tables

1.0 Introduction

1.1 Background

The automotive industry is under significant pressure from strict government regulations aimed to reduce vehicle emissions and promote improved fuel efficiency. Current fuel economy standards such as the Corporate Average Fuel Economy (CAFÉ) regulations in the United States require manufacturers to meet ever-increasing standards in future model years or face monetary fines. The standard for light trucks (including SUVs) will increase from 29.1-29.4 miles per gallon (mpg) in the 2017 model year to 39.3-40.3 mpg in the 2025 model year. Passenger cars will see a similar increase from 39.6-40.1 mpg to 55.3-56.2 mpg from 2017 to 2025 [1]. The required increase in fuel economy has resulted in the development of new technologies, including improvement of aerodynamics to reduce drag, and more efficient powertrains, such as small displacement turbocharged engines and gas-electric hybrid drives.

Another important means of improving fuel economy is through the reduction of vehicle mass, which is a focus of this thesis. The standards for vehicle crash safety are also increasing, so mass reduction must be achieved while maintaining or improving crash performance. The demand for lightweight materials for the mass production automotive industry has resulted in the development of new lightweight materials and manufacturing processes. One such metal forming process is hot stamping, wherein a boron steel blank is heated above its austenitization temperature for several minutes, giving it good formability at this elevated temperature. It is then formed into the desired shape between water-cooled dies, causing rapid cooling of the sheet and phase transformation from austenite to martensite, as described by Karbasian and Tekkaya [2]. The resulting fully martensitic material condition corresponds to an ultra-high strength steel (UHSS) with tensile strengths as high as 1,500 MPa. This strength level allows for mass reduction through reduction in sheet thickness, requiring less material to achieve similar or higher load capacity compared to conventional mild steels. Springback is also very low because the flow stress and elastic modulus are small at the elevated forming temperature, and forming stresses are largely eliminated during the martensitic transformation, as noted by Mori *et al.* [3].

One limitation of the UHSS martensitic parts formed using hot stamping is their relatively low ductility which causes them to fracture at relatively low strains. This is undesirable for application in front and rear crush structures where there is significant potential for weight reduction, because

they need to absorb a large amount of crash energy by undergoing large deformation. This limitation has motivated the current research that considers tailoring strategies to introduce more ductile regions within components to enable absorption of crash energy.

1.2 Automotive Steels

1.2.1 Overview

The body-in-white of an automobile, comprising stamped and welded sheet metal, can be built from many different materials, as shown in Figure 1. Traditionally mild steels with low tensile strengths were used in early car models, but lightweight materials such as aluminum, magnesium, and composites have become more common. In order to stay competitive, the steel industry has evolved in recent years with much higher strength grades becoming available for mass production that enable weight reduction through decreases in sheet thickness. The strengths reported in this thesis refer to the tensile strength, not the yield strength.

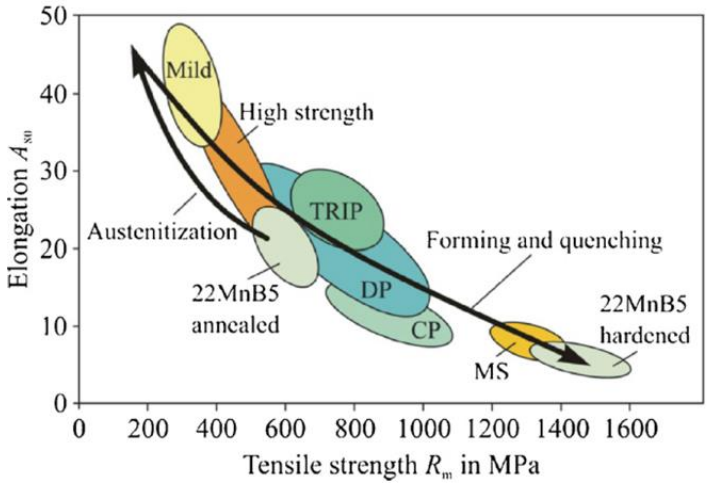

Figure 1: Mechanical properties of different steel sheet grades, adapted from [2].

High strength low alloy steels (HSLA) have a low alloying content and achieve strength using precipitation and grain refinement. These range in tensile strength from 260 to 550 MPa [4].

Dual phase (DP) steels contain martensite islands or bainite dispersed in a ferrite matrix, giving high strength while maintaining some ductility. They are available in grades ranging from 450 to 1180 MPa [4].

Transformation induced plasticity (TRIP) steels consist of a soft ferrite matrix with islands of retained austenite. When deformed, the austenite transforms into martensite, imparting strong

work hardening with good formability and drawability. TRIP steels are available in grades with tensile strengths of 590, 690 and 780 MPa [4].

Hot stamped boron steel (22MnB5) forms a fully martensite microstructure after hot stamping. This microstructure imparts an ultra-high strength of about 1,500 MPa in traditional hot stamped grades, such as Usibor® 1500-AS [5], for example, and over 1,800 MPa in new hot stamp alloys, such as Usibor® 2000-AS [5]. Other more ductile alloys, such as Ductibor® 500-AS, a focus of the current research, and emerging grades such as Ductibor® 1000-AS can also be hot stamped [5]. These softer hot stamped grades form either a ferrite/martensite microstructure after hot stamping, as in Ductibor® 500-AS, which has a strength of about 600 MPa [6], or are fully martensitic but with a lower carbon content that results in a strength of about 1,000 MPa, but with increased ductility (Ductibor® 1000-AS). Hot stamped alloys of differing strength and ductility are often combined in tailor welded blanks (TWBs) to impart intrusion resistance (high strength) in one region and energy absorption (high ductility) in another.

Most vehicles built today contain a mixture of steel grades as well as non-ferrous metals, as shown in Figure 2. The SUV shown uses a hot stamped door ring, 590 MPa front rails and floor, 980 MPa header and roof rails, an aluminum bumper beam, and a magnesium member across the dashboard, while much of the rear of the car uses lower strength steel. Clearly there still exists an opportunity for significant weight savings by increasing material strength.

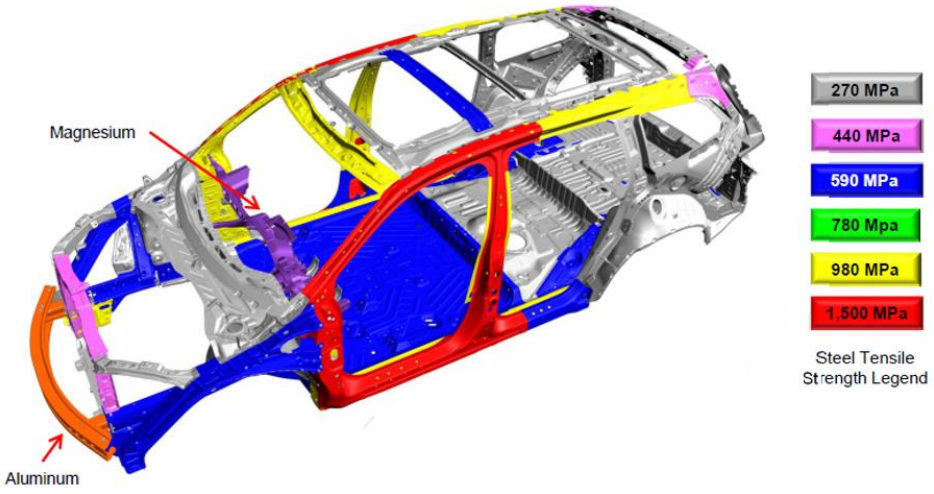

Figure 2: Various steel grades used in a 2016 model year SUV, adapted from Honda [7].

1.2.2 Hot Stamping Process

The direct hot stamping process begins with placing the forming blank in an oven at approximately 930°C for several minutes to convert the microstructure to austenite. The austenitized blank is then rapidly transferred to a die set in which it is simultaneously formed and quenched, as shown in Figure 3(a). In the indirect hot stamping process shown in Figure 3(b), there is a cold pre-forming step prior to austenitization. This means that most of the forming is done cold, and the hot stamping process is only used to austenitize and quench the final part.

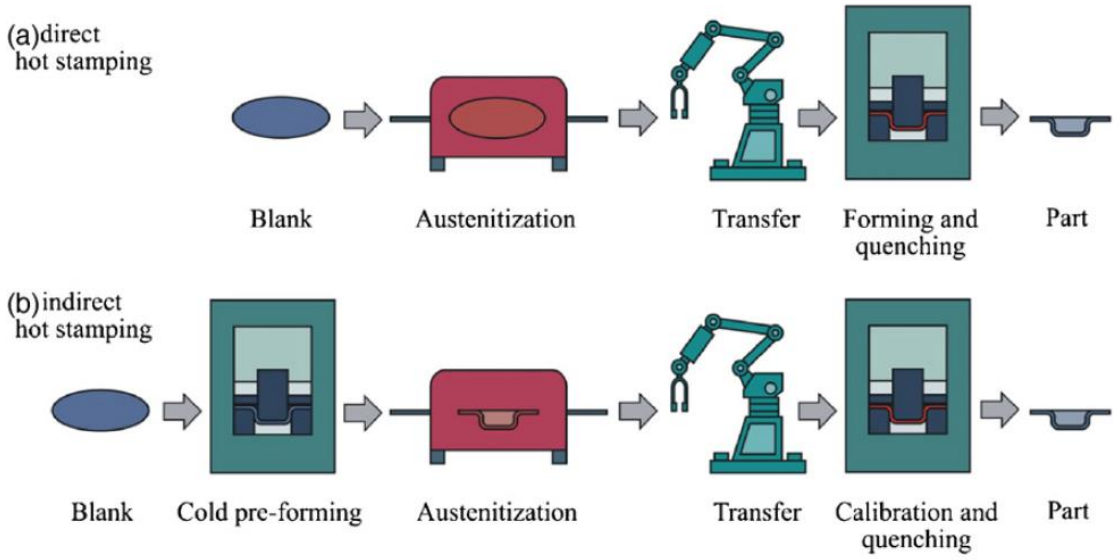

Figure 3: Direct and indirect hot stamping processes [2].

The material properties of the formed part are controlled by the rate of cooling (quench rate) that the blank experiences during hot stamping. If a cooling rate in excess of 30°C/s is achieved, the microstructure will be fully martensitic and have a very high strength. At lower cooling rates the microstructure will form other phases including bainite and ferrite by passing through their respective regions on the Continuous Cooling Transformation (CCT) diagram (Figure 4) during quenching. Deformation of the sheet while in the austenitic state shifts the ferrite and bainite zones to the left in the CCT diagram, requiring a higher critical cooling rate of about 50°C/s to create a fully martensitic microstructure.

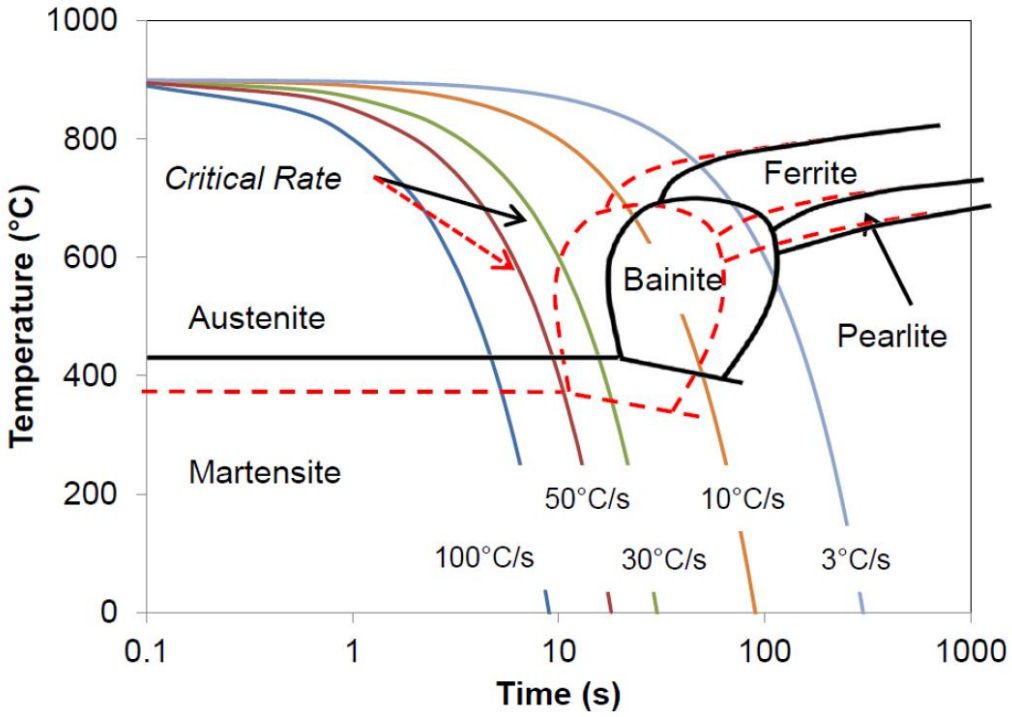

Figure 4: Continuous Cooling Transformation (CCT) diagram for Usibor® 1500-AS, from George [8]. The black lines represent quenching without any imposed deformation, while the dashed red lines show a sample that is deformed during quenching.

1.2.3 Automotive Applications for Hot Stamping

After the hot stamping process was developed in Sweden in 1977 [2], it was first used in a vehicle in 1983 in the Saab 9000 [9] for side impact beams in the front and rear doors. Hot stamped bumper beams were introduced in the 1990s, and by 2000, B-pillars and roof rails had been added, such that a total of 9% of the body in white (BIW) mass can be hot stamped, according to Belanger [9]. Since the mid-2000s hot stamping has expanded worldwide with applications including the transmission tunnel, A-pillar, underbody cross members, and side sills. With the advent of tailored properties, hot stamped door rings and rear rails have been introduced, adding to the long list of parts that can be optimized using the process. In 2014, the Volvo XC90 launched with the BIW containing 40% hot stamped parts by weight [3]. Figure 5 shows some of the applications of hot stamped parts.

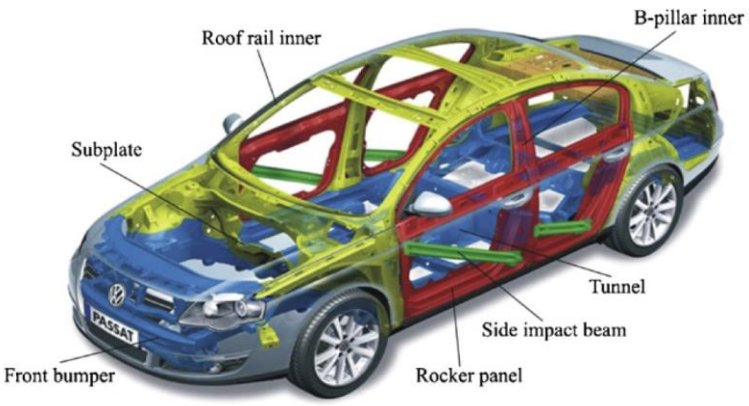

Figure 5: Applications of martensitic hot stamped components in a vehicle [2].

1.3 Tailoring Techniques

Hot stamped parts can be produced with improved ductility by using tailored hot stamping processes. These processes allow ductile zones to be introduced into an otherwise UHSS component to promote local folding and energy absorption where desired. Two common processes are hot stamping of monolithic blanks using tailored in-die heating (IDH), studied by Omer *et al.* [10] and George *et al.* [11]; or tailor-welded blanks (TWBs), studied by Peister *et al.* [12, 13, 14, 15].

1.3.1 Tailored In-Die Heating

The tailored in-die heating (IDH) process, sometimes referred to as "tailored tempering" (strictly speaking a misnomer), takes advantage of the cooling rate dependent properties of boron steels by using a stamping die with cartridge heaters inserted into certain areas. In these heated regions, the cooling rate is reduced, resulting in formation of bainitic and/or ferritic microstructures [2], while martensite continues to be formed in the cooled areas of the die where the quench rate remains high. These bainitic and/or ferritic microstructures have reduced strength compared to the martensitic material, however they exhibit much better ductility and are still stronger than mild steel. Heaters are added in sections where folding and ductility are desired (to absorb energy), while water-cooling channels are used in sections where ultra-high strength for intrusion resistance is needed, creating a part with tailored properties.

Many studies have been conducted that evaluate the advantages that IDH holds over traditional hot stamping. George *et al.* [16, 11] used IDH to form lab-scale B-pillar parts that had an ultra-high strength zone for intrusion resistance and a region with moderate strength and lower ductility

to absorb energy. Tooling temperatures between 100°C and 400°C were used to vary the properties of the soft zone. Other studies on B-pillars with IDH tailoring were performed by Banik *et al.* [17] and Wilsius *et al.* [18]. Prajogo [19] tailored the flanges of side impact beams to suppress fracture in three-point bending experiments. Omer *et al.* [10, 20, 21] used a segmented channel forming die with heated sections to produce axial crush members with tailored properties along their length. Eller *et al.* [22] created hat channel sections with similar axial tailoring and subjected them to 4-point bending.

1.3.2 Hot Stamped Tailor-Welded Blanks (TWBs)

TWBs comprise at least two sheets of differing thicknesses and/or material properties that are welded together before forming, as described by Merklein *et al.* [23]. The sheets are welded together either along their edges, as in the current study, or as overlapping patches. Laser welding is commonly used, but mash seam and friction stir welding are other options. These blanks allow for thicker or stronger materials to be used in areas where they are needed, while thinner or weaker materials can be used elsewhere to reduce weight or cost. In a crush rail a region of thinner gauge steel can be used in the crush tip to initiate folding, with a transition to a thicker gauge steel to more aggressively absorb energy and prevent intrusion. TWBs can also be used to reduce scrap when forming a part with large cutouts such as a door ring or body side.

Hot stamped tailor-welded blanks are composed of two or more hot stamping steels that can have the same or different thicknesses. The different sections of the blank can be composed of the same alloy, or multiple alloys that respond differently to the rapid quench during forming. While Usibor® 1500-AS achieves an ultimate strength of 1500 MPa, but lower ductility, Ductibor® 500-AS reaches a lower strength of about 600 MPa with much better ductility [6]. Ductibor® 1000-AS reaches an intermediate strength of about 1100 MPa with moderate ductility. By using tailor-welded blanks that mix Usibor® and Ductibor® materials, a part with tailored properties can be produced, as shown in Figure 6. Múnera *et al.* [6] performed numerical studies to compare a door ring composed of four monolithic parts to one made from a single hot stamped TWB. They also compared lab-scale axial crush rails formed from monolithic blanks to those formed from hot stamped TWBs using Usibor® 1500-AS and Ductibor® 500-AS.

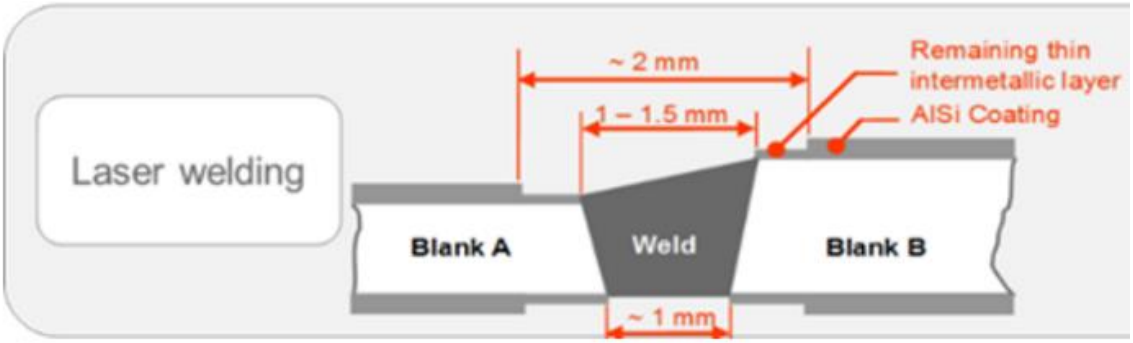

Figure 6: Laser welded blank of AlSi coated material with different sheet thicknesses, from ArcelorMittal [24].

The laser weld joint between Ductibor® 500-AS and Usibor® 1500-AS in hot stamped TWBs was studied by Kang *et al.* [25]. They measured the hardness across the weld line between the two materials and found that the hardness of the fusion zone was higher than that of the Ductibor® base metal. They conducted tensile tests of hot stamped TWBs and found that fracture always occurred in the Ductibor® base metal.

To date there has been little published research into the performance of front rails with axial tailoring provided by hot stamped TWBs, with the exception of the numerical studies mentioned previously. This lack of prior research provides justification for the current research which investigates the crash performance of hot stamped axial crush members that use TWBs comprising Usibor® 1500-AS laser welded to Ductibor® 500-AS to provide axial tailoring.

1.3.3 Other Tailoring Techniques

While IDH and TWBs have been the focus of the current and prior work at the University of Waterloo (UW), there are several other techniques that can be used, as described by Merklein *et al.* [26].

Partial austenitization is a strategy where parts of the blank are heated above their austenitization temperature where martensite is desired, while the rest of the blank is kept below this transition temperature to prevent austenite formation. This causes a softer microstructure to form in the areas that are not heated. This tailored blank heating can be achieved using a furnace with separated chambers, localized resistance heating, or radiant heaters and shields.

Differential cooling is achieved in the IDH process by heating sections of the die to elevated temperature. It can also be implemented by building sections of the die from tool steels with

differing thermal conductivity. Another method is to leave a gap between the tool and blank in a section of the die. All of these methods locally manipulate the cooling rate of the blank, causing different microstructures to form.

Tempering after hot stamping can be used to soften sections of the part after forming. This process, termed tailored tempering, can be accomplished in several ways, such as laser, magnetic induction, and flame. In each case, the part is locally heated then allowed to slowly cool, softening the microstructure. Depending on the heating method, tailored tempering can be performed over a large area of the part, or a very localized area.

1.4 Crashworthiness

The demand for lighter vehicles has motivated designers to reduce the weight of crash safety structures. These lightweighting efforts must be balanced with the crashworthiness requirements to maintain or improve occupant safety in a crash. In a rear end collision, rear crush rails will crumple to absorb energy. In a side impact, the impact beams in the door and side sill will transmit loads through the pillars to the roof and underbody. In a frontal impact such as a full width barrier impact, the front rails of the vehicle (Figure 7) are the primary crush structure. These thin walled, closed section rails must plastically deform to absorb the energy of the impact, while minimizing the magnitude of the peak forces exerted on the occupants. They also must control how far the crush extends into the vehicle to prevent intrusion into the passenger compartment.

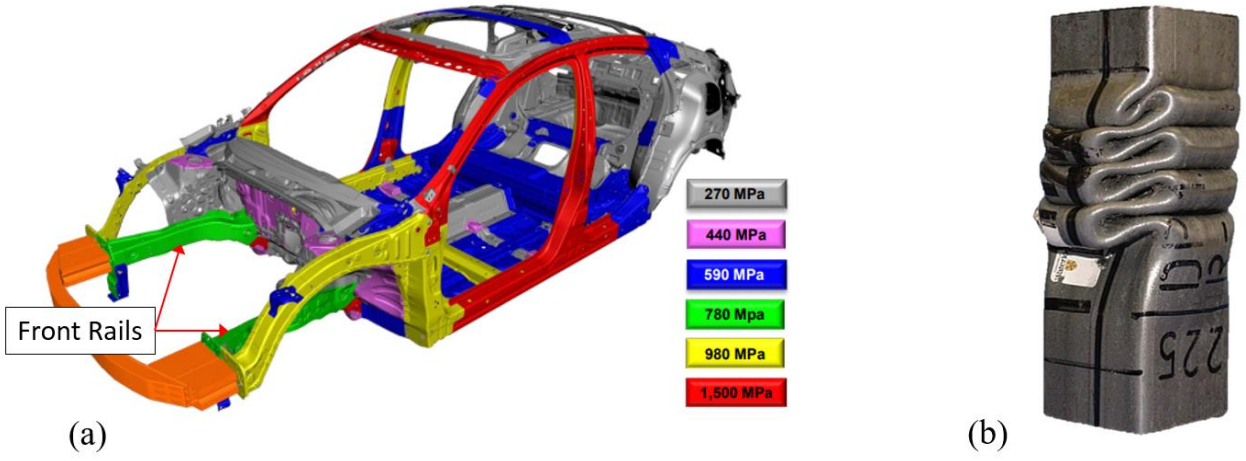

Figure 7: (a) Front crush rails in a 2016 model year sedan, adapted from Honda [27], (b) Deformed tubular axial crush rail made from DP600 steel, adapted from Adebrabbo *et al.* [28].

The folding mechanics of thin walled rectangular crush tubes was studied by Wierzbicki and Abramowicz in 1983 [29]. They developed a theory for predicting fold formation and crush force in structures consisting initially of planar surfaces, using a quarter-symmetry assumption. Their model assumes that the material is rigid-perfectly plastic, isotropic, and has no rate sensitivity. It also assumes that the local buckling wavelength remains constant as each buckle or fold is produced, and that folding occurs progressively.

Additional work on the collapse modes of thin-walled structures was performed by Hayduk and Wierzbicki in 1984 [30]. They explained that these structures typically deform through a mostly inextensible deformation mode. This means that the folds are formed primarily by bending, rather than stretching, of the structure's thin walls, however some stretching is inevitable. The opposite mode is extensible, where the length of the walls changes as they undergo stretching. Figure 8(a) shows a flat element being folded inextensibly along the hinge line AB. Figure 8(b) reaches the same final state inextensibly by folding first along AB, then straightening at AB while simultaneously bending at AC. Figure 8(c) shows an extensional deformation where the flat element is stretched in an extensible deformation to reach the final state.

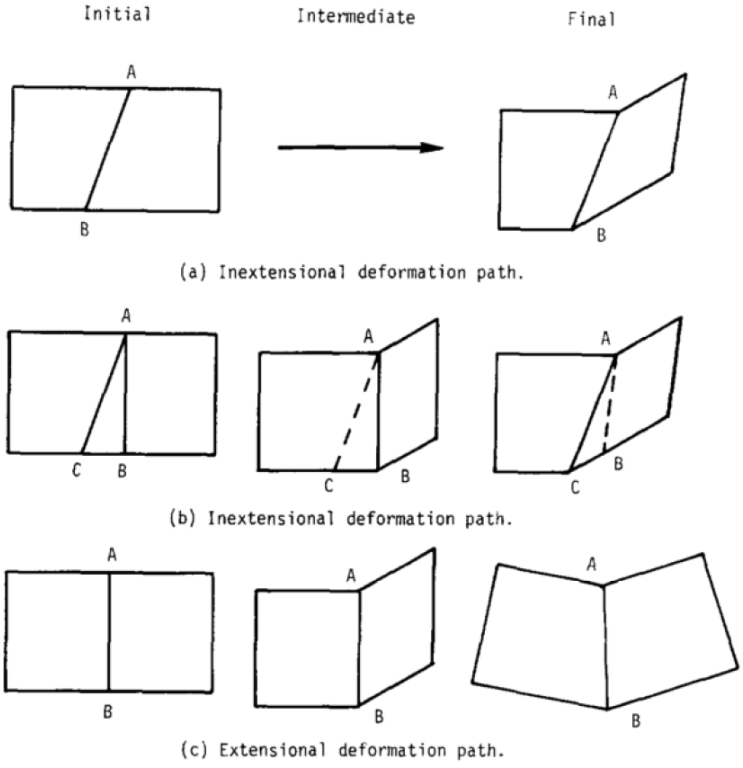

Figure 8: Inextensional and extensional folding modes [30].

In Figure 9, the straight hinge line has been replaced by a continuous and smooth displacement field consisting of four regions. Section I refers to four planar trapezoidal elements moving as rigid bodies. Section II is two cylindrical surfaces that bend continuously without extension. Section III is two conical surfaces in which material is bent and unbent as it flows from one flange to the other. Finally section IV is a toroidal surface that deforms extensibly in the circumferential direction and continuously changes its curvature. This shows that extensible deformation is limited to a small fraction of the total area, but up to one third of the total work is dissipated here [30]. The remaining two thirds or more of energy dissipation occurred in inextensional deformation at the hinge lines.

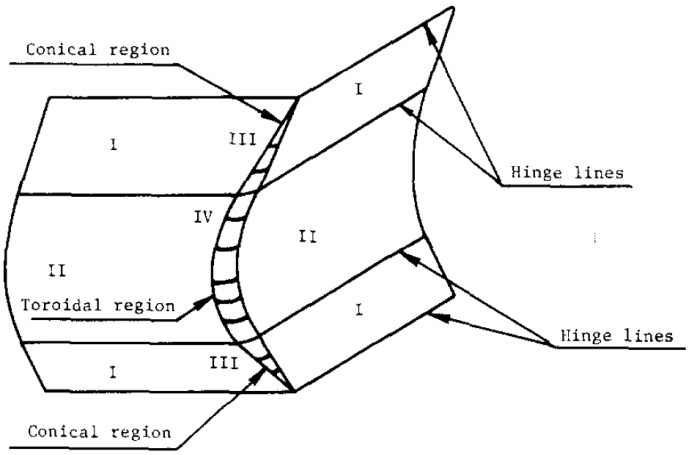

Figure 9: Basic folding mode of a rectangular thin walled tube [30].

Abramowicz and Wierzbicki [31] extended this work in 1989 for thin walled columns with an even number of corners. The most important conclusion in this work was that the plastic resistance and collapse mode were highly dependent on the angle between the intersecting sidewalls of the column. For elements with acute angles the deformation was quasi-inextensional, while for obtuse angles the deformation was primarily extensional. This is important because the extensional mode predicts thirty percent less energy absorption than the inextensional mode.

Abramowicz and Jones [32] studied axial crush of thin-walled mild steel columns both dynamically and quasi-statically with several different square and circular cross sections. Their study included columns with a range of lengths that would encompass both local progressive crush and global buckling. They found that in quasi-static tests of rails that buckled locally in the elastic range, local progressive crush was the predominant deformation mode. In longer columns, the

deformation could begin with progressive crush before transitioning to a global bending. In columns that initially deform plastically, global buckling was the dominant mode. In some cases the column could transition back to progressive crush. They found that the performance in dynamic tests was similar, but the crushing forces were higher due to strain-rate effects. The higher inertial forces in the dynamic tests inhibited buckling in the early stages of deformation, promoting the formation of a few progressive folds.

Further study on quasi-static and dynamic crush testing of circular tubes made of stainless steel, aluminum alloy, and mild steel was performed by Hsu and Jones [33]. They concluded that the stainless steel tubes absorbed the most energy, but the aluminum alloy tubes were the most efficient. They also found that the critical length where deformation transitioned from progressive crushing to global buckling was very similar for the three different materials.

Schneider and Jones [34] conducted a similar study that considered spot welded top-hat and laser welded square sections made from two high strength steels and a mild steel. They found that the collapse modes were similar for the three materials with progressive folding occurring in the majority of the tests. The remaining specimens experienced unstable global buckling.

Tarigopula *et al.* [35] studied quasi-static and dynamic axial crush performance of thin walled square tubes and spot-welded top hat sections made from DP800 high strength steel, shown in Figure 10. They found that the top-hat sections absorbed 15% more energy than the square sections at both deformation rates, but were less efficient when comparing mass-specific energy absorption. In quasi-static testing, all specimens underwent progressive folding, however in dynamic testing some specimens exhibited irregular plastic folding. They observed partial pull-out of spot welds during quasi-static testing due to the flanges separating in the folds. In dynamic tests they observed complete and partial pull out of spot welds. They modelled these experiments in LS-DYNA with good agreement of the predicted collapse modes and mean force levels.

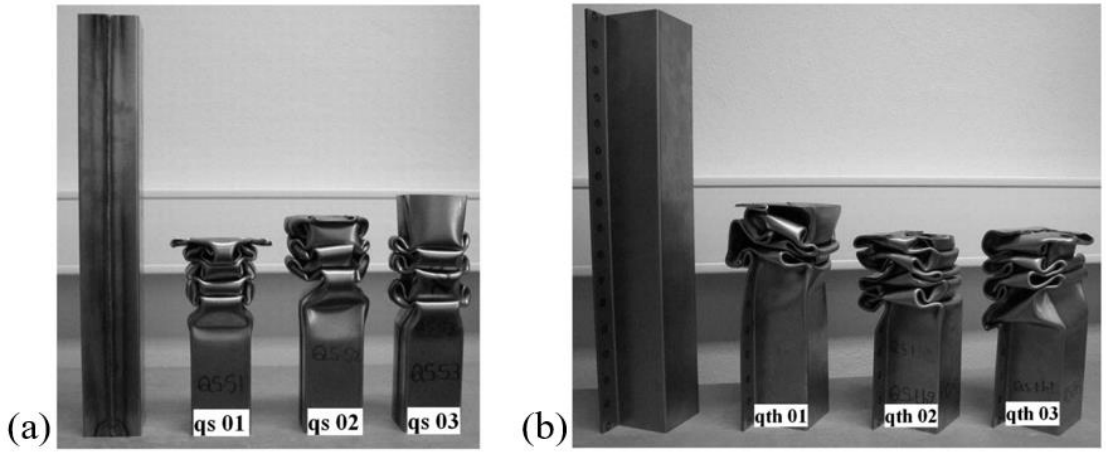

Figure 10: Axial crush specimens with (a) Square profile, (b) Top-hat profile, adapted from [35].

Williams *et al.* [36] studied the effects of tube hydroforming on the axial crush behaviour of EN-AW 5018 aluminum alloy tubes. The numerical model consistently over-predicted the crush loads compared to the experiments. They recommended focusing on characterization of fracture behaviour and anisotropy to improve the model accuracy.

Adebrabbo *et al.* [28] conducted a similar study on the dynamic crash response of hydroformed advanced high strength steel tubes. They found that the tubes formed using a low pressure hydroforming process had higher energy absorption than those formed with the high pressure process, due to the thickness reduction in the high pressure process. Each of the conditions deformed through a progressive axial crush.

Grantab *et al.* [37] investigated dual crush mode welded aluminum crash structures that undergo combined dynamic axial crush and bending collapse deformation modes, similar to the front rails in a vehicle. In this work they performed experimental dynamic testing of isolated tubular s-rails and axial crush rails to determine the collapse load of each section, as shown in Figure 11. Then a numerical study was performed to create a structure that underwent both axial crush and bending collapse folding modes. Parametric studies showed that by increasing the cross-sectional aspect ratio of the s-rail section, the crush load could be increased and the displacement decreased. A separate parametric study showed that increasing the wall thickness of the axial section increased the shearing offset that occurs in that section. By combining these two deformation modes into a single structure, the average and peak loads during crushing were reduced.

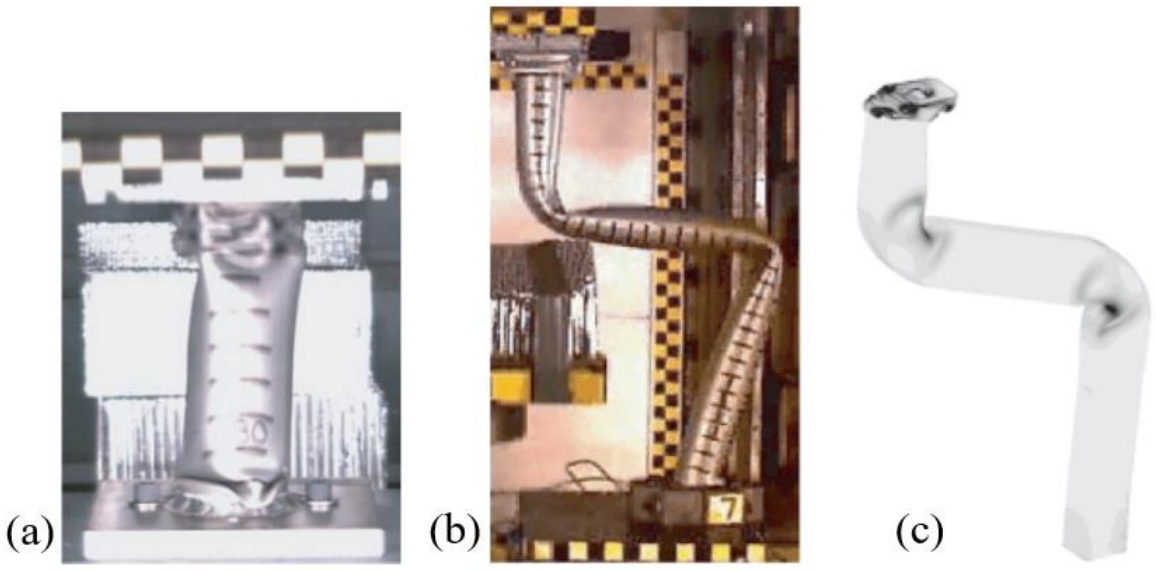

Figure 11: (a) Axial crush test, (b) S-rail crush test, and (c) Dual mode crush model, all adapted from [37].

1.5 Crash Performance of Tailored Hot Stamped Components

The crash performance of tailored hot stamped components can be evaluated in several ways, including: total energy absorption, sustained loads, and the deformation behaviour.

The use of hot stamped components in side impact structures has been investigated in several studies. Eller *et al.* [22] prepared 1.5 mm thick hot stamped IDH top-hat specimens with half of the tool's length heated to 530°C and the other half cooled to 30°C, as shown in Figure 12. Backing plates were spot welded to the bottom of the channels to close the section, and the specimens were subjected to a four-point bend test. They supported a peak load of 45 kN before cracks formed in the fully quenched part of the specimen.

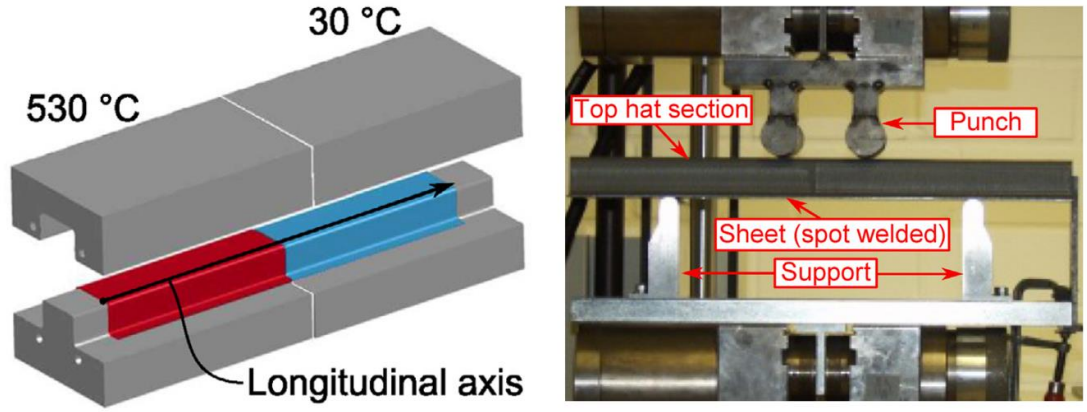

(a) (b)

Figure 12: (a) Axially tailored IDH rail forming tool, (b) Four-point bend test setup, adapted from Eller *et al.* [22].

Sato *et al.* [38] conducted three-point bend tests of several steels, including fully martensitic hot stamped material. These were similar top hat channels with backing plates as were used in other studies [22]. The 1.6 mm thick martensitic material experienced local fracture and supported a 140 kN peak load. This study also investigated the effect of changing the span of the supports used in the bend test. At larger spans the specimen would slide along the face of the impactor and form a tight fold in the center, whereas with a smaller span the specimen wrapped around the impactor.

Prajogo [19] formed top-hat channels with IDH applied to the flanges at temperatures of 25°C and 600°C, as well as an intermediate temperature. Backing plates were spot welded on similar to [22] to create side impact beams. These were tested dynamically in a three-point bend configuration. It was found that the peak loads of the fully quenched and tailored beams were 21.6 kN and 20.0 kN respectively for 1.2 mm thickness, and 42.0 kN and 37.0 kN respectively for 1.8 mm thickness. The extent of fracture was reduced in the tailored beams. They found that two folding modes could occur depending on friction, either a tight fold/collapse or a wrapping mode (Figure 13) similar to what was seen by Sato *et al.* [38].

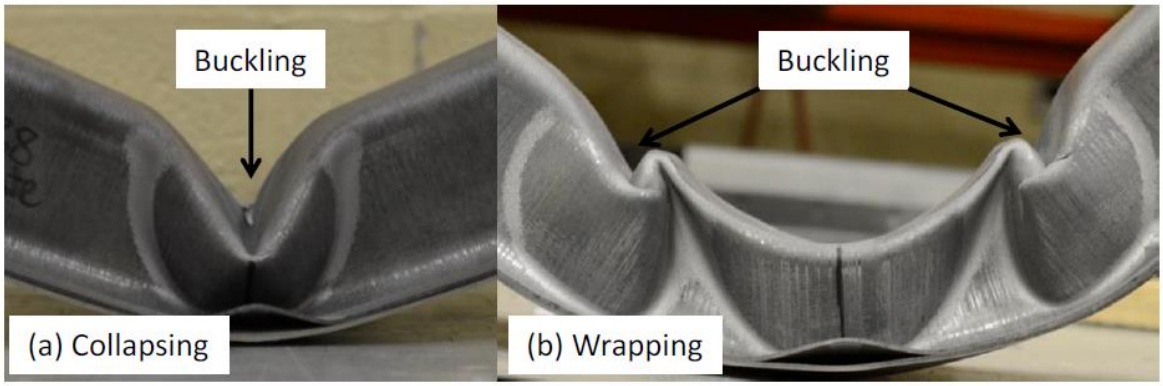

Figure 13: (a) Folding/Collapsing mode and (b) Wrapping mode observed by Prajogo [19].

The performance of resistance spot welds in hot stamped UHSS steel was studied by O'Keeffe *et al.* [39, 40] in various IDH conditions. They tested individual welds in lap shear and cross tension geometries, as well as groups of welds. These group weld tests consisted of two top hat channels spot welded along their flanges, being pulled apart at one end in the through thickness direction as a Mode I loading. They found that failure of welds in the fully martensitic parent metal occurred at low displacements, due either to the severity of the heat affected zone (HAZ) or a low interfacial weld strength, whereas in lower strength tailored parent metal conditions there was more plastic work before failure and a higher weld toughness. In weld group experiments, the low energy absorption of the welds in the martensitic parent metal caused rapid propagation of weld failure through unzipping. The tailored parent metal conditions slowed failure propagation due to their higher energy absorption. Eller [41] also studied spot welded hot stamped material and found similar trends with the HAZ softening being the most severe in base materials with the highest hardness.

There has also been prior work completed on the implementation of tailored hot stamping in frontal crash structures. Omer *et al.* [10, 20, 21] produced crush rails with axially tailored properties using IDH, as was described in Section 1.3.1 and shown in Figure 14. Four different quench conditions were used: fully martensitic, single soft zone 400°C, single soft zone 700°C, and graded soft zone. Each of the tailored parts had a fully martensitic section along one-half of its length, and the die heated to the respective temperature along the other half. The graded parts had the soft zone split into 400°C and 700°C zones. Two of these channels were then spot welded together along their flanges to form a tubular crush rail and subjected to quasi-static and dynamic axial crush tests. In the 165 mm of free crush for the 1.2 mm thickness, the fully martensitic specimens absorbed the

most energy of 14.8 kJ but experienced extensive tearing and fracture (Figure 15) that is undesirable in a vehicle. The single soft zone 400°C and 700°C specimens absorbed 11.4 kJ and 10.4 kJ respectively and underwent mixed buckling and folding deformation. The graded soft zone parts absorbed 12.6 kJ and deformed though the desired progressive folding.

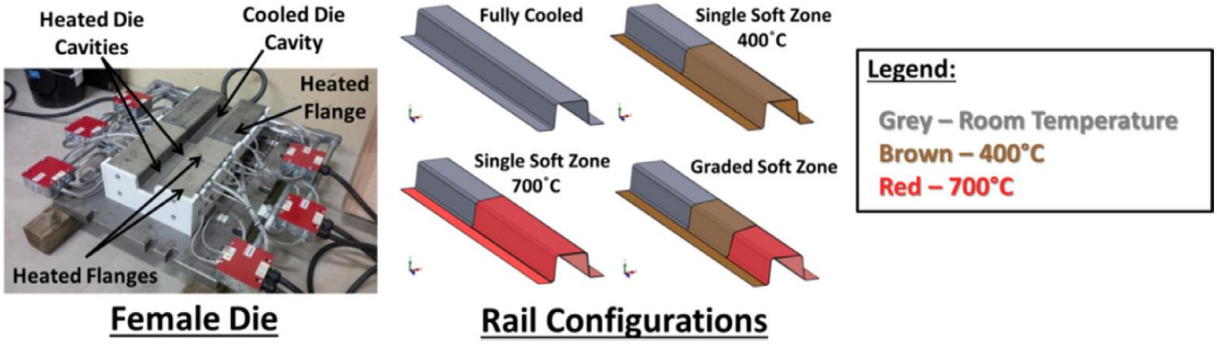

Figure 14: Axial tailoring using IDH sections [21].

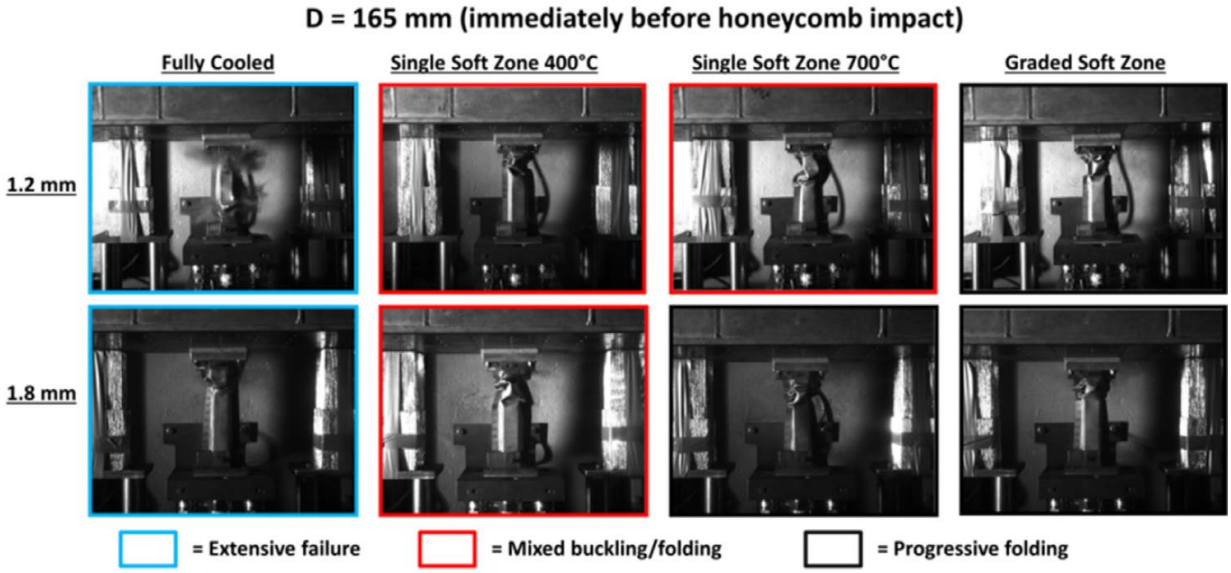

Figure 15: Crush modes for various tailored rails studied by Omer *et al.* [21].

Múnera *et al.* [6] formed top hot channels with axial tailoring comprising TWBs of Usibor® 1500-AS and Ductibor® 500-AS. In three point bend testing performed at 8 m/s, they found that folding and tearing was concentrated in the Ductibor® 500-AS region away from the weld (Figure 16). Axial crush tests were also performed with a closing plate spot welded to the open side of the top hat section. Stable folding was observed in the Ductibor® 500-AS section that was impacted first, with a force level similar to a DP600 steel, and no failure occurred in either base material or in the

weld line. They then performed several numerical case studies on application of hot stamped TWBs to door rings for side impact, and front and rear rails for axial crush. The door ring simulations predicted a reduction in passenger compartment intrusion at the A-pillar while reducing weight by 20% compared to a multi-part door ring composed of mixed high strength steel (HSS) and boron steel. In rear rails, the use of a Ductibor® 500-AS crush tip on a fully martensitic boron steel rail gave similar performance while achieving a 38% weight savings compared to a HSS rail. Similarly a front rail with a Ductibor® 500-AS crush tip and fully martensitic boron steel elsewhere reduced weight by 43% while matching performance of the reference HSS rail.

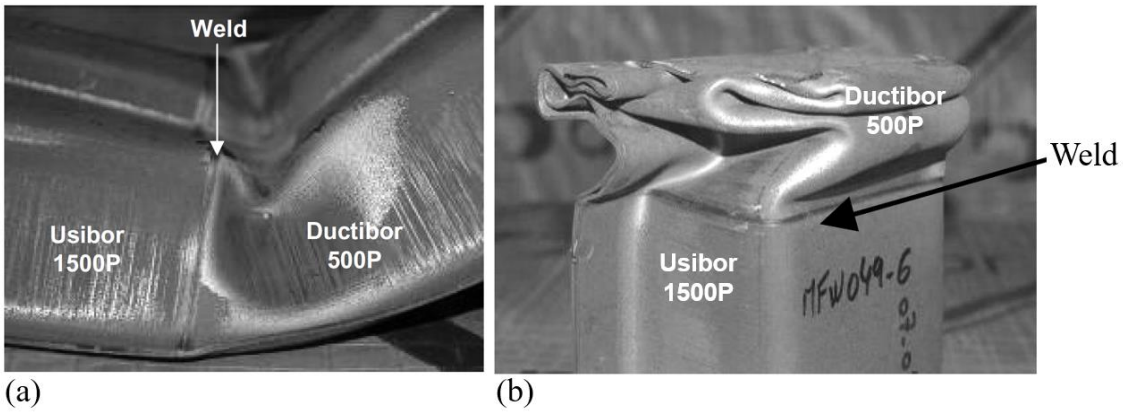

Figure 16: Hot stamped TWBs under (a) Three-point bend test and (b) Axial crush test, adapted from [6].

Apart from those mentioned above, forming and crash performance of Usibor® 1500-AS and Ductibor® 500-AS TWBs have not been studied extensively apart from in publications by this thesis author [12, 13, 14, 15, 42]. The behavior of such TWB axial crush rails is the focus of this thesis.

1.6 Material Model for Hot Stamped Material

In order to numerically model the deformation of tailored components in an impact, the distribution of material properties throughout the part must be known. Forming simulations are used to predict the phase composition of martensite, austenite, and bainite in each element of the model based on the strains and quenching that it experiences. Åkerström *et al.* [43] developed a material model that was implemented in LS-DYNA by Olsson [44] to predict the Vickers hardness and corresponding phase composition in each element.

Bardelcik *et al.* [45] developed the Tailored Crash Model (TCM) to characterize the strain rate-sensitive constitutive response of boron steel after hot stamping by using a Voce-type hardening model and assuming that the coefficients were a function of the Vickers micro-hardness. This model accounted for the presence of martensite and bainite only. Bardelcik *et al.* [46] then created the Tailored Crash Model II (TCM II) that also accounts for ferrite in the microstructure, which gives a better prediction of constitutive response. The parameters in the TCM II are functions of the area fraction of the martensite, bainite, and ferrite phases instead of the Vickers hardness like in the original TCM. Omer *et al.* [21] defined a hardness dependent material model called eTCM (extended TCM) based on the TCM II to predict the behaviour of Usibor® 1500-AS at any hardness ranging from soft IDH ranges to fully quenched martensite (Figure 17).

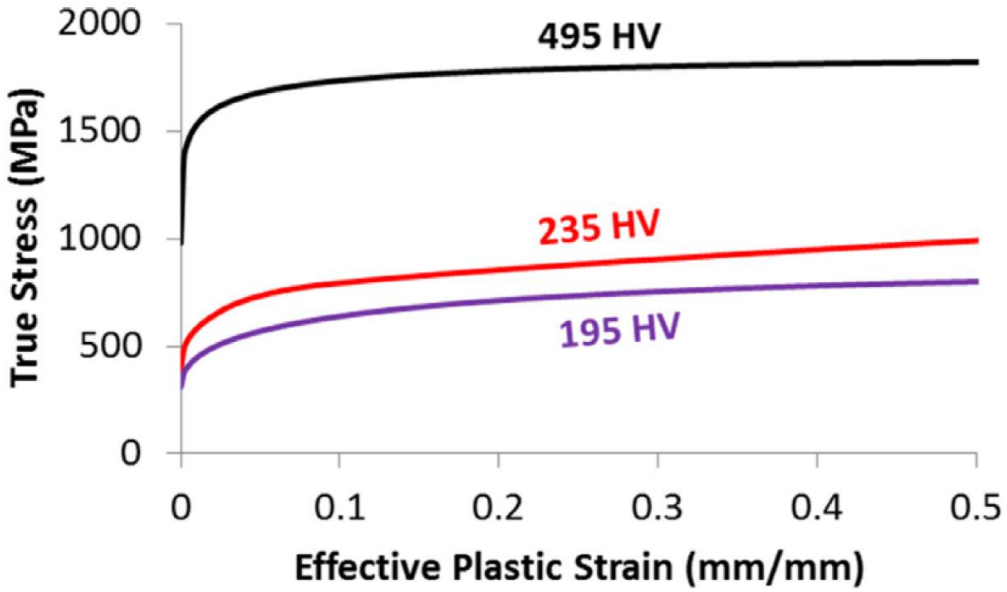

Figure 17: Flow stress curves for several IDH quench conditions of Usibor® 1500-AS [21].

When modelling crash events involving materials with low ductility, the fracture behaviour must also be characterized in order to predict the initiation of cracks. The onset of fracture must be accurately predicted in order to accurately simulate the experiment, as deformation modes can change significantly. The Generalized Incremental Stress State dependent damage MOdel (GISSMO) is a commonly used phenomenological damage (fracture) model, described by Haufe *et al.* [47]. It uses Eq. (1) to define a scalar damage variable, D, that is a function of a user defined damage exponent (n), the equivalent plastic strain (ε_p), and the plastic strain at failure (ε_f) that is

defined by a fracture *loci*. The fracture loci for hot stamped components formed using various IDH conditions were developed by ten Kortenaar [48] and are shown in Figure 18.

$$\Delta D = \left(\frac{nD^{\left(1-\frac{1}{n}\right)}}{\varepsilon_f} \right) \varepsilon_p \tag{1}$$

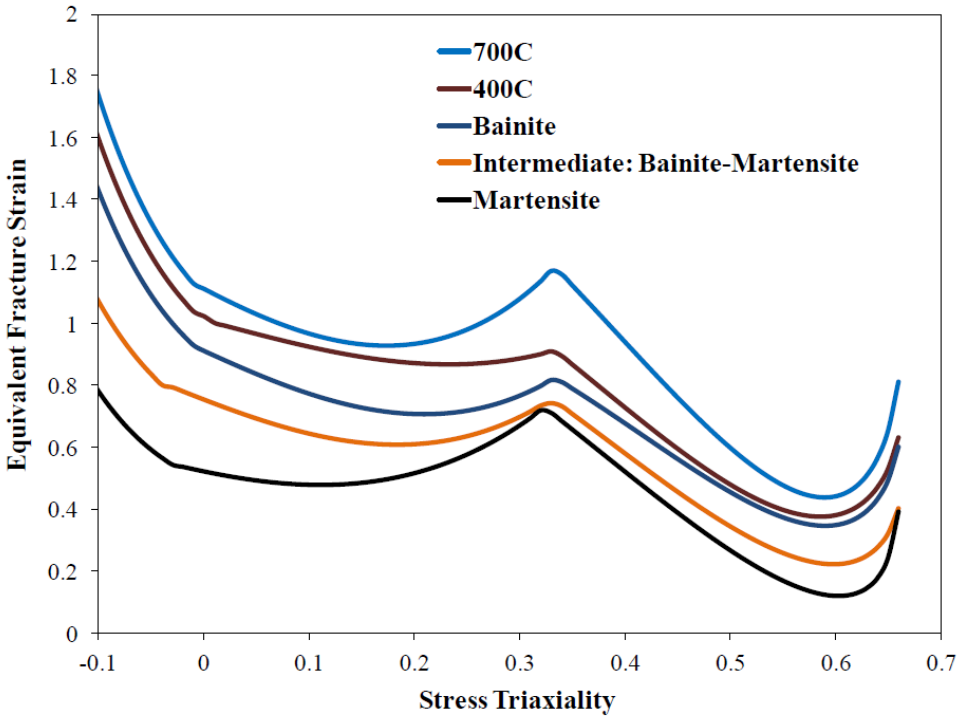

Figure 18: Fracture loci for Usibor® 1500-AS in several IDH die temperature conditions [48].

1.7 Numerical Modelling of Crash Events

Crash experiments of automotive components made from sheet metal are typically modelled using shell elements in order to limit the computational load of a full vehicle crash simulation. In component level simulations, the shell elements at the non-impacted end of the specimen are often constrained in all directions to simulate being clamped to a fixture [49, 50, 51]. The impactor is modelled as rigid, with either an initial velocity and mass for dynamic tests, or a prescribed constant velocity for quasi-static tests. Contact is defined between the impactor and the specimen, as well as between the specimen and itself to account for folding. For each contact a friction coefficient must be specified. Force-displacement response of the part can be obtained by tracking

displacement of nodes on the impactor, and the contact force between the impactor and specimen. Integration of the area under the force-displacement curve gives the energy absorption.

Prajogo *et al.* [49] modelled the quasi-static axial crush of a hot stamped channel section by constraining the nodes within 25.4 mm of each end of the rail. At the fixed end, the nodes were fully constrained to simulate being bolted to a fixed wall. At the impacted end the nodes were constrained in five degrees of freedom, allowing movement only in the direction of the impactor. The impactor was modelled as a rigid flat face and was given a prescribed velocity.

Bardelcik *et al.* [50] simulated the three point bend impact test on a B-pillar using a quarter-symmetry model. The flanges where the pillar would be welded to the side-sill of a vehicle were fully constrained to simulate this joint. The specimen was impacted with a cylindrical impactor at a speed of 10 m/s.

Another rail crush model was created by Ma et al. [51]. They fixed the nodes at one end of the rail, and impacted the other end with a flat plate.

1.8 Current Work

This review of the current literature has shown that a great deal of knowledge exists relating to the hot stamping process. The production and performance of fully martensitic components is well understood and they have been adopted by many OEMs to improve crashworthiness and reduce weight.

Tailoring through IDH has also been the subject of many studies, both experimental and numerical. The effect of locally heating the forming die has been characterized for both side impact and axial crush loading conditions. The TCM, TCM II, and eTCM constitutive models have been validated experimentally and shown to predict the crash performance of IDH tailored components. This process has been applied extensively in side impact, and has seen use in commercial rear impact structures such as in the 2016 Honda Civic, for example.

There is less understanding of the hot stamping of Usibor® 1500-AS and Ductibor® 500-AS TWBs. Some numerical studies have been performed, as well as a few crush test experiments performed by the material supplier, but extensive crush characterization has not been published as far as the author of this thesis is aware. Hence, the focus of this thesis is to characterize the axial crush and side impact performance of these TWBs.

The work done in this thesis is a part of a larger collaborative research project sponsored by Honda R&D Americas, Promatek Research Centre, and ArcelorMittal. The overall aim of this larger project is to support the application of TWBs to reduce vehicle weight within vehicle front structures. The project goals include assessment of the crash energy absorption and weight reduction potential using TWBs comprising Ductibor® 500-AS welded to Usibor® 1500-AS, as well as Ductibor® 1000-AS to Usibor® 1500-AS.

In support of these goals, the current thesis is focused on TWBs comprising Ductibor® 500-AS welded to Usibor® 1500-AS, and addresses three primary objectives:

1. Establish the baseline crush performance of a current, driver's side front side frame structure within a current production SUV.
2. Characterize and model the axial crush and side impact performance of single- and multi-gauge hot stamped TWBs comprised of Ductibor® 500-AS welded to Usibor® 1500-AS.
3. Develop numerical models predicting the crush behaviour of the SUV front side frame after replacement of the current JAC590R crush tip with Ductibor® 500-AS.

The first objective involved the design of fixtures and conducting crash tests on the driver's side front side frame using the University of Waterloo (UW) crash sled. These tests have served to characterize the performance level of the current production side frame, which are used to assess future versions of the side frame utilizing hot stamping technology. Research in support of the side frame crash tests is presented in Chapter 2 of this thesis.

The second objective was pursued through a detailed study of the crash response of hot stamped TWBs utilizing Ductibor® 500-AS welded to Usibor® 1500-AS. Experiments were developed that involved the forming of hot stamped monolithic (Ductibor® 500-AS only) and TWB top-hat channels that were subsequently used to fabricate axial crush rails and side impact beams. The forming process and characterization of the as-formed top-hat channels is presented in Chapter 3 of this thesis. These laboratory-scale assemblies were impact tested using the UW crash sled and quasi-static experiments were also tested using hydraulic test frames. The mechanical testing procedures and experimental results are presented in Chapters 4 and 5, respectively. Numerical models of each test condition were developed and validated against the experimental results, as described in Chapters 6 and 7 of this thesis.

The validated constitutive and fracture models for hot stamped Ductibor® 500-AS were then used to develop a numerical model of the baseline front side frame structure. Specifically, the crush behaviour of the crush tip section of a hot stamped side frame was modelled to assess whether Ductibor® 500-AS is a viable alternative material for this application. These simulation results are presented in Chapter 8 of this thesis.

The thesis closes with discussion of the results, followed by major conclusions and recommendations for future work (Chapter 9).

2.0 Establishing the Baseline Performance of a SUV Front Side Frame

A great deal of prior crashworthiness research has been done at UW (and elsewhere) using lab scale components, including work by George [16], Omer [20], Prajogo [19], and Kim [52], for example. These simplified geometries allow for less complicated forming tools and easier assembly of test specimens. The drawback of lab scale components is that they fall short of replicating the complex part geometry, loads, and boundary conditions that exist in an actual vehicle structure.

For this reason, a lightweight demonstrator hot stamped side frame component is under development as a part of the broader research project of which this thesis project is one part. This demonstrator component will incorporate hot stamped laser-welded blanks within the side frame of a current mass production SUV in an effort to assess the potential for weight savings. As a first step in the development of a hot stamped demonstrator structure, an existing baseline structure was developed based on the current mass production SUV. This chapter presents the design and results of experiments performed to assess the crash behavior of this baseline structure which is fabricated primarily of cold stamped JAC590R sheet. Subsequent chapters in this thesis examine hot stamped TWBs and the incorporation of hot stamped Ductibor® 500-AS sheet into the axial crush tip of the baseline structure.

This chapter opens with an overview of the demonstrator structure design (which is due to Tummers [53]), followed by the experimental design which was developed as part of the current work. The experimental results from testing of the first three baseline demonstrator structures is then presented, which serves to validate the testing method and provides an understanding of the structural behavior of the demonstrator structure.

2.1 Baseline Commercial Side Frame Demonstrator Structure

The commercial SUV front side frame assembly, shown in Figure 19 and Figure 20, consists of left and right side frames, each with three main sections. The first is the axial crush tip section, which is a straight rail section designed to collapse through progressive folding to absorb energy. The second section is an axial buckling region that buckles outwards once the crush tip is fully consolidated and the crush loads increase. The buckling action serves to prevent overloading of

the third (s-rail) section, while at the same time absorbing impact energy. This third section is the intrusion resistant s-rail zone. This intrusion resistant zone transmits crash loads to the lower structure of the vehicle, while preventing deformation (intrusion) into the area occupied by the occupant's feet.

Figure 19 shows a left-right pair of front side frames with the materials and sections labelled. Figure 20 shows the location of these side frames in the overall structure of the SUV. The baseline commercial front side frame is composed primarily of JAC590R, a ferritic/bainitic steel with a strength of about 600 MPa. The exception to this is a single stiffener panel made of JAC980Y, a dual phase steel with a strength of about 1,000 MPa. This stiffener is used to reinforce the intrusion resistant s-rail zone.

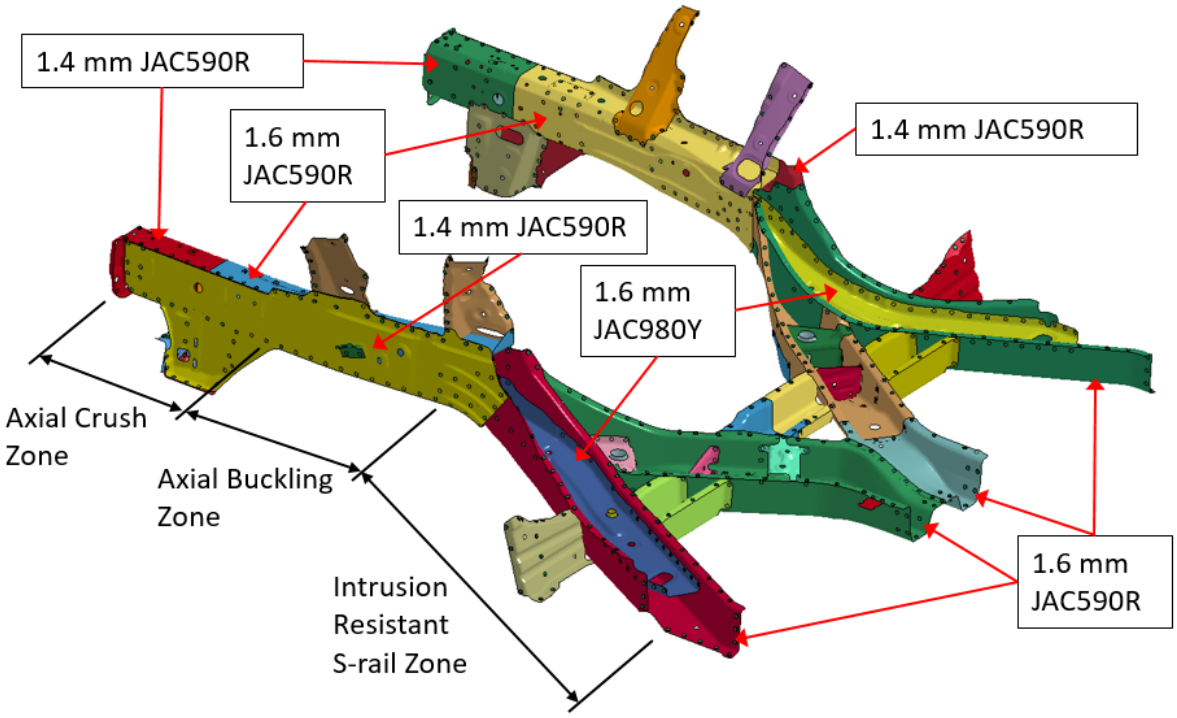

Figure 19: Left-right pair of baseline commercial side frame assemblies, showing gauges and sheet alloys used in major components.

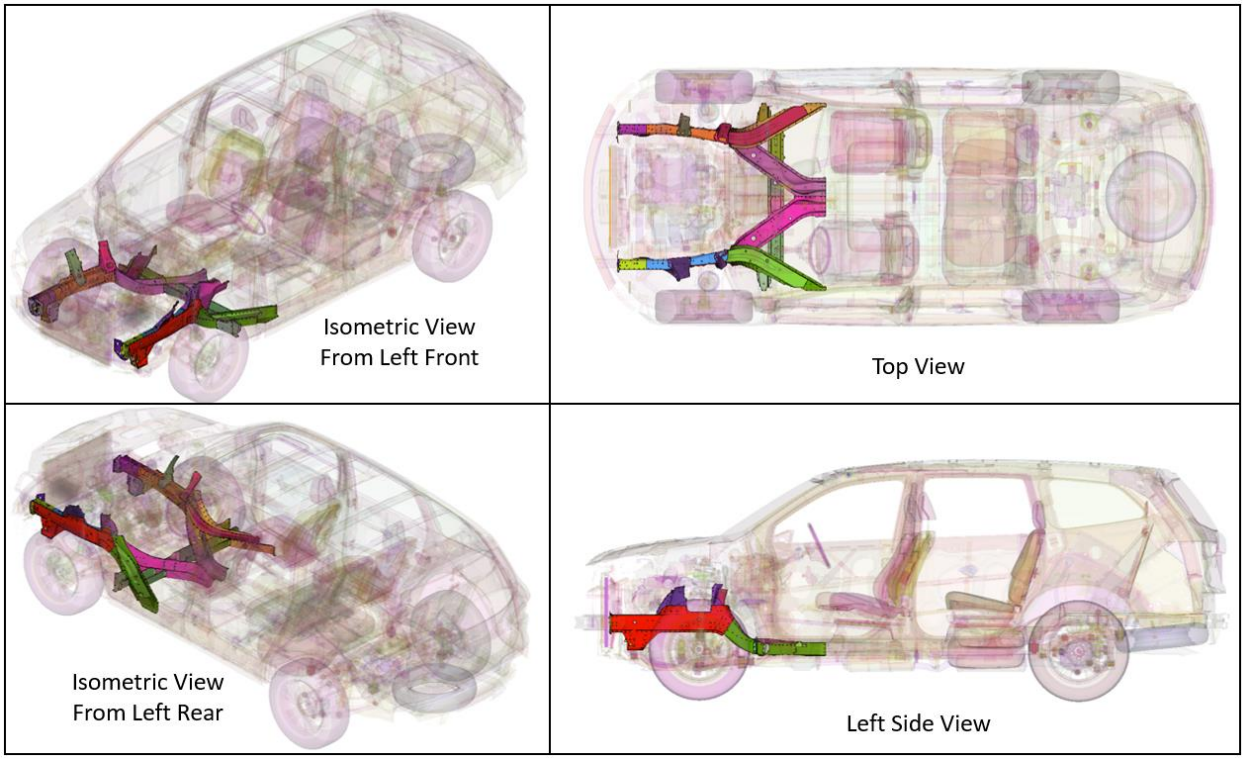

Figure 20: Location of baseline commercial side frames in the SUV body. Adapted from Malcolm [54] by Tummers [53].

2.1.1 Overview of Demonstrator Structure Design

The design of the baseline demonstrator structure was developed as part of related research by Tummers [53]. In that work, numerical simulation was used to establish the minimum extent of supporting structure required to ensure that the side frame components (Figure 19) deformed in a manner similar to that observed in a full vehicle during a US New Car Assessment Program (NCAP) Full Width Rigid Barrier frontal crash test, in which the vehicle hits a stationary barrier at a speed of 56 km/h [55]. To reduce cost and simplify the required fixtures, testing is conducted only on the left hand side frame. Figure 21 shows several views of the demonstrator structure which comprises a left-hand side frame and shock tower assembly, along with portions of the lower firewall and floor pan. Figure 22 shows where the demonstrator structure components are located in the overall body structure of the SUV. One additional component required for the demonstrator structures is the plastic “battery base” shown in Figure 23. Because this plate bolts to the side of the crush tip, it could have an effect on the folding behaviour so it was included in the tests.

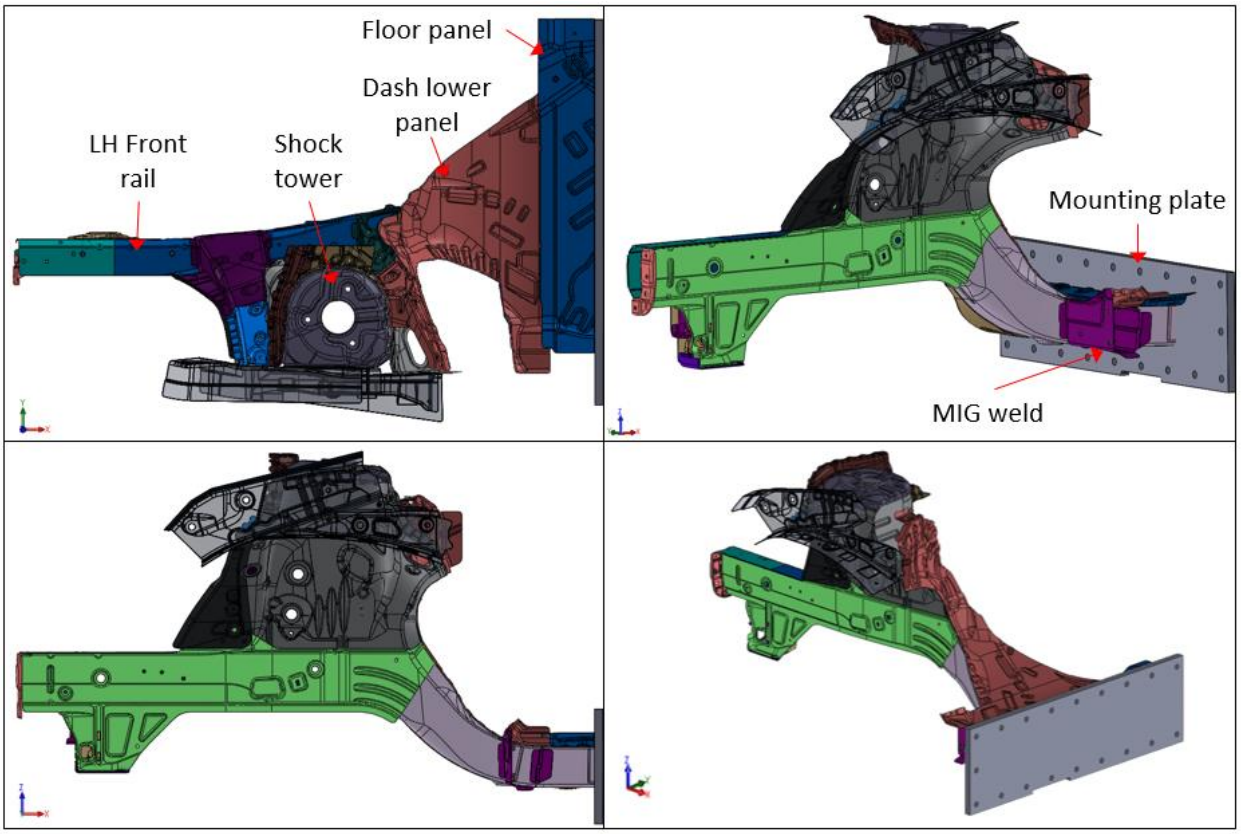

Figure 21: Baseline demonstrator structure specimens for testing on UW sled.

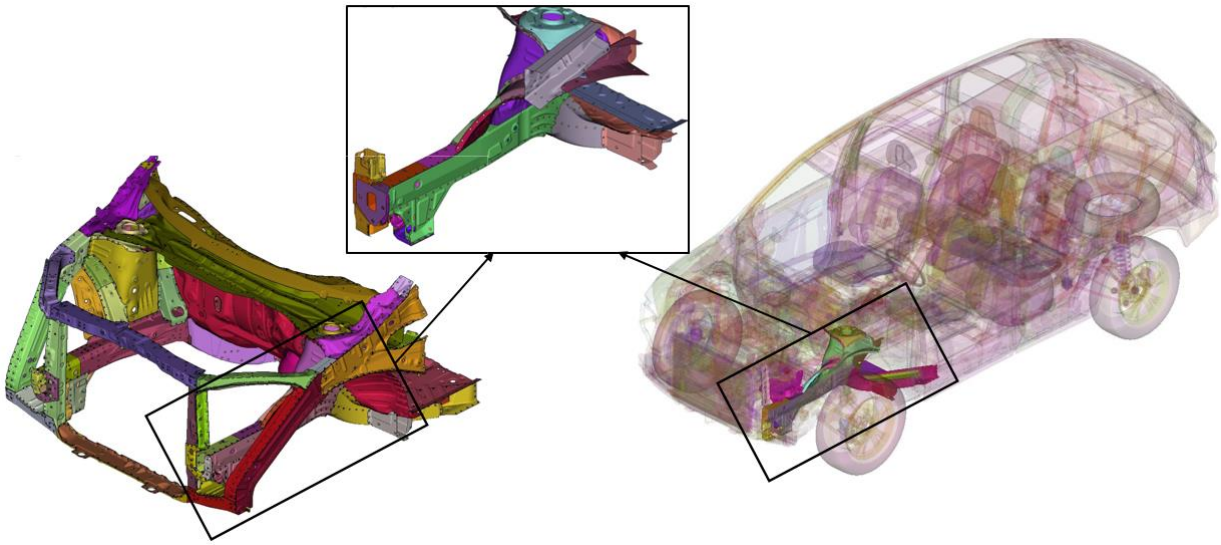

Figure 22: Reduced side frame for baseline demonstrator structure shown in the full SUV body structure. Adapted from Malcolm [54] by Tummers [53].

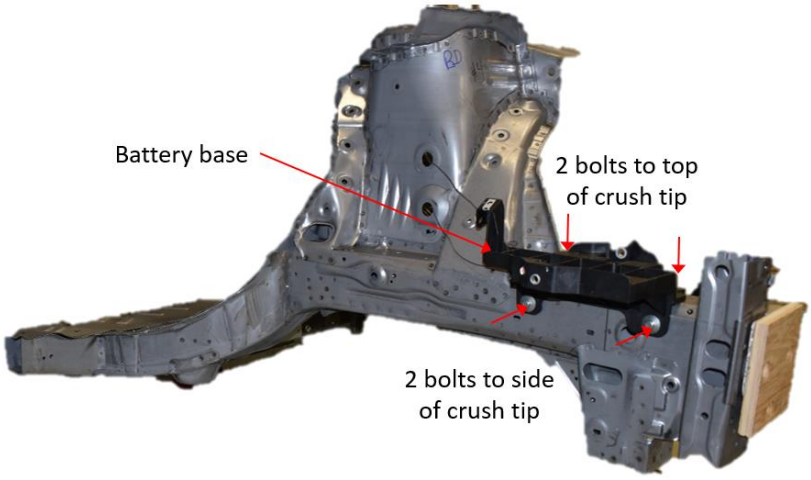

Figure 23: Position and mounting of battery base for the baseline demonstrator structure.

The demonstrator structures were fabricated by the fabrication group at Honda Research and Development Americas (HRA) using components sourced directly from their manufacturing division and assembled using production spot and MIG welding techniques. This means that the parts being used are identical to those that are sent to the production lines to build into vehicle bodies.

To facilitate attachment to the fixed barrier wall, Figure 24 shows how the irregular s-rail end of the part was laser cut off along the back edge of the cross-member (red dashed line) to give a flat plane that is welded to a 19.1 mm (¾") steel plate. This plate contains 19 holes that are used to bolt the specimen to the fixed barrier wall. Welding was performed around the inside and outside of the two C-channel cross sections using a MIG welder. Once welded, the open cross-section of the channels was closed in by spot welding sections of the vehicle's lower dash and floor panels into place. These panels were also sourced from the production division and laser cut to the shape of the specimens (Figure 24). All of the cutting, welding, and other modifications to these test specimens was performed by the fabrication department at HRA. Once assembled, these specimens were shipped to UW for testing.

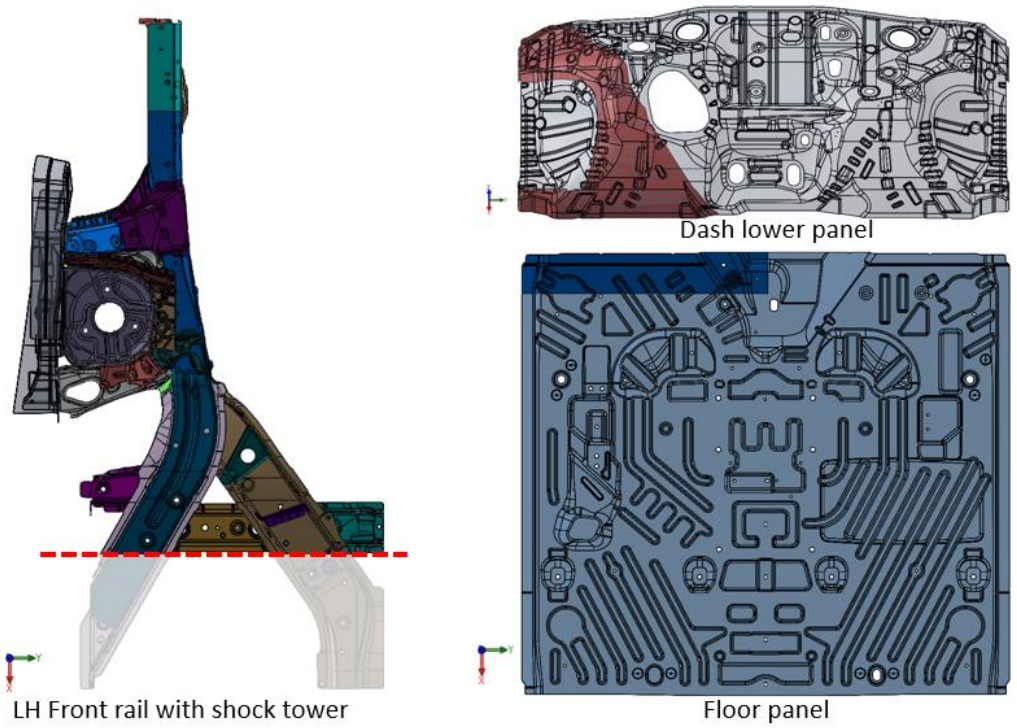

Figure 24: Laser cutting lines for front rail, dash lower, and floor panels.

2.2 Design of Crush Experiment for Baseline Demonstrator Structure

The test fixtures for the demonstrator structure were developed as part of the current research and are shown in Figure 25. The plate welded to the end of the intrusion-resistant s-rail section is mounted to the fixed barrier wall, with the impacted end extending forward and upwards to meet the crash sled. The shock tower support (Figure 27) is bolted to the fixed barrier wall and serves to react the moment induced by the vertical offset of the s-rail and resulting uplifting force that would cause the rail to buckle. The commercial shock tower (also known as damper housing) is used as the attachment point to the shock tower support. This is an approximate representation of the support given by the shock tower being spot welded into the structure of the A-pillar and fender area, which ties into the roof structure of the car. The A-pillar structure was not used in order to simplify the demonstrator structure design.

The other key elements of the test design are the sled impact wall and the primary honeycomb arrestors which dissipate excess kinetic energy (not absorbed by the test article) and decelerate the sled to avoid damage to the sled. The demonstrator structure is more than twice as long as the parts

typically tested on the UW crash sled. In addition, the structure is quite wide which complicated the positioning of the primary honeycomb arrestors.

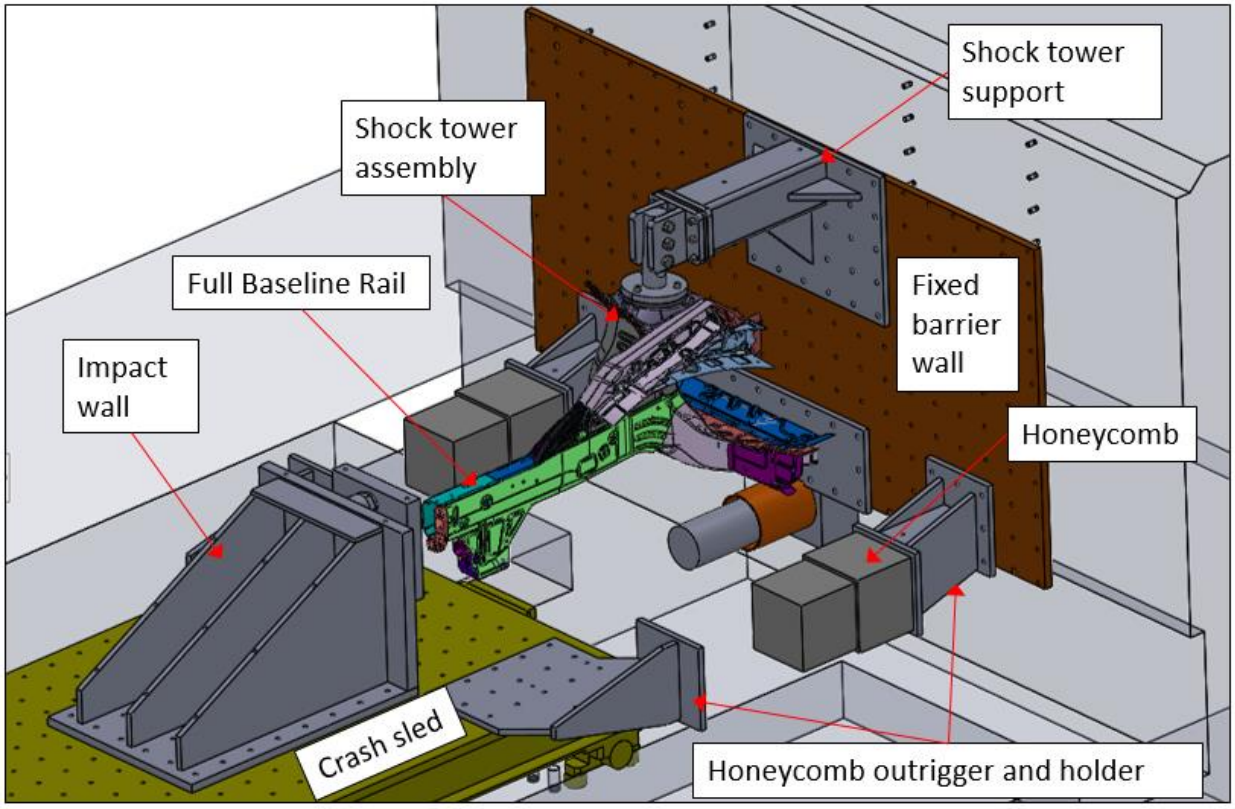

Figure 25: Finalized testing setup design for demonstrator structures.

To address these issues, a new, more compact impact wall was designed that would bolt to the top face of the sled and would serve to locate the impact wall towards the rear of the sled. To accommodate the width of the demonstrator structure, new honeycomb arrestors were developed that mount further outboard than normal. On the sled, outriggers bolt to its surface and strike the honeycomb mounted outboard of the sled. On the wall side, honeycomb holders support the blocks of honeycomb at the proper height and outboard position to engage with the sled outriggers. During the test, the front of the sled passes under the front of the rail specimen until the rail is impacted by the impact wall. As the rail crushes, the sled continues to advance until either the rail absorbs all of the energy, or the honeycomb attenuators engage to absorb the remaining energy. The peak loads predicted by the numerical model (due to Tummers [53], Figure 26) were used to design the test fixtures.

The test fixtures were manufactured by the UW Engineering Machine Shop and installed on the Seattle Safety D780-3.7 crash sled [56] at UW.

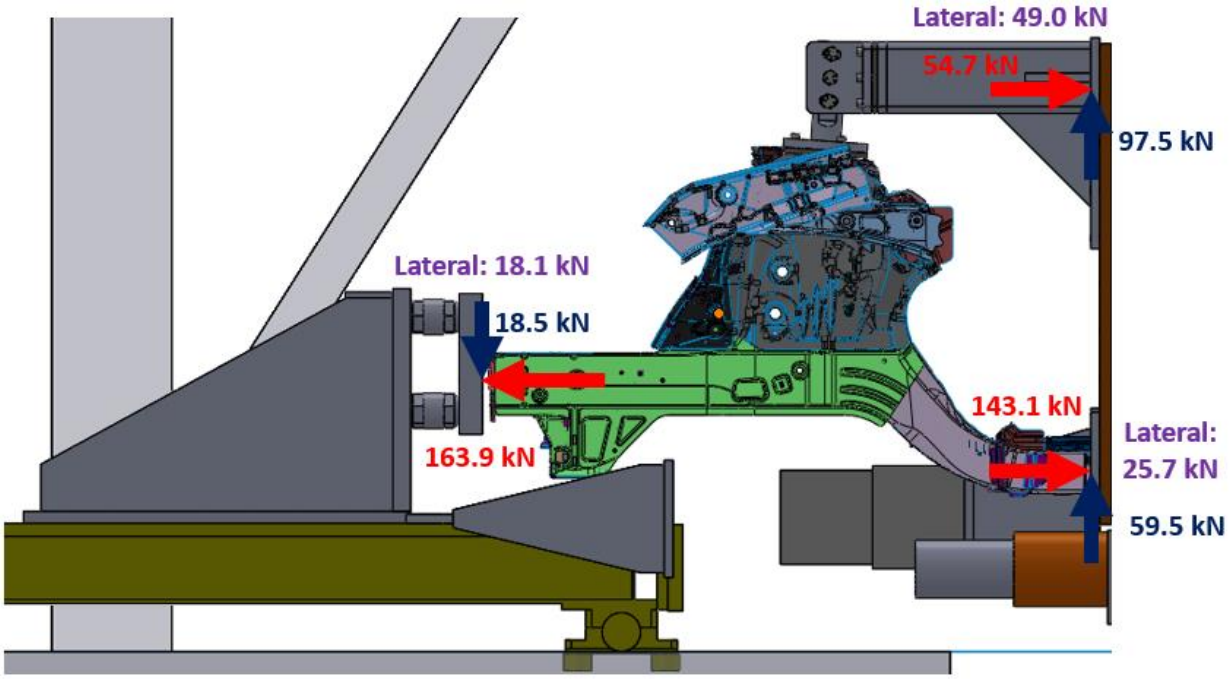

Figure 26: Peak loads predicted by the numerical model (due to Tummers [54]) at the shock tower support, fixed s-rail end, and impact wall in testing of baseline demonstrator structures.

2.2.1 Shock Tower Support

The support at the shock tower is needed to withstand an uplifting force of 97.5 kN, and a lateral load of 49 kN. Figure 27 shows a mount that was designed to insert into the top of the shock tower and sandwich it between a 19.1 mm (¾") thick steel plate above and a 12.7 mm (½") thick steel plate below, with bolts passing through the original holes in the shock tower that would mount the front strut. These holes in the shock tower were enlarged from 11.5 mm to 13.5 mm in diameter to allow the bolts to pass through. A 63.5 mm (2.5") diameter steel round bar is welded to the upper of the two plates and extends upward. The upper end of this bar has two sides machined flat, and three holes drilled through it. These allow the bar to be bolted in double shear to a 19.1 mm (¾") steel bracket. This bracket was later modified to remove one side of it and put the bolts in single shear, as will be discussed in Section 2.3. This bracket is mounted to the end of a 152 mm x 152 mm x 12.7 mm (6" x 6" x ½") hollow structural steel (HSS) box section extending out from the fixed barrier wall. At the wall, this HSS is welded to a large piece of 19.1 mm (¾") thick steel plate, which is held to the barrier wall by 26 M12 socket head cap screws. These screws thread

into M12 threaded holes in a 100 mm grid on the fixed barrier wall. Gussets are added to the sides and bottom of the HSS to support the transverse loads.

It was anticipated that there may be a small amount of geometric variation between the prepared test specimens due to their large size. To account for potential variation, the shock tower support was designed to be shimmed up and down at the top of the shock tower, and forward and backward where the bracket is bolted to the end of the HSS. The holes on the bracket are also slotted to allow it to move from side to side, and for the bar to rotate about the center bolt hole.

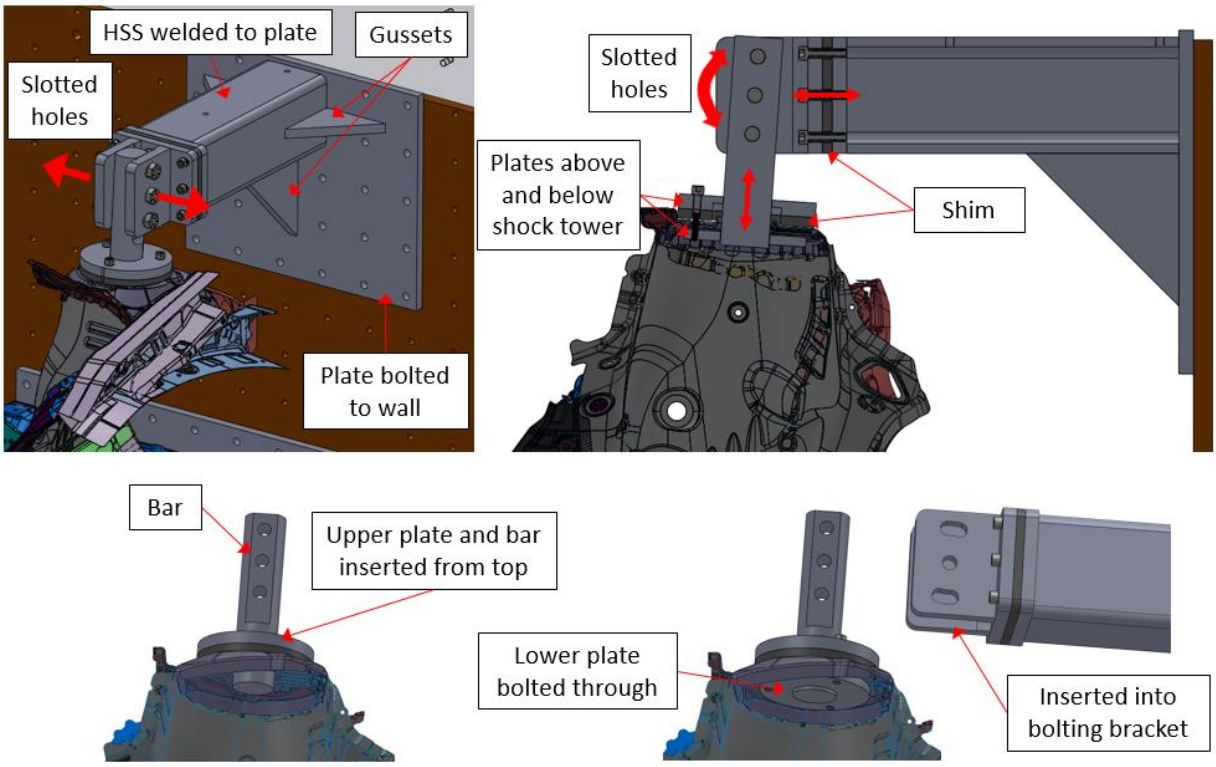

Figure 27: Shock tower support detail.

2.2.2 Sled Impact Wall

The impact wall shown in Figure 28 is constructed as a large weldment from hot rolled (HR) steel plate. It bolts to the 100 mm grid of M12 threaded inserts on the top face of the crash sled. The overall size of this impact wall is 580 mm wide by 500 mm tall, with the base plate extending 825 mm in length. It is designed to be extremely stiff because deflection during a test will affect the load cell measurements. The base plate is machined from 25.4 mm (1") thick HR steel plate and contains 48 clearance holes for bolting to the top of the sled. The vertical impact face is machined from 38.1 mm (1-½") thick HR plate and welded to the top of the base plate, aligned

with its front edge. Three 19.1 mm (¾") thick supports brace the impact face against the base plate. A fourth support joins the tops of the other three. These plates are MIG welded together along all of their contacting edges with a 15 mm fillet weld. After welding the bottom of the base plate is machined flat, and the front of the impact face is machined flat and perpendicular to the base. Three threaded holes are added to the impact face for mounting of load cells.

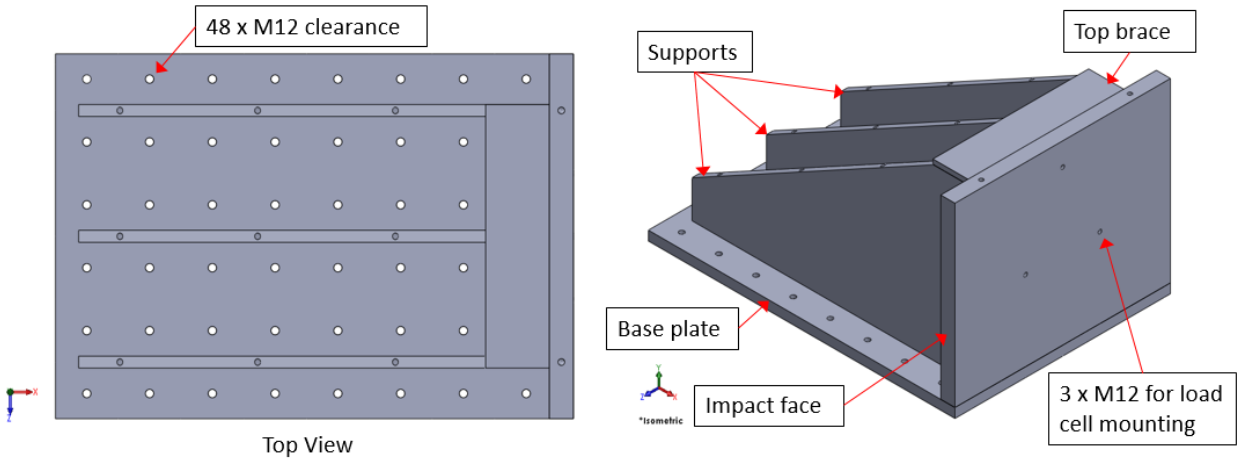

Figure 28: Sled impact wall detail.

2.2.3 Honeycomb Outrigger System

The honeycomb outrigger system (Figure 29) was designed to move the honeycomb attenuators outboard of the sled so that they could mount on either side of the test specimen. This system also moves the honeycomb down lower than normal so that its centerline is even with the top face of the sled. This reduces the uplifting force on the front wheels of the sled when the honeycomb is impacted.

On the sled side, identical outriggers mount on either side at the front edge. This simple design consists of just three parts, all cut from 19.1 mm (¾") HR steel plate. The base plate is about 400 mm wide by 550 mm long and contains 15 clearance holes that are used to bolt it to the M12 inserts on the top of the sled. At the front of this base plate is the 250 mm square impacted plate. This plate gets additional support from a triangular shaped plate along the side of the base plate. These three parts are MIG welded together to form a rigid structure on either side of the sled. The impacted face is machined after welding to ensure it is flat.

On the wall side, honeycomb holder blocks were designed that mount the honeycomb 290 mm in front of the fixed barrier wall, lowered to align with the sled outriggers. Each honeycomb holder

is attached to the 100 mm M12 grid on the fixed barrier wall with seven M12 bolts through the back plate. Two side plates drop the front plate by about 100 mm, and are stabilized by boxing in the profile with top and bottom plates. The front and back faces of these holders are machined after welding to ensure they are flat and parallel to each other. A stack of two or three honeycomb blocks is used in these tests, with an expected size of 220 x 220 mm and 200 x 200 mm. These are attached to the front plate of the honeycomb holder using adhesive duct tape. The initial design allowed for 250 mm of "free crush distance" corresponding to the sled travel after impacting the demonstrator structure and prior to engagement of the honeycomb arrestors. As described below, several different honeycomb arrestor configurations were considered during testing.

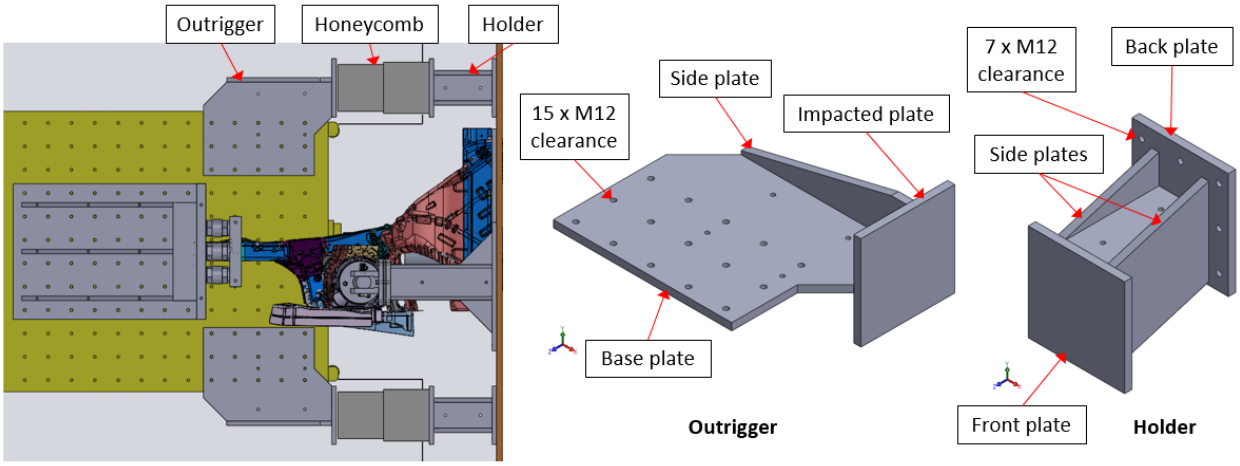

Figure 29: Honeycomb outrigger system detail.

2.3 Baseline Demonstrator Structure Experimental Setup

The baseline demonstrator structures were impact tested using the Seattle Safety D780-3.7 crash sled [56] at UW. This sled can travel up to 91 km/h and carry a payload of up to 1400 kg, with an upper bound of 169.5 kJ of energy. The sled itself measures 1.2 m wide by 2.5 m long and weighs about 356 kg, not including the 23 kg crush can mounted on the front of it. This sled rolls along rails in the lab floor. It is propelled by opening an electronically controlled butterfly valve that releases compressed air from a reservoir into a cylinder in the floor beside the sled, pushing a piston that pulls a rope attached to the sled.

In the current tests, a consistent crush speed was desired, so the sled was propelled with more kinetic energy than the demonstrator structure could absorb. The total mass of the sled and test fixtures was 795.3 kg. The honeycomb arrestors were Plascore 5056 with 3.2 mm (1/8") cells

which has a crush strength of 3.69 MPa (535 psi) [57]. An additional higher stiffness tubular honeycomb column was mounted beneath the specimen with a longer free crush distance from the sled (Figure 25). In the event that the primary arrestors failed to stop the sled, this "emergency honeycomb" would rapidly stop the sled once engaged.

Just before the sled struck the end of the specimen, it crossed a laser trigger (Figure 30) that began logging test data at 10,000 Hz for a period of 1 second. The measurements from three 120 kN Kistler 9731B piezoelectric load cells mounted between the impacted plate and the sled wall are summed to measure the force transmitted through the baseline demonstrator rail. The sled is instrumented with an accelerometer on each side, which are averaged to measure its deceleration. After initial contact with the specimen, this deceleration is integrated to find the velocity and double integrated to calculate the displacement of the sled. Four high speed cameras are used to record the crush event at 10,000 frames per second. A Photron SA-4 camera was mounted directly above the rail, a Photron SA-1 was mounted on one side of it, and two Photron SA-5s were mounted on the other side. A spot welded flange on the left side of the crush tip was recorded at 5,000 frames per second using a Telops FAST-IR 2K thermal imaging camera to capture the heat generated by folding and spot weld failure. A wider field view was also recorded at a much lower speed of 60 frames per second using a Nikon D3500 DSLR camera.

Each test generates a series of spreadsheets logging the measurements acquired from the sled mounted load cells and accelerometers with respect to time. A master spreadsheet is built to capture all of the test data for the series of tests. This sheet calculates displacement with respect to time by integrating and filtering the accelerometer data, and zeroing the displacement until the time of first impact. The time dependent force and displacement data can then be related to each other to determine force versus displacement. From this, the energy versus displacement curve is determined by integrating the area under the force versus displacement curve using the trapezoid rule shown in Equation1:

$$E_i = E_{i-1} + 0.5(F_i + F_{i-1})(d_i - d_{i-1}) \quad (1)$$

E_i is the total energy absorbed, F is the force in the specimen, and d is the displacement of the sled. The subscripts i and $i-1$ indicate the value at the current and previous time step respectively.

Since the load cells are mounted on the sled in this test configuration, the deceleration of the sled will have an inertial effect on the impactor mounted to these load cells. At each time step, the mass

of the impactor multiplied by the acceleration of the sled is subtracted from the measured load to account for this.

Figure 30 also shows the wheel assembly that is mounted on each of the four corners of the sled. Wheels above and below the rail react uplifting and downward loads, while wheels along the edge of the rail react lateral loads. The load capacity of the sled is largely dictated by the rating of the bearings on these wheels.

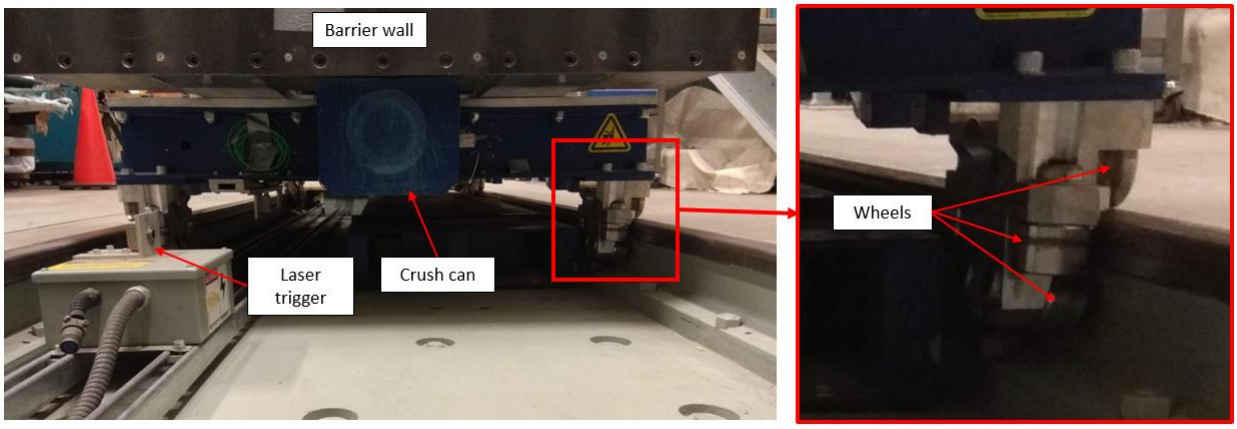

Figure 30: Laser trigger to begin data logging, crush can and wheel assembly also shown.

After installing the first test specimen on the fixture, the bracket used in the shock tower support (Figure 27) was found to be too stiff, preventing sufficient clamping force between the bracket and the bar on the shock tower. Undesirable movement within the clearance of the bolt holes was anticipated in the tests, so to improve the clamping force, the bracket was modified as shown in Figure 31. By removing one side of the bracket, it allowed for more clamping force between the bracket and the bar on the shock tower, inhibiting movement during the test. It also made it much easier to align the part prior to bolting it in place. The bracket was significantly over designed initially, so the remaining half of it is sufficiently strong to withstand the loads seen in these tests.

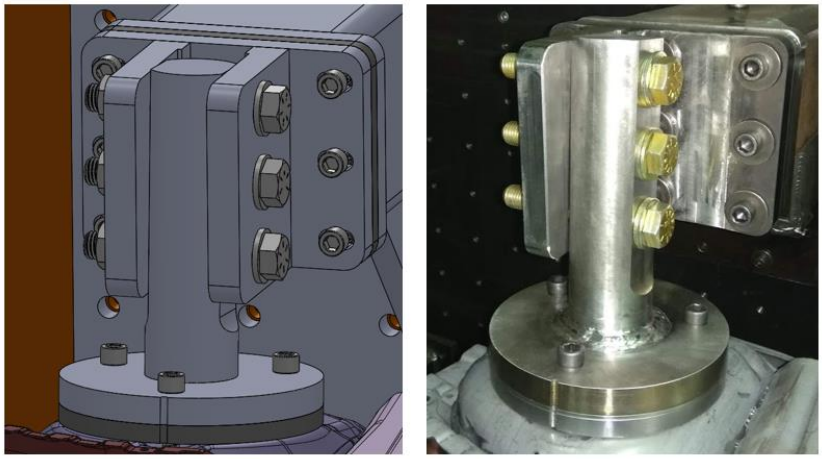

Figure 31: Modification made to shock tower support bracket.

A total of three demonstrator structures were tested as part of this research. The testing configurations used for each structure are summarized in the following.

2.3.1 Test 1: Baseline Demonstrator #1 (bd_1)

Figure 32 shows the first baseline demonstrator specimen (bd_1) mounted in the fixture for testing. A stack of two blocks of honeycomb, 230 mm x 230 mm and 195 mm x 195 mm was installed on the honeycomb holder on either side of the specimen. This honeycomb stack had a total height of 396 mm, leaving a free crush distance of 247 mm before the sled impacted the honeycomb. The plastic "battery base" shown in Figure 32 is a mass production part used to support the battery in this SUV. A piece of plywood was glued to the impacted end of the rail to attenuate vibration during impact, and to protect the impacting face from damage.

The arrangement of high speed cameras and lighting for the first test is shown in Figure 33. The Photron cameras are arranged to capture perpendicular views of the rail from the top and both sides, as well as an isometric view. Due to the high frame rate of these tests, a great deal of light is needed to illuminate the specimen. Two large lights and three smaller lights were carefully aimed to avoid casting shadows on the specimen. The views from the four high speed cameras are shown in Figure 34 at the point of first contact between the sled and specimen.

The sled was fired using a charging pressure of 606 kPa (88.0 psi) to achieve a speed of 15.3 m/s (55.2 km/h), with a total mass of 795.3 kg. The targeted speed of 56.0 km/h is the test speed used in the NCAP frontal crash test which is being used as the design case for this study.

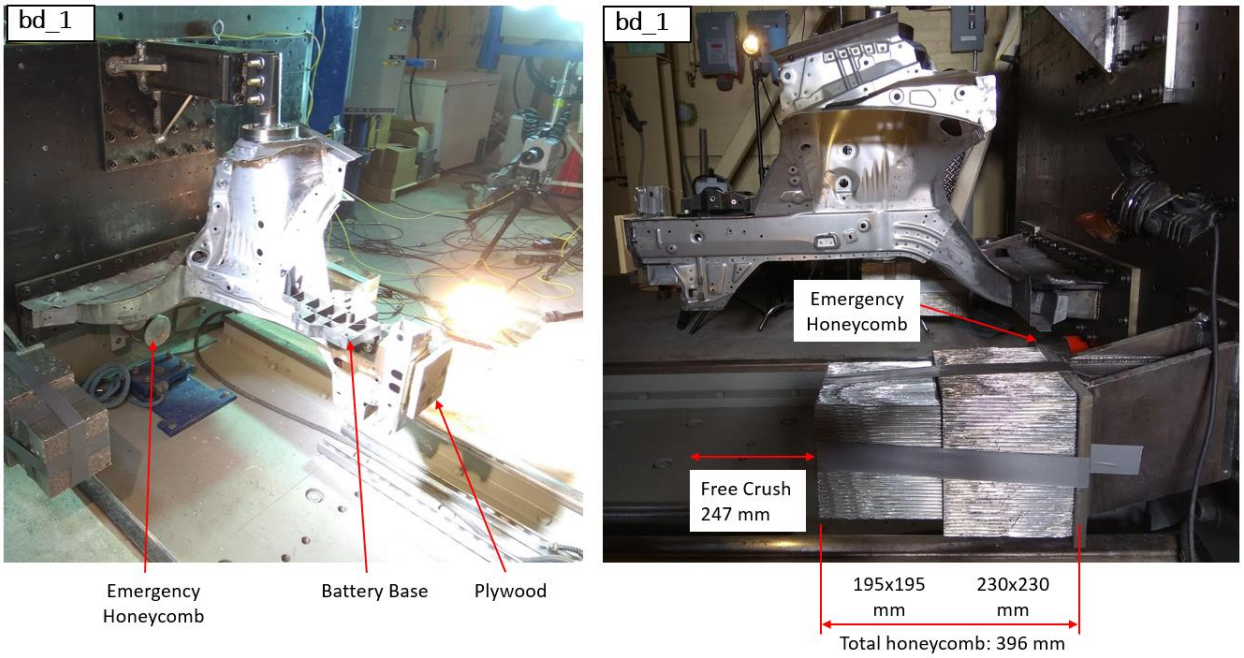

Figure 32: Mounting of the specimen and arrestors for the first baseline demonstrator test (bd_1).

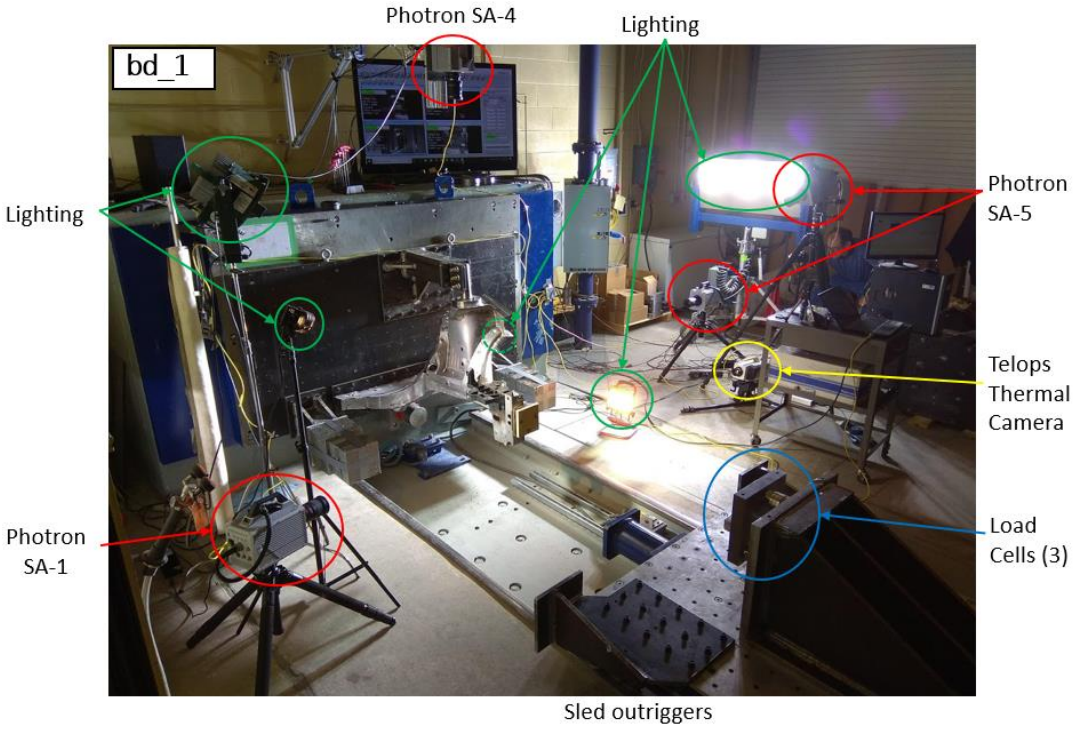

Figure 33: Arrangement of high speed cameras and lighting around the specimen in the first baseline demonstrator test (bd_1).

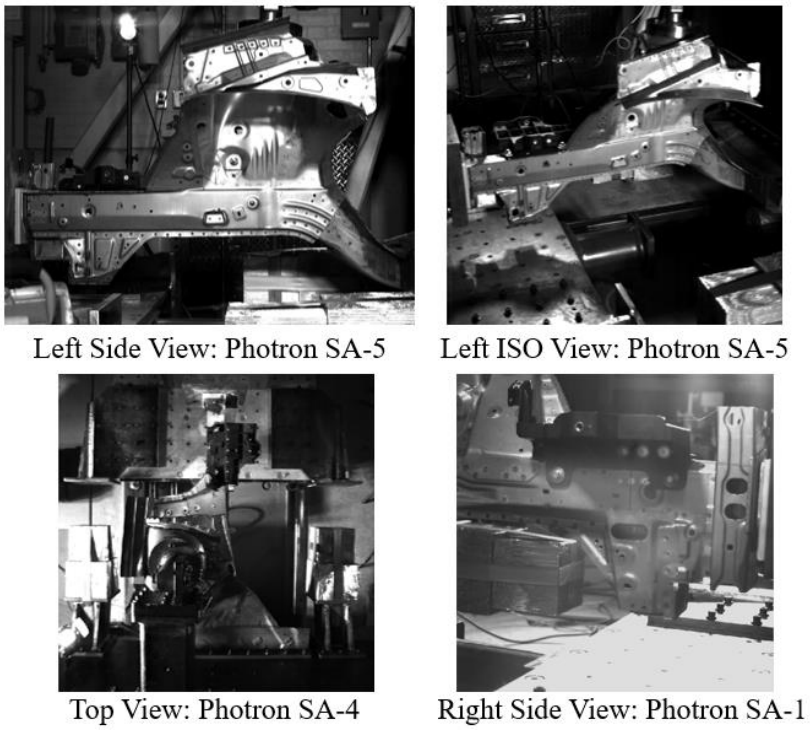

Figure 34: Views from the four high speed cameras used in the first baseline demonstrator test (bd_1).

2.3.2 Test 2: Baseline Demonstrator #5 (bd_5)

The second baseline demonstrator specimen (bd_5) is shown in Figure 35 with a modified honeycomb arrestor arrangement. To better match the deceleration profile that occurs in the full vehicle, additional energy absorbing material is needed to assist the baseline rail. A third honeycomb arrestor block with a height of 147 mm was added, and the cross-sectional area of the first two blocks was made smaller. The outriggers on the crash sled were moved forward by one hole in the bolt pattern, reducing the free crush distance by a further 100 mm to zero. In this arrangement, the honeycomb engages at the same time as the rail, giving a free crush distance of zero. The first block on each side measured 145 mm x 145 mm, the second 160 mm x 160 mm, and the third 200 mm x 200 mm.

The arrangement of high speed cameras and lights used in this test (bd_5) and the subsequent test (bd_4) is shown in Figure 36. The main change from the first test is that the largest light was moved to the other side of the specimen to improve the lighting conditions. The high speed camera on the right side of the specimen was also moved to be more perpendicular to the crush direction.

In the first test this camera was on an angle, resulting in the sled obscuring the later part of the test (Figure 37).

The sled was fired using a charging pressure of 493 kPa (71.5 psi) to achieve a slightly reduced speed of 13.9 m/s (50.0 km/h). A lower firing speed was selected to better represent the difference in velocity between the front and back of the demonstrator structure components in an actual full vehicle NCAP test, in which a full moving vehicle impacts a barrier wall. The deformable bumper and other components in front of the side frame cause the difference in velocity between the front and back of the demonstrator structure to be less than the vehicle's velocity.

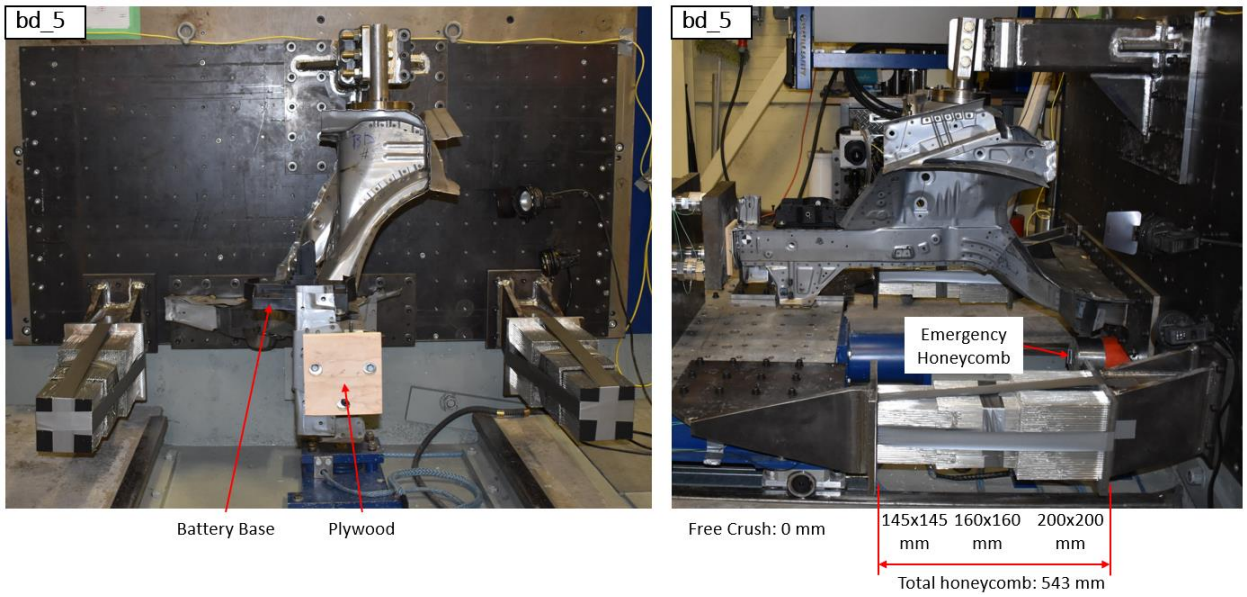

Figure 35: Mounting of the specimen and arrestors for the second baseline demonstrator test (bd_5).

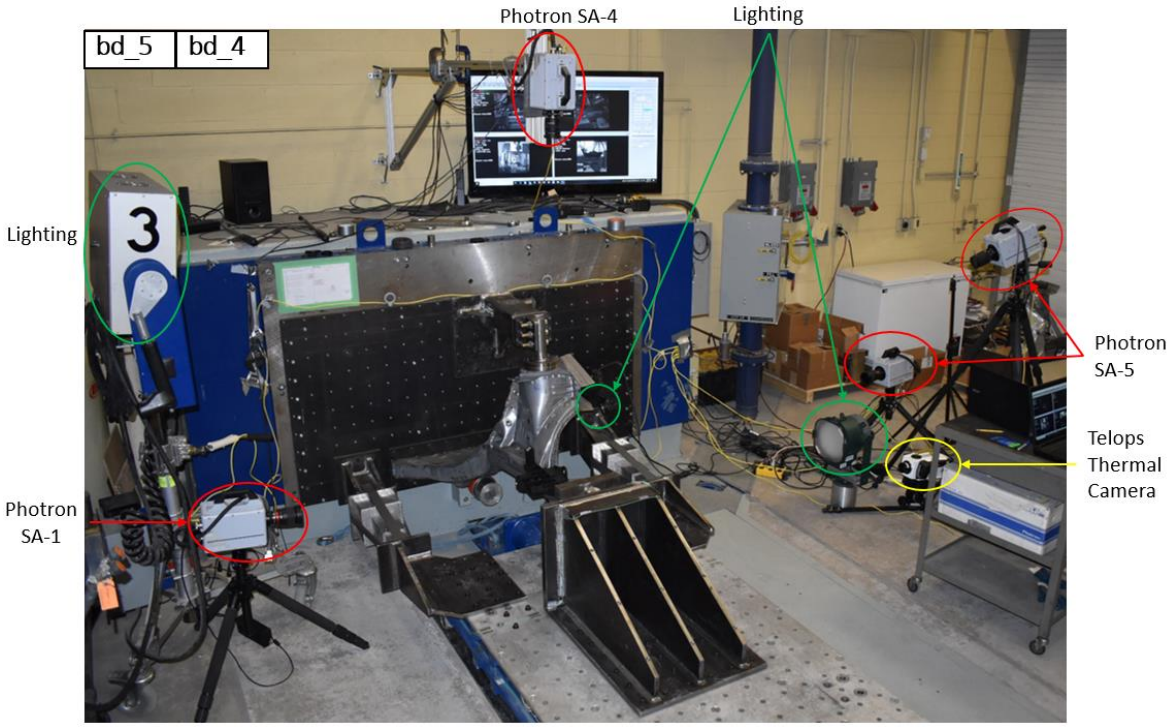

Figure 36: Arrangement of high speed cameras and lighting around the specimen in the second and third baseline demonstrator tests (bd_5 and bd_4).

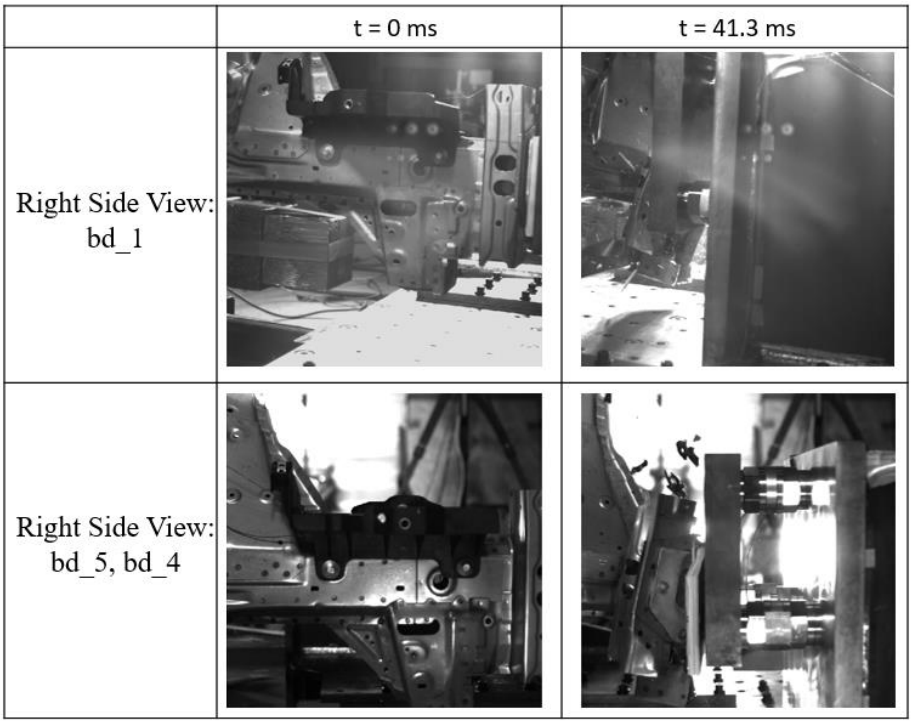

Figure 37: Photron SA-1 on right side of specimen relocated after testing of bd_1 to prevent sled from blocking views of the specimen.

2.3.3 Test 3: Baseline Demonstrator #4 (bd_4)

Figure 38 shows the mounting of the third baseline demonstrator specimen (bd_4). The deceleration provided by the honeycomb blocks in the second test was too severe, slowing the sled too quickly. Consequently, for this test the first two honeycomb blocks were reduced in size to 100 mm x 100 mm and 115 mm x 115 mm respectively, while the third block remained at 200 mm x 200 mm. The same arrangement of cameras and lighting shown in Figure 36 was also used for this test.

A charging pressure of 496 kPa (72.0 psi) was used to fire the sled to a speed of 13.9 m/s (50.0 km/h), identical to the previous test.

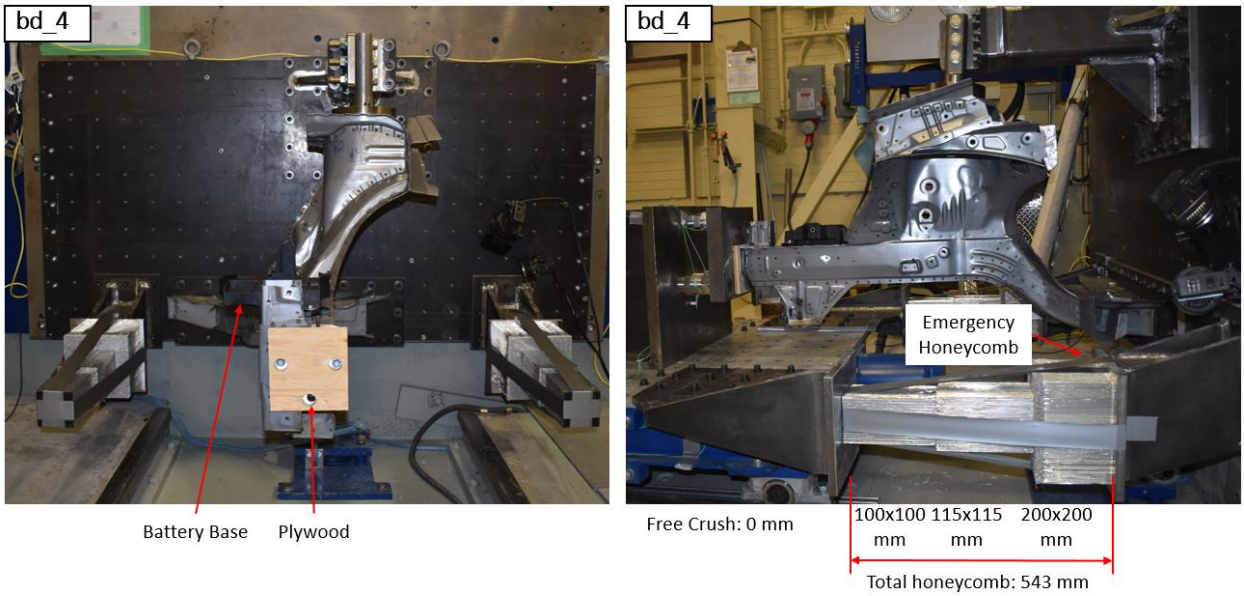

Figure 38: Mounting of the specimen and arrestors for the third baseline demonstrator test (bd_4).

2.3.4 Summary of Baseline Demonstrator Test Configurations

The three baseline demonstrator tests were conducted with two different initial velocities, and three different configurations of honeycomb attenuators. The different configurations are shown in Figure 39. It is important to note that the load path between the specimen and the load cells is independent of the honeycomb, so the contribution of the specimen alone is always recorded by the load cells.

The resulting velocity versus time responses for the three tests are shown in Figure 40. The first test (bd_1) has a higher initial velocity of 15.3 m/s compared to the other two tests (bd_5 and bd_4) initially at 13.9 m/s. The first test has a low slope initially because of the 247 mm free crush

distance, but once engaged the larger honeycomb causes a steeper slope. The difference in slope due to the larger honeycomb cross-section used in bd_5 compared to the smaller cross-section in bd_4 is also apparent.

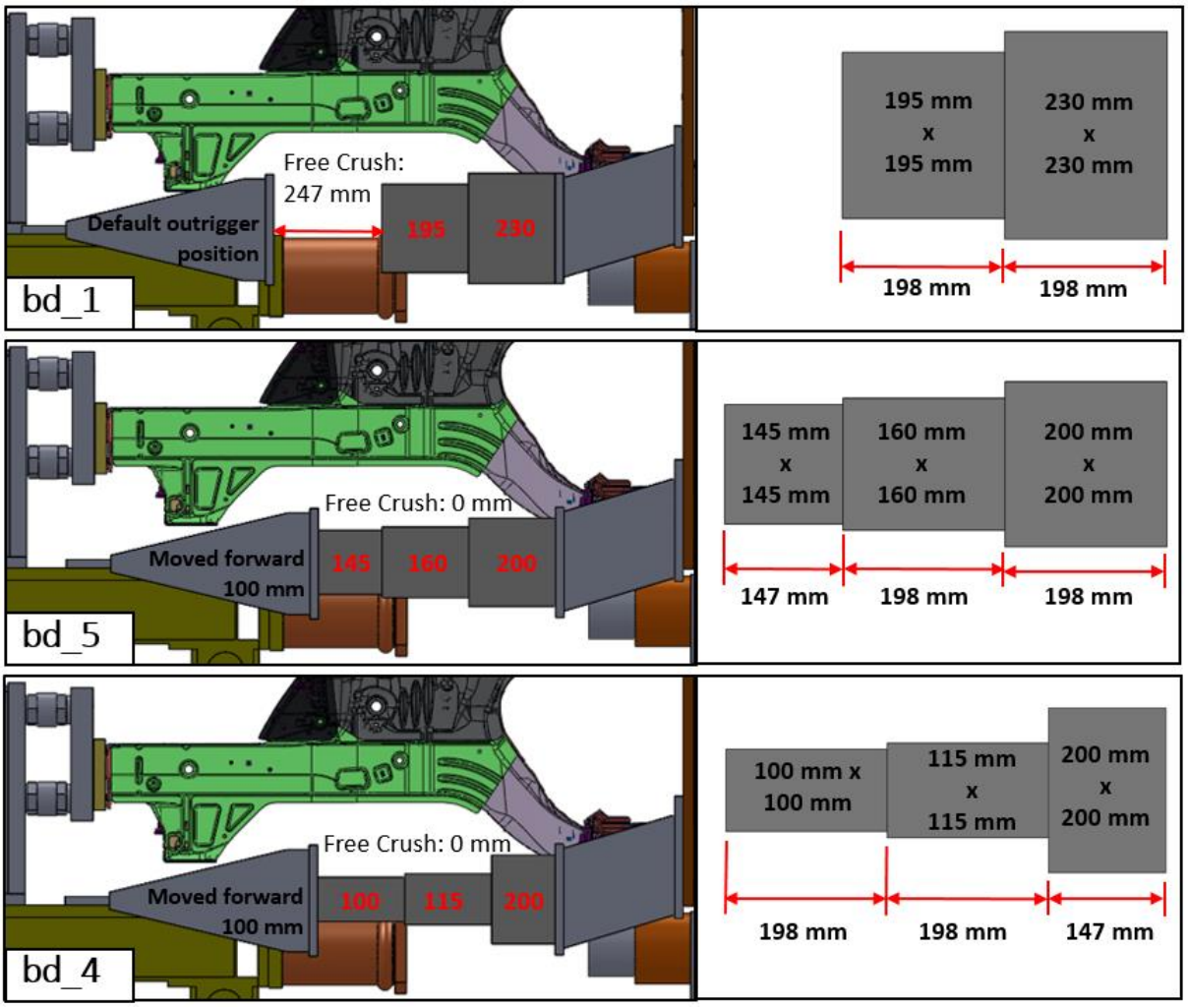

Figure 39: Configuration of honeycomb attenuators for the baseline demonstrator structure tests.

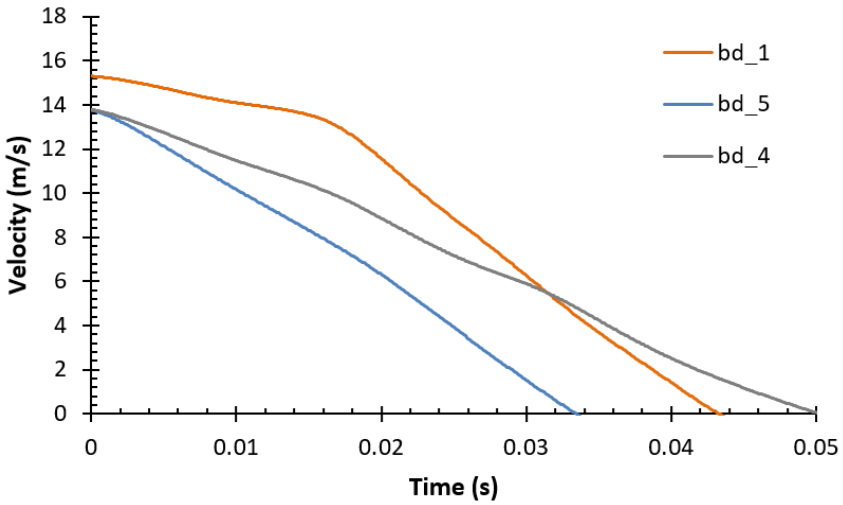

Figure 40: Velocity versus time response of the crash sled in baseline demonstrator structure tests.

2.4 Baseline Demonstrator Structure Experimental Results

2.4.1 Loads and Energy Absorption

The force-displacement and energy absorption results measured from three baseline demonstrator structure tests are shown in Figure 41 and summarized in Table 1. These three tests have very similar force profiles with the curves being nearly identical for the first 200 mm of displacement. After 200 mm, bd_5 stops deforming because so much of the sled energy was absorbed by the larger honeycomb (as described in Section 2.3.2). The other two specimens continue to deform, and the results differ slightly after 250 mm of displacement.

Table 1: Summary of loads and energy absorption over the full crush distance in the baseline demonstrator structure tests.

Test Designation	Velocity (m/s)	Initial Peak Force (kN)	Absorbed Energy (kJ)	Final Crush Distance (mm)	Average Crush Force (kN)
bd_1	15.3	113.8	35.8	391	91.3
bd_5	13.9	121.4	18.9	210	90.1
bd_4		136.6	34.5	357	96.7

The first and third specimens that crushed fully, bd_1 and bd_4, absorbed 35.8 kJ and 34.5 kJ of energy after their full crush distances. The second specimen that partially crushed, bd_5, absorbed 18.9 kJ in its 210 mm crush distance. Due to the use of a number of crush initiators to control folding in these parts, the initial peak forces are relatively low and very repeatable. Figure 41

shows that there are three peaks in close succession at the start of the crush. The final and largest of these three peaks has an average force of 161.6 kN in the three specimens after 20 mm of displacement. After this initial peak, the load drops to about 50 kN at a 40 mm displacement, then increases back to 120 kN at 110 mm of displacement. Following this second peak, the load drops again to around 55 kN at 130 mm of displacement, slowly increases to 75 kN at 180 mm, then increases more rapidly to 150 kN at 210 mm of displacement. At this point bd_5 stopped deforming, while in the other two specimens the force plateaus at this level and slowly decreases back to 135 kN at 250 mm. Beyond this displacement, bd_1 and bd_4 diverge from each other, but their loads both slowly decrease as the sled is decelerated by the honeycomb attenuators, stopping after 400 mm and 360 mm respectively.

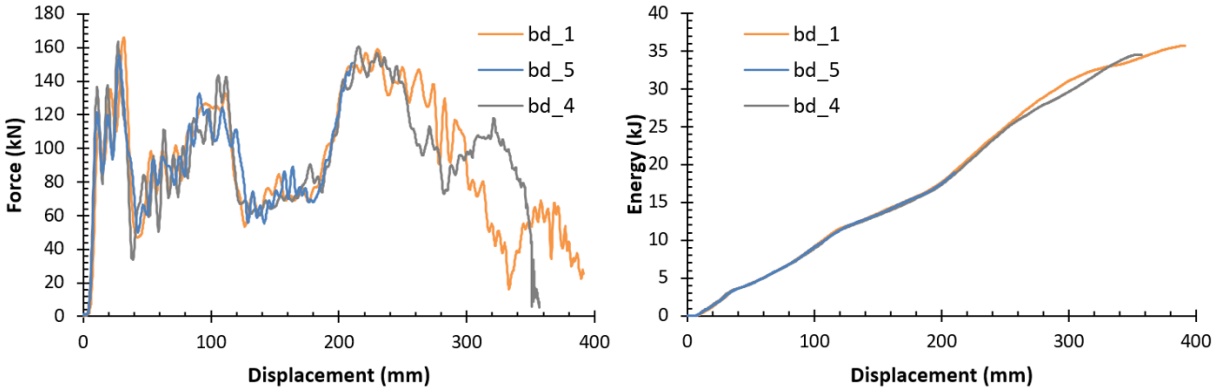

Figure 41: Force-displacement and energy absorption results for three baseline demonstrator structure crush tests.

The average crush forces over the first 100, 200, and 300 mm of crush distance are summarized in Table 2. It shows that the crush tip has an average force level of 90.6 kN with a standard deviation of 1.36 kN. Over 200 mm of displacement the average crush force is lower at 87.5 kN due to the large force drop between 130 mm and 180 mm, and the standard deviation is lower at 0.83 kN. Since bd_5 stopped deforming at 210 mm, the average crush force of 101.1 kN over 300 mm of displacement is taken from the other two specimens, with a standard deviation of 3.36 kN. The large increase in force after 210 mm of displacement contributed to raising the overall average.

Table 2: Average crush force in baseline demonstrator structures in 100, 200, and 300 mm of displacement.

Displacement Range (mm)	Average Crush Force (kN)				
	bd_1	bd_5	bd_4	Average	Standard Deviation
0 – 100	91.7	91.0	89.1	90.6	1.36
0 – 200	88.3	87.6	86.7	87.5	0.83
0 – 300	103.5	-	98.7	101.1	3.36

2.4.2 High Speed Video of Crush Behaviour

Figure 42 shows six frames from the high speed video looking at the left hand side of bd_1. Below each frame, the time in milliseconds from the first contact between the sled and specimen is shown. The first four frames show folding in the crush tip at the impacted end of the rail. The fifth frame shows the impacted crush tip folding at the forward end of the shock tower and deflecting down and to the right. The fifth and sixth frames show that the large initiator under the shock tower triggers deflection of the middle of the rail towards the left.

Figure 43 shows six frames from the left hand isometric view of bd_1, taken at the same times as in Figure 42. It more clearly shows the lateral deflections of the impacted crush tip to the right, and of the middle section to the left.

The top view of bd_1 at the same times is shown in Figure 44. The black battery base obscures a great deal of the early folding behaviour, but some details can still be observed. The third and fourth frames show the deflection of the crush tip to the right, shown by the changing orientation of the battery base. After the battery base breaks off, the fifth and sixth frames show the deflection in the middle of the rail back towards the left as the large crush initiator triggers a fold. Comparing the fifth and sixth frames shows that there is a considerable amount of deformation in the front part of the shock tower.

A closer view of the right side of the specimen is shown in Figure 45. Unlike the other three views that show bd_1, these images are taken from the third test, bd_4, because it has an improved camera angle (comparison shown in Figure 37). With this test having a different deceleration profile than bd_1, the timing of different folding events is different between the two tests, so direct comparisons cannot be made with the other high speed images, though the folding modes are

similar. The folding of the crush tip is captured in the first through fourth frames, and the deflection downward and to the right (towards the camera) is shown in the fourth, fifth, and sixth frames. The deflection of the middle section back to the left is not captured from this view. The battery base can also be observed breaking off of its rear mounting bolt in the third frame, and moving away from the specimen in the fifth frame before being absent from the sixth frame.

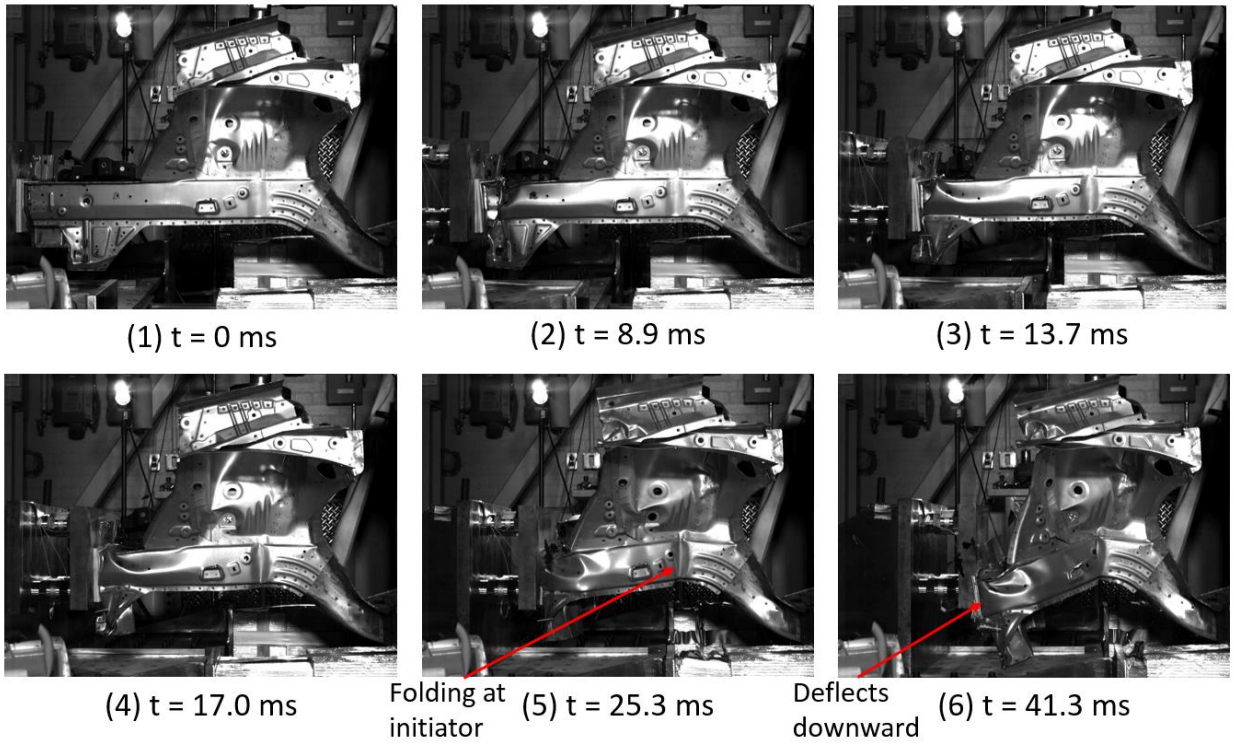

Figure 42: Crush deformation of the first baseline demonstrator test (bd_1) from the left side high speed camera view.

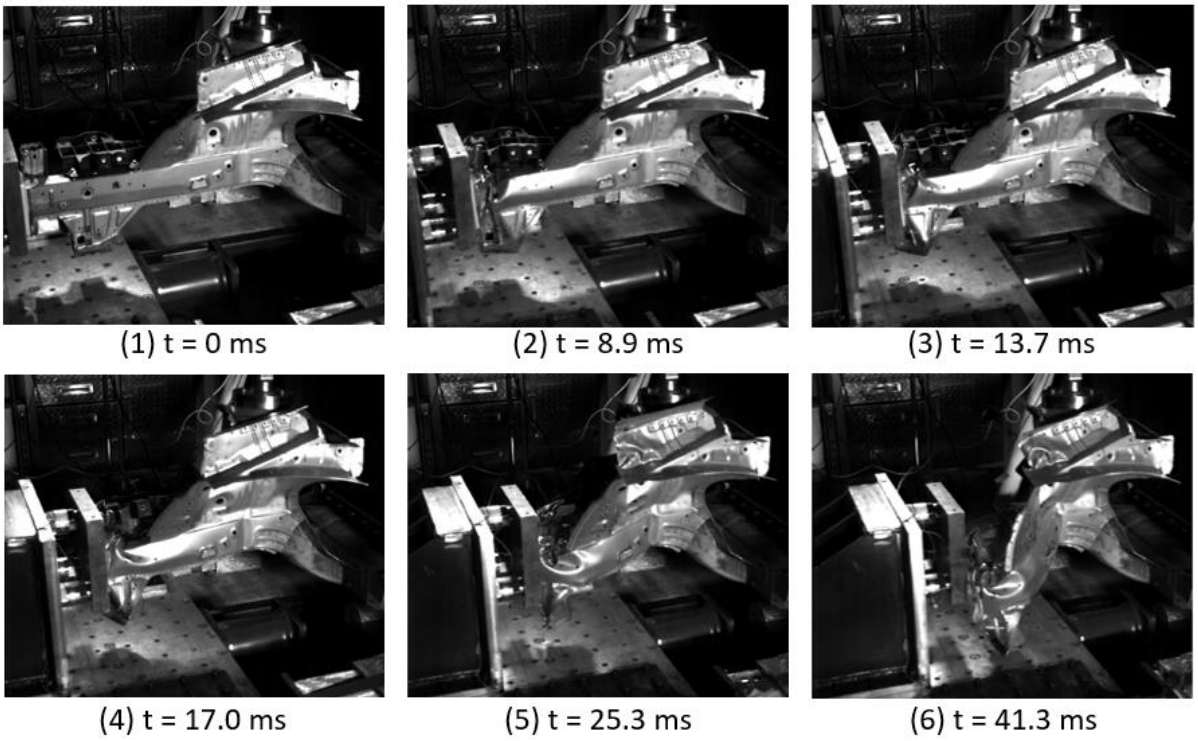

Figure 43: Crush deformation of the first baseline demonstrator test (bd_1) from the left isometric high speed camera view.

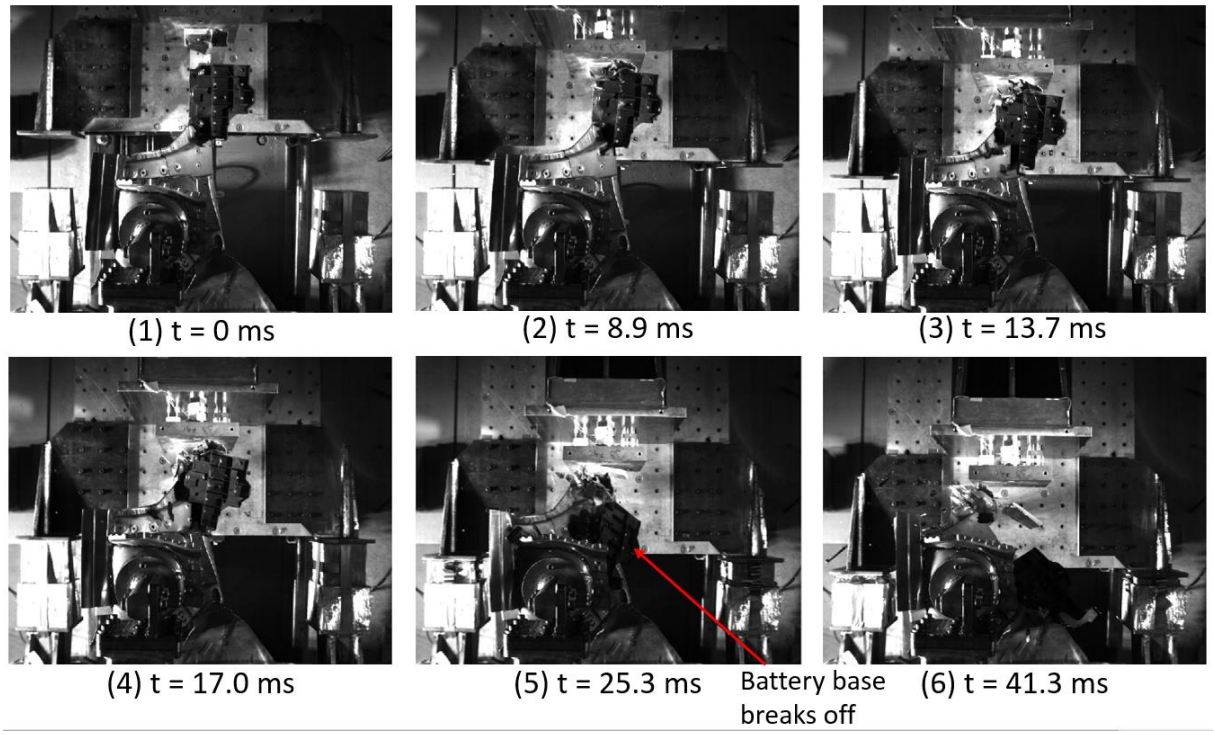

Figure 44: Crush deformation of the first baseline demonstrator test (bd_1) from the top high speed camera view.

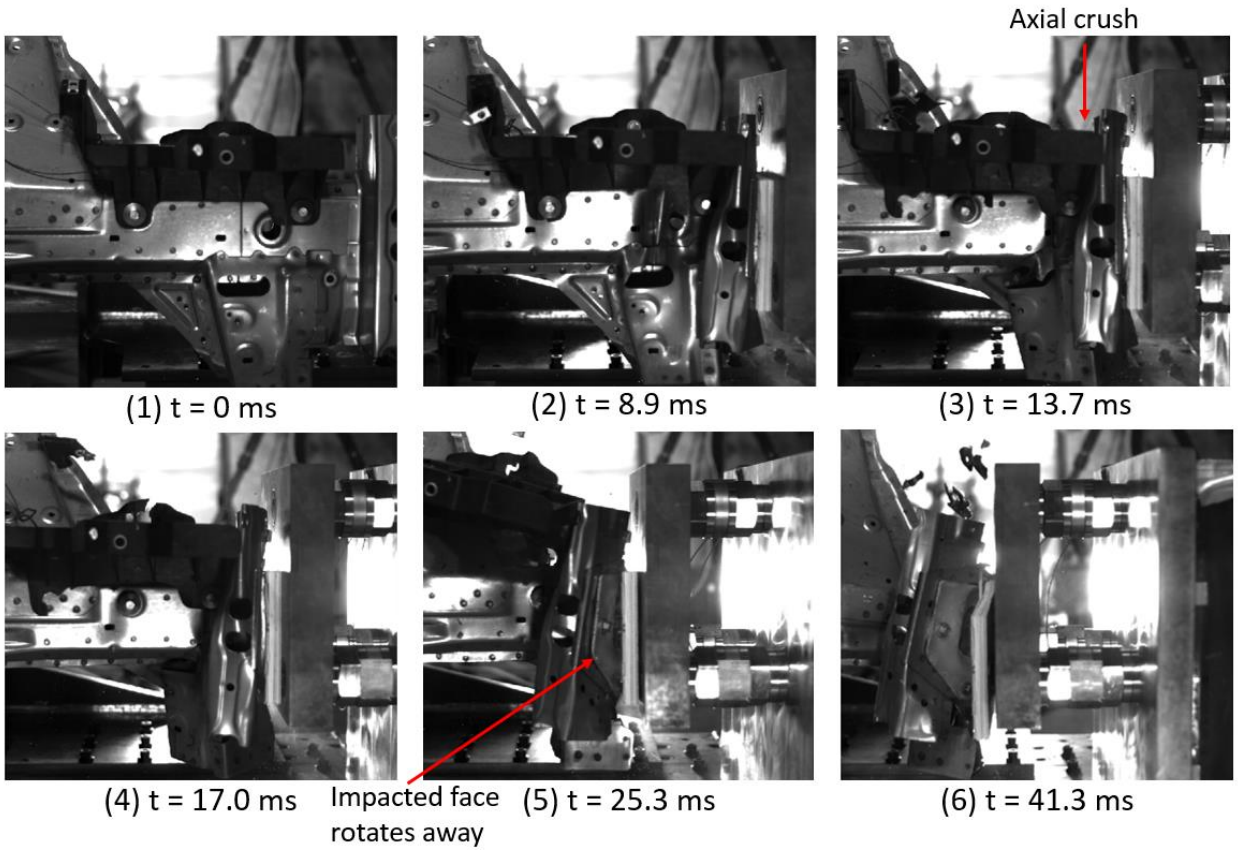

Figure 45: Crush deformation of the third baseline demonstrator test (bd_4) from the improved right side camera view.

2.4.3 Infrared (IR) Thermal Imagery

The four images shown in Figure 46 were captured using the Telops IR thermal camera. It captures the crush tip of the demonstrator structure specimens from the left side, showing a portion of the view captured by the left side high speed camera (Figure 42). The temperatures indicated by the scale are inflated due to the reflection of heat from the large lights used for these tests, so only the temperature differences should be studied. The first frame shows the specimen at a uniform temperature just before impact from the sled, with the pink and teal coloured areas caused by the lighting. The second and third frames show the onset of folding, with the tight folds near the top of the part reaching the highest temperatures. Deformation in the base material around two spot welds is also shown inside the white circles. The fourth frame shows further folding and heat generation as the crush continues.

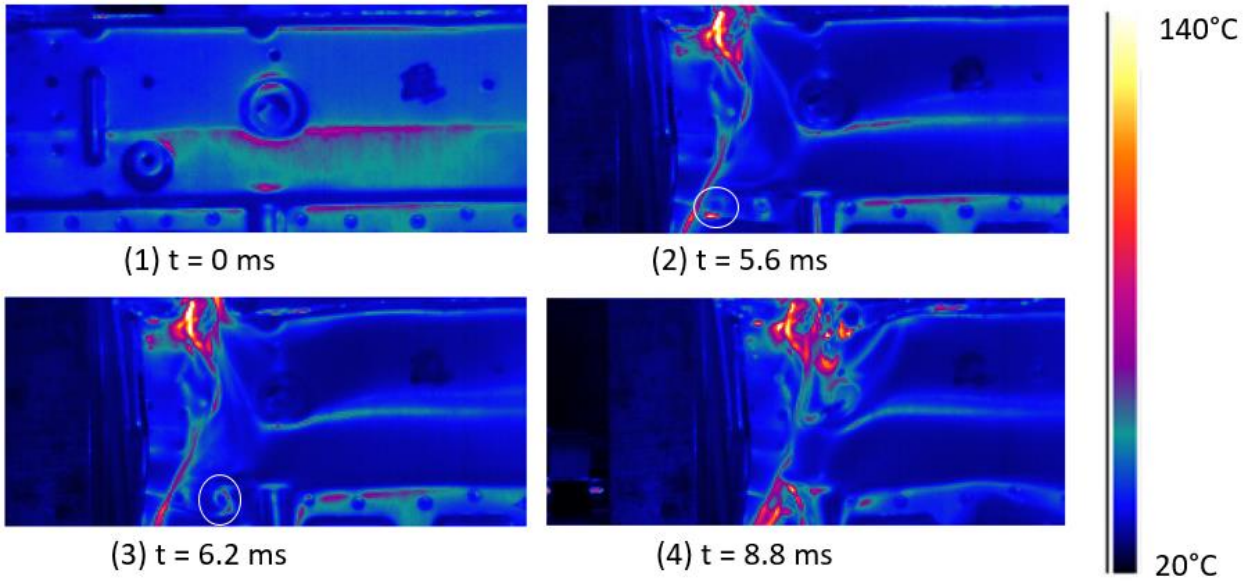

Figure 46: IR thermal video of the first baseline demonstrator test (bd_1) from the left side focusing on the crush tip section of the side frame.

2.4.4 Final Deformed Shape After Impact Testing

The deformed shape of the first test specimen (bd_1) after being impacted by the crash sled is shown in Figure 47. The impacted end of the side frame folds axially then deflects down and to the right. The aluminum plate under the plywood on the impacted end bends severely, causing the plywood to delaminate between its layers and fall off of the plate. The large fold initiator underneath the shock tower was triggered, causing the middle part of the side frame to deflect downward and to the left. This is in agreement with the description in Section 2.1, with the first section intended for progressive axial crush, and the middle section intended for buckling collapse. The intrusion resistant s-rail section deformed only slightly in this test, protecting the intrusion resistant design intent of this part of the side frame structure.

Figure 48 shows a comparison of the initial and deformed shapes captured from the low speed video on the DSLR camera from the left side. Several features are highlighted in red, including folding at the large initiator and the subsequent downward deflection of the forward part of the specimen. Rotation about two axes at the shock tower support is also noted. The bracket rotates on the end of the wall support, and the bar connecting to the shock tower rotates on the bracket. Overall deformation of the shock tower is shown, along with the slight deformation of the s-rail section of the structure.

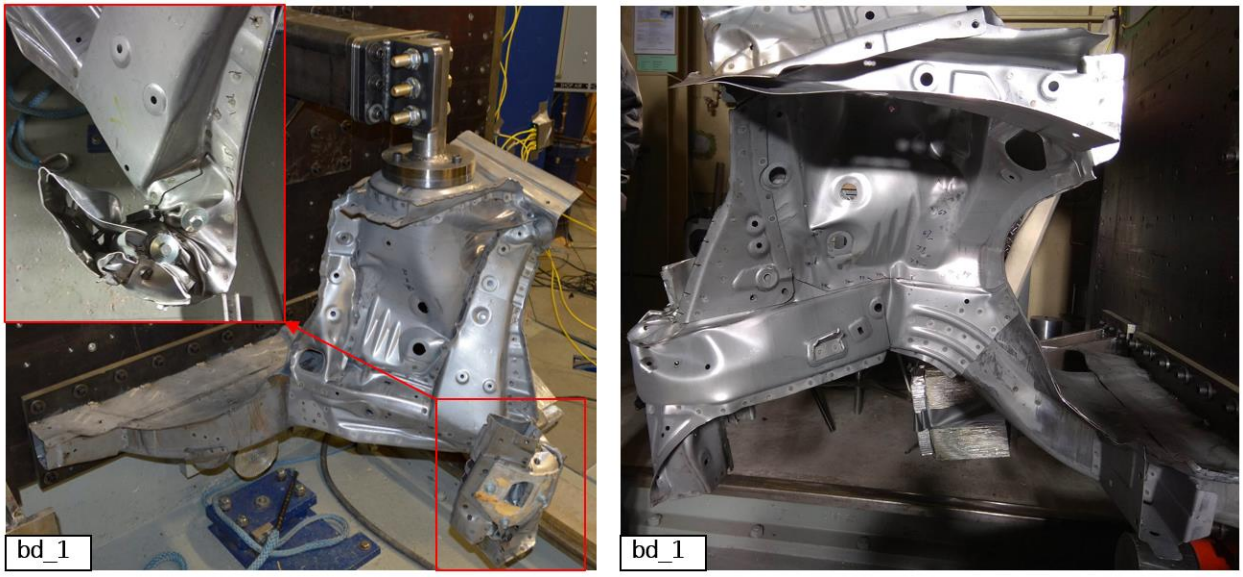

Figure 47: Deformed specimen after the first baseline demonstrator test (bd_1).

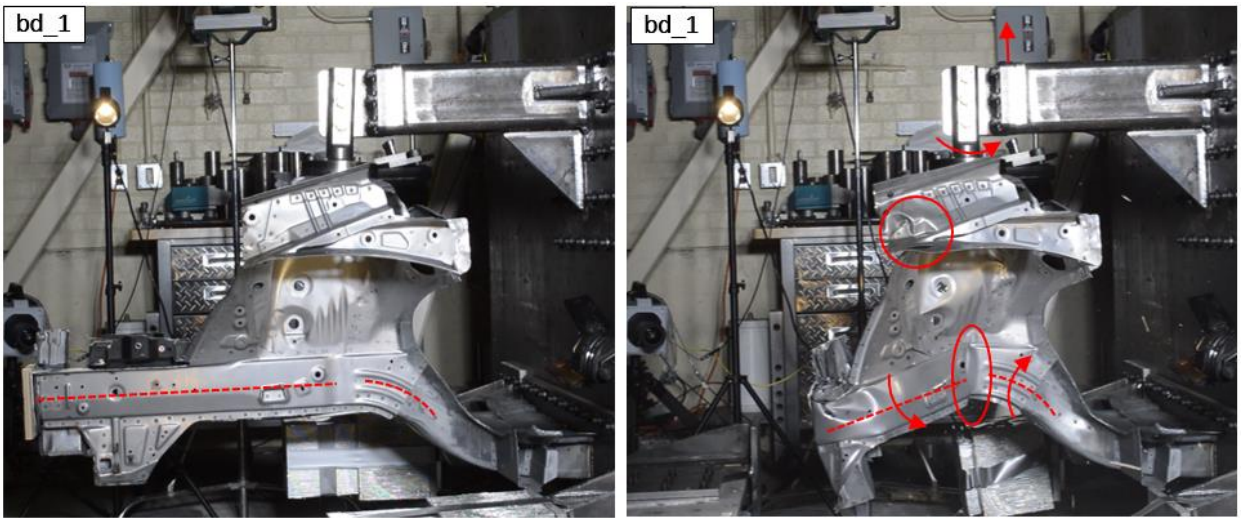

Figure 48: Images from the DSLR video show initial and deformed shape of the first baseline demonstrator specimen (bd_1).

The second test specimen (bd_5) is shown after testing in Figure 49. It is not deformed as severely as bd_1 because the sled was slowed significantly by the larger honeycomb attenuators that were used. The impacted end folded and deflected to the right, but to a lesser degree than in the first test. The large initiator under the shock tower deformed slightly, but not enough to cause the rail to deflect significantly to the left.

The comparison of initial and deformed shapes from the DSLR video in Figure 50 shows that there was much less downward deflection in the second test than in the first. It also shows that there is little to no movement of the bolted connections of the shock tower support. A very small amount of movement in the s-rail section can be seen when carefully comparing these images.

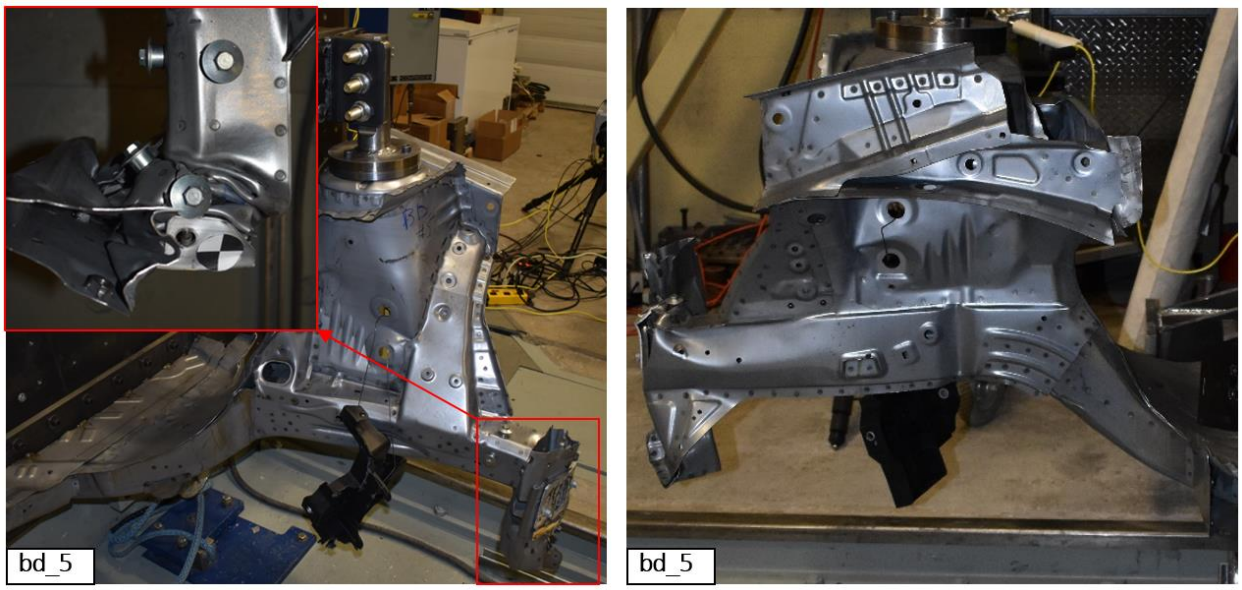

Figure 49: Deformed specimen after the second baseline demonstrator test (bd_5).

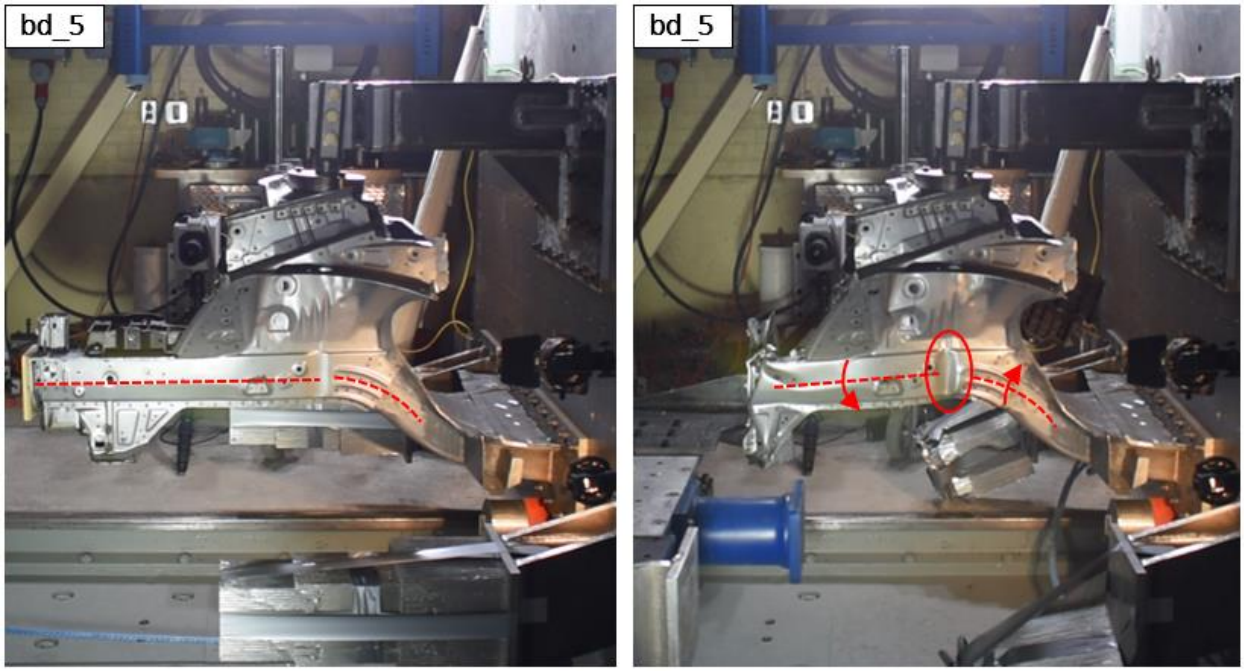

Figure 50: Images from the DSLR video show initial and deformed shape of the second baseline demonstrator specimen (bd_5).

The deformed shape of the third specimen (bd_4) is shown in Figure 51. It closely resembles the first test, bd_1, with the impacted end folding axially initially, then deflecting downward and to the right. The aluminum plate bends severely, causing failure of the plywood, and the large initiator under the shock tower engages and causes deflection of the middle part of the specimen downward and to the left.

Figure 52 compares the initial and deformed shape of the specimen from the left side view. The initial image is taken from the DSLR mounted on its tripod, however the video was not recorded so the deformed image was taken separately from a similar angle. The shock tower support had already been removed prior to taking this picture, so the deflection of the bolted connections is not shown, though they moved in a similar way as in bd_1. Similar to bd_1, a fold forms at the initiator and the front of the specimen deflects downward, there is deformation at the top of the shock tower, and slight deformation of the s-rail.

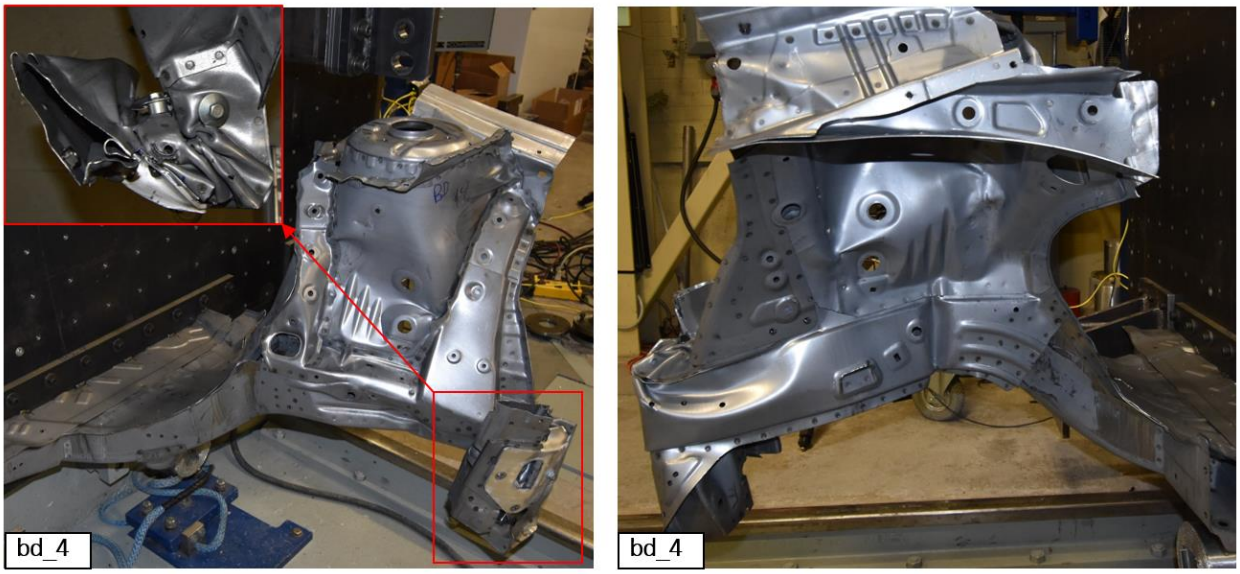

Figure 51: Deformed specimen after the third baseline demonstrator test (bd_4).

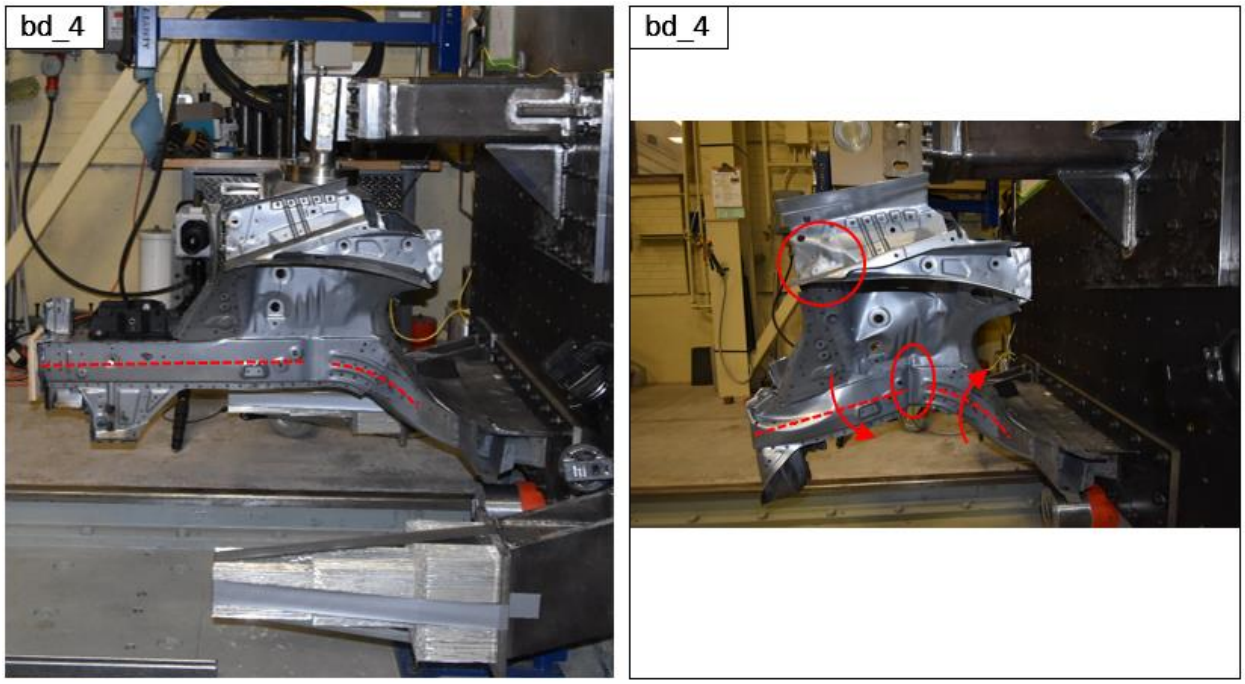

Figure 52: Images from the DSLR video and camera show initial and deformed shape of the third baseline demonstrator specimen (bd_4).

2.4.5 Discussion of Experimental Results

Through these three experiments, the crush behaviour of the baseline demonstrator structure was characterized. The crush load profile and folding behaviour was very consistent between the three tests despite changing experimental parameters, giving a reliable baseline performance level for the commercial side frame structure.

The next chapters of this thesis (3-7) present the investigation of the crush performance of Ductibor® 500-AS based hot stamped TWBs using a simplified top hat channel geometry. This effort includes development of numerical models of the crash behavior of Ductibor® 500-AS TWBs. The demonstrator structure then is revisited in Chapter 8 which presents the numerical simulation of hot stamped Ductibor® 500-AS as a substitute for JAC590R within the axial crush tip of the demonstrator structure.

3.0 Ductibor®-Usibor® TWB Axial Crush Rails – Specimen Fabrication

3.1 Overview of Materials and Specimens

A key focus of this research was: (i) to characterize the crush performance of axial crush members that have tailored properties along their length imparted using hot stamped tailor-welded blanks; and (ii) to validate numerical models of these crash tests. The TWBs comprise: Usibor® 1500-AS, a 22MnB5 hot stamping steel that reaches a tensile strength of about 1500 MPa after quenching; and Ductibor® 500-AS, a hot stamping steel which forms a ductile material with about 600 MPa tensile strength after quenching. The Ductibor® 500-AS was implemented in the impacted end of the crush rails as an energy absorber, while the Usibor® 1500-AS was used to represent an intrusion resistant zone at the rear end of the rail. This chapter describes the methods used to hot stamp and join the bending and axial crush specimens. Chapter 4.0 describes the mechanical test methodology.

Formed hat channel specimens were investigated (Figure 53) considering five different material conditions/thickness combinations (Figure 54). To characterize the ductile base material and act as a baseline for tailoring comparisons, non-tailored rails of monolithic Ductibor® 500-AS were hot stamped in 1.2 mm and 1.6 mm thicknesses. TWB rails were made in two uniform thicknesses of 1.2 mm and 1.6 mm, where both materials in the TWB had the same thickness. Lastly, TWBs with non-uniform thickness comprising 1.2 mm Ductibor® 500-AS welded to 1.6 mm Usibor® 1500-AS were investigated. These formed specimens were top hat channels which consist of a 50 mm deep by 65 mm wide C-channel with flanges bringing the total width to 125 mm. The 590 mm long channels, shown in Figure 53 and Figure 54, have tabs at each end to aid in alignment for forming.

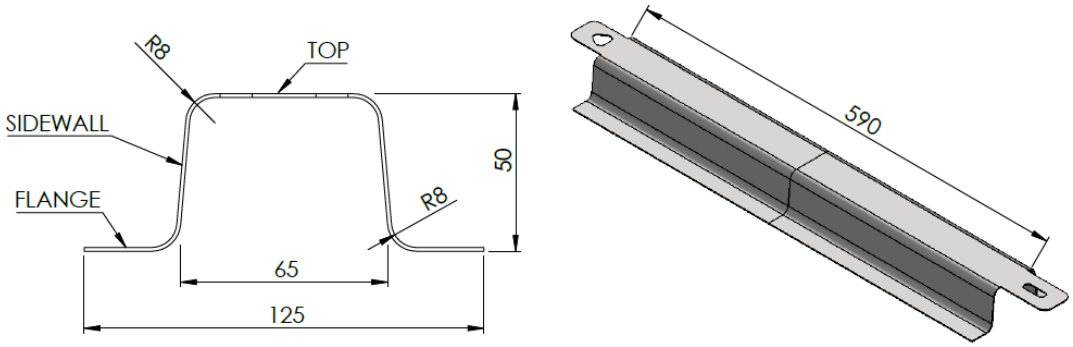

Figure 53: Dimensions of formed top hat channels. Dimensions in millimeters.

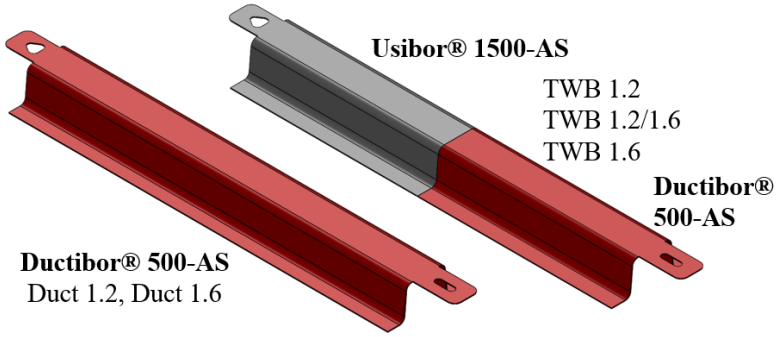

Designation	Ductibor® 500-AS	Usibor® 1500-AS
Duct 1.2	1.2 mm	-
Duct 1.6	1.6 mm	-
TWB 1.2	1.2 mm	1.2 mm
TWB 1.2/1.6	1.2 mm	1.6 mm
TWB 1.6	1.6 mm	1.6 mm

Figure 54: Specimen material combinations.

ArcelorMittal provided sheets of laser welded TWBs and monolithic Ductibor® 500-AS in each of the thickness combinations described in Figure 54. Prior to laser welding, partial ablation was used to remove the AlSi coating from the edges of the sheets being joined to prevent mixing of the coating with the base metal. During laser welding, Feedibor™ filler wire was used to fill the weld area [58]. The provided sheets were roughly 205 mm x 725 mm, with the laser weld line through the center across the shorter dimension. From these sheets, the forming blanks shown in Figure 55 were water jet cut. These blanks are 200 mm x 590 mm, with an added tab at each end with a triangular hole and a slot to align the part in the die when being formed. The weld line was offset from the center of the TWB blanks by 5 mm to ensure adequate clearance in the forming tool for multi-gauge parts.

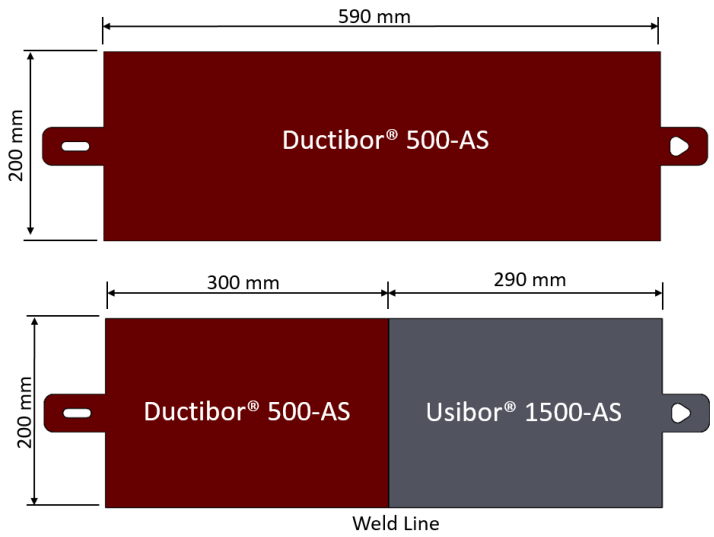

Figure 55: Forming blank geometries.

3.2 Description of Forming Tooling

The monolithic Ductibor® 500-AS and the common gauge 1.2 mm and 1.6 mm TWB blanks (Table 3) were formed using the same rail forming tool designed by George [11] that was used by Omer [20], Prajogo [19], and O'Keeffe [40] for IDH tailoring. For this work the tool was used in its "tailored flange configuration", shown in Figure 56, in which the punch and die cavity were water cooled. The binder and flange regions did not have cooling and were used at room temperature. To ensure that the specimens were properly quenched, a period of 10 to 15minutes was allowed between each quench cycle for the non-cooled areas of the die to cool back to within 25°C of room temperature. In this tool the punch is fixed, the binder is mounted on nitrogen cylinders, and the die cavity is attached to the press cylinder and displaced downward. There are four nitrogen cylinders, each with a diameter of 25 mm. The system is charged to an initial pressure of 10.34 MPa (1500 psi), producing a force of 5.08 kN in each nitrogen spring, for a total binder force of 20.3 kN at the top of the stroke [59]. At the bottom of the 48 mm stroke this spring force increases to 6.69 kN, for a peak binder force of 26.7 kN that is maintained during quenching. The force profile for the nitrogen cylinders is shown in Figure 57.

Table 3: Gauge and material conditions formed in each die.

Tailored Flange IDH Die	Multi-Gauge Fully Cooled Die
1.2 mm Monolithic Ductibor® 500-AS 1.6 mm Monolithic Ductibor® 500-AS 1.2 mm Common Gauge TWB 1.6 mm Common Gauge TWB	1.2/1.6 mm Multi-Gauge TWB

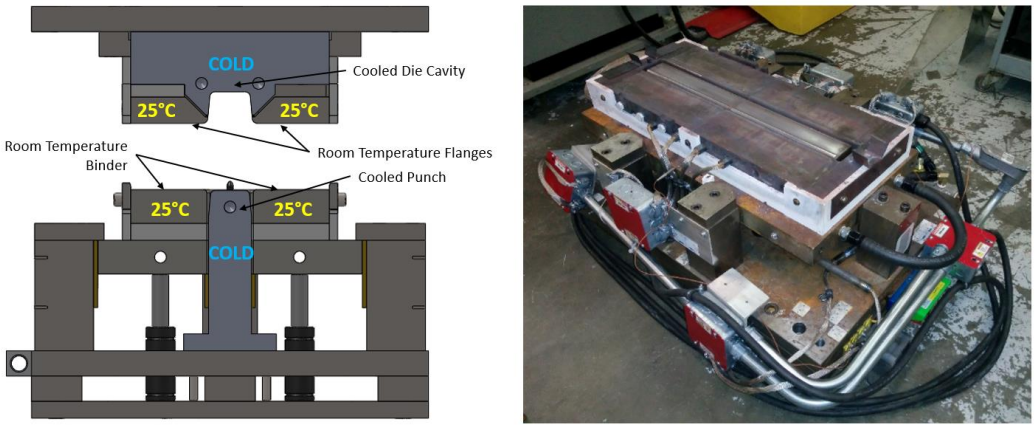

Figure 56: Original IDH die used for monolithic and common gauge blanks, adapted from [12].

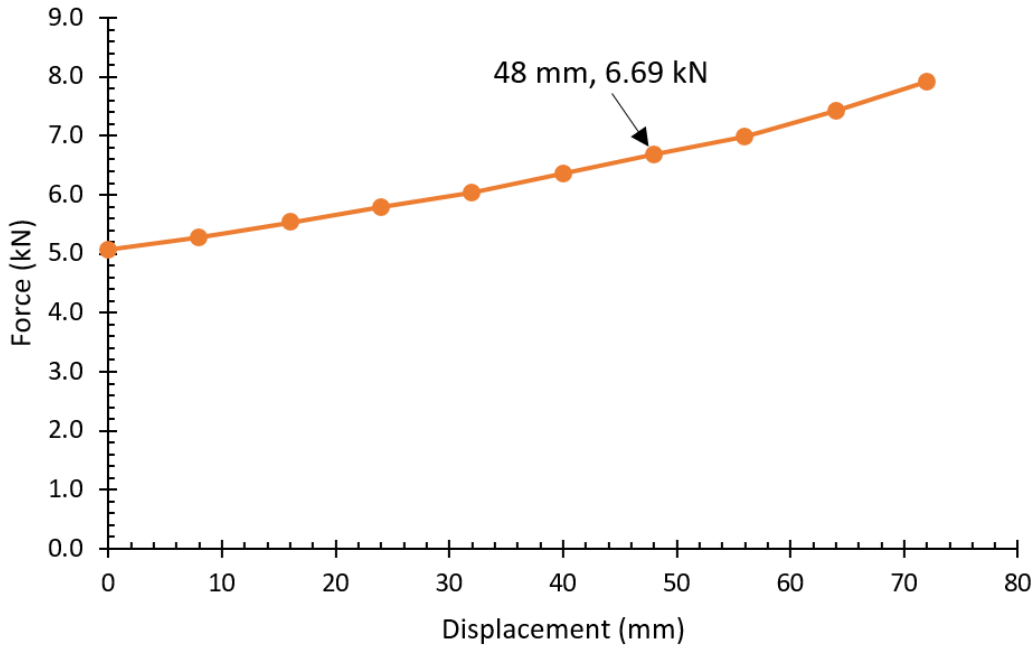

Figure 57: Force versus displacement profile for the nitrogen cylinders. Shown is the force in one cylinder. Produced using data from [59].

To form the 1.2/1.6 mm multi-gauge blanks, either the die cavity or the binder and punch needed to have a step in thickness. Without such a step there would be good contact pressure on the thick part of the blank, but poor contact pressure on the thinner part of the blank leading to a poor quench rate. The punches were already segmented at the center line of the die, and both 1.2 mm and 1.6 mm punches had already been machined for use in the IDH tool for monolithic parts. Therefore it was decided that a stepped binder was required, and to allow for future flexibility, it would be made up of two pieces and able to be shimmed to any combination of thicknesses. Due to demand for this heated tool from other researchers, the lack of cooling on the flanges, and overall wear on the existing tool, it was decided that a completely new rail forming tool would be built. This new tool uses a one piece die cavity that includes cooling of the flanges and the stepped binder (Figure 58, Figure 59), but is otherwise nearly identical to the previous tool. It was machined by project partner Promatek and assembled at UW.

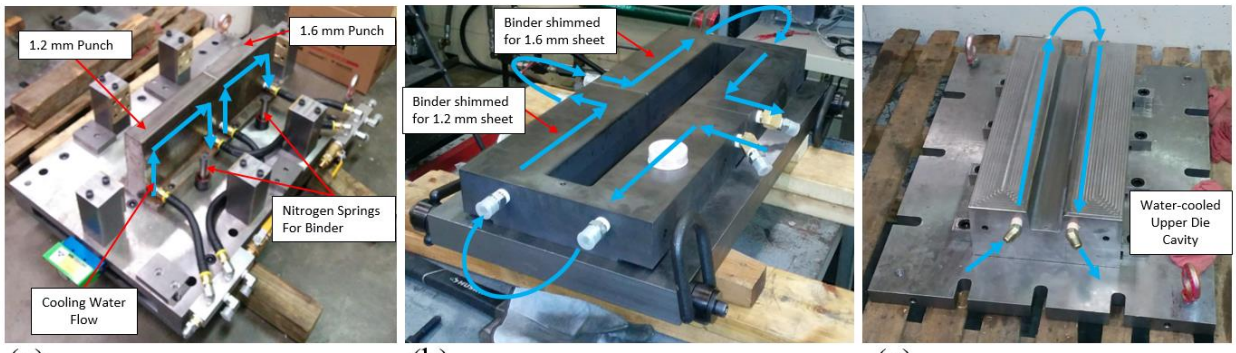

Figure 58: Fully cooled multi-gauge forming tool with blue lines showing flow of chilled water within the die: (a) Cooled punches, (b) Cooled segmented binder, (c) Cooled die cavity

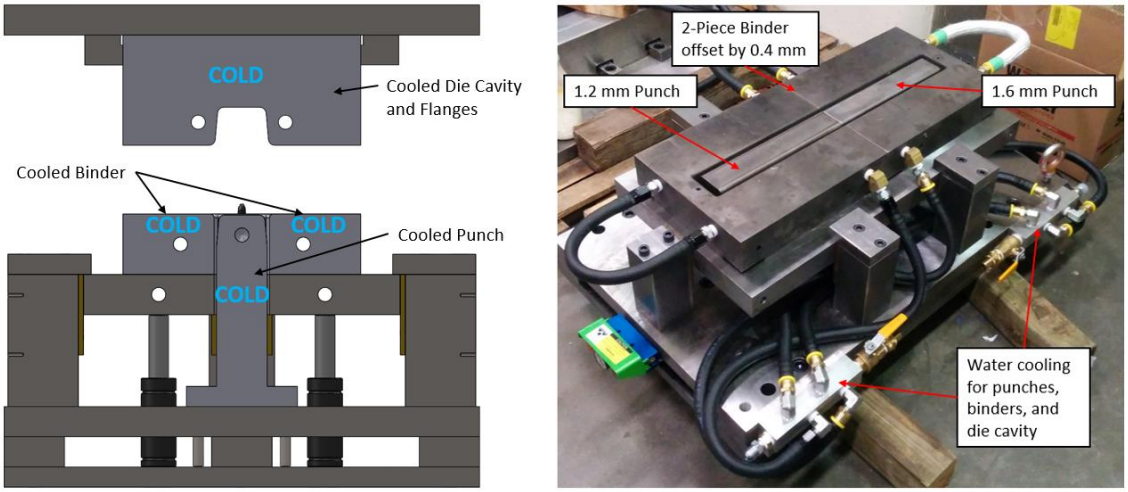

Figure 59: Fully cooled multi-gauge rail forming tool.

3.3 Press, Furnace, and Transfer System

3.3.1 Press

These forming tools were installed in a hydraulic press manufactured by Macrodyne Technologies Inc., shown in Figure 60. The bed size of the press is 762 mm x 1372 mm (30” x 54”), which constrained the overall size of the tooling. The press is single-acting, with a 120 ton actuator, and utilizes a 100 GPM servo valve and twin 15 gallon accumulators to achieve a displacement speed of approximately 250 mm/s. This fast displacement speed is needed to minimize cooling of the blank before the full tonnage of the press is applied.

The press is controlled using an MTS FlexTest servo controller, operating in closed-loop position control. A custom LabView program running on a PC is used to generate program signals through a PC-based Digital-to-Analog card [16]. This card also has data acquisition channels used to record punch force and displacement. Punch force is calculated based on pressure transducers at the inlet and outlet of the actuator and the actuator dimensions, while punch position is measured using a string potentiometer.

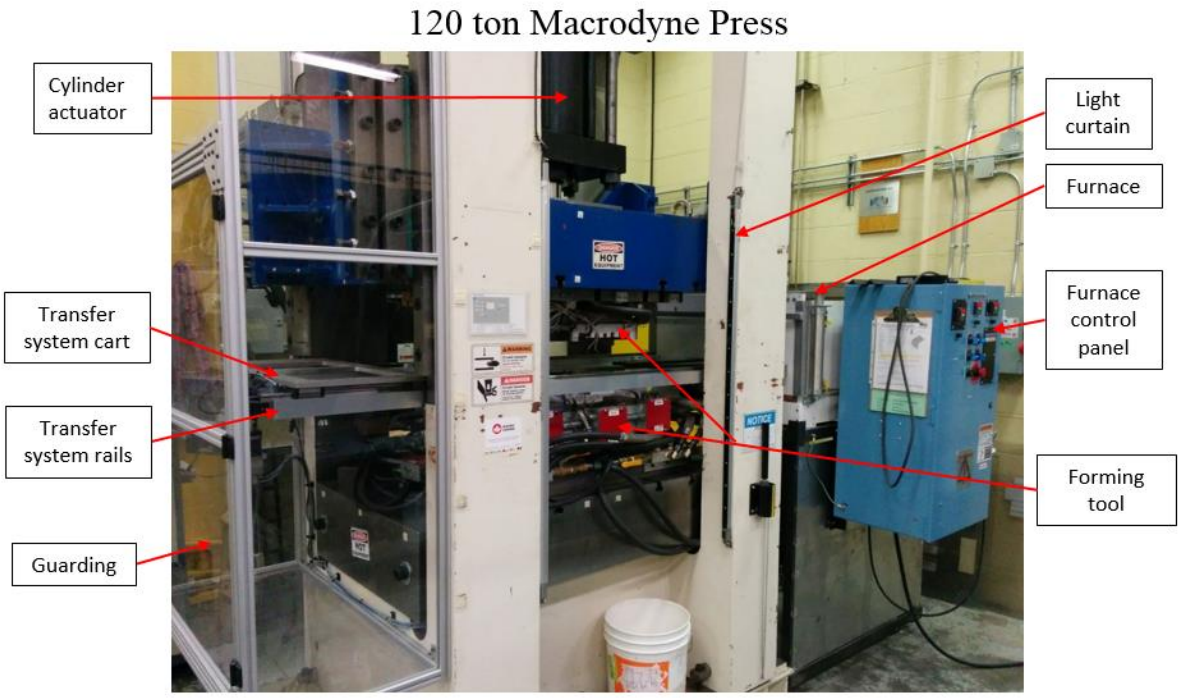

Figure 60: 120 ton Macrodyne press with Deltech furnace.

3.3.2 Furnace

A furnace built by Deltech Inc. is mounted adjacent to the press (Figure 60) and used for austenitizing prior to hot stamping. This furnace has internal dimensions of 610 mm wide by 203 mm tall, with a depth of 915 mm (24” x 8” x 36”). An 18 kW heating capacity is provided by six electric heating elements, which are arranged in three control zones for the front, middle, and back of the furnace. This allows for more uniform heating of the blank because it reduces the thermal gradient from the front to the back of the furnace after the door closes. The door of the furnace is opened and closed automatically using control logic, minimizing the time that it is open for heat to escape. The furnace is placed directly adjacent to the end of the press, in line with the rails of the transfer system, as seen in Figure 60. Inside the furnace there are two pieces of stainless steel 25.4 mm x 25.4 mm (1” x 1”) angle sections mounted along the depth of the furnace. The blanks slide along these angle sections when inserted and removed from the furnace, and rest on them while austenitizing.

3.3.3 Transfer System

The transfer system installed in this press is used to load cold blanks into the oven to austenitize, and to move hot blanks from the oven into the tooling for forming (Figure 61). This system was

custom-built by ACRP Ltd. for this purpose. It consists of two linear bearing rails mounted to the sides of the press and a cart that rides on these rails that is powered by a stepper motor-controlled linear drive. The cart has a pneumatic gripper with ceramic gripping surfaces that grasp the blank and reducing heat loss at the point of contact during transfer. The pneumatic actuator for the gripper operates through a long linkage to keep the pneumatics away from the hot furnace.

During the first trials of this transfer system there were some challenges with the vertical alignment of the furnace relative to the press and transfer system. The blank had to fit within a narrow window of the grip opening on the transfer system, otherwise it would miss the blank when trying to unload it from the oven. This was compounded by the tendency for the blank to sag in the furnace once heated. This was solved by adding a lead-in bend to the angle iron rails in the furnace to allow the blank to slide up into the oven when being loaded, then sag back down to align with the grips for unloading. With these early alignment issues solved, this automated system moves quickly and provides a repeatable transfer time that is desirable in a sensitive forming process like this.

Figure 61: Transfer system in press with furnace and rail die, blank is loaded.

3.4 Forming Process

The hot stamping process consists of four key steps: austenitizing, transfer, forming, and quenching.

The austenitizing process begins with the operator loading a blank into nesting pads on a platform in front of the furnace door, as shown in Figure 61. The operator ensures that the tab with a triangular shaped cutout is oriented closest to the oven, and for multi-gauge parts, that the flat side of the blank is facing upwards. The operator then initiates the loading sequence by pressing the touch pad that controls the transfer system. The transfer system pushes the blank into the furnace and starts a timer. The furnace is maintained at 930°C, managed by a three-zone controller with thermocouples.

After seven minutes of austenitizing, the operator initiates the unload and form process using the transfer system and press controllers. The blank is retrieved from the furnace and transferred into the die, dropping it onto two alignment pins within about 8 seconds.

As soon as the transfer system cart contacts a limit switch to indicate that it has reached its home position and is out of the way of the press, the punch descends to form the part. The first point of contact is between the binder surfaces on the flange of the part. As the press depresses the nitrogen springs, the blank is formed over the punch until it bottoms out in the die cavity, taking about 1.5 seconds. The transfer and forming process for a multi-gauge blank is shown in Figure 62. The differential cooling rates in the different sheet thicknesses are evident from the colour differences.

Once the punch bottoms out in the die cavity at the end of the forming stroke, the tool is held closed with 100 tons of force for 10 seconds. After the quench, the tool re-opens and the formed part is removed. It is set down with each tab resting on a support and the center floating to allow it to cool uniformly.

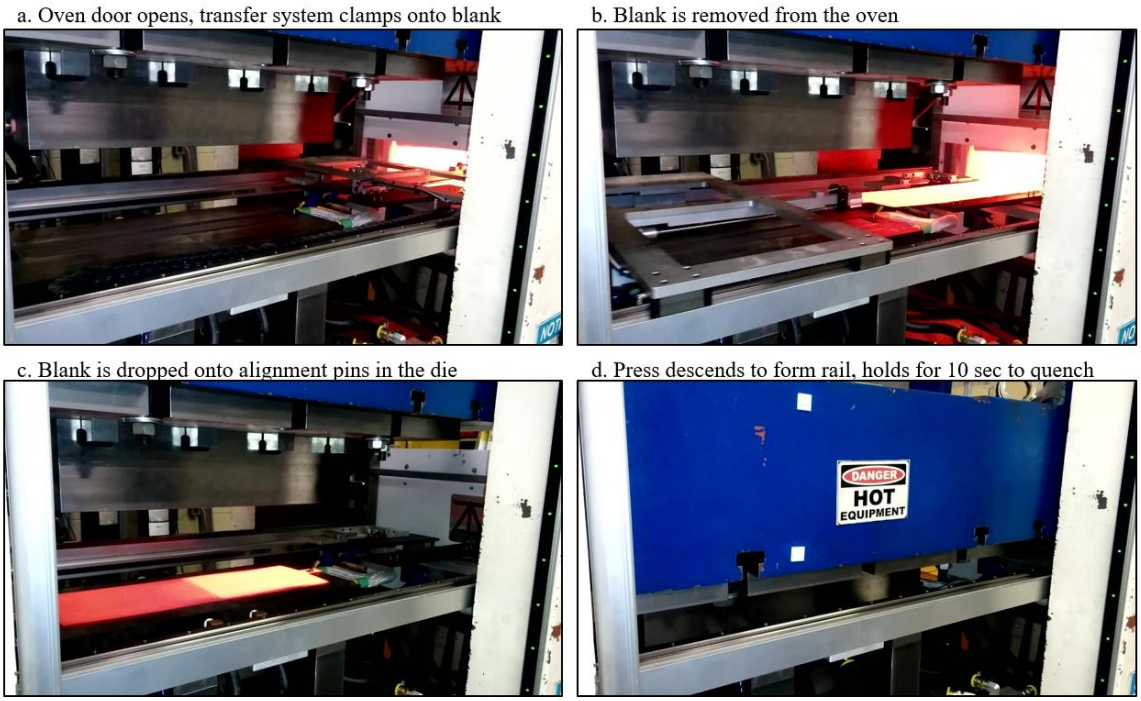

Figure 62: Transfer and forming of austenitized blank.

3.5 Micro-Hardness Measurements on as-Formed Parts

After forming of the top hat channels, micro-hardness measurements were taken to verify that the hot stamping process being used was resulting in the desired microstructure in the formed parts. To do this, samples needed to be removed from the formed rails to test the through-thickness hardness. The hot stamped Usibor® 1500-AS is too hard to be cut with a shear or a band saw, so other cutting methods were needed [3]. An abrasive saw was considered, but the heat generated in the cuts was likely to affect the material hardness. Strips were water jet cut from the top, sidewall, and flange regions of 1.2 mm and 1.6 mm thickness common gauge TWBs, 200 mm in length and centered on the laser weld line, as shown in Figure 63. The 200 mm strips were cut into 10 pieces, each 20 mm long. For the multi-gauge TWBs, these strips were laser cut instead to reduce cost, and a water cooled abrasive saw was used to section the strips into 9 pieces each 20 mm long. The weld line would have fallen on a cutting line if these strips were cut into 10 pieces, so the cut pattern was shifted and it was cut into 9 pieces instead. Once sectioned, the small pieces were hot mounted into resin pucks, with one strip fitting into each puck. The monolithic Ductibor® 500-AS rails were not tested for hardness, as it was expected that they would have the same hardness as the corresponding TWB section.

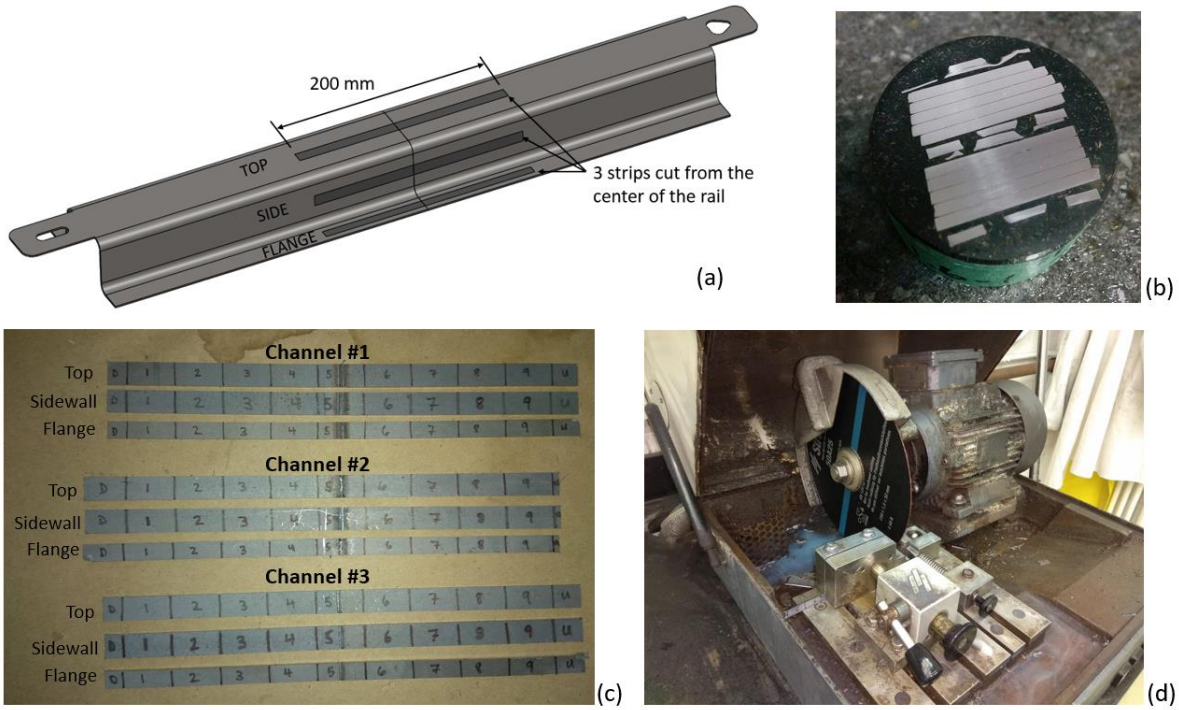

Figure 63: (a) Locations where specimens were cut from formed channels [12], (b) Puck containing sectioned strip [12], (c) 200 mm long strips for three repeats of one TWB condition, (d) Water cooled abrasive saw used to section strips for multi-gauge TWBs.

The pucks were polished using silicon carbide grit paper in the order: 240, 500, 800, 1200, and 2400 using a Struers TegraPol-15 automated polishing apparatus. Each grit was used for about 4 minutes to obtain a mirror finish. A Wilson Hardness micro-hardness tester (Figure 64) was used to take Vickers hardness measurements with 500 gf of indentation force, a 10 second dwell time, and a pyramidal indenter. These measurements were taken at 20 mm intervals along the length of the strip, except across the weld line where five smaller 0.5 mm intervals were measured. At each measurement point, three through-thickness hardness measurements were taken and averaged. Three specimens were measured to check for variation between parts in seven of the nine conditions. The exceptions to this were the top and side section of the 1.2/1.6 mm TWBs, where the samples for one of the three rails were overheated during preparation for hardness testing, resulting in thermal softening. For these two sections the average was taken from just two rails.

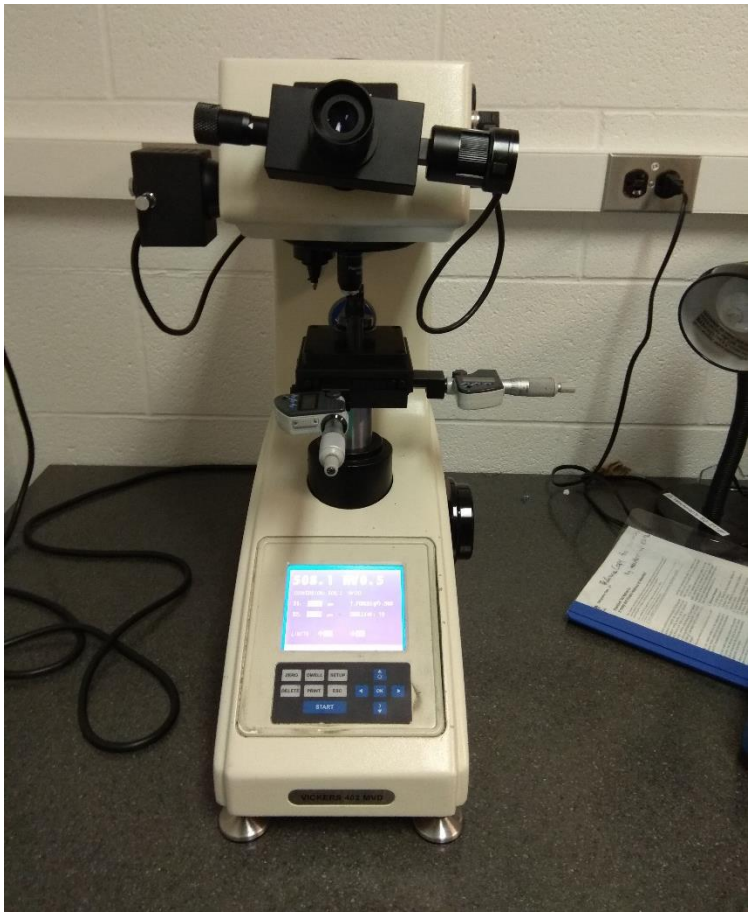

Figure 64: Wilson Hardness micro-hardness testing machine.

3.6 Micro-Hardness Measurement Results on Formed Hat Channels

The average hardness profiles measured in the top, sidewall, and flange of the TWB channels in 1.2 mm, 1.6 mm, and 1.2/1.6 mm multi-gauge conditions are shown in the nine plots in Figure 65. In these measurements the position along the length is measured from the tip of the Ductibor® 500-AS end of the rail, with the laser weld line being located at the 300 mm point. The solid lines show the average of three measured specimens of each condition, and the scatter bands show the standard deviation of the measurements at each point. The data represents a total of about 1200 hardness measurements taken from 27 pucks each containing a strip cut from the top, side, or flange of one of 9 rails.

3.6.1 Micro-Hardness Trends

Figure 65 shows that there is a significant difference in hardness between the Ductibor® 500-AS and Usibor® 1500-AS zones of the channels, so tailored properties have been achieved along the

length of these channels. The hardness is very uniform along the length of the parts, with an abrupt transition from the properties of one material to the other.

The 1.2 mm TWBs had the most repeatable hardness measurements between the three repeats that were measured, as shown by the small scatter bands in each of the top, side, and flange sections. The percentage scatters were between 3.7% and 4.2%, shown in Table 4. The profile is very uniform along the length of each parent material.

The 1.6 mm TWBs had higher scatter in the top (7.3%) and sidewall (9.2%), but the flange had low scatter (3.7%). The Usibor® 1500-AS section had lower scatter than the Ductibor® 500-AS section. In the top section an increase in hardness was observed in the Ductibor® 500-AS next to the weld line.

The 1.2/1.6 mm TWBs had the highest scatter in the top section at 9.7%. The sidewall (5.8%) and flange (6.7%) also had moderate scatter. As with the 1.6 mm common gauge parts, there was more scatter in the Ductibor® 500-AS than in the Usibor® 1500-AS. The hardness of the parent materials was less uniform in this condition than in the other gauge conditions.

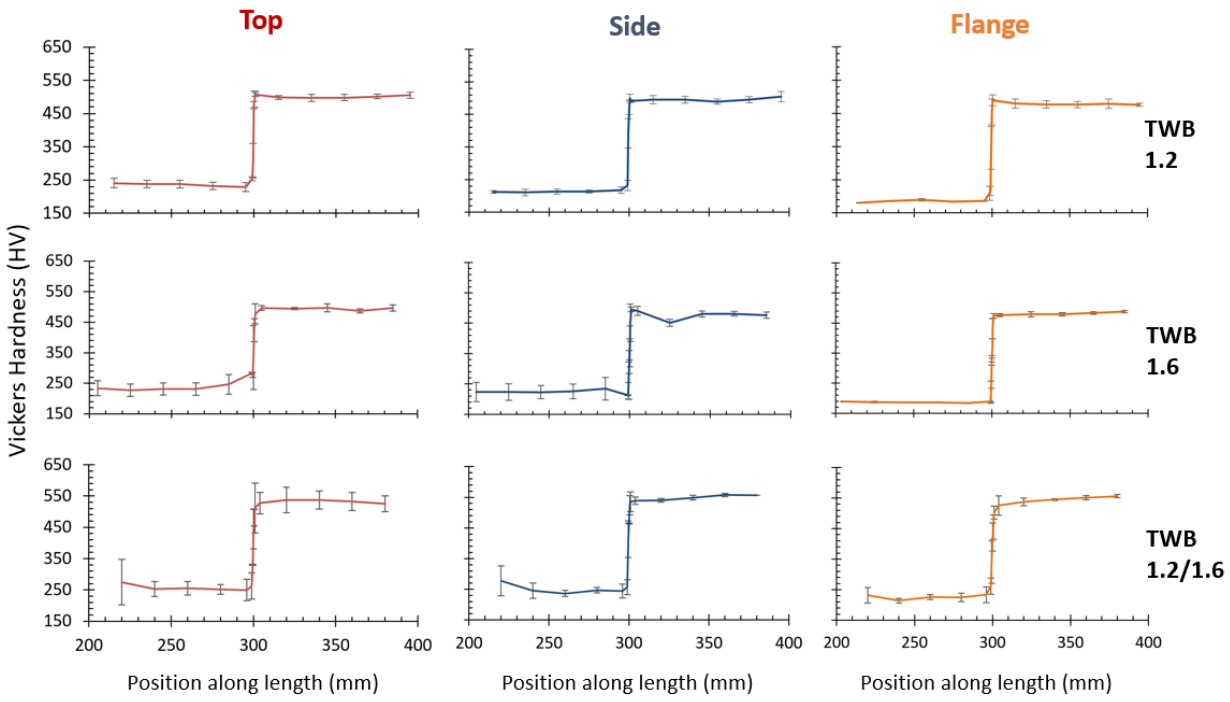

Figure 65: Measured hardness traverses along length of top, side, and flange of 1.2, 1.6, and 1.2/1.6 mm TWB channels.

Table 4: Percentage scatter in hardness measurements.

Gauge Condition	Top (%)	Sidewall (%)	Flange (%)
1.2 mm TWB	4.1	3.7	4.2
1.6 mm TWB	7.3	9.2	3.7
1.2/1.6 mm TWB	9.7	5.8	6.7

The average hardnesses in the two material sections of each TWB condition are summarized in Table 5. Along with Figure 66, it shows several trends in hardness. In the 1.2 mm and 1.6 mm TWB conditions the hardnesses were very similar in both the hard and soft zones and across the weld line. In each of the sections, the difference in hardness between the two material thicknesses is within the standard deviation of the measured data. The top section had the highest hardnesses of about 235 and 500 HV in the soft and hard zones respectively. This result is anticipated because there was very good contact between the top of the punch and the bottom of the die cavity under the full press tonnage. In the sidewall the hardnesses were slightly lower at about 220 and 485 HV respectively. This reduction is likely due to the contact force being reduced by the large angle between the press direction and the normal to the sidewall, which reduces the rate of heat transfer. Another contributing effect could be the strain in the sidewall causing the CCT diagram to shift [8], causing formation of some softer bainite. In the flange region the hardnesses were quite a bit lower, 185 and 480 HV respectively. This drop can be attributed to two properties of the flange area in the IDH forming tool that were described in Section 3.2. The contact force available at the binder from the nitrogen springs is an order of magnitude lower than the press tonnage, reducing the rate of heat transfer. In addition, the binder and flange area lacks water cooling, so it reached a higher steady state temperature of about 50°C between forming of successive blanks. These two factors reduced the rate quenching, reducing the hardness of the flange area.

Figure 66 shows that the 1.2/1.6 mm multi-gauge TWBs, which were formed in a newer custom tool, had measured hardnesses that were 12% higher than in the common gauge parts. The Ductibor® 500-AS section had hardnesses of 259 HV in the top, 251 HV in the sidewall, and 224 HV in the flange. The Usibor® 1500-AS section had hardnesses of 533 HV in the top, 551 HV in the sidewall, and 547 HV in the flange. This difference can be largely attributed to the use of the new multi-gauge forming die. The old IDH die was heated as high as 700°C to form channels

in the past, so its surface was heavily scaled and uneven. In contrast, the new die has smooth machined surfaces that were hardened through gas nitriding, improving the contact and increasing the rate of heat transfer, speeding up the quench rate. The quench rate in the flange region was further increased by the addition of water cooling to this part of the die which would reduce the steady state temperature between parts.

Table 5: Average hardness of each TWB condition in the Ductibor® 500-AS and Usibor® 1500-AS section respectively.

Gauge Condition	Top (HV)		Sidewall (HV)		Flange (HV)	
1.2 mm TWB	236	500	213	495	185	477
1.6 mm TWB	234	494	225	476	186	481
1.2/1.6 mm TWB	259	533	251	551	224	547

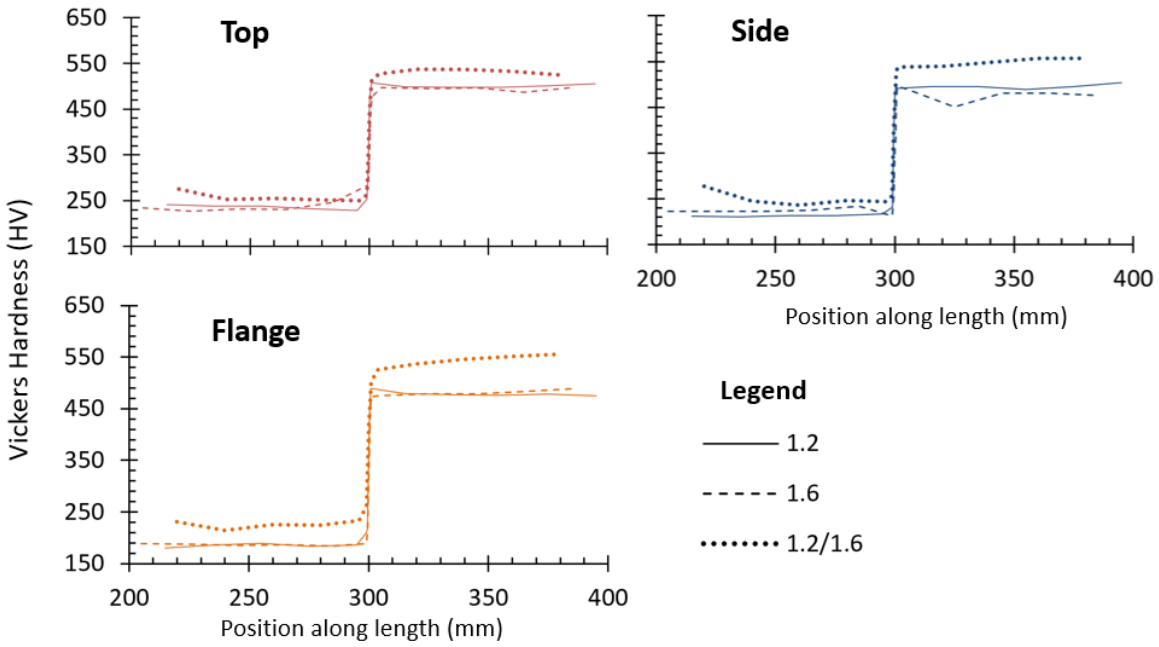

Figure 66: Comparison of hardnesses in different TWB gauge conditions in each location.

3.6.2 Comparison with In-Die Heating Results

It is of interest to compare the measured hardness distributions from the current TWB hot stampings with those from in-die heating (IDH) tailored components. In Figure 67, the micro-hardnesses measured in the 1.2 mm common gauge TWB parts are compared to those formed by Omer [20] using IDH tailored hot stamping. The work by Omer was described in Section 1.3.3.

The hardness profiles shown are from monolithic rails composed of 1.2 mm Usibor® 1500-AS that were formed in a tailor heated configuration of the rail die, with half of its length heated to 700°C and the other half cooled by chilled water. The entire length of the flange region was heated in these parts.

The hardnesses in the fully cooled Usibor® 1500-AS section are very similar in the top region. In the sidewall the fully cooled section is slightly softer in the IDH configuration than the TWB. The flange region is fully heated in the IDH part, so no direct comparison to the fully cooled TWB flange is appropriate. In the soft zone, it is shown that the 700°C IDH tailoring condition achieves a very similar hardness to the quenched Ductibor® 500-AS in each of the top, side, and flange regions. Outside of the transition zone, these two tailoring strategies achieve similar hardnesses along the length of the rail in the top and sidewall sections.

The size of the transition zone is the biggest difference between the final hardness profiles of these two tailoring strategies. Due to thermal conduction along the length of the part beyond the heated die zone, a large transition zone of about 70 mm in length [20] exists between the zones with fully cooled and IDH properties. In contrast, the transition zone in TWBs is very abrupt.

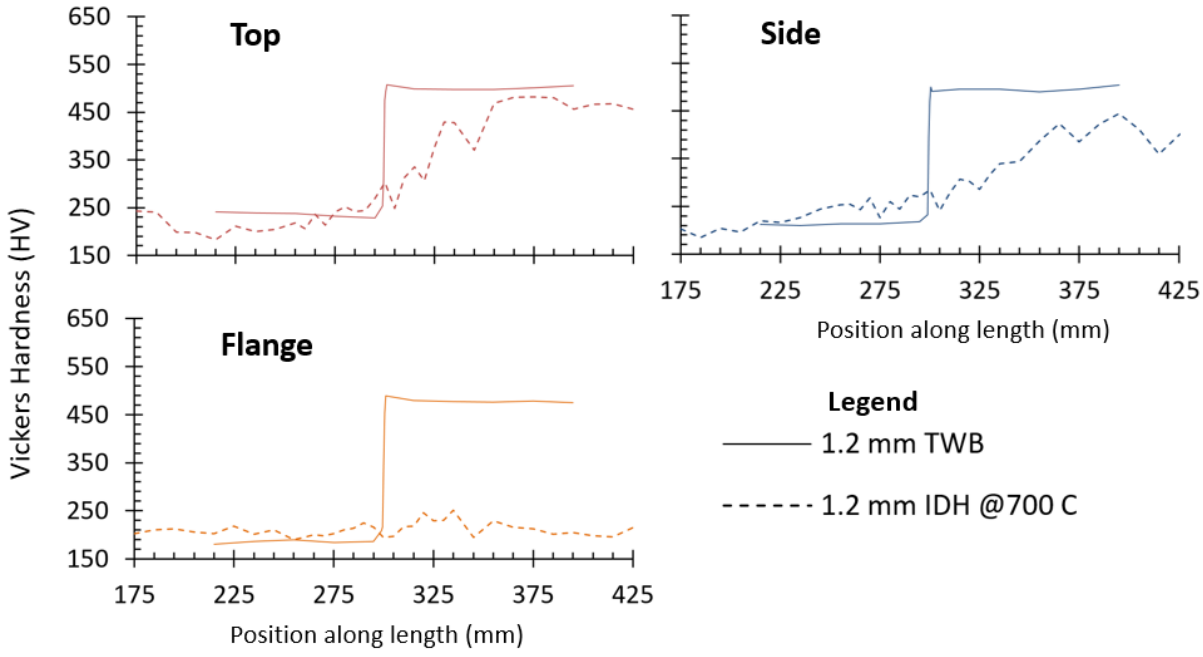

Figure 67: Comparison of hardness traverse in TWBs to IDH parts formed in a 700°C die, at a common 1.2 mm thickness. IDH data from Omer [20].

The transition in hardness between the soft Ductibor® 500-AS and hard Usibor® 1500-AS in TWB rails occurs over a very short distance, shown in Figure 68 to be about 2 mm wide. In each of the measurement regions, the transition between them exhibits a smooth, relatively steady increase. Importantly, there is not a weakened heat affected zone area of reduced hardness in the Ductibor® 500-AS adjacent to the weld, which is consistent with work by Múnera *et al.* [6] and Kang *et al.* [25]. This smooth transition in hardness is caused by carbon dilution in the molten zone of the weld between the low-carbon Ductibor® 500-AS and the higher carbon Usibor® 1500-AS [6].

The short transition in hardness in hot stamped TWBs is beneficial from a design perspective, because the precise properties that are desired can be inserted exactly where they are needed. However, this abrupt change in stiffness will cause a notch effect that could cause folding to initiate at it, as will be discussed later in Section 7.2.5.

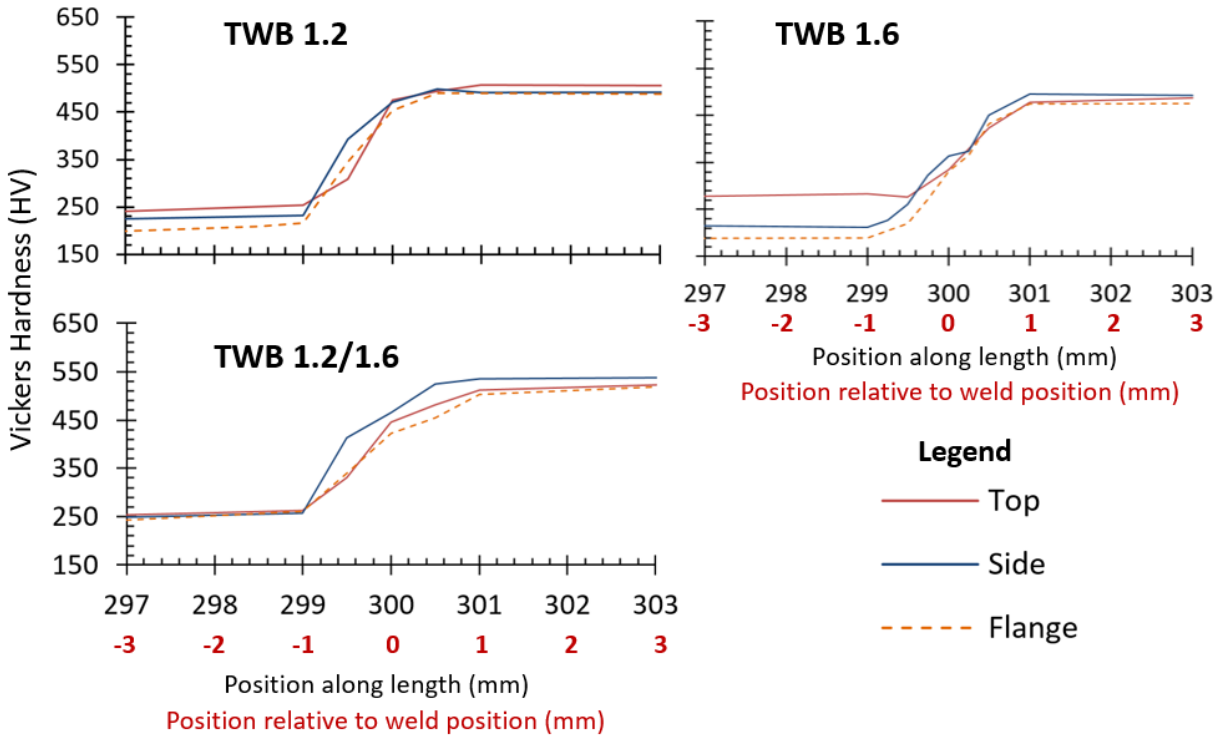

Figure 68: Detailed hardness traverse across the laser weld line in each gauge condition.

3.7 Preparation of Rail Specimens

The formed hat channels were used to produce side impact beams and axial crush rails for testing.

3.7.1 Side Impact Beams

Side impact beams for three point bend testing consist of one top hat channel spot welded to a flat backing plate, and were assembled (spot welded) at Promatek Research Centre, a sponsor of the project.

The backing plates are made of 1.6 mm thick JAC590R, a ferritic/bainitic steel produced by ArcelorMittal with a 590 MPa tensile strength. These plates measure 590 mm by 125 mm and were cut from larger sheets using a shear. These sheets, as well as monolithic hot stamped channels, were shipped to Promatek for cutting and welding. Side impact beams were produced only from monolithic Ductibor® 500-AS in 1.2 mm and 1.6 mm thicknesses. TWBs were not used for these tests.

The laser cutting for these rails is very simple, requiring only the tabs to be cut off. They were then spot welded to the backing plates using 12 welds on each side with a pitch of 50 mm, as shown in Figure 69 and Figure 70.

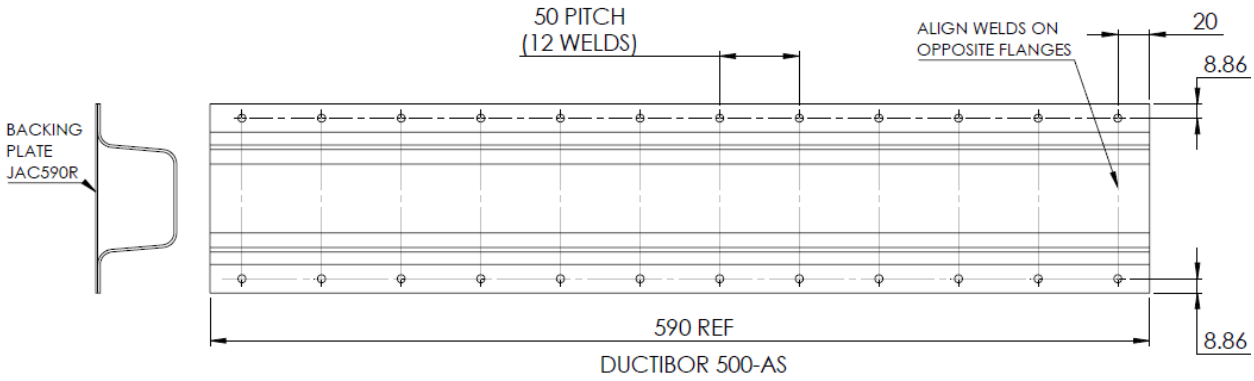

Figure 69: Spot welding of channels to backing plates to create side impact beam specimens. Dimensions in millimeters.

Up to this point, the specimens were still coated with the Aluminum-Silicon (AlSi) coating applied by the steel supplier. This coating is critical for the austenitizing process to prevent rapid scaling and oxidation in the furnace. However, in side impact and crush tests, this coating flakes off of the parts as they fold, causing a large cloud of dust that obscures the high speed cameras and coats the equipment as it settles. After initial tests showed this issue, all subsequent rails were sandblasted

to remove this coating from the outside. The coating remained on the inside of the specimens due to lack of access, but it did not go airborne as readily. Sandblasting prior to welding was not desirable because in a vehicle application this coating is left on, and it is expected to affect the strength of the spot welds.

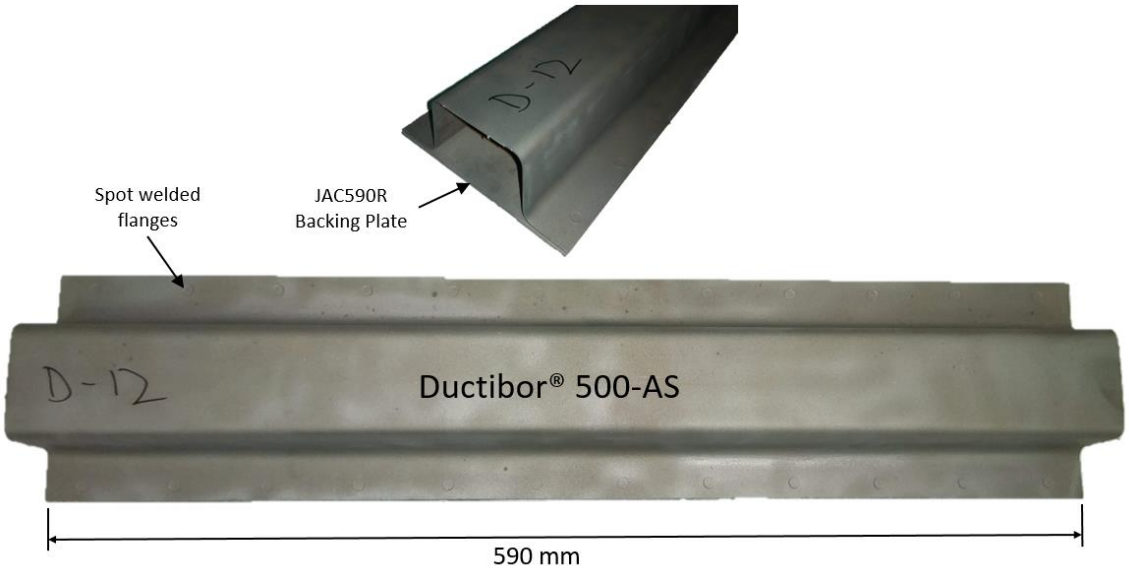

Figure 70: Welded side impact beam specimen with coating removed by sandblasting.

3.7.2 Axial Crush Rails

The axial crush rails are composed of two hat channels spot welded together along their flanges, with laser cut holes to facilitate mounting in fixtures for testing. As with the side impact beams, the laser cutting and spot welding was performed by Promatek Research Centre.

Laser cutting was used to shorten the channels by 90 mm to an overall length of 500 mm. There was 10 mm removed from the Ductibor® 500-AS section of the TWBs to eliminate edge effects on the impacted end, and 80 mm removed from the Usibor® 1500-AS section, as shown in Figure 71. The reduction in the length of the martensitic zone reduces the tendency for global buckling while preserving the full ductile crush zone. In monolithic specimens, 90 mm was removed from one end and just the tab was removed from the other. Four 12.7 mm (½") diameter holes were also cut into each end of the channels for bolts to pass through into the bosses used to clamp the rails for testing (Figure 72).

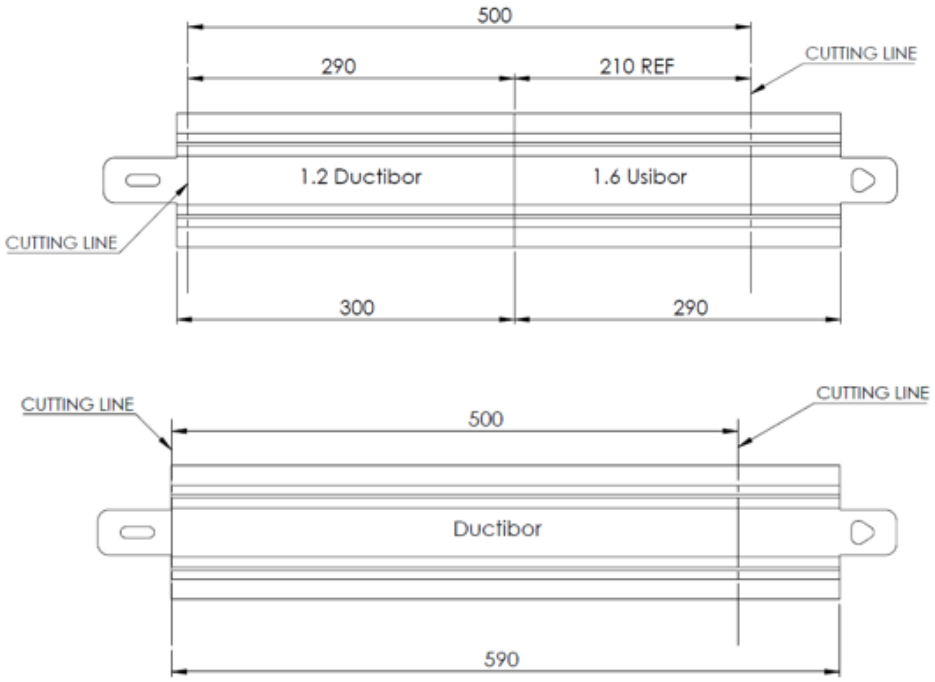

Figure 71: Trim lines on channels for axial crush. Dimensions in millimeters.

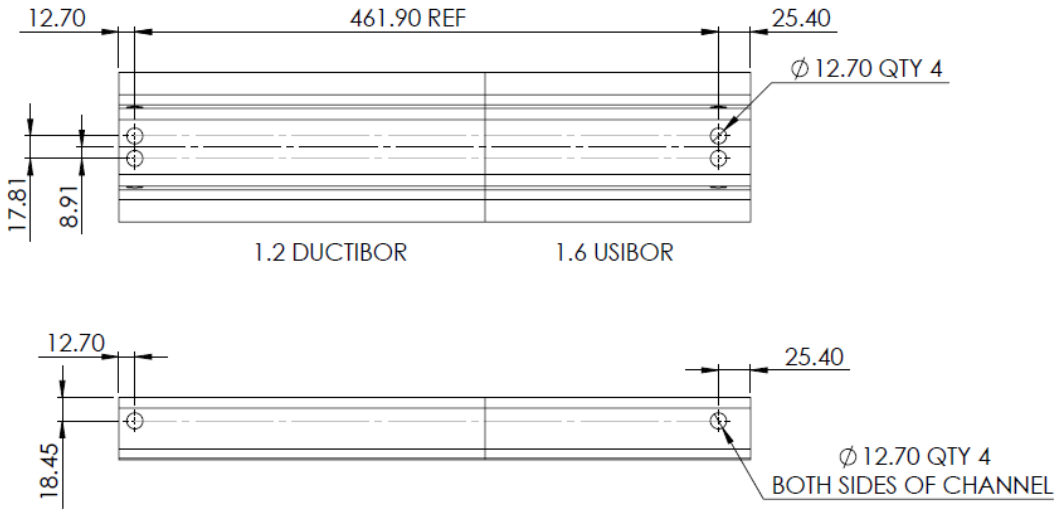

Figure 72: Laser cut holes for fixturing. TWB part is shown, monolithic parts are identical. Dimensions in millimeters.

The trimmed channels were spot welded together along the center of their flanges at a pitch of 25 mm, for a total of 20 welds along each flange. The weld pattern was slightly offset so that a weld did not fall directly on the laser weld line in TWB parts (Figure 73). The spot weld parameters of time, current, and force were developed by the Promatek Research Centre to ensure that they aligned with typical industrial practice, and to ensure repeatability between parts. The settings used

for each material thickness, regardless of alloy, are shown in Table 6. For the 1.2/1.6 mm multi-gauge parts, the 1.6 mm parameters were used for all of the welds.

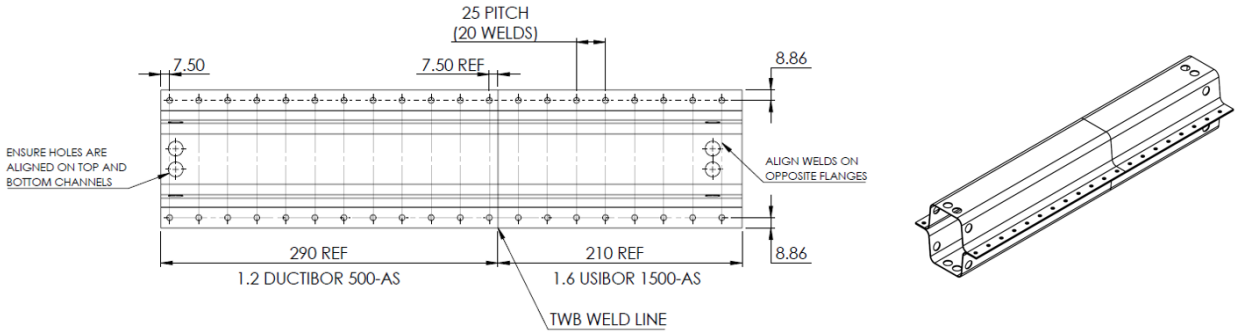

Figure 73: Spot welding of channels to create crush rails. TWB part shown, monolithic are identical. Dimensions in millimeters.

Table 6: Resistance spot weld settings [40].

Thickness (mm)	Pre-heat		Weld		Force (N)
	Time (ms)	Current (kA)	Time (ms)	Current (kA)	
1.2	33	8	400	7	3425
1.6	33	10	400	7	4003

After welding was complete, the assembled crush rail specimens were shipped back to UW for further preparation and testing. To reduce the peak load, and control the location of fold initiation during the crash tests, crush initiators were formed 65 mm from the impacted end of each part. These were formed using a small 40 ton hydraulic press operated by a hand pump, and a simple punch with a 25 mm x 10 mm indenter with a 5 mm profile radius, as shown in Figure 74. A die was inserted inside the rail to keep the profile from collapsing under the punch load. This setup was initially designed for use with channels before they were welded, but an added spacer allows for indenting welded rails. These dimples were formed into both sides of each rail specimen to a depth of approximately 4 mm. At UW these were then sandblasted to remove the AlSi coating from the outside. Monolithic and TWB crush rails prior to sandblasting are shown in Figure 75.

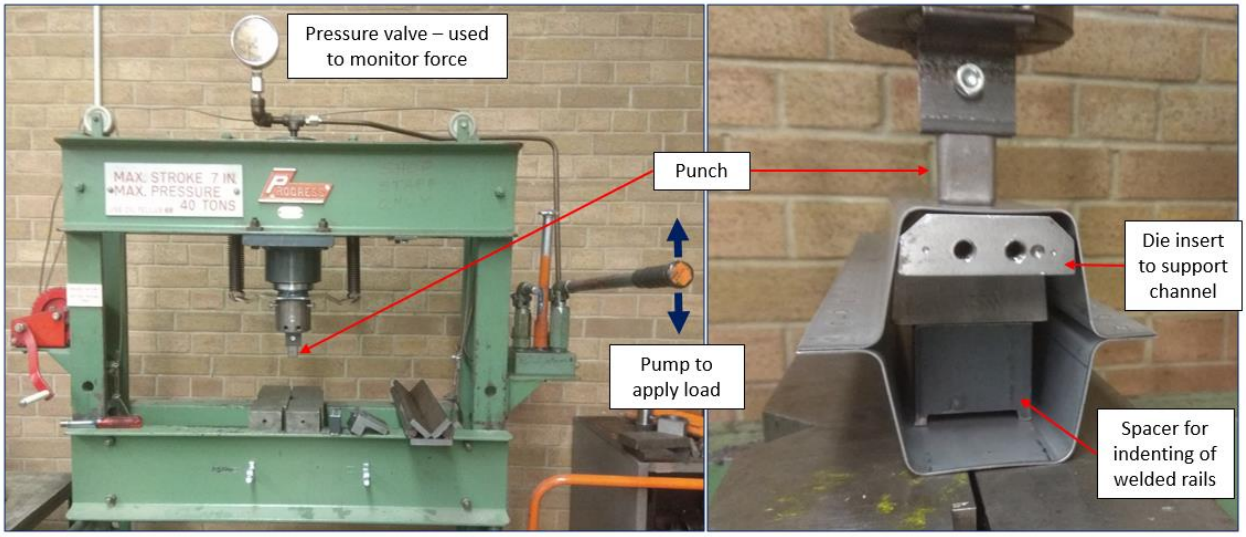

Figure 74: Manual press and punch for adding crush initiators to rails.

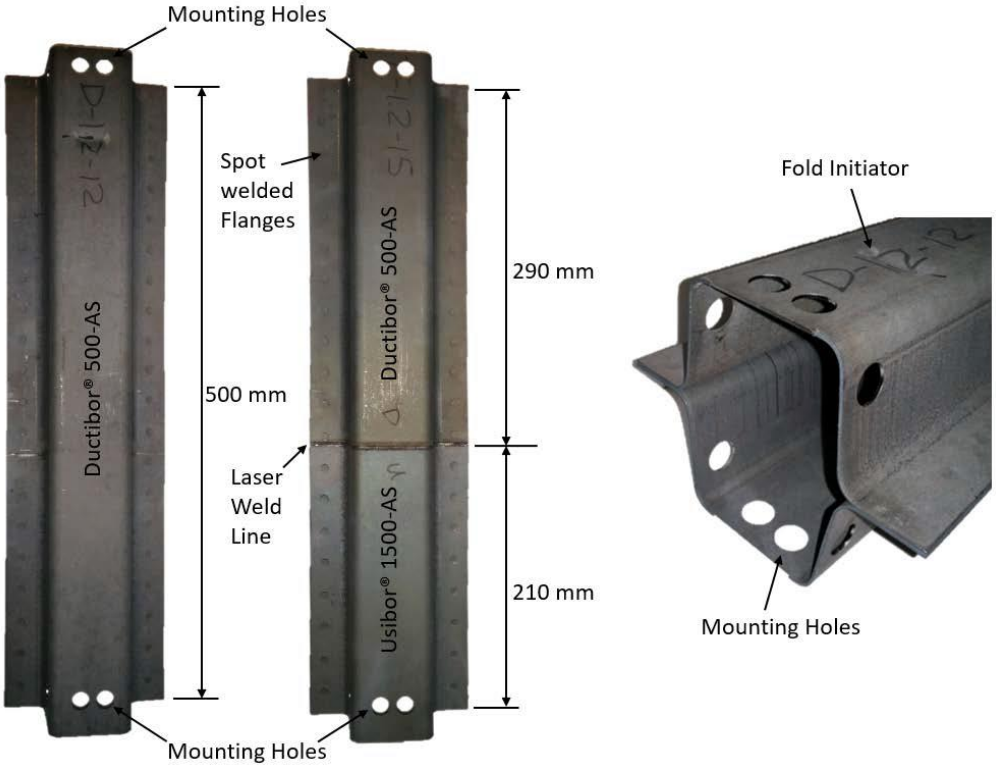

Figure 75: Monolithic and TWB axial crush rail specimens before sandblasting [13].

4.0 Mechanical Test Methodology

The mechanical testing program (beyond the larger demonstrator structures presented in Chapter 2) comprised both static and dynamic three point bend experiments on monolithic Ductibor® 500-AS samples, as well as static and dynamic axial crush experiments conducted on monolithic Ductibor® 500-AS and Ductibor® 500-AS:Usibor® 1500-AS TWBs. Lastly, axial crush experiments were conducted on the left side (LH) and right side (RH) crush tips extracted from baseline commercial side frames. Table 7 is a test matrix for all of the dynamic and quasi-static crush testing that was conducted.

Table 7: Test matrix for axial crush and three point bend testing.

Materials	Designation	3 Point Bends		Axial Crush	
		Dynamic	QS	Dynamic	QS
1.2 mm Ductibor® 500-AS	Duct 1.2	6	4	3	3
1.6 mm Ductibor® 500-AS	Duct 1.6	5	4	3	3
1.2 mm Ductibor® 500-AS to 1.2 mm Usibor® 1500-AS TWBs	TWB 1.2	/	/	3	3
1.2 mm Ductibor® 500-AS to 1.6 mm Usibor® 1500-AS TWBs	TWB 1.2/1.6	/	/	3	3
1.6 mm Ductibor® 500-AS to 1.6 mm Usibor® 1500-AS TWBs	TWB 1.6	/	/	3	3
Left Side Baseline Crush Tip	LH Crush Tip	/	/	6	/
Right Side Baseline Crush Tip	RH Crush Tip	/	/	6	/

4.1 Three Point Bend Experiments

4.1.1 Dynamic Three Point Bend

Dynamic three point bend experiments were conducted using the Seattle Safety crash sled at UW. This sled is described in Section 2.3 for the baseline demonstrator testing. In the experiments described in this chapter, a different vertical barrier wall is mounted to the top of the sled (Figure 76) that impacts the test articles. This sled-mounted barrier wall weighs 476 kg. In addition, the

outriggers required for the wider demonstrator structure were not required, such that the total sled and barrier wall mass was 855 kg before installation of the three point bend impact tup and load cells.

Figure 76: UW Seattle Safety crash sled used for smaller test articles in this thesis.

Two 500 mm long supports with 50 mm diameter cylindrical support faces made from machined 4140 cold rolled steel were mounted to the fixed barrier wall of the reaction block, as shown in Figure 77 and Figure 78. These supports were 178 mm (7”) long to support the 125 mm width of the side impact beam specimen, and were mounted with a center-to-center distance of 375 mm. 200 mm thick Plascore 5056 honeycomb was cut to a 150 mm x 300 mm size and mounted to a single standoff below the test specimen. The honeycomb serves to stop the sled after an initial free crush distance of 120 mm. An emergency honeycomb tube was also used, though it is not installed in the photograph in Figure 78.

A cylindrical loading tup with a 100 mm diameter made from 4140 hot rolled steel was mounted to a plate, which in turn is attached to two load cells on the sled face. A sheet of 12.7 mm (1/2”) plywood is sandwiched between the tup and the plate to dampen vibration caused by the impact. The contacting surfaces of these three cylindrical supports were carburized to prevent surface damage. These supports were developed for work by Prajogo [19] and were also used by Kim [52].

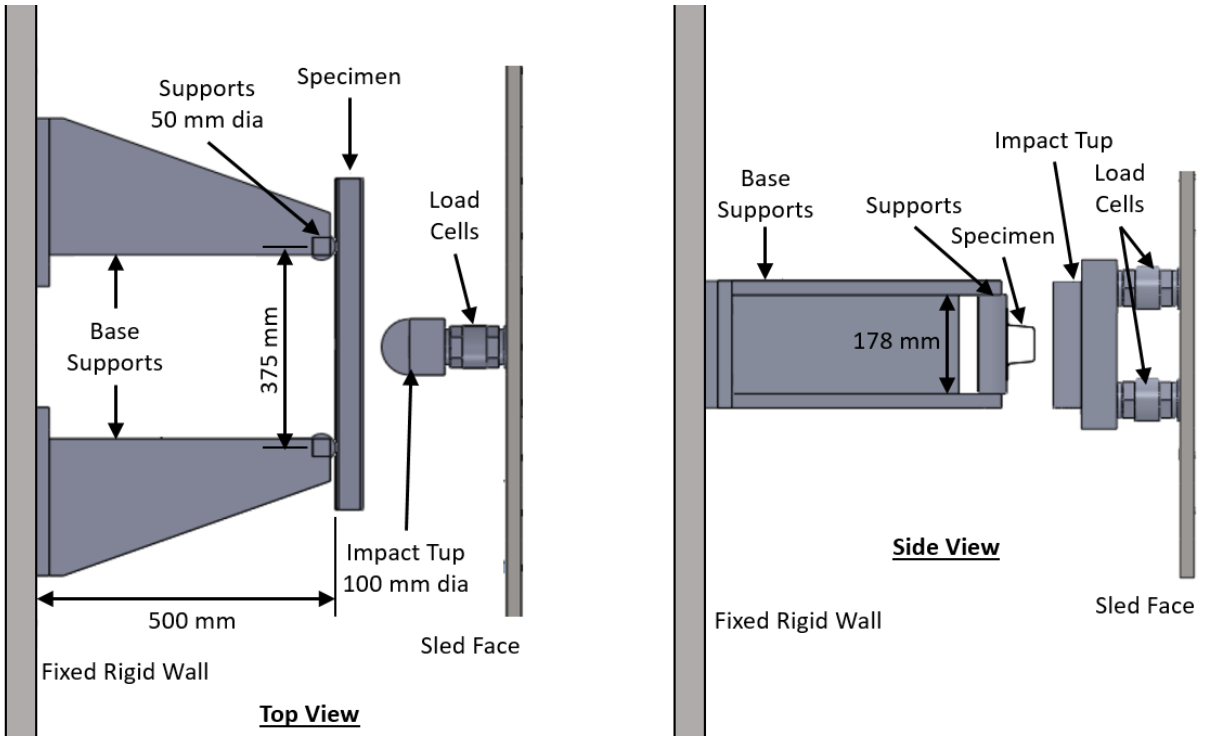

Figure 77: CAD layout showing dynamic three point bend experiment from Top and Side views. Adapted from [19].

Figure 78: Dynamic three point bend support setup.

The specimen was loosely attached to the face of the supports using steel wire attached to the impact wall, in between the span of the supports. As soon as the impactor contacts the specimen, these wires lose tension and do not affect the experiment. The sled was fired using a charging pressure of 138 kPa (20 psi) to achieve an impact velocity of 6.5 m/s (23.5 km/h), with a total mass of 865 kg. The extra 10 kg compared to the sled and barrier wall mass accounts for the mass of the

load cells and impact tup. When the laser trigger was activated, test data was logged at 10,000 Hz for 1 second. Figure 79 shows two Kistler 9731B piezoelectric load cells mounted between the impact tup and the sled face. The signals from these load cells were summed to find the total impact force. The two on-board accelerometers were averaged to give the sled deceleration, which was integrated for velocity and double integrated to find displacement. Two Photron SA-4/5 high speed cameras recorded the test at 5000 frames per second from top and side views, as shown in Figure 80. Video images of the impacted area on the rail were also recorded using a Telops FAST-IR 2K thermal imaging camera to measure the heat generated in the folds due to the plastic work being done.

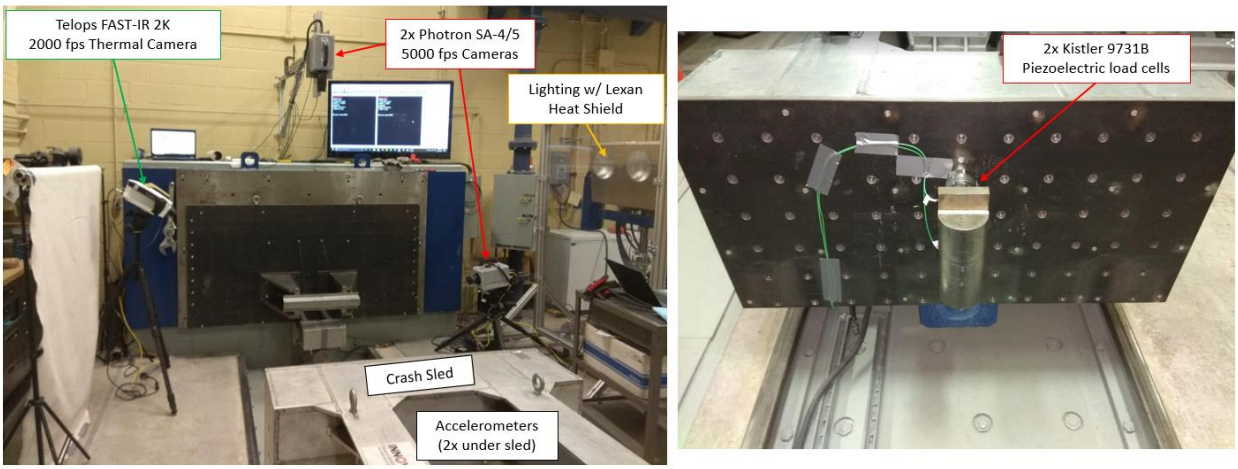

Figure 79: Cameras and instrumentation used for three point bend tests.

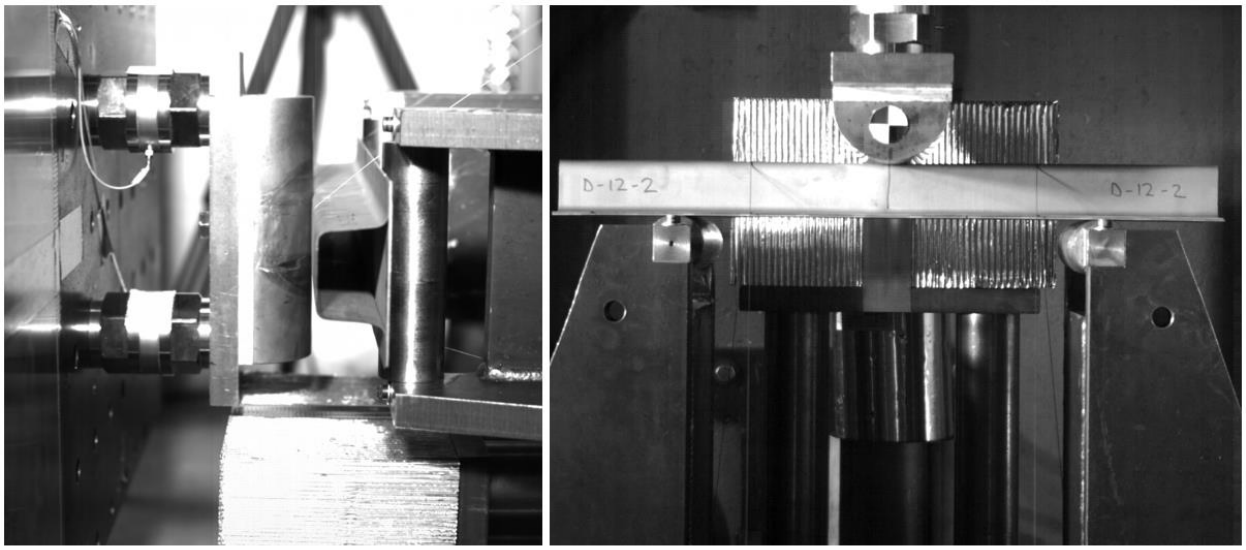

Side View: Photron SA-5 Top View: Photron SA-4

Figure 80: Static images of three point bend tests prior to testing from high speed video cameras.

Dynamic three point bend tests were performed on side impact beam specimens from two different material conditions, with several repeats of each condition. Similar to the baseline demonstrator tests, spreadsheets were generated logging the measurements from the load cells and accelerometers with respect to time. As with the baseline demonstrator tests, the inertial effect caused by mounting the load cells on the sled was accounted for.

4.1.2 Quasi-Static Three Point Bend

Quasi-static three point bend experiments were performed using a compressive hydraulic frame capable of exerting 496 kN (50 ton) of force, shown in Figure 81. This test frame was chosen because fixtures for three point bend testing had been previously developed for it by Prajogo [49] and Kim [52]. It has a wide bed that gives good access for setting up tests and for camera angles. The same supports and impactor used in the dynamic tests were also used in these quasi-static tests. The supports were bolted upright to the press bed with the same span of 375 mm, and the impact tup was bolted to the press actuator. The side impact beam specimens were placed with the backing plate on top of the supports, centered under the loading tup. With the experiment being rotated by 90 degrees compared to the dynamic test, there was no need for wire to hold the specimen in place; they were held only by gravity.

The press was controlled using a LabVIEW program running on a PC, which interfaces with the press using a MTS 407 servo controller through a Digital-to-Analog data acquisition (DAQ) card.

To begin the test, the 407 controller was used to manually move the cylinder down until the impact tup had just made contact with the top of the specimen. Then the LabVIEW program was used to move the press downward at a displacement speed of 0.508 mm/s (0.02 in/s) to a total displacement of 115 mm. The load on the impactor was measured using a 480 kN load cell, and the displacement was measured through a linear variable differential transformer (LVDT) within the actuator. These signals were recorded by the PC through the DAQ at a frequency of 50 Hz. Video was recorded from two angles using two Nikon D3200 DSLR cameras mounted on tripods, with the camera views shown in Figure 82.

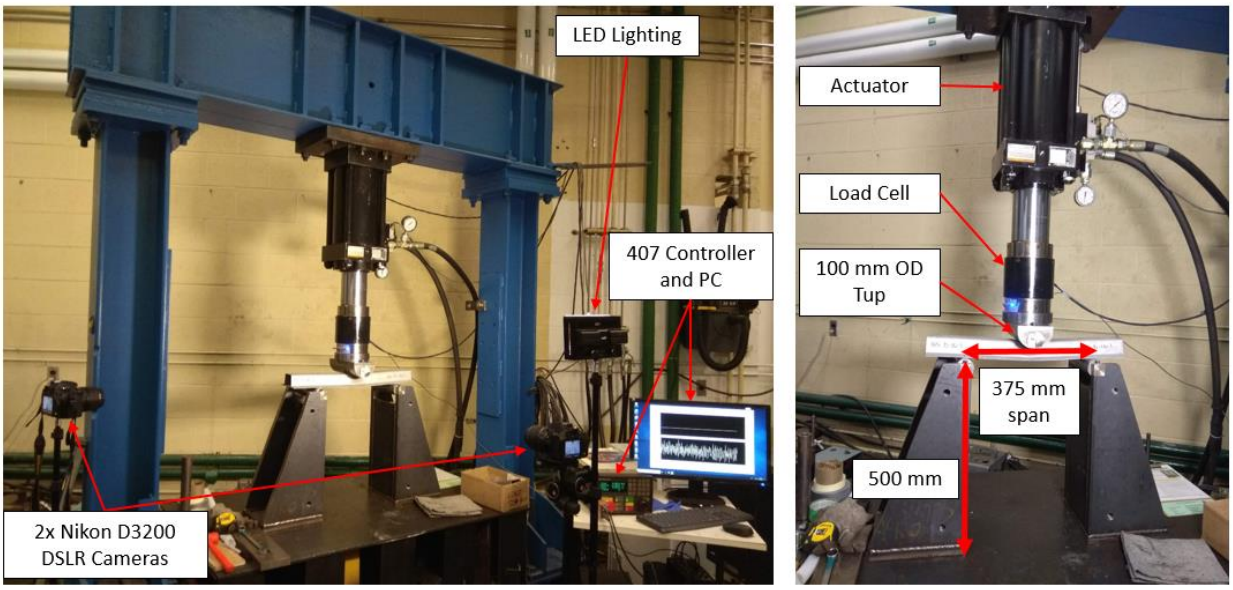

Figure 81: Hydraulic frame with cameras and tooling installed for three point bend tests.

Front View: Nikon D3200 Side View: Nikon D3200

Figure 82: Static images from DSLR cameras of quasi-static three point bend arrangement prior to testing.

In the quasi-static three point bend tests, the load and displacement history were logged into a data file for each test. Then the trapezoid rule described in Section 4.1.1 was used again to calculate the energy absorbed by the side impact beams.

4.2 Axial Crush Experiments

4.2.1 Dynamic Axial Crush

Dynamic axial crush experiments were performed on the same UW crash sled with the barrier wall that was used for three point bend tests, but with a differing mounting configuration. For these tests, the rail was mounted to the wall on a 50 mm deep boss that is machined to match the rail profile. These bosses were developed for the work done on IDH rails by Omer [10, 20, 21]. The laser-cut holes in the rail allow clamping bolts to pass through. At the impacted end, a similar boss with a 25 mm depth is installed. A piece of 19 mm (¾") thick plywood is bolted to the impacted face of the boss to attenuate the impact from the sled, as shown in Figure 83. In TWB parts, the Usibor® 1500-AS end was clamped to the wall side boss so that the ductile Ductibor® 500-AS end was impacted by the sled. The wall side clamping boss was mounted to the wall through a load cell sandwich plate (Figure 84). This assembly consists of two 63.5 mm (2.5") thick plates with three load cells mounted between them in a triangular pattern. One of these plates is bolted to the fixed barrier wall, and the boss is mounted to the other. In these tests, the sled assembly had a total mass of 855 kg and was fired using a reservoir pressure of 310 kPa (45 psi) to achieve a speed of 10.6 m/s (38.2 km/h). A sheet of 12.7 mm (1/2") plywood was mounted to the face of the sled to limit how far the impacted end of a specimen could slide along the face in the event that it had a global buckling mode.

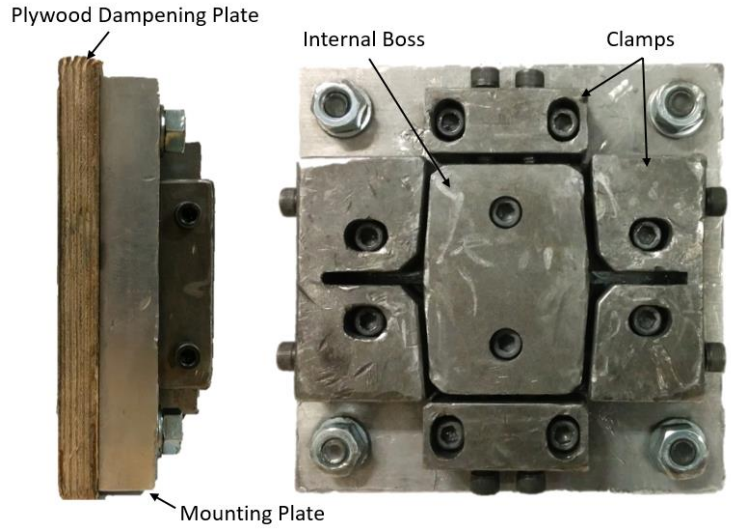

Figure 83: Boss (25 mm depth) and external clamps that are mounted to the impacted end of the rail. Boss at fixed end of the rail has identical profile but a 50 mm depth [13].

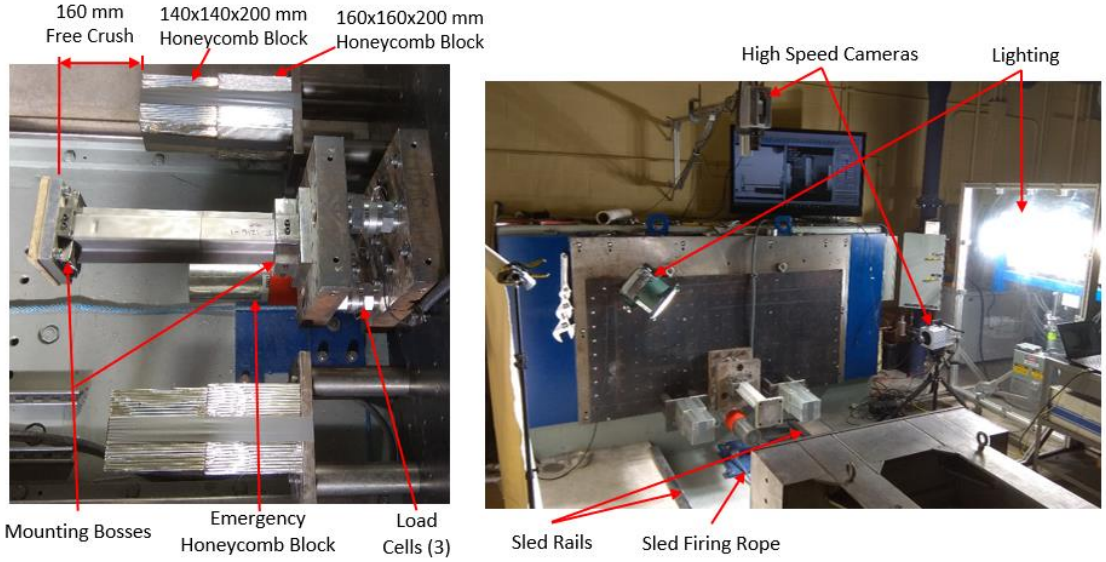

Figure 84: Dynamic axial crush test setup on the UW crash sled [14].

Honeycomb arrestors comprising stacked blocks of 200 mm thick Plascore 5056 aluminum honeycomb, 160 mm x 160 mm and 140 mm x 140 mm in size, were mounted on standoffs on either side of the crush rail. Test data was logged at 10,000 Hz for 1 second after the sled crossed the laser trigger. The measurements from three 120 kN Kistler 9731B piezoelectric load cells mounted in the load cell sandwich plates were used to measure crush load, and deceleration was measured by two accelerometers on board the sled. Two high speed cameras were used to record

these tests at 5,000 frames per second. A Photron SA-4 was mounted directly above the rail, and a Photron SA-5 was mounted on one side of it, with sample images shown in Figure 85.

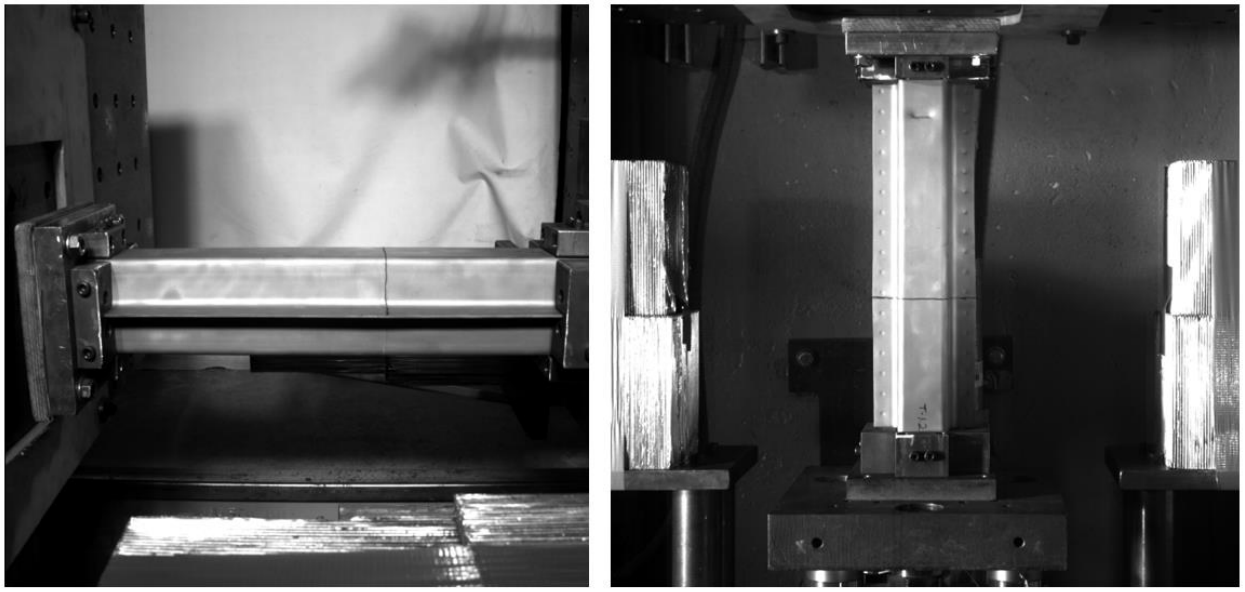

Side View: Photron SA-5

Top View: Photron SA-4

Figure 85: Still images of axial crush rails prior to testing from high speed video cameras.

Similar to the baseline demonstrator and dynamic three point bend tests, spreadsheets were generated logging the measurements from wall mounted load cells and sled mounted accelerometers with respect to time. Force versus displacement and energy versus displacement curves were then derived using the same methods as before.

4.2.2 Quasi-Static Axial Crush

Quasi-static axial crush experiments were performed using the 670 kN servo-hydraulic press shown in Figure 86. This press was chosen for axial crushing because there are four vertical guide posts that support the punch to react any lateral loads during crushing and protect the actuator. The same bosses were used as in the axial crush tests (Figure 83), with the fixed end mounted in the lower, 50 mm deep boss which was clamped to the press lower platen, and the impacted end mounted in the 25 mm deep boss. Initial trials left the impacted end unclamped like in the dynamic tests, however at this much lower quasi-static displacement speed the boss moved laterally and rotated along the press upper platen surface as the specimen crushed. For the remainder of the tests, this top boss was clamped to the upper platen with the plywood damping plate removed.

The quasi-static crush experiments were conducted at a constant displacement speed of 0.5 mm/s for a total displacement of 250 mm. A LabVIEW program running on a PC was used to move the punch into position, set the desired displacement and speed, and log data. Similar to the Macrodyne forming press described in Section 3.3.1, this program interfaces with the press through an MTS FlexTest servo controller. Displacement was measured using an LVDT in the cylinder, and force was measured using a pack of three load cells mounted between the upper and lower parts of the punch. Video was recorded from two angles using two Nikon D3200 DSLR cameras mounted on tripods.

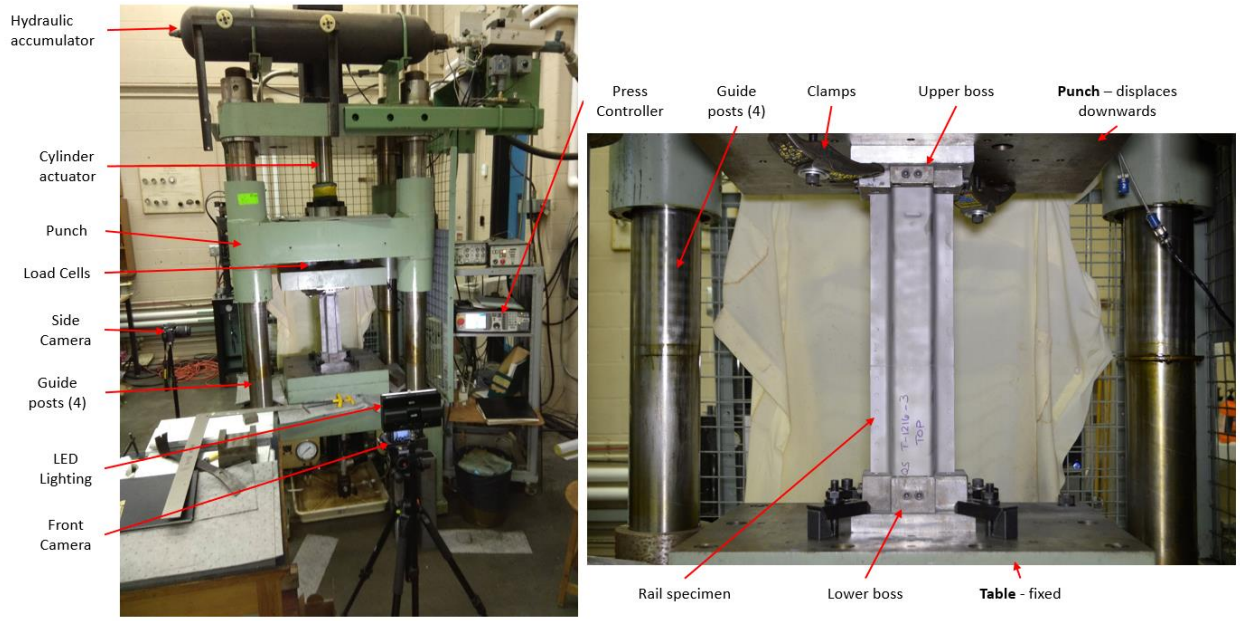

Figure 86: Quasi-static axial crush test setup.

In the quasi-static crush tests, the voltage outputs from the load cells and the hydraulic cylinder LVDT were logged into a data file for each test. Afterwards this data file was interpreted by a calibration spreadsheet to convert these voltages to forces and displacements. Then the trapezoid rule described in 4.1.1 was used again to calculate the energy absorbed by the rails.

4.3 Baseline Crush Tip Dynamic Crush Experiment Setup

To determine the collapse load of the axial crush tip in the baseline front side frames, specimens were produced that isolated the LH and RH crush tips from the rest of the baseline front side frames. The first 340 mm of the side frame was removed with a band saw and then MIG welded perpendicular to a 12.7 mm (1/2") thick steel plate, 200 mm by 300 mm in size, as shown in Figure

87. The large bracket on the front of the crush tips was trimmed away using a cut off wheel on an angle grinder. This bracket could not be left in place because it would impact the sled before the main part of the crush tip.

Figure 87: Specimen preparation for baseline axial crush tip testing.

The dynamic crush testing was performed on the UW crash sled in a similar configuration as was used for the axial crush experiments, described in Section 4.2.1. Figure 88 shows a typical crush tip specimen and testing arrangement. Plascore 5056 honeycomb was cut into pieces 320 mm wide by 130 mm high, with the standard height of 197 mm. This was mounted to standoffs 100 mm off of the wall on either side of the load cell plates, giving a free crush distance of 285 mm. The specimen was bolted to the front of the load cell plates, using two bolts at the top that thread into the plate. The bottom was attached using two bolts from the back that threaded into nuts welded to the specimen plate, to allow easier access to remove the bolts. In early trials the part folded over the lower bolt heads, making them difficult to remove. A piece of 12.7 mm (1/2”) thick plywood 300 mm x 300 mm was mounted to the face of the sled to impact the specimen. This helped to dampen the impact, as well as protect the sled face from damage. This piece of plywood was consumed during each test and replaced.

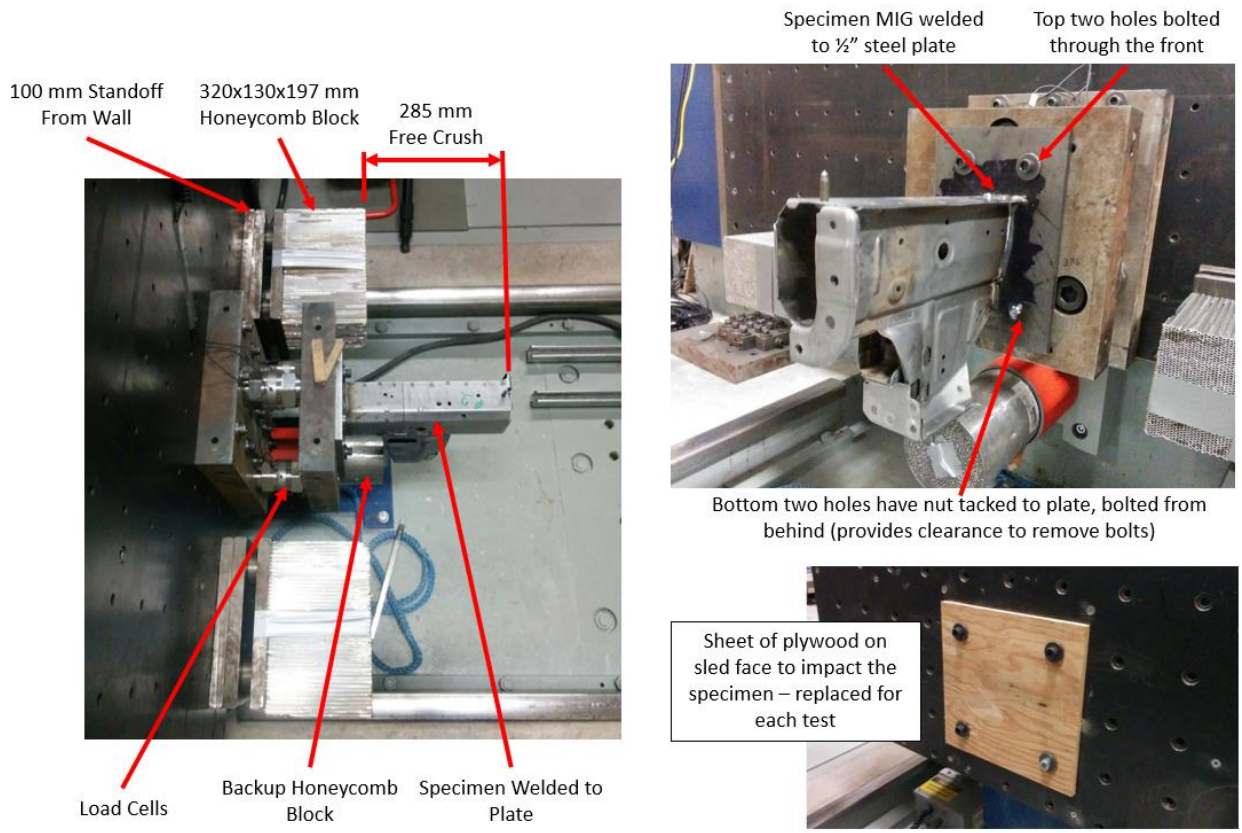

Figure 88: Mounting of baseline axial crush tip specimen and honeycomb.

The sled was fired using a charging pressure of 172.4 kPa (25 psi) to achieve a speed of 7.5 m/s (27.1 km/h), with a total mass of 855 kg. After crossing the laser trigger, test data was logged at 10,000 Hz for 1 second. As with the previous axial crush tests, Figure 88 shows that three Kistler 9731B piezoelectric load cells mounted between the sandwich plates on the barrier wall were summed to find the total crush force. The two on-board accelerometers on the sled were averaged and used to determine displacement. Figure 89 shows that three Photron SA-4/5 high speed cameras recorded the tests at 5000 frames per second from the top and both side views (Figure 90). In addition to the main lights, three smaller lights were arranged around the specimen to attempt to illuminate the entire part.

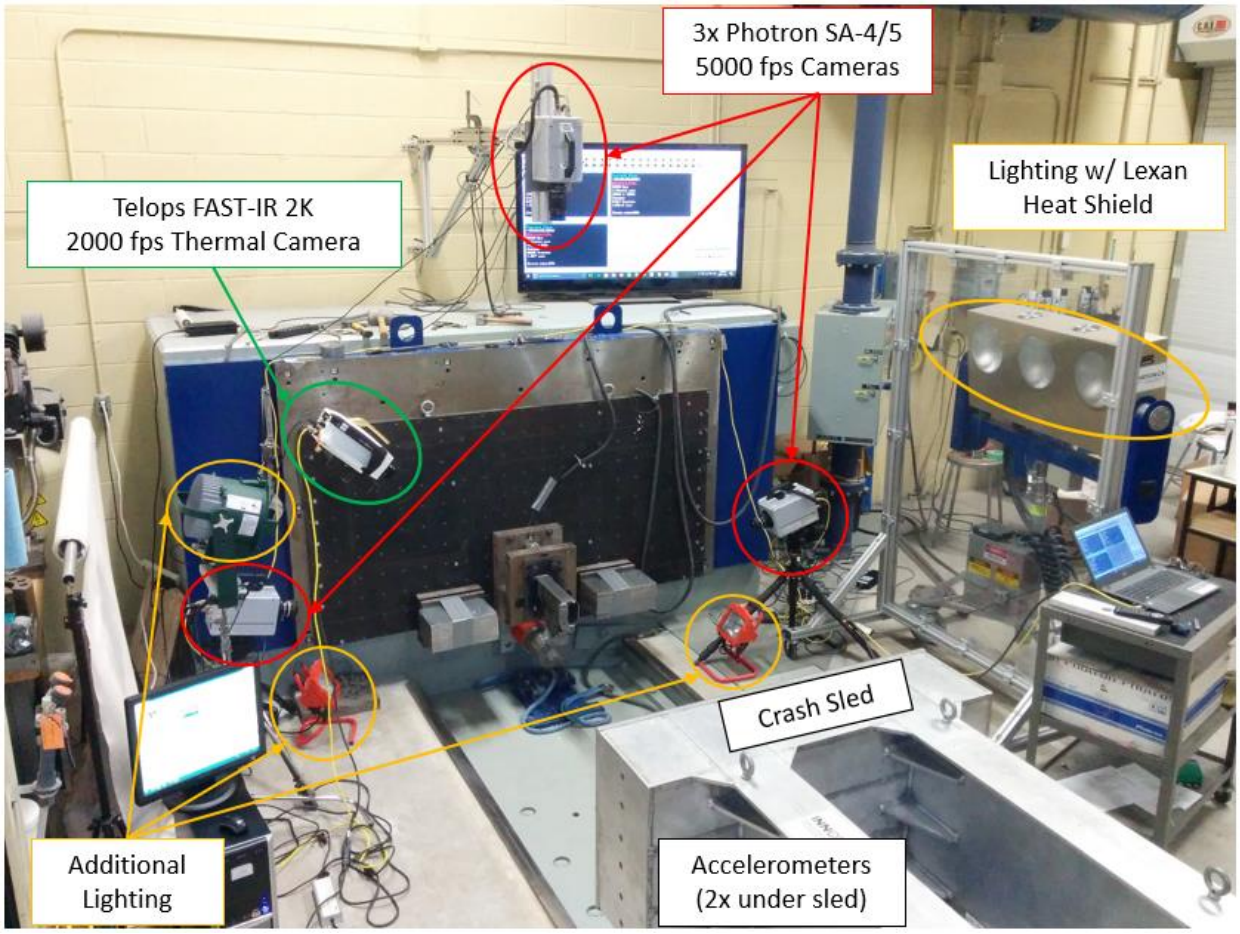

Figure 89: Cameras, lighting, and instrumentation used for baseline crush tip testing.

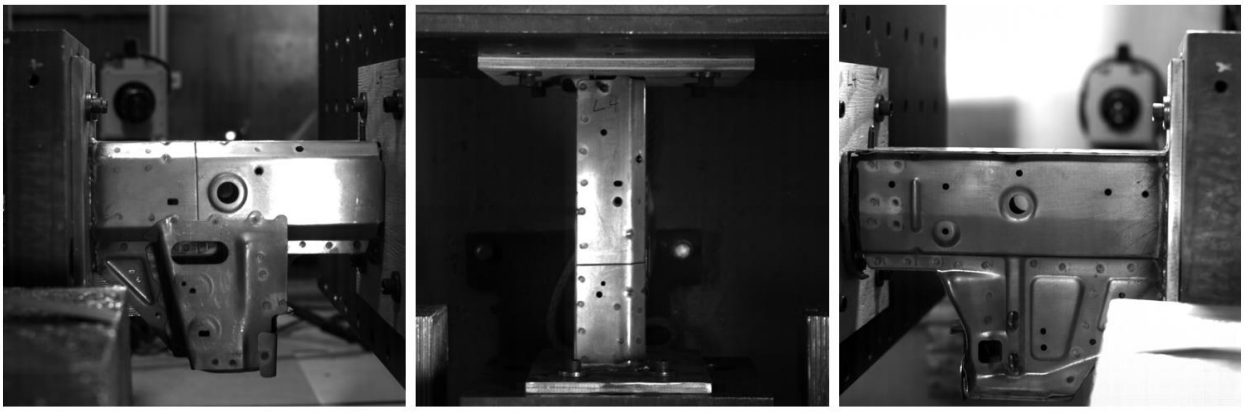

Left Side View: Photron SA-5 | Top View: Photron SA-4 | Right Side View: Photron SA-5

Figure 90: High speed camera views of test specimens.

5.0 Numerical Modelling of Crush Experiments

5.1 Material Models

5.1.1 Fully Quenched Usibor® 1500-AS

The constitutive behaviour of fully quenched Usibor® 1500-AS was modelled using a simplification that assumed that the hardness achieved after forming was uniform. Though the hardness testing showed that this wasn't quite the case, the range of about 20 HV in hardness was not significant enough to require multiple material zones. The hardness testing in Section 3.6 established an average hardness of about 490 HV across the different thicknesses and locations, indicating a fully martensitic microstructure. The material stress strain response and strain rate sensitivity was predicted using the eTCM (Section 1.6) [21] for a fully martensitic microstructure. The flow stress curves at different strain rates are shown in Figure 91.

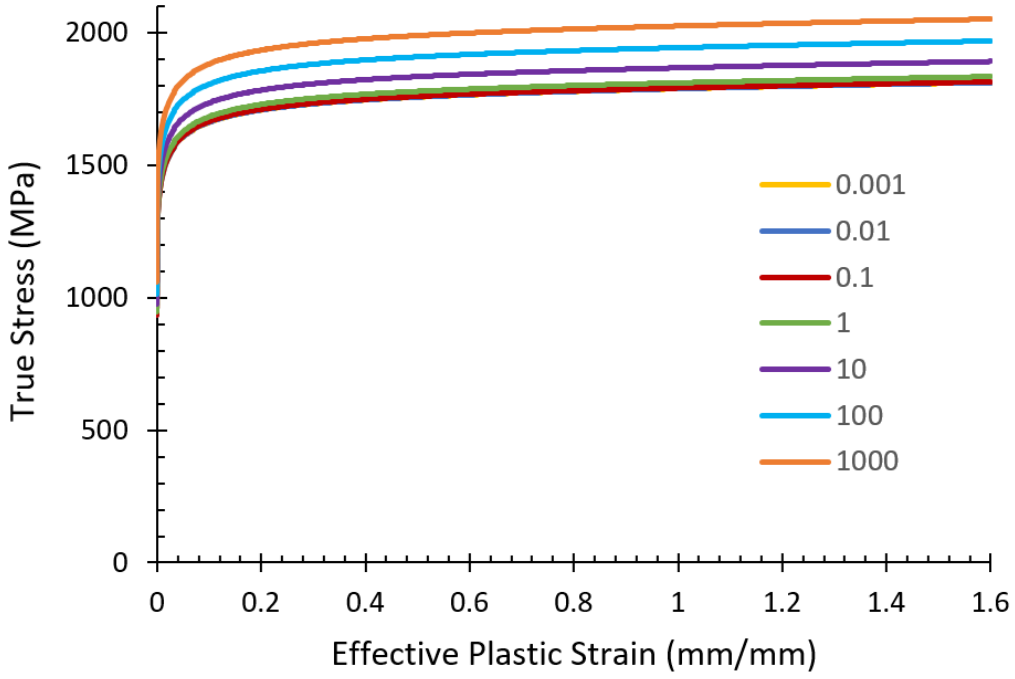

Figure 91: Constitutive curves for fully martensitic Usibor® 1500-AS [21].

Failure in the fully quenched Usibor® 1500-AS material was predicted using the Generalized Incremental Stress State dependent damage Model (GISSMO) [47] based on characterization work performed by ten Kortenaar [48]. The fracture curve used for this material is shown in Figure 92.

The regularization curve is shown in Figure 93. Element deletion is triggered once 60% of the integration points within an element have failed.

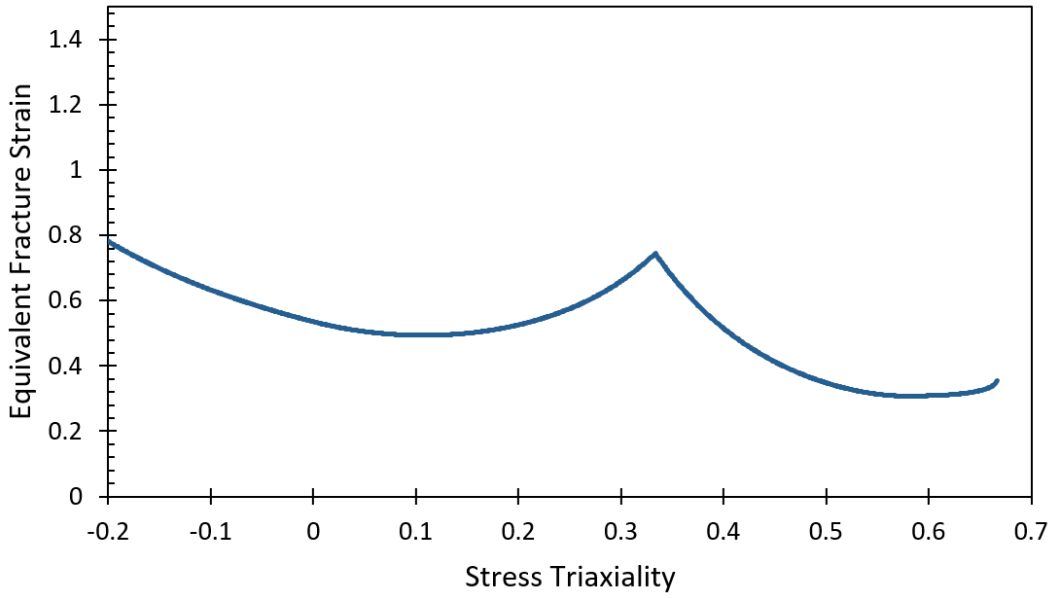

Figure 92: Fracture curve for fully martensitic Usibor® 1500-AS [48].

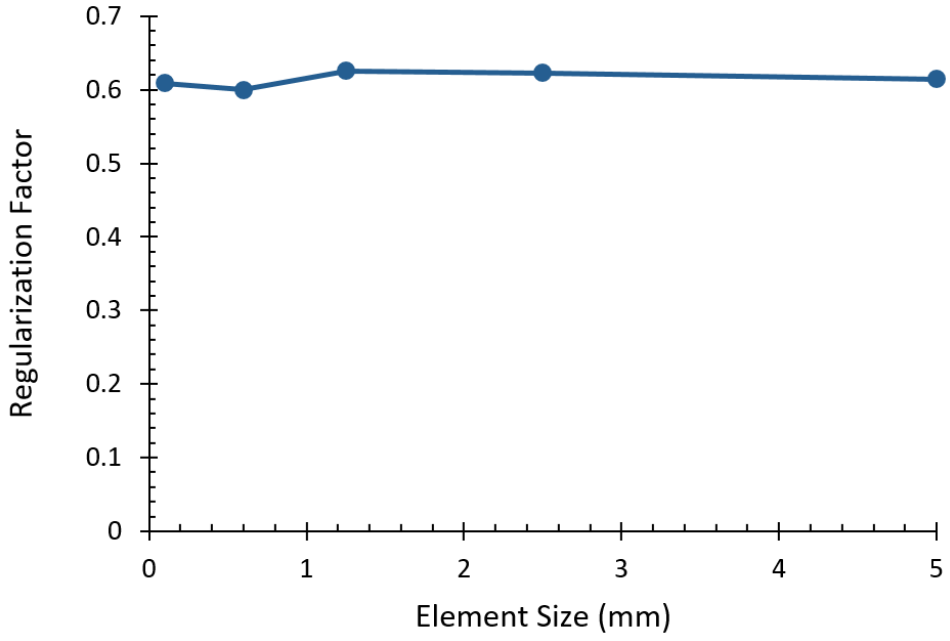

Figure 93: Regularization curve for fully martensitic Usibor® 1500-AS [21].

The curves for constitutive and fracture behaviour of Usibor® 1500-AS at a given hardness were generated using a "re-mapping" program that was developed by George [50]. This program uses

the eTCM model [21] and ten Kortenaar's fracture model [48] to generate a hardness dependent material model.

5.1.2 Ductibor® 500-AS

The constitutive and fracture behaviour of die quenched Ductibor® 500-AS was characterized by Abedini *et al.* [60]. This characterization was performed at a range of strain rates from 0.01/s to 1000/s using three different testing apparatus. A 100 kN MTS tensile frame was used to test at low strain rates, and a hydraulic machine was used to test at intermediate rates. High rate behaviour was tested using a tensile split Hopkinson bar. The flow curves used in these models are shown in Figure 94. Failure was modelled using GISSMO [47], with the fracture curve shown in Figure 95 and using a constant regularization factor of 0.646 (Figure 96) [60]. Element deletion is triggered occur once 70% of the integration points within an element fail. This is slightly higher than the value used for Usibor® 1500-AS because crack propagation will be slower in the softer material.

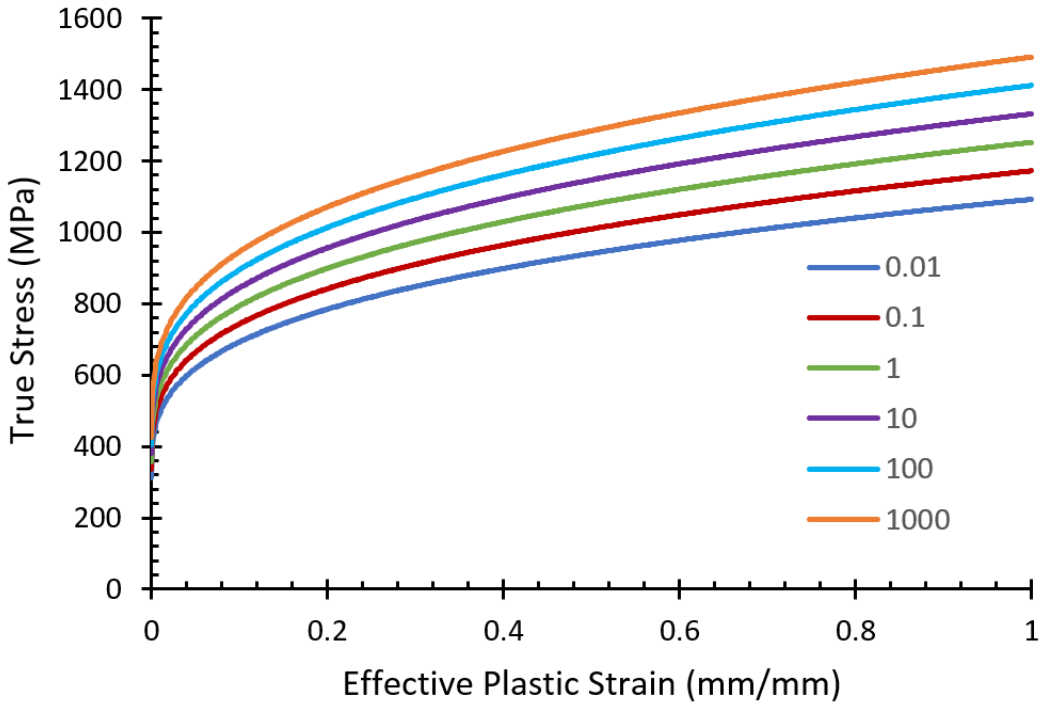

Figure 94: Constitutive curves for fully quenched Ductibor® 500-AS [60].

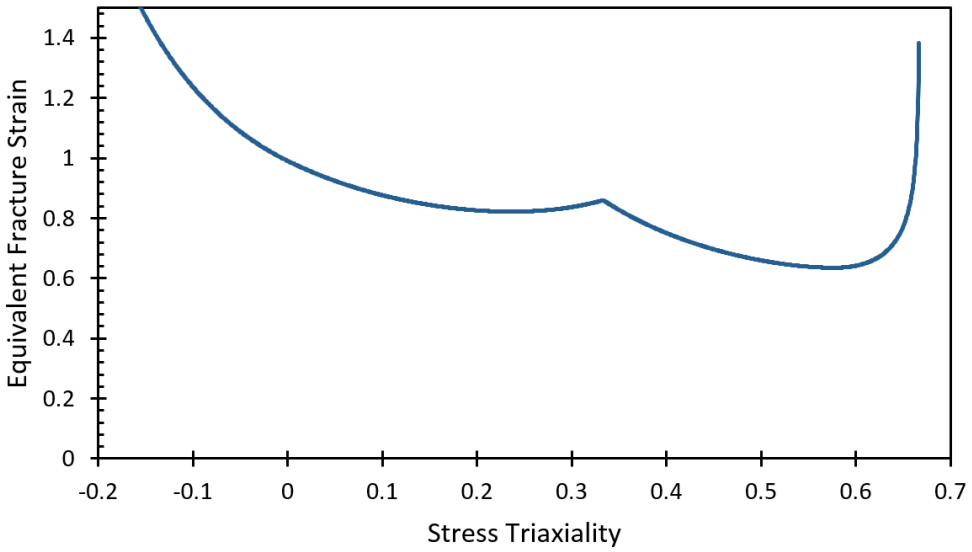

Figure 95: Fracture curve for fully quenched Ductibor® 500-AS [60].

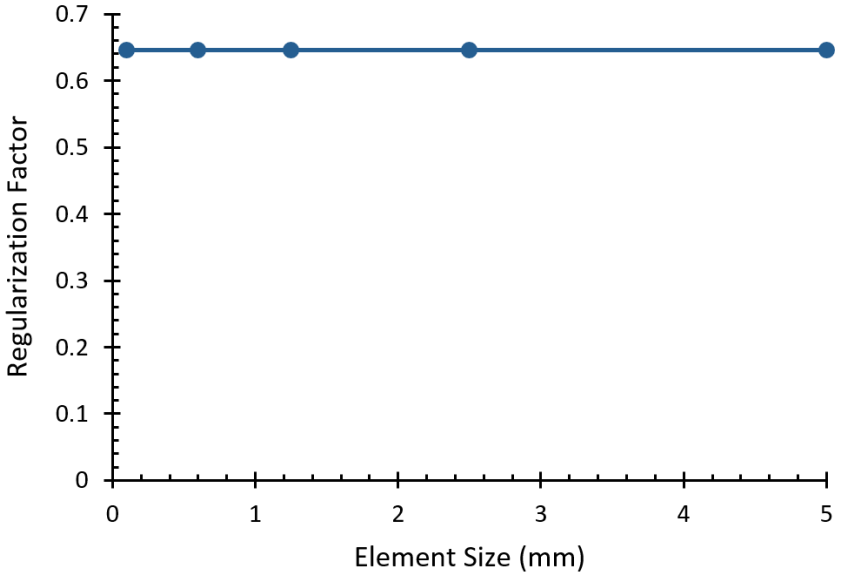

Figure 96: Regularization curve for fully quenched Ductibor® 500-AS [60].

5.1.3 JAC590R

Proprietary rate sensitive constitutive characterization of JAC590R was provided by Malcolm [54] for use in numerical models for this project. Due to the confidential nature of these flow curves, they cannot be published in this thesis. Nonetheless, Prajogo [19] published a quasi-static flow curve for JAC590R which is shown as the dashed black curve in Figure 97. In addition, constitutive curves published by the Steel Market Development Institute (SMDI) [61] for an unspecified

DP600 dual phase steel at different strain rates are plotted alongside the JAC590R in Figure 97 to show the approximate strain rate sensitivity. The dual phase DP600 steel has a lower yield strength and higher hardening rate than the ferritic/bainitic JAC590R, but their strain rate sensitivities are similar. Failure was not considered for the JAC590R material.

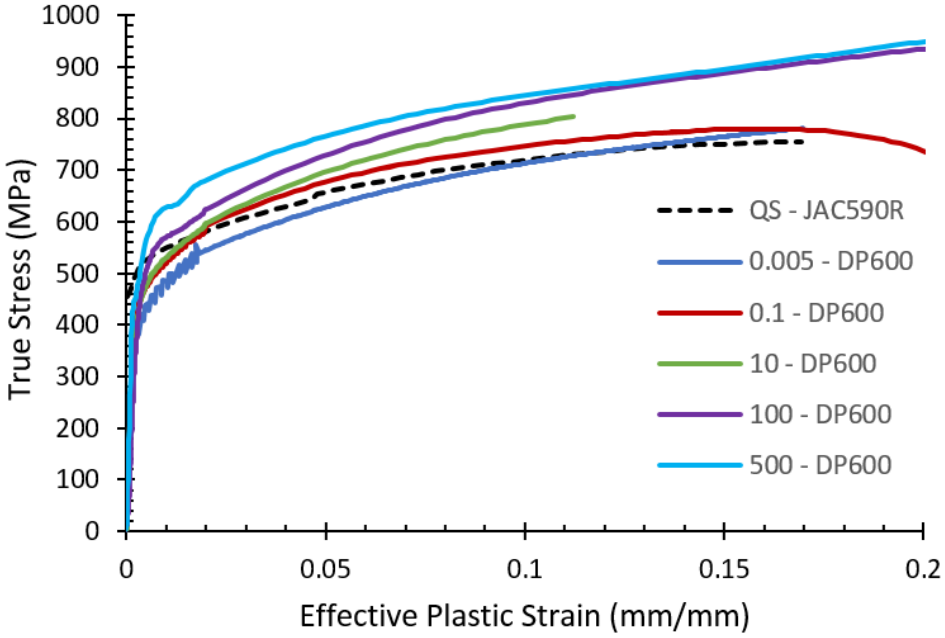

Figure 97: Quasi-static constitutive curve for JAC590R published by Prajogo [19] (black curve), and rate sensitive constitutive data for an unspecified DP600 steel published by SMDI [61]. The strain rates (1/s) are indicated for the DP600 data.

5.2 Three Point Bend Model

The LS-DYNA R8.1 commercial finite element package was used to create the three-point bend models, and meshing was performed in HyperMesh 13.0. The mesh of the top hat channel (Figure 98) uses 2.5 mm fully integrated quadrilateral shell elements (LS-Dyna Type 16 [62]) with seven through-thickness integration points. This element formulation was used for all of the parts in this model. With these channels being the full 590 mm in length, 18,800 elements were used in their mesh. The backing plate was similarly meshed with 11,800 shell elements of the same type and 2.5 mm size. The two cylindrical supports were meshed as hollow cylinders of 1,600 rigid shell elements each. These elements had side lengths of 4 mm in the circumferential direction and 8.9 mm in the longitudinal direction. Lastly, the impact tup was similarly modelled as a hollow half cylinder of 1,025 shell elements with side lengths of 5.1 mm and 7.1 mm in the circumferential and longitudinal directions respectively. Penalty-based contact was defined between the side

impact member and the rigid supports, as well as for self-contact within the hat channel and backing plate during folding.

The hot stamped materials used in this work (Ductibor® 500-AS and Usibor® 1500-AS) are coated with a 25 micron thick AlSi coating on both sides of the sheet. This coating is incorporated into the total thickness of the sheet, but does not contribute any strength or stiffness. Therefore in the models, the 50 micron total coating thickness is subtracted from the sheet thickness. Thus, the 1.2 mm and 1.6 mm sheets are modelled as being 1.15 mm and 1.55 mm thick, respectively, in order to predict the correct structural response.

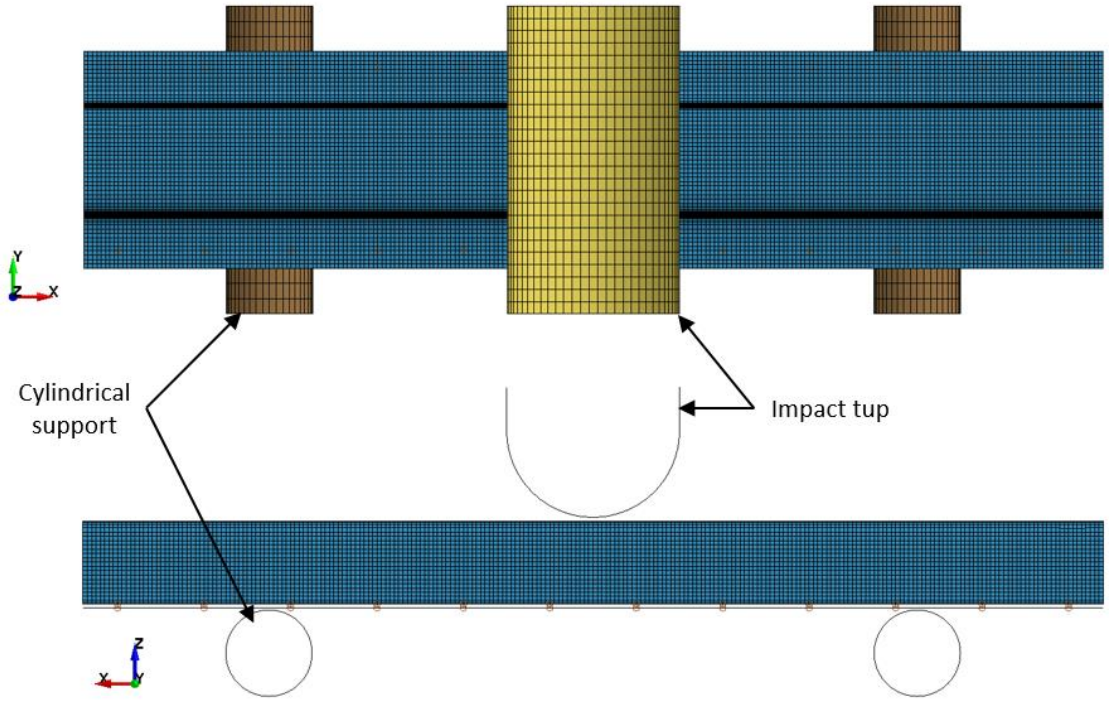

Figure 98: Mesh for three point bend test model.

5.2.1 Modelling Spot Welds

Spot welds were modelled using the MAT_100 material card and spot weld beam elements as shown in Figure 99. This material card was written specifically for spot welds, and can be used for both beam and solid elements [62]. Contact between these beam elements and the two shell surfaces of the channels was defined using the tied contact algorithm. These spot weld elements were created along the flanges, 4 nodes (10 mm) from the edge, at an interval of every 20 nodes (50 mm) along the length. These side impact beams were made of Ductibor® 500-AS and

JAC590R, both with relatively low strengths of around 550-600 MPa. Previous work by O'Keeffe [40] showed that lower strength parent metals have better spot weld performance than higher strength materials like martensitic Usibor® 1500-AS because the strength of the heat-affected zone around the spot weld is close to the softer parent metal. Based on this knowledge and the lack of failure observed in experiments, no spot weld failure model was used.

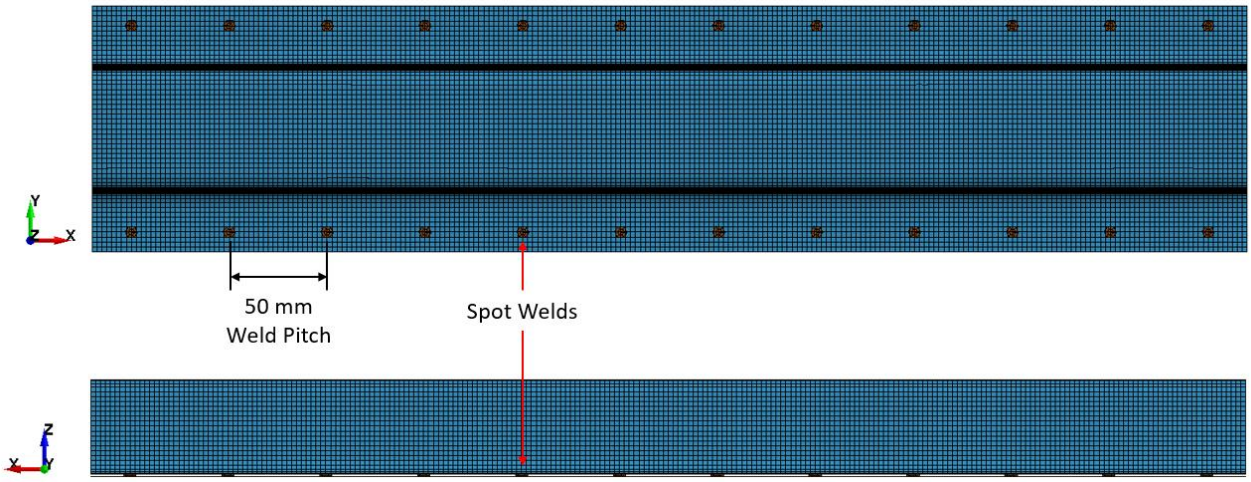

Figure 99: Spot weld locations on side impact members.

5.2.2 Boundary Conditions – Dynamic

In the dynamic three point bend model shown in Figure 100, boundary conditions were applied to simulate the test conditions. The two cylindrical supports were constrained in all six degrees of freedom to represent the fixed supports that are mounted to the barrier wall. These are mounted on heavy weldments to the wall, so a rigid assumption is adequate. The side impact beam specimen is initially placed with the backing plate resting on the surface of the supports. Since the shell elements are positioned at the mid plane of the sheet, there is an apparent gap between them and the supports/loading tup when looking at the edge of the mesh. (This gap is not real and is accounted for using a thickness offset in the contact treatment, described below.) The impacting tup is given an initial velocity of 6.5 m/s and a mass of 865 kg to reflect the inertia of the crash sled colliding with the specimen. This impactor was constrained so that it could only move in the Z-direction to represent the sled constrained on rails. Gravity is not modelled, so the specimen does not move prior to contact from the impactor. Penalty-based contact was assigned between the hat channel, backing plate, rigid impactor, and rigid supports, and for self-contact of the channel section during folding.

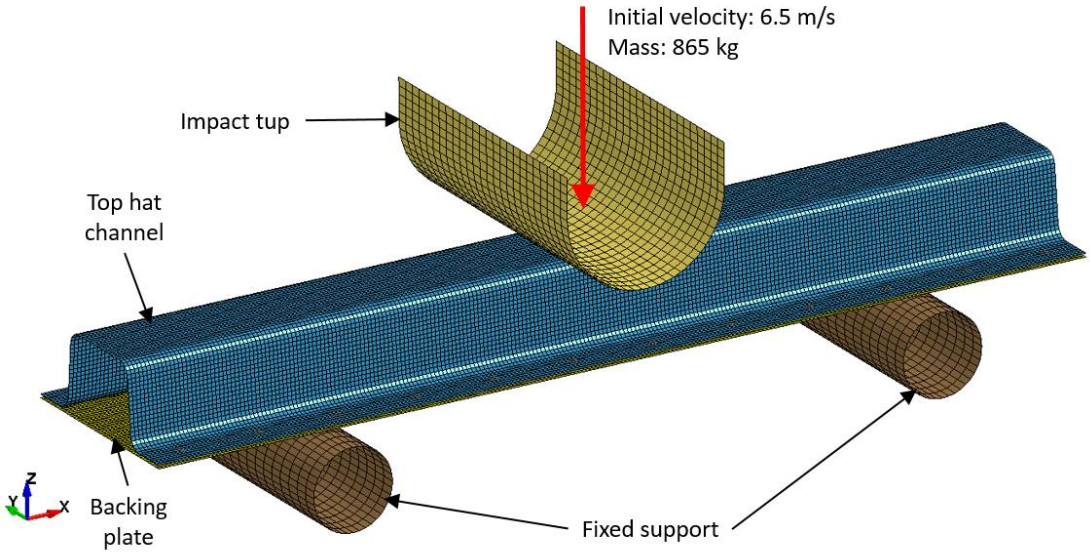

Figure 100: Boundary conditions for the dynamic three point bend model.

5.2.3 Boundary Conditions – Quasi-Static

The boundary conditions for the quasi-static three point bend models were very similar to the dynamic ones. The main difference was with the impactor being given a prescribed constant velocity of 0.5 mm/s, instead of an initial velocity. Additionally, time scaling was used to reduce the computational time needed to solve the model. The prescribed velocity of the impacting plate was multiplied by a factor of 1000 from 0.5 mm/s to 500 mm/s. This causes the material in the model to deform 1000 times faster than in the experiment, which would cause the model to over-predict the stiffness of the material due to strain rate sensitivity. To account for this, the reference strain rate for each load curve in the material card was also scaled up by a factor of 1000. In this way, if the model measures strain rates of 100/s and 10/s, it will use the properties taken from experiments at 0.1/s and 0.01/s, respectively, for example. To ensure that dynamic effects from this time scaling did not affect the solution, the kinetic energy was checked to ensure it was much smaller than the internal energy.

5.3 Axial Crush Model

As with the three point bend models, LS-DYNA R8.1 was used to create the numerical crush models, with meshing performed in HyperMesh 13.0. The top hat channels were modelled using four-noded fully integrated quadrilateral shell elements with seven through-thickness integration points. These shell elements were 2.5 mm x 2.5 mm in size, requiring 16,000 elements to model

each of the two top hat channels that make up the rail. Tetrahedral, selectively reduced integrated solid elements, 9.5 mm in size, were used by Omer [20] to model the mounting boss on the impacted end of the rail, which was carried over into the current models. With this boss being significantly stiffer than the rails being crushed, it was assigned rigid material properties to simplify the solution.

5.3.1 Fold Initiator

As was described in Section 3.7, fold initiators were formed into the top of each channel, 65 mm from the impacted end of the rail. The most accurate way to model this is to simulate the forming of the initiator to account for local work hardening and strains in the material. To greatly simplify the model, the fold initiators were introduced by simply displacing the nodes in the indented region, as shown in Figure 101. Two rows of 13 nodes were moved inward by 4 mm, with the center of the indent at 65 mm from the impacted end of the specimen. This indent provides a sufficient discontinuity to initiate formation of folding in the crush rail.

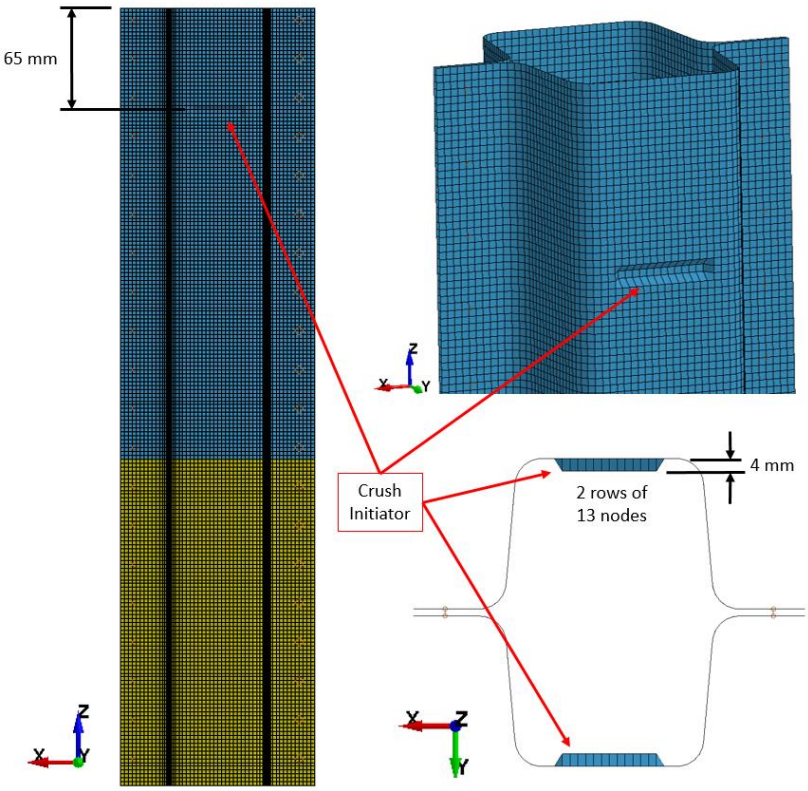

Figure 101: Crush initiators formed into impacted end of rails.

5.3.2 Modelling Spot Welds

Spot welds were modelled using the MAT_100 material card and spot weld beam elements as shown in Figure 102, in the same manner used for the three point bend model described in Section 5.2.1. These spot weld elements were created along the flanges, 4 nodes (10 mm) from the edge, at an interval of every 10 nodes (25 mm) along the length.

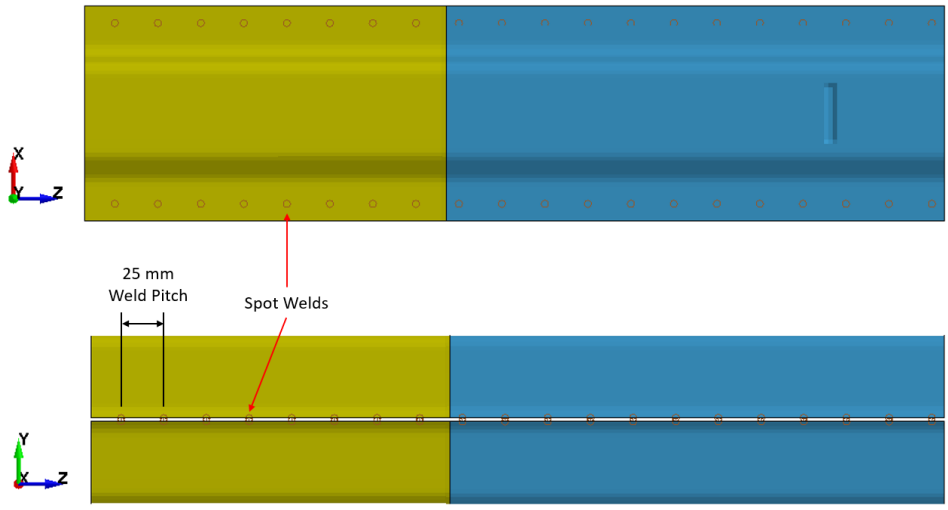

Figure 102: Spot weld elements on crush rail model.

In these axial crush experiments, very little weld failure was observed in the ductile Ductibor® 500-AS crush zone, so weld failure was not included for this section. Some weld failure occurred in the more rigid Usibor® 1500-AS zone due to heat affected zone softening in high strength materials, so spot weld failure was added to the model. The failure parameters used were calibrated through research into spot weld failure performed by O'Keeffe *et al.* [39, 40], which was discussed in Section 1.3.3. They created numerical models of weld coupon experiments and calibrated the MAT_100 material card to match the experimental results of the same tests. The results of this work for 1.2 mm thick fully quenched Usibor® 1500-AS are shown in Figure 103. It was found that if a spot weld was deleted once reaching its failure parameter, the load it was supporting would be passed to the next weld, which would in turn fail, causing rapid failure propagation through an unzipping behaviour. To prevent this, the fade energy parameter in the spot weld material card was used to simulate the load sharing and pull out that occurs as a weld fails. This approach prevents this rapid unzipping by promoting a smoother load transfer between welds after the onset of weld

failure until a defined amount of energy has been absorbed. Fade energies between 230 mJ and 500 mJ were studied [40].

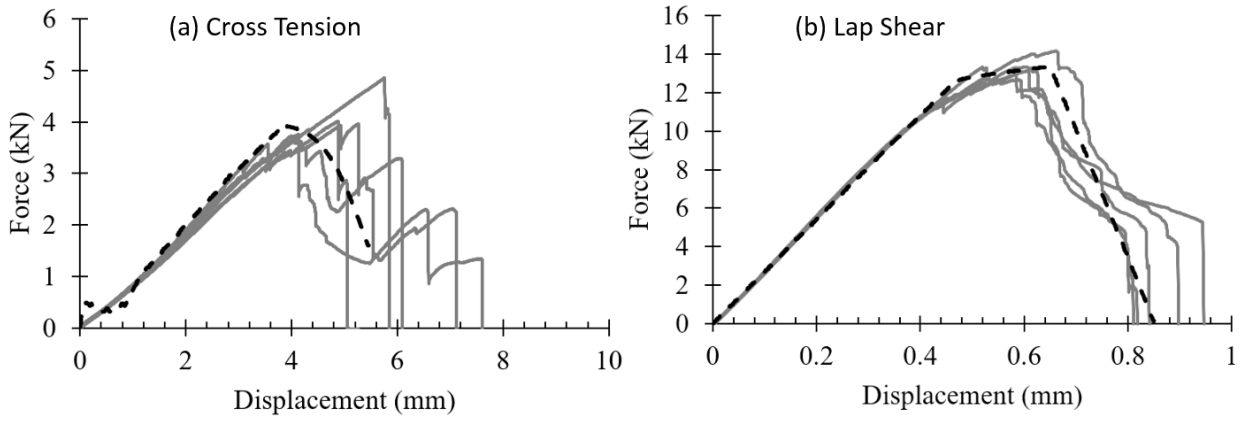

Figure 103: Numerical (dotted) and experimental (solid) results from (a) cross tension and (b) lap shear testing of Usibor® 1500-AS (due to O'Keeffe [39]).

5.3.3 Modelling the Laser Weld Line

To determine the properties of the laser weld line in the TWB components, a small flat sheet sample of the weld line area of a common gauge 1.2 mm TWB was quenched on the room temperature binder of the IDH rail forming die. After quenching, a strip of this sheet was sectioned, mounted in resin, and polished in the same manner as is described in Section 3.5. Detailed hardness measurements were taken at 2 mm increments away from the weld line, and at 0.25 mm increments across the weld line. As was described in Section 3.6.2, the measured micro-hardnesses in Figure 68 showed that there is not a heat affected zone of reduced hardness in the Ductibor® 500-AS adjacent to the weld. From these results the simplification was made to assume that failure would not occur in the weld, therefore a failure model for the laser weld was not included in the rail crush model. The nodes at the boundary between the two material zones are made coincident, creating an immediate change in properties at the weld line. In multi-gauge parts, the mid-plane of the 1.2 mm and 1.6 mm parts are offset from each other by 0.2 mm. This is accounted for by having the last row of elements in the Usibor® 1500-AS section transition from the mid-plane of one part to the other, as shown in Figure 104. This approximates the thickening of the weld across its width, from the 1.2 mm thickness on one side to the 1.6 mm thickness on the other. With the 2.5 mm mesh, this transition is slightly wider than the 2 mm transition reflected in the hardness tests.

Failure of the laser weld was not observed in the experiments, so was not considered in the models. This approach is consistent with previous work on TWBs by Kang *et al.* [25] and Múnera *et al.* [6] who found that fracture would occur in the Ductibor® 500-AS base metal, not at the weld.

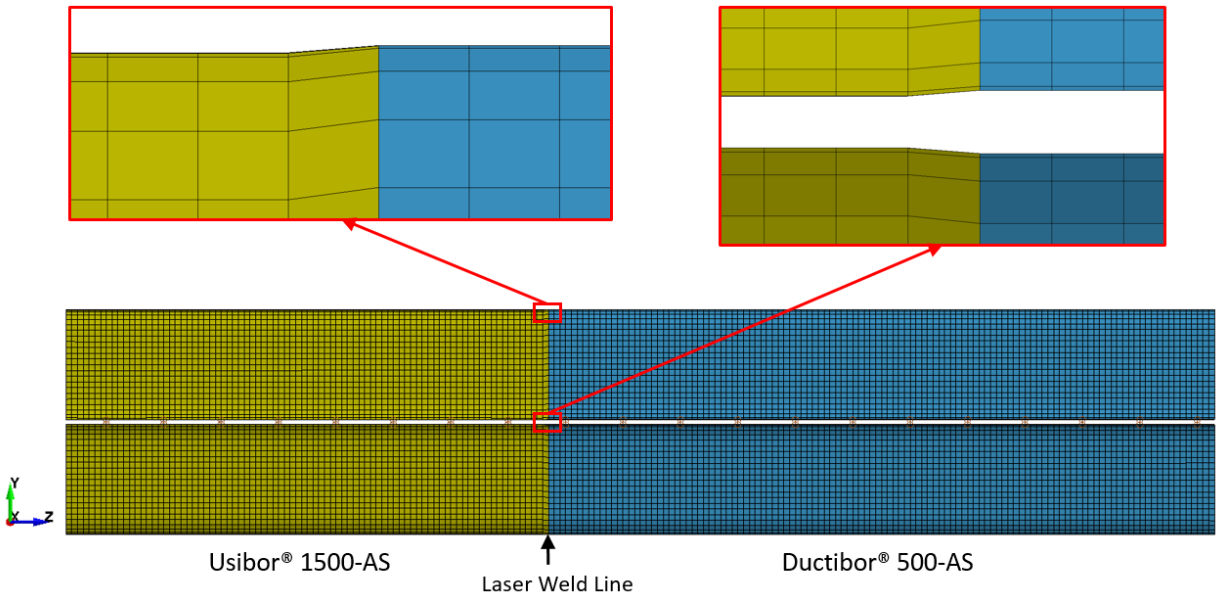

Figure 104: Weld line transition in multi-gauge TWBs.

5.3.4 Boundary Conditions – Dynamic

In the dynamic axial crush model shown in Figure 105, boundary conditions were applied to simulate the conditions of the axial crush experiments with the rail fixed to the stationary wall and being impacted by the moving crash sled. At the fixed end of the rail, 20 rows (50 mm) of elements were fully constrained in all rotational and translational degrees of freedom to simulate being clamped to the barrier wall. At the impacted end of the rail, the clamps modelled by Omer [20] as rigid solid elements were used to clamp the first 25 mm of the rail. Tied contact was defined between the rigid clamps and the shell elements at the end of the specimen. Penalty-based contact was assigned between the rail sections and the rigid bosses, and for self-contact of the rail sections to themselves during folding. The impacting crash sled was modelled as a sheet of rigid shell elements with the 855 kg mass and 10.6 m/s initial velocity of the crash sled. This impacting plate was constrained so that it could only move in the Z-direction, analogous to the crash sled moving forward along the rails.

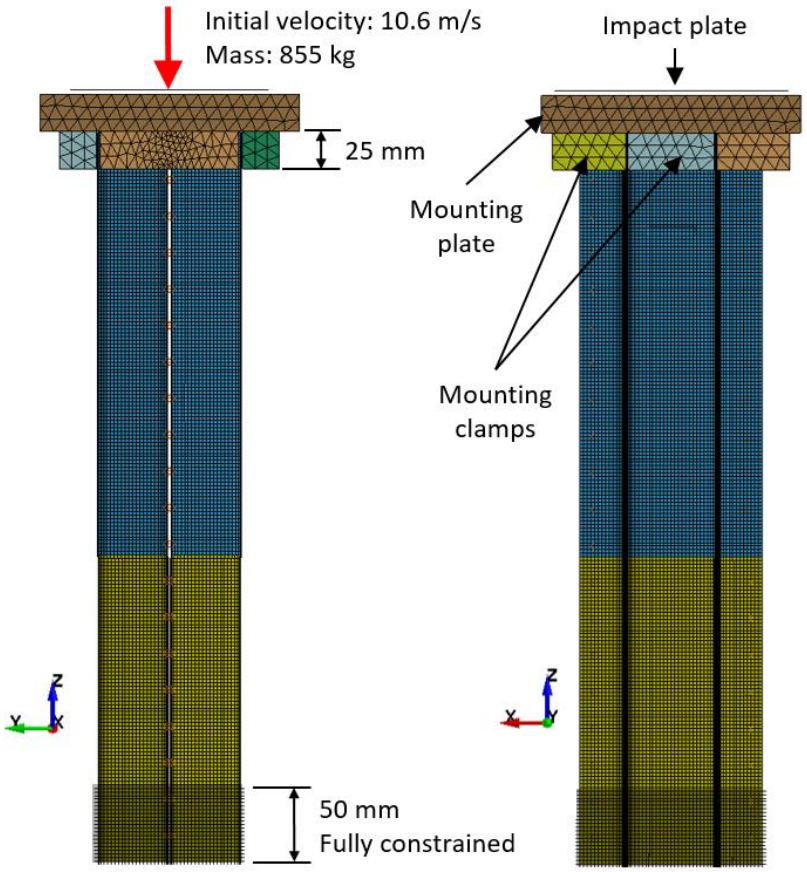

Figure 105: Dynamic axial crush model boundary conditions.

5.3.5 Boundary Conditions – Quasi-Static

The quasi-static axial crush model used similar time scaling to that adopted in the quasi-static three point bend model. The impactor was given a prescribed constant velocity of 0.5 mm/s, and then time scaled by a factor of 1000 to a velocity of 500 mm/s. The reference strain rate for each rate sensitive load curve in the material model was scaled up by the same 1000x factor to reflect this.

5.4 Numerical Model for Baseline Crush Tip Axial Crush

The project sponsor Honda provided an LS-DYNA numerical crush model of this mass production front rail [54]. It included the entire mesh of both front crush rails, spot welds, boundary conditions, and an impactor plate. The rail was meshed with four-noded fully integrated quadrilateral shell elements with five through thickness integration points, and an element size of about 5 mm. This model was modified to fully constrain three rows of nodes across the part cross section, with the first of the rows 340 mm from the impacted end. A rigid sheet of shell elements was added across each side of the rail at this 340 mm distance to represent the rail being cut off and welded to the

12.7 mm (½”) backing plate in the experiments. Penalty-based contact was assigned for contact between the rails and the impactor plates, and backing plates, as well as self-contact during folding.

Two independent impactor plates meshed with rigid shell elements were each given the initial velocity and mass of the crash sled in the experiments (7.5 m/s, 855 kg). This set up the model to simulate two independent crash experiments at once, one for each side of the rail. This was less complicated than modifying the model to isolate each part of the front rail in its own simulation. Each impactor decelerates independently, and the load versus displacement response is extracted separately for each side. The boundary conditions and mesh are shown in Figure 106.

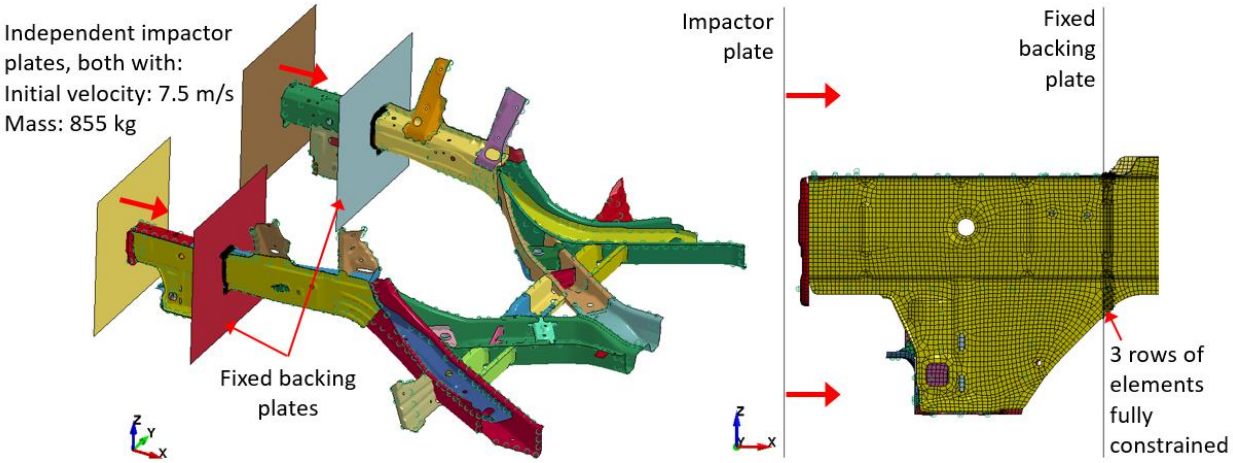

Figure 106: Numerical model setup and boundary conditions for baseline crush tips.

6.0 Three Point Bend Experimental and Numerical Results

6.1 Three Point Bend - Dynamic Experiments

6.1.1 Overview of Dynamic Three Point Bend Results

Dynamic three point bend tests were performed on side impact member specimens (sample preparation is described in Section 3.7.1) fabricated from 1.2 and 1.6 mm Ductibor® 500-AS monolithic hat sections with a JAC590R closure panel (Figure 70). For each of the two material conditions, at least five bend tests were performed. The averaged results of these tests are shown in Figure 108 and Figure 109. In the 1.2 mm material, two different modes were observed, so two curves are shown for that material. The curves are cut off at a displacement of 120 mm, at which point the sled impacts the honeycomb arrestor blocks and the data becomes very noisy.

The Duct 1.2 (1.2 mm monolithic Ductibor® 500-AS, see Table 7 for specimen designations) specimens reach an initial peak force of 14.3 kN after 10.3 mm of displacement. The load then drops to 10 kN before building back up to about 15 kN, which is sustained as the rail deforms until 40 mm of displacement. At the 40 mm point, two very distinct load paths and deformation modes were observed. Four specimens exhibited a folding mode (Figure 107), in which the 15 kN load was sustained until 50 mm, then decreasing to 6 kN as the rail folds. Two specimens exhibited a wrapping mode (Figure 107), in which the load increases to a peak of 24.6 kN at 68 mm, then steadily decreases to about 10 kN. The energy absorption of the two modes differed greatly, with the folding mode absorbing 1.05 kJ and the wrapping mode absorbing 1.81 kJ over the 120 mm crush distance. The peak load and energy absorption for the two material conditions are compared in Figure 110.

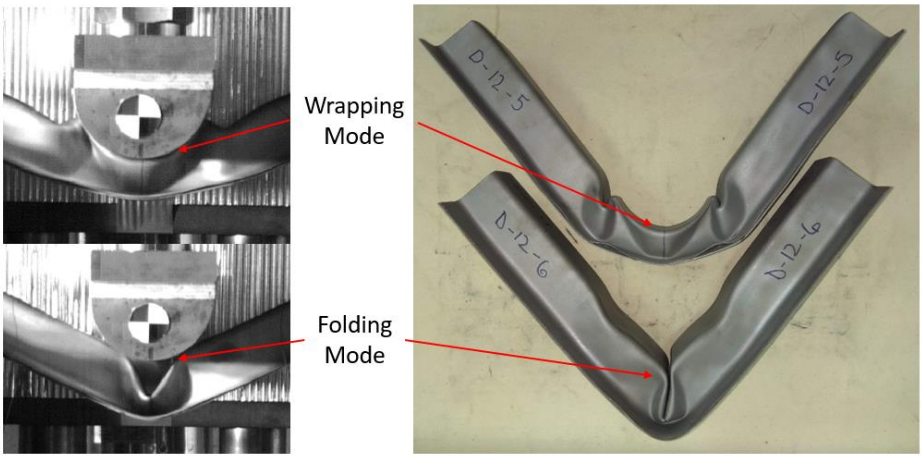

Figure 107: Comparison of folding and wrapping modes of deformation in 1.2 mm Ductibor® 500-AS side impact beams.

The Duct 1.6 specimens initially sustain the highest peak force of 27.6 kN after 9.8 mm of displacement. After this point the load drops to 15 kN then begins increasing again to about 21 kN, which is sustained as the rail folds until 50 mm of displacement. After this point the load drops below 10 kN as folding continues. These Duct 1.6 specimens absorb 1.77 kJ of energy over the 120 mm free crush distance. All of the Duct 1.6 specimens exhibited a folding mode of deformation.

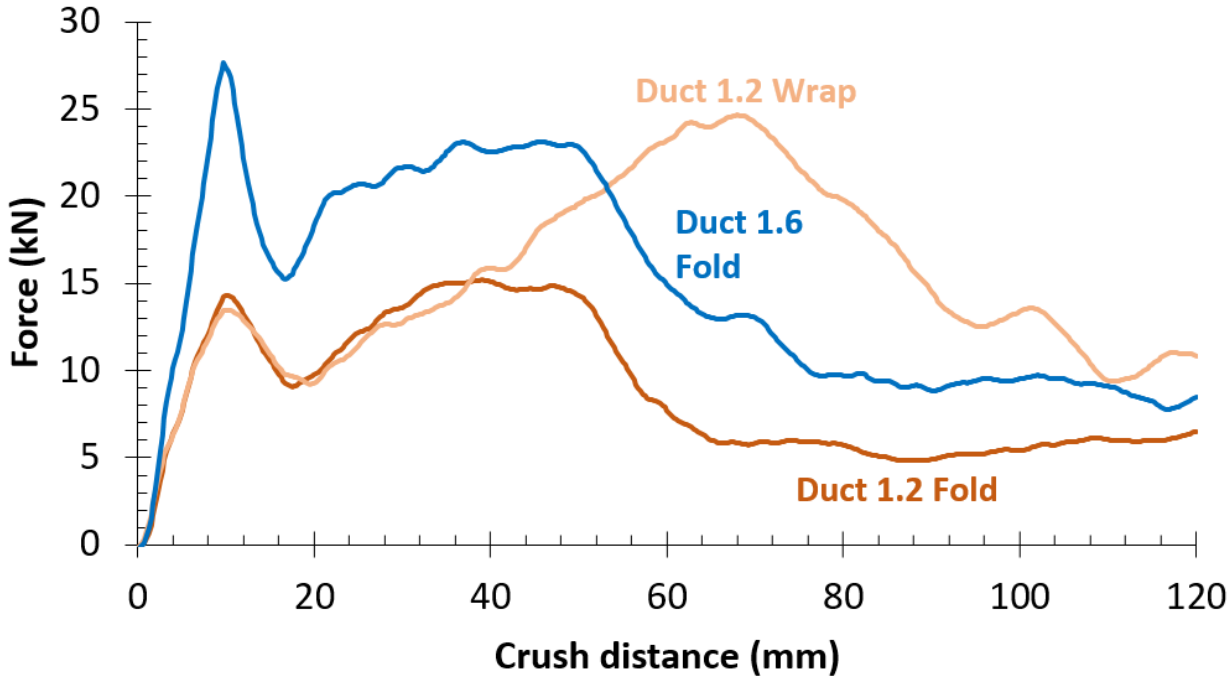

Figure 108: Force versus displacement for all dynamic three point bend conditions.

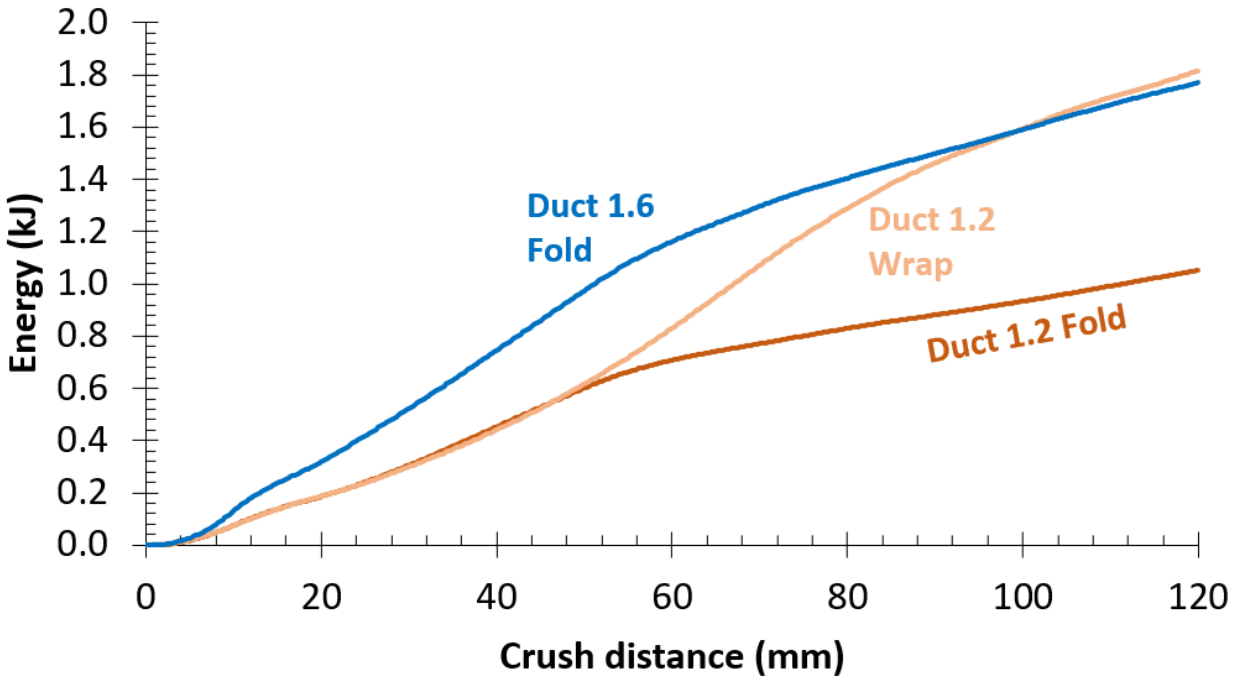

Figure 109: Energy versus displacement for all dynamic three point bend conditions.

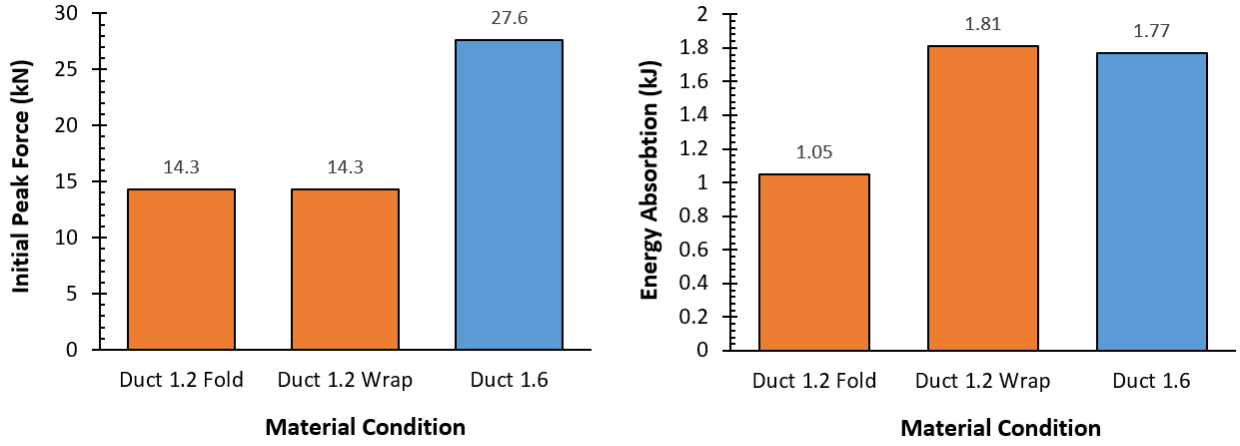

Figure 110: Summary of initial peak force and energy absorption in the first 120 mm of displacement for the three material and behaviour conditions of dynamic three point bend tests.

6.1.2 Dynamic Bend Response of 1.2 mm Ductibor® 500-AS Specimens

The still images in Figure 111 are taken from the overhead high speed video of the dynamic three point bend tests of two 1.2 mm monolithic Ductibor® 500-AS side impact beams. The upper four frames show that as the impactor hit the center of the specimen, it initially maintained contact with static friction causing the specimen to start to wrap around the outside of the impact tup. After a short amount of displacement, the static friction was overwhelmed and the part slid off of the

impactor, forming a tight fold. Figure 112 shows that this “folding mode” occurred in four of the six tests that were performed. In most of the folding mode tests, secondary indents were formed on the top of the channel on either side of the fold, as shown in Figure 113. These were caused by the beams beginning to wrap around the sides of the punch as it reached its maximum displacement between the supports.

The test shown in the lower four frames of Figure 111 exhibited a different “wrapping mode” of deformation. The test began the same as the previous, but the static friction was never overcome so the part never slid off of the surface of the impactor tup. As the impactor moved forward into the part it continued to wrap around the radius.

The load-displacement and energy absorption data is shown in Figure 114. As with the axial crush tests, the grey lines represent each experiment, and red lines represent the average of the experiments. The solid lines indicate folding mode specimens while the dashed lines indicate the wrapping mode. The plot shows that the two different deformation modes have very distinct load profiles. The folding mode specimens have their force reduce to a low level as the folding specimen loses its stiffness. The wrapping mode specimens build to a much higher peak force since the punch contributes to support the bending moment at the center of the beam. Each of the modes is quite repeatable with a relatively small amount of scatter between their multiple repeats. However, as an overall specimen type encompassing both modes, this specimen type is very unrepeatable because it can behave in one of two dramatically different ways.

The tight radius folds in these specimens did not exhibit any signs of fracture in the base material (Figure 112), which is another indicator of the high ductility of Ductibor® 500-AS. The spot welds are not under a great deal of stress in this configuration, so no spot weld failure was observed.

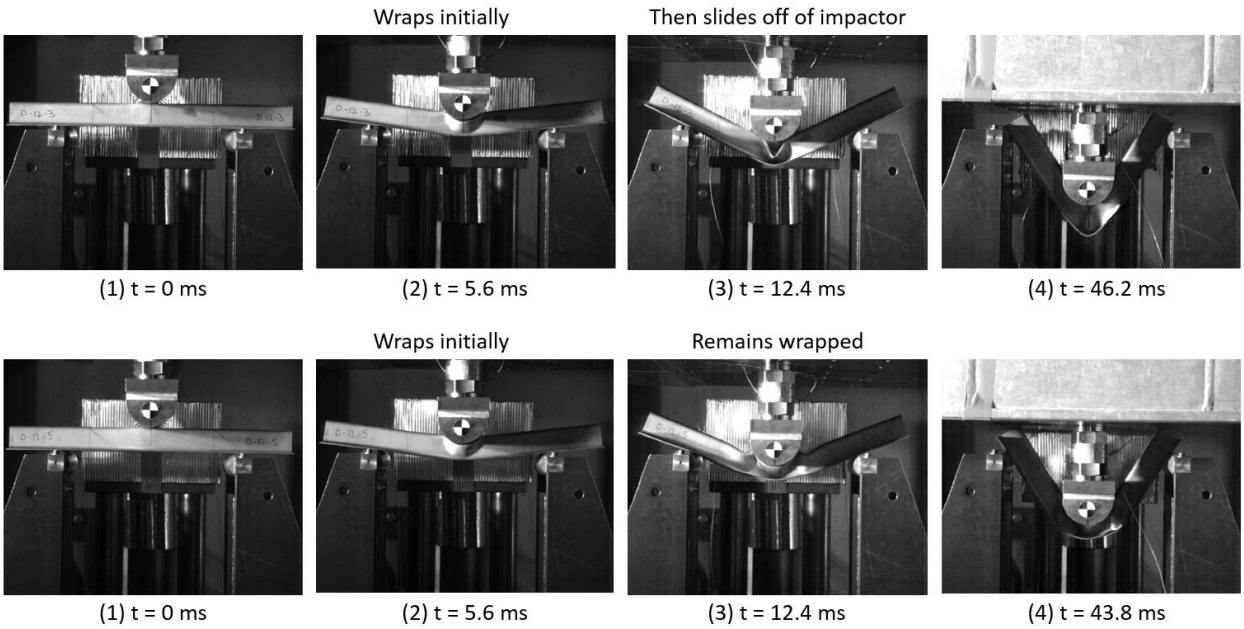

Figure 111: Dynamic three point bend deformation of two 1.2 mm Ductibor® 500-AS specimens. Upper specimen exhibits folding mode, lower specimen exhibits wrapping mode.

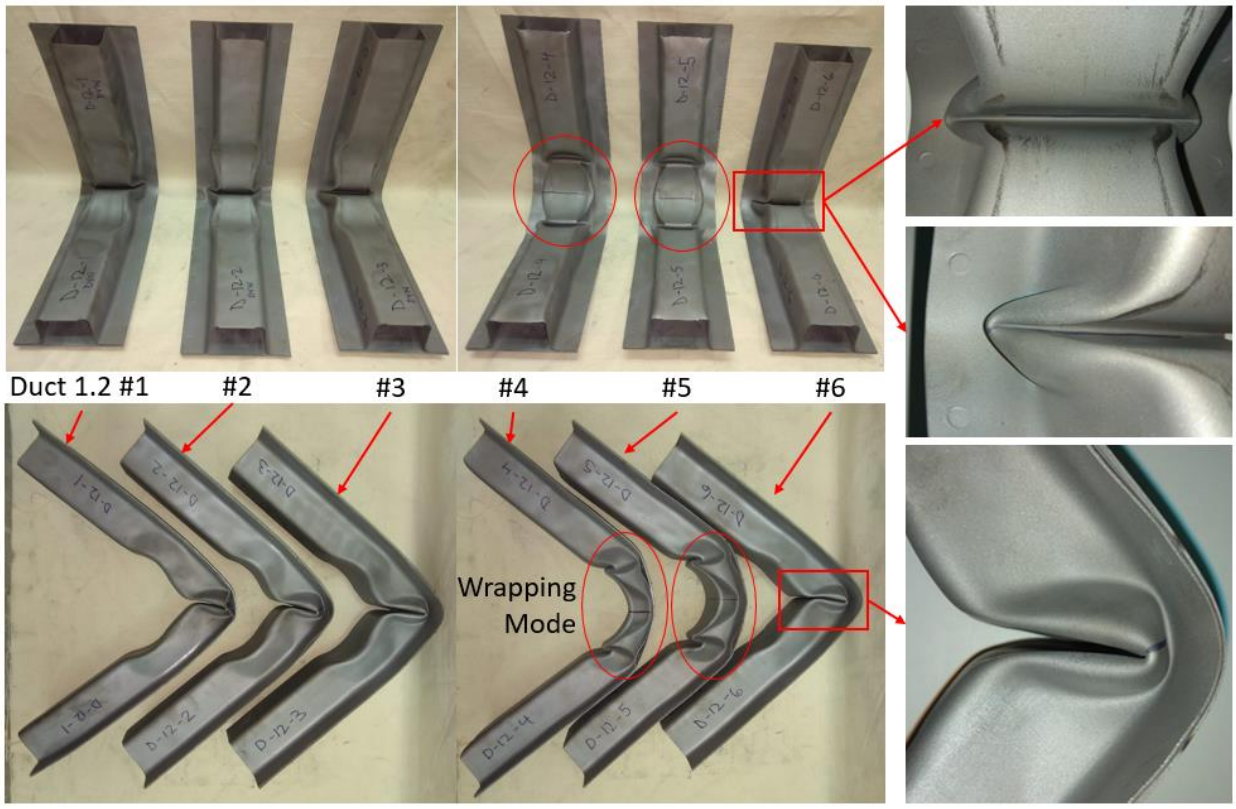

Figure 112: Final shape of six 1.2 mm Ductibor® 500-AS specimens after dynamic three point bending.

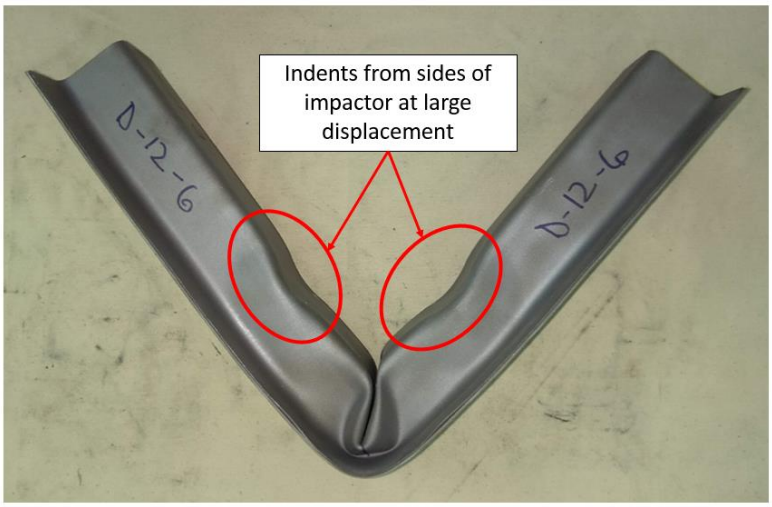

Figure 113: Secondary indents on top of 1.2 mm channel caused by wrapping into the sides of the impactor.

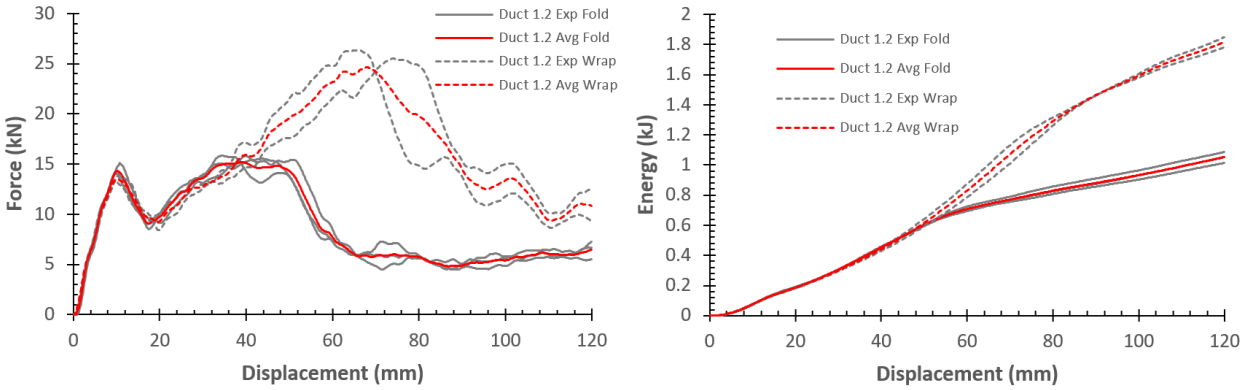

Figure 114: Dynamic force-displacement and energy absorption data for 1.2 mm Ductibor® 500-AS specimens.

6.1.3 Dynamic Bend Response of 1.6 mm Ductibor® 500-AS Specimens

Figure 115 shows still images of a dynamic three point bend test on a 1.6 mm monolithic Ductibor® 500-AS side impact beam. The specimen initially stuck and started to wrap around the impactor, but after a short time it slid off and deformed through the folding mode seen before. To prevent the wrapping seen in the 1.2mm specimens and investigate the effect of friction, Teflon film was wrapped around the impactor and both of the supports to reduce friction and promote the folding mode in three of the five tests. The remaining two tests were performed without Teflon, with identical boundary conditions to the 1.2 mm tests. Figure 116 shows that the specimens deformed through the folding mode in all five of the tests that were performed. All of these

specimens also showed secondary indents on the tops of the channels like were seen in Figure 113 in the 1.2 mm specimens.

Figure 117 shows the load-displacement and energy absorption data from these tests. The tests without Teflon maintained a higher force for longer because of the increased friction. With the friction on the supports, the entire beam could be put in tension, which helped to resist the impactor. The tests with Teflon had lower force and energy absorption levels after the first 30 mm of displacement. The results were very repeatable for each of the surface friction conditions. The specimens tested with Teflon film absorbed 1.42 kJ in 120 mm of crush, while those tested without Teflon absorbed 1.77 kJ in the same crush distance.

Figure 116 shows that there was no fracture in the tight radius folds formed in the part. There was also no failure of spot welds.

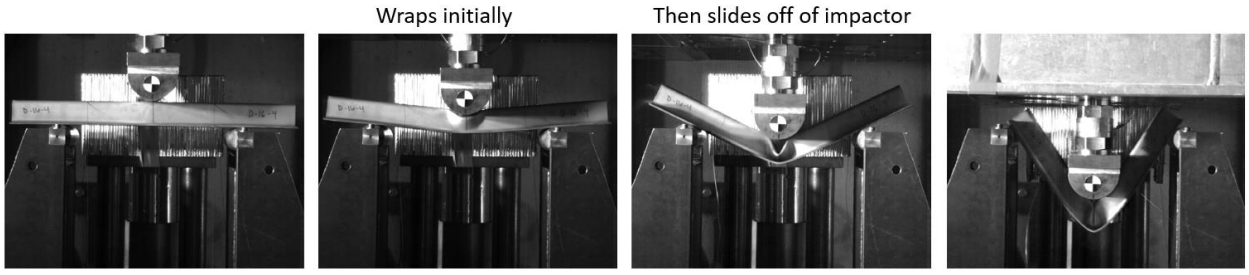

Figure 115: Dynamic three point bend deformation of a 1.6 mm Ductibor® 500-AS specimen.

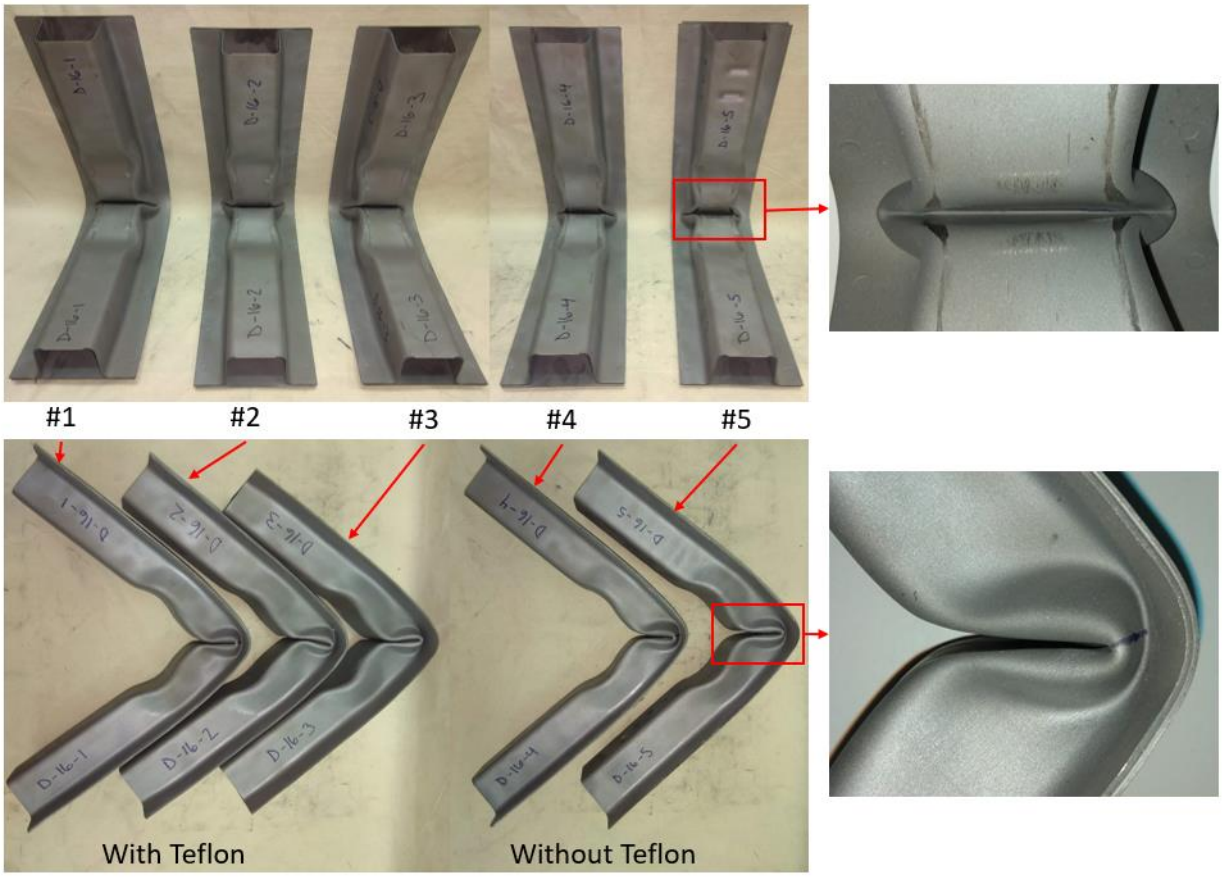

Figure 116: Final shape of five 1.6 mm Ductibor® 500-AS specimens after dynamic three point bending.

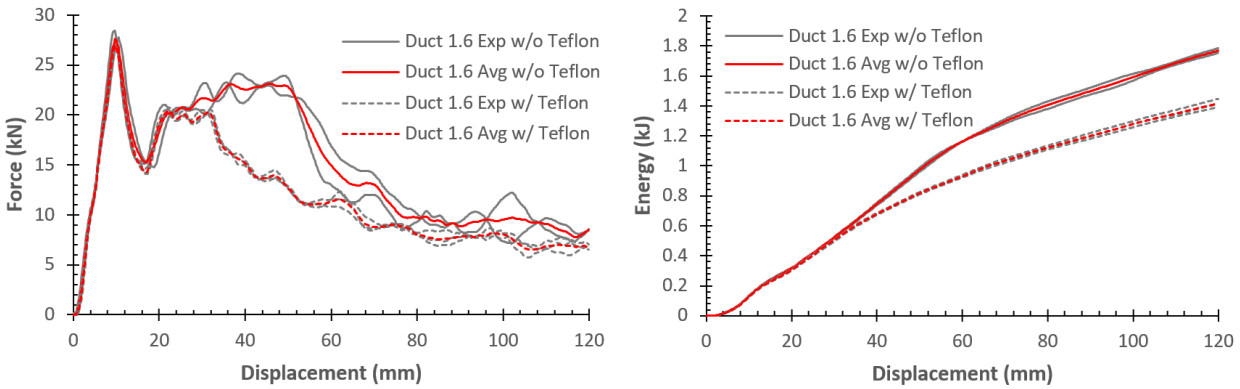

Figure 117: Dynamic force-displacement and energy absorption data for 1.6 mm Ductibor® 500-AS specimens.

6.2 Three Point Bend - Quasi-Static Experiments

6.2.1 Overview of Quasi-Static Three Point Bend Results

Quasi-static three point bend tests were performed on side impact member specimens from the same two material conditions as were used for dynamic testing. For each of the two material conditions, four repeat bend tests were performed. For the Duct 1.2 material, the first two tests were mistakenly performed at 1.016 mm/s, then the remaining two tests were performed at 0.508 mm/s. For the Duct 1.6 material, all tests were performed at 0.508 mm/s.

This data was rather noisy, with the load level oscillating by about 0.3 kN between each data point. The *smooth* function in MATLAB was used to reduce the noise level. This function uses a moving average filter, with the span of points being averaged configurable by the user [63]. For this data, a span of 13 points was found to give a good result. The force versus displacement and energy absorption results were derived from this filtered data. The averaged results from these tests are shown in Figure 118 and Figure 119. The curves are cutoff at the total displacement of 115 mm.

The Duct 1.2 specimens reach an initial peak of 9.8 kN after a displacement of 10 mm. The load decreases slightly before increasing again to an eventual peak at 29 mm of displacement of 11.1 kN for tests at 1.0 mm/s, and 10.8 kN for tests at 0.51 mm/s. The energy absorptions after the full displacement are 0.87 kJ and 0.86 kJ respectively for the 1.016 mm/s and 0.508 mm/s rates. It is clear that the difference in results between these two deformation rates is extremely small. The initial peak force and total energy absorption of the two material conditions are compared in Figure 120.

The Duct 1.6 specimens reach an initial peak force of 16.7 kN after a displacement of 9.75 mm. After a slight load drop, the load reaches a peak of 17.5 kN after 27.5 mm of displacement. The total energy absorption is 1.53 kJ.

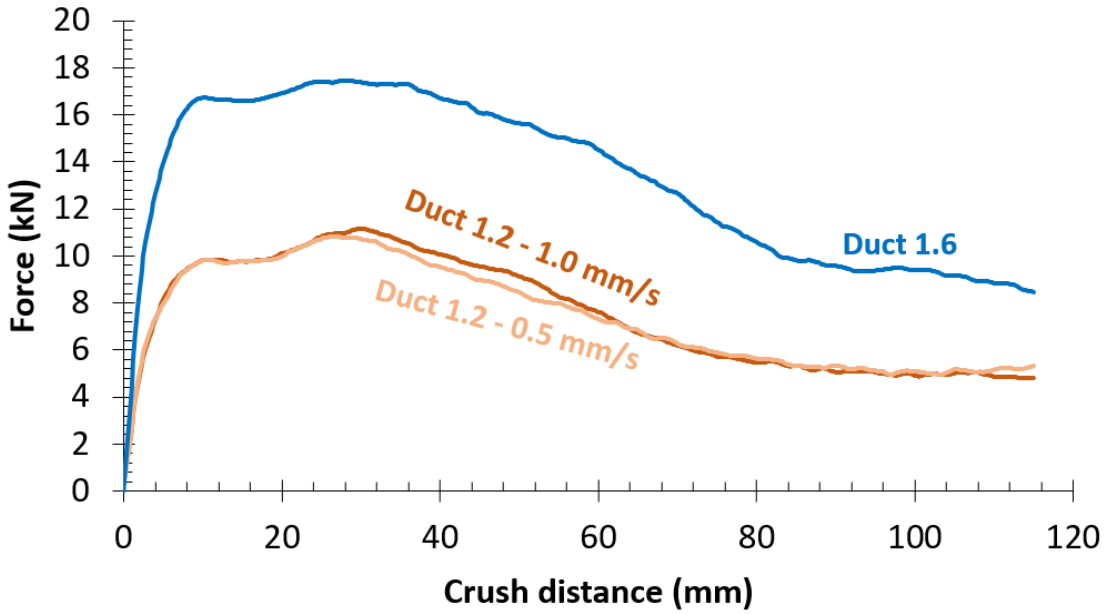

Figure 118: Force versus displacement for all quasi-static three point bend conditions.

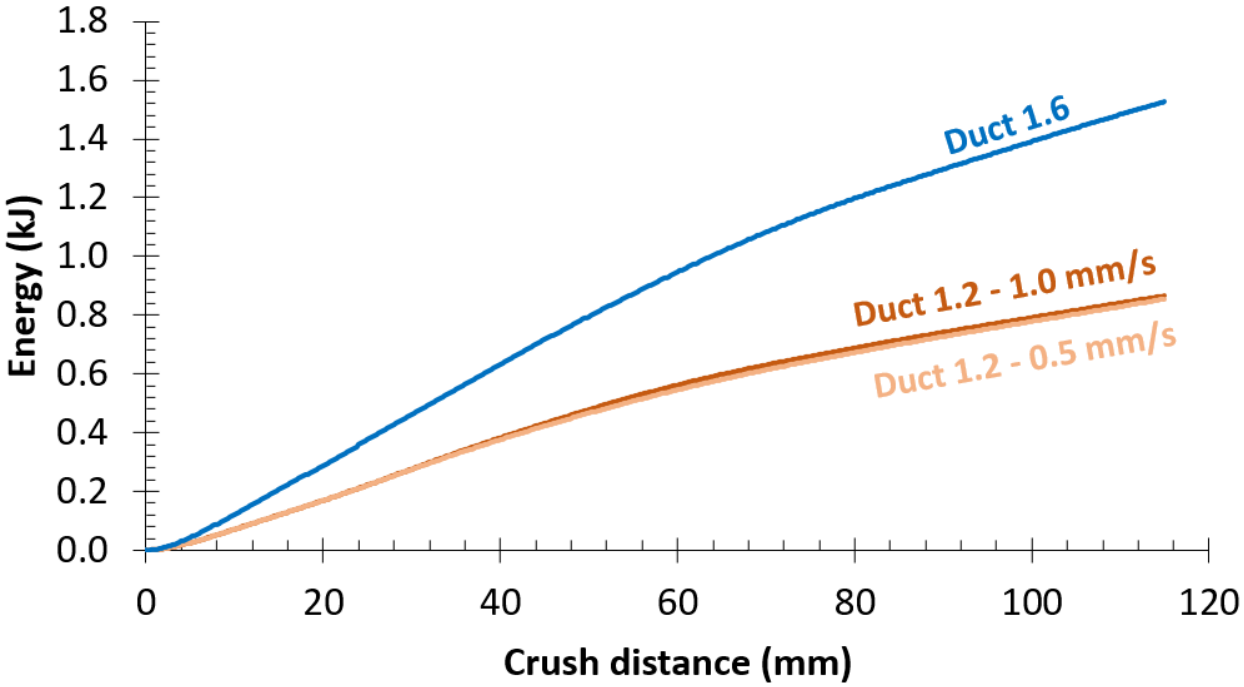

Figure 119: Energy absorption for all quasi-static three point bend conditions.

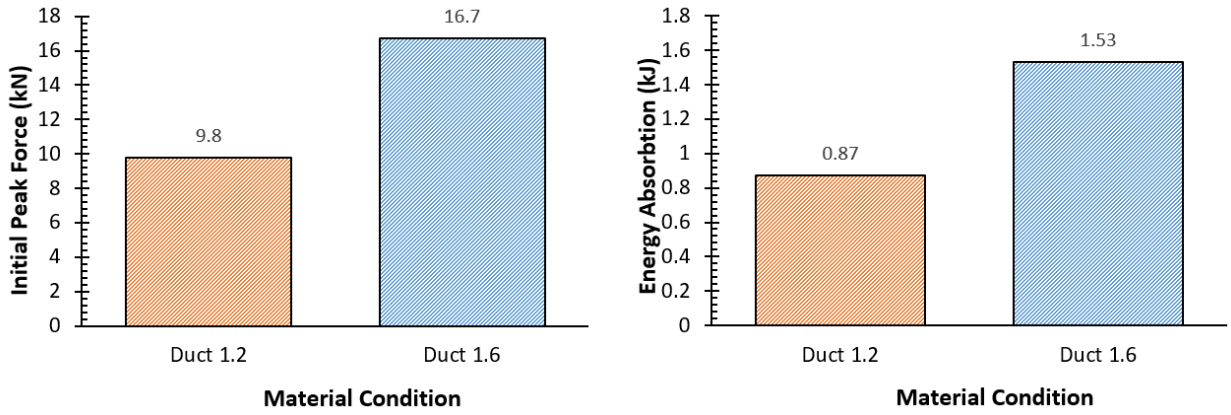

Figure 120: Summary of initial peak force and energy absorption in the full 115 mm displacement for the two material conditions of quasi-static three point bends.

6.2.2 Quasi-Static Bend Response of 1.2 mm Ductibor® 500-AS Specimens

Figure 121 shows four still images taken from the front camera used to record the quasi-static three point bend test of a 1.2 mm monolithic Ductibor® 500-AS side impact beam. As was observed dynamically, the impactor initially sticks to the specimen before sliding off and forming a tight fold in the beam. Figure 122 shows that all four repeat tests folded in a very similar manner. The wrapping mode that was observed in some of the dynamic tests did not occur in these quasi-static tests.

The load-displacement and energy absorption results are shown in Figure 123. As with the previous test data that was presented, the grey lines represent each experiment, and the red lines are the average of these experiments. The solid lines indicate tests that were performed at 1.016 mm/s, while the dashed lines indicate the 0.508 mm/s tests. It is clear that the difference in deformation rate is not significant enough to cause a large difference in performance. The small difference observed could be the result of strain rate effects, but it is nearly within the scatter of the experiments. The results were very repeatable with this scatter being very small.

As was the case in the dynamic tests, no fracture occurred in the Ductibor® 500-AS base material due to its high ductility. There was also no failure in the spot welds.

Figure 121: Quasi-static three point bend deformation of a 1.2 mm Ductibor® 500-AS specimen.

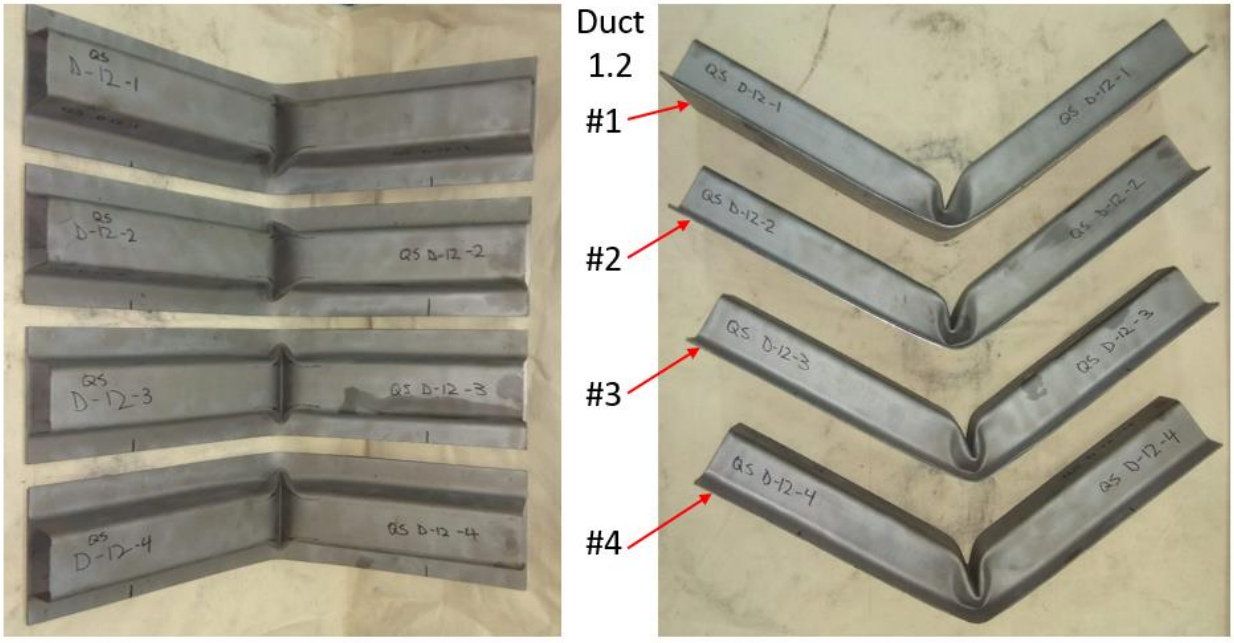

Figure 122: Final shape of four 1.2 mm Ductibor® 500-AS specimens after quasi-static three point bending.

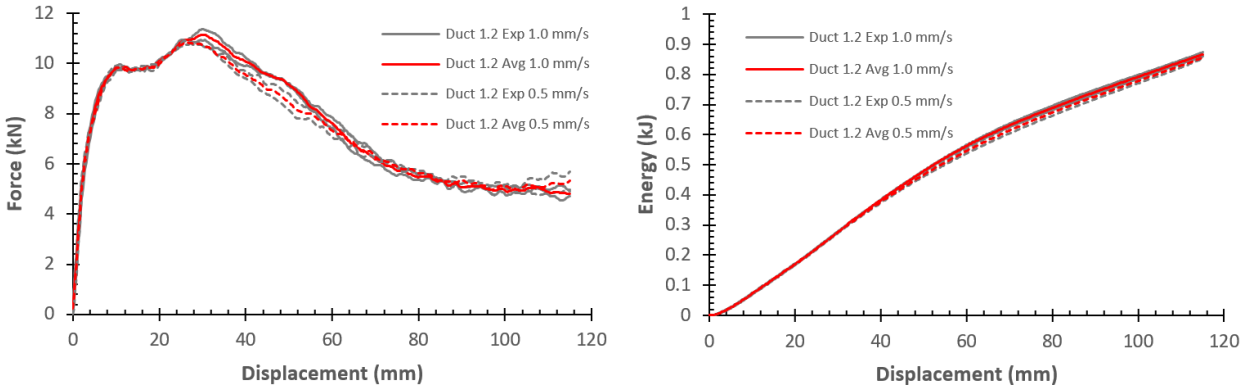

Figure 123: Quasi-static force-displacement and energy absorption data for 1.2 mm Ductibor® 500-AS three point bend specimens at two displacement rates.

6.2.3 Quasi-Static Bend Response of 1.6 mm Ductibor® 500-AS Specimens

The still images in Figure 124 are taken from the front camera recording the quasi-static crush test of a 1.6 mm monolithic Ductibor® 500-AS side impact beam. These performed similarly to the 1.2 mm specimens with a folding mode occurring in each of the tests. The folding mode was very similar for each of the tests, as shown by the deformed specimens in Figure 125.

The load-displacement and energy absorption results in Figure 126 show that three of the repeats had very similar results, while the final repeat was a significant outlier. This outlier was excluded from the average curves for load and energy absorption. The video of this test was studied and no clear difference was observed compared to the other three repeats. One possible explanation is that the previous seven tests caused surface imperfections on the impactor and supports, which were polished with sandpaper before the first test. These imperfections would have increased the friction level, which could have delayed the transition from wrapping to folding and caused more tension in the bottom part of the specimen. Another possible cause is misalignment of the specimen on the supports. If the specimen was loaded on a slight angle, the fold would have to form along a longer line through the top hat profile.

Figure 124: Quasi-static three point bend deformation of a 1.6 mm Ductibor® 500-AS specimen.

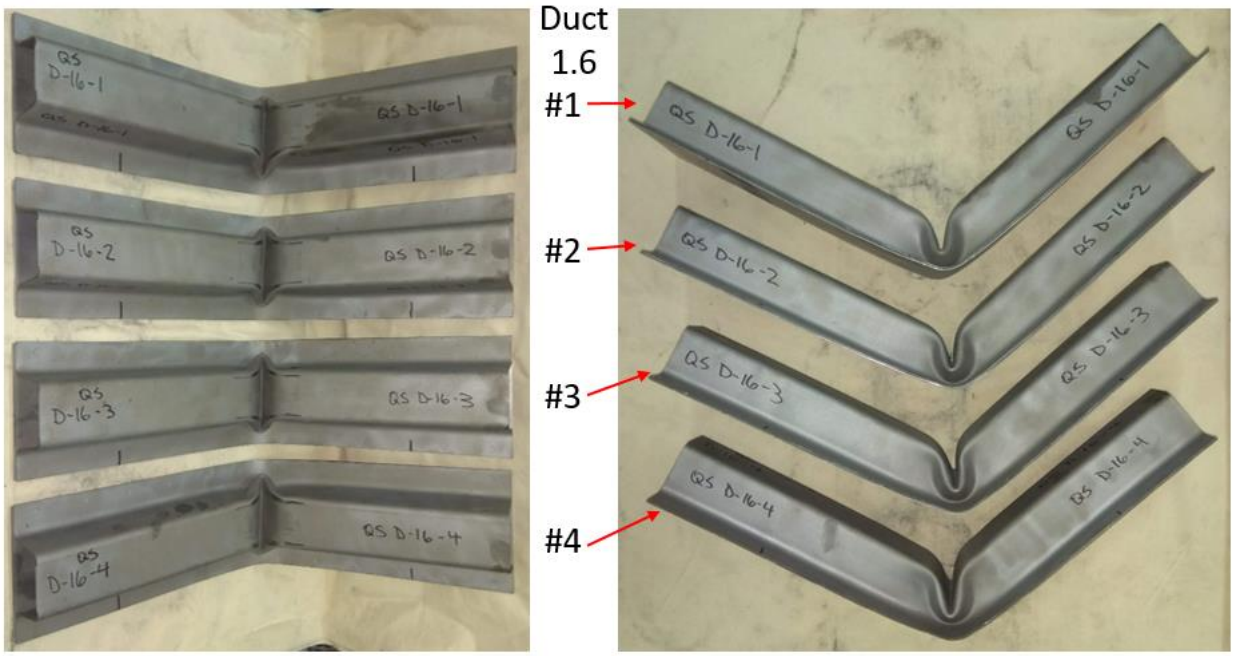

Figure 125: Final shape of four 1.6 mm Ductibor® 500-AS specimens after quasi-static three point bending.

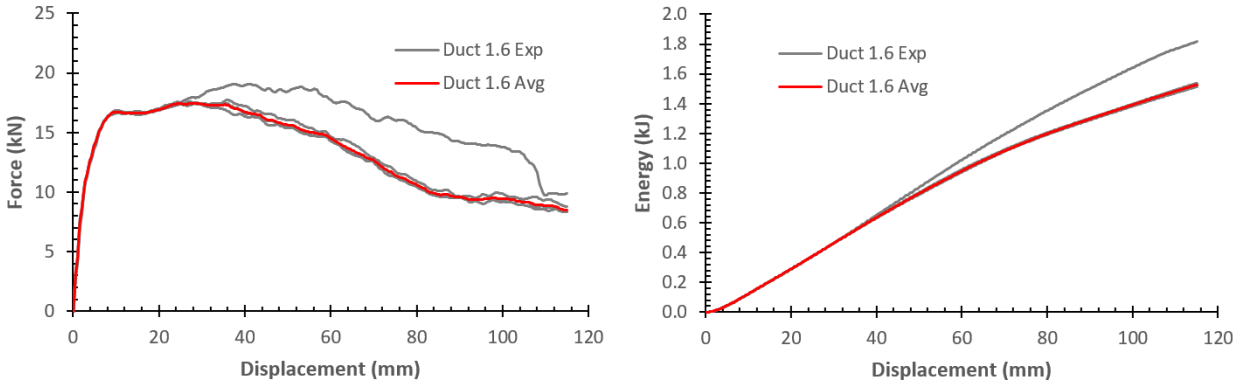

Figure 126: Quasi-static force-displacement and energy absorption data for 1.6 mm Ductibor® 500-AS three point bend specimens.

6.3 Three Point Bend - Dynamic vs. Quasi-Static Comparison

The average force-displacement and energy absorption curves for the two material conditions of side impact beams that were tested dynamically and quasi-statically are compared in Figure 127. The solid lines represent dynamic tests, and the dashed lines represent quasi-static tests. To simplify the plots, a subset of the results are shown that compare the same test conditions and results. The dynamic results show the average of the 1.2 mm specimens that folded rather than

wrapped, and the 1.6 mm specimens that folded without Teflon. The quasi-static results show the average of the specimens that were tested at a rate of 0.508 mm/s.

The initial peak force measured in the quasi-static tests is about 60-70% as high as that observed in the dynamic tests. The dynamic tests had a large load drop after this initial peak, while in the quasi-static tests this load stayed steady. The quasi-static load level stayed relatively consistent while the dynamic tests reached a second large peak. The energy absorption plots show the effect of this large second peak, with the dynamic tests absorbing more energy in each of the conditions. The initial peak force and energy absorption are compared for the different material conditions and loading rates in Figure 128, and summarized in Table 8.

For the specimens that exhibited a folding mode, the deformation of the rails was very similar between the dynamic and quasi-static tests. The main difference was the addition of the wrapping mode that occurred only in the dynamic tests.

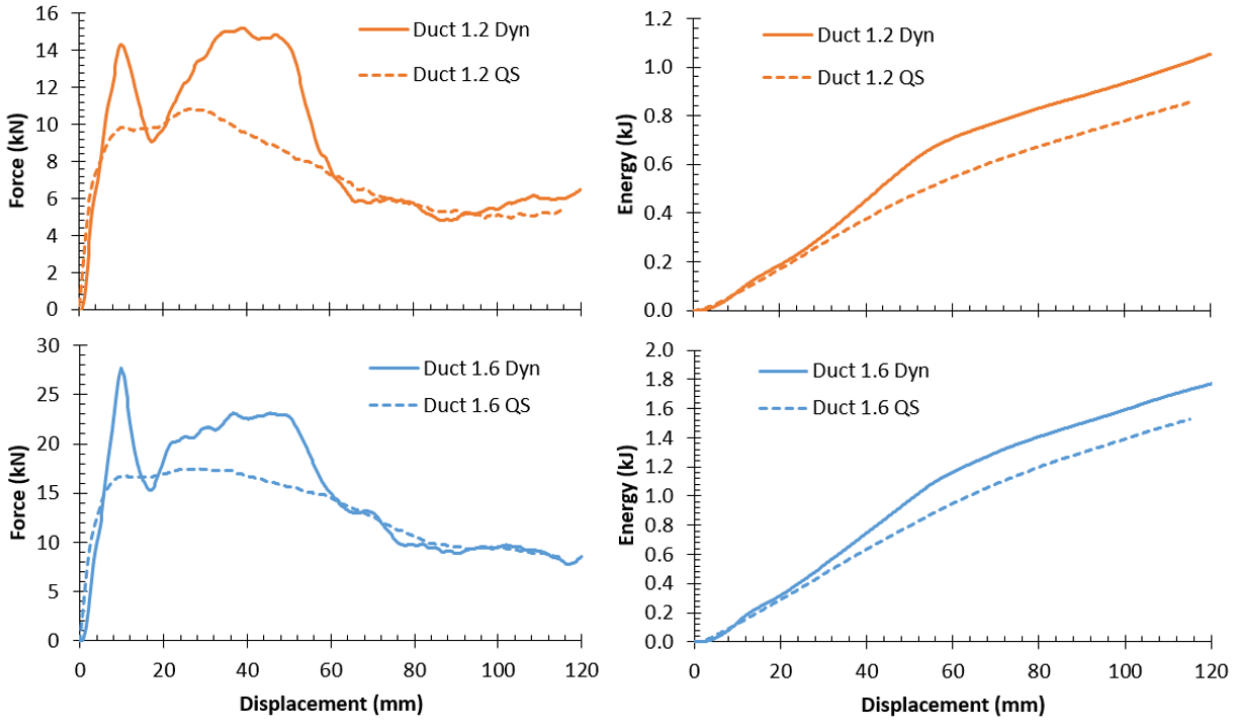

Figure 127: Comparison of dynamic and quasi-static three point bend results for the two conditions tested.

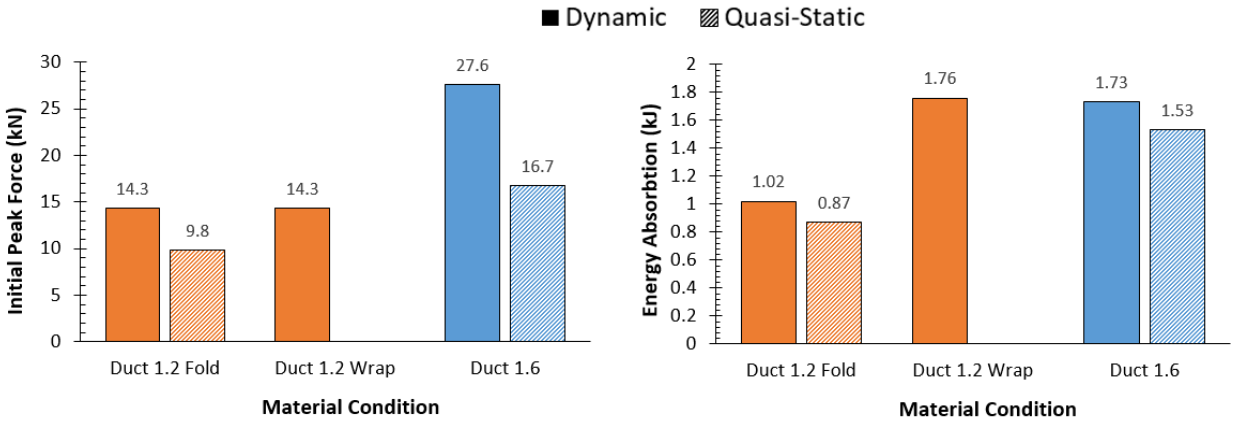

Figure 128: Comparison of initial peak force and energy absorption over the first 115 mm for the two material conditions of three point bend rails tested dynamically and quasi-statically.

Table 8: Summary of loads and energy absorption over the first 115 mm of crush for the three point bend rails tested dynamically and quasi-statically.

Test Designation	Velocity	Deformation Mode	Initial Peak Force (kN)	Absorbed Energy (kJ)	Average Crush Force (kN)
Duct 1.2	6.5 m/s	Fold	14.3	1.02	8.87
		Wrap		1.76	15.3
	0.5 mm/s	Fold	9.8	0.87	7.43
Duct 1.6	6.5 m/s	Fold	27.6	1.73	15.0
	0.5 mm/s	Fold	16.7	1.53	13.3

6.4 Three Point Bend - Dynamic Models - Results and Comparison with Experiments

Figure 129 shows the predicted force-displacement and energy absorption from the numerical model compared with the experimental average for dynamic three point bend tests considering both thicknesses. For the 1.2 mm thickness, models were run with two different friction coefficients (0.25 and 0.40) to trigger the folding and wrapping modes, respectively. The agreement with experiments is quite close with the 1.2 mm wrapping condition deviating the most near the end of the test. The simulations did not predict the large initial peak that was measured in the experiments.

A comparison between the numerical and experimental crush modes is shown in Figure 130. It is clear that the predicted fold behaviour for each condition is very similar to the experiment. No

fracture was predicted in the model, which agrees with the experiments in which no cracking or tearing was observed.

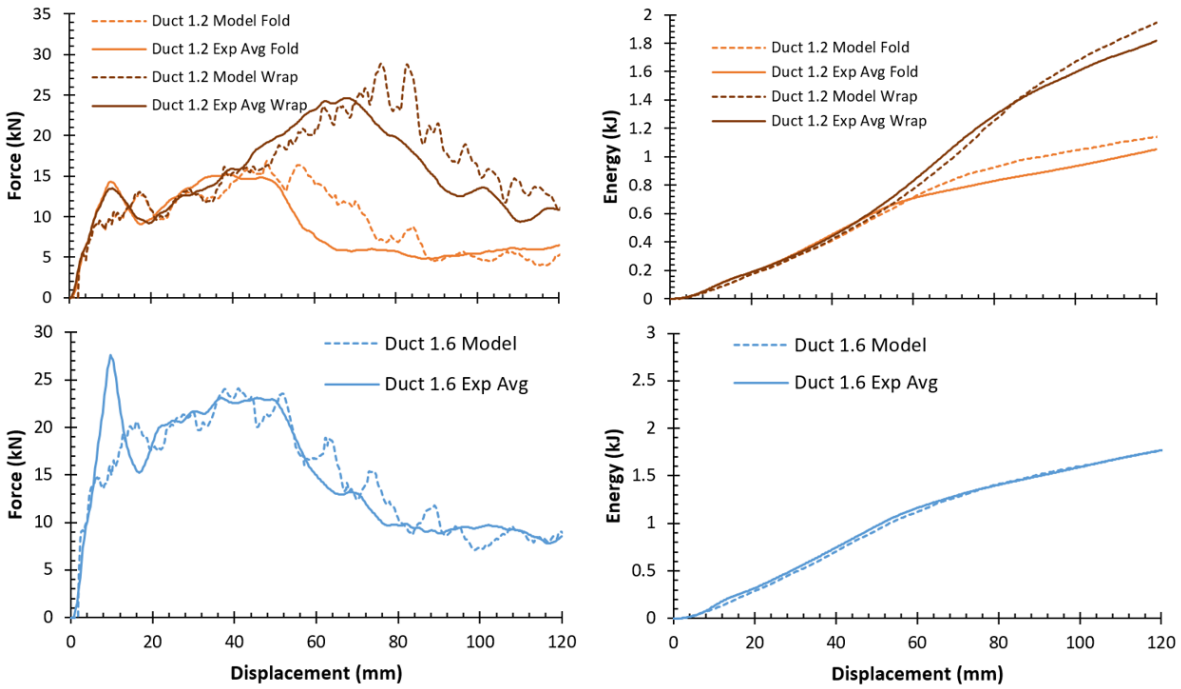

Figure 129: Comparison of experimental average with the numerical prediction for dynamic three point bend tests.

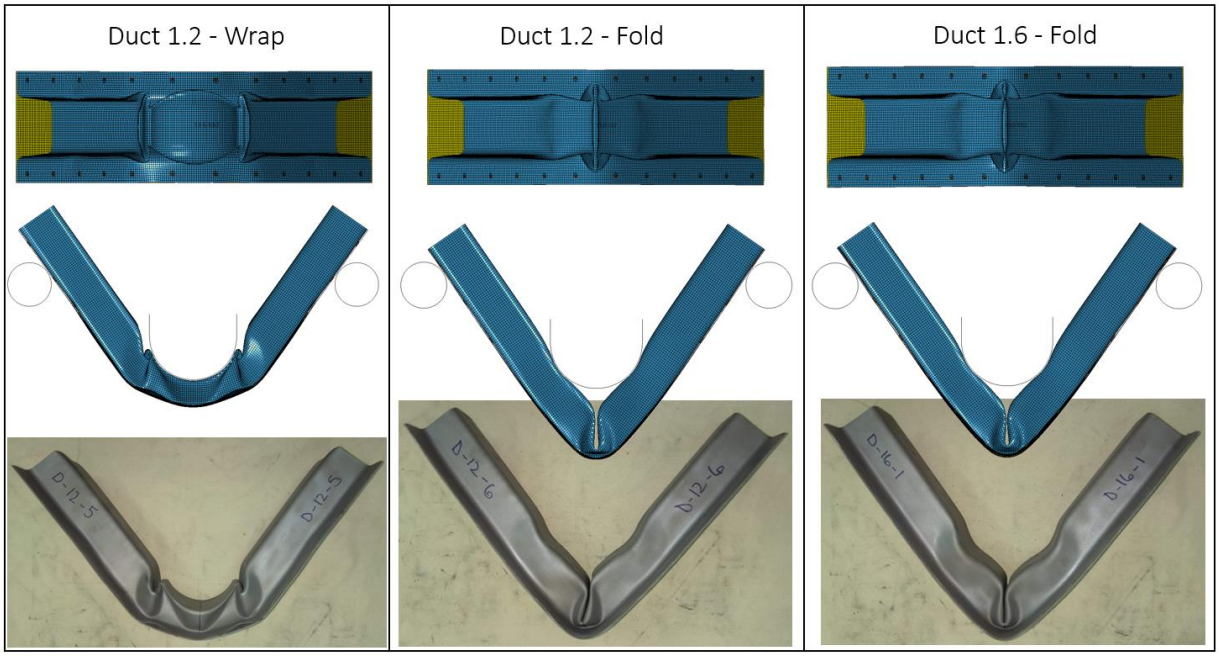

Figure 130: Comparison of experimental crush modes with the numerical prediction for dynamic three point bend tests.

6.5 Three Point Bend - Quasi-Static Models - Results and Comparison with Experiments

The predicted force-displacement and energy absorption for quasi-static three point bend tests is compared to the experiments in Figure 131. In the Duct 1.2 case, the peak force in slightly under-predicted, but otherwise the prediction is good for the first 80 mm of displacement. After this the model begins to slightly under predict the result. In the Duct 1.6 condition the under prediction is more pronounced after 40 mm of displacement.

The folding modes seen experimentally and in the model are shown in Figure 132. Once again the model correctly predicted that there would be no fracture during folding of the side impact beams. In these quasi-static tests the wrapping mode did not occur, as reflected in the model (friction coefficient of 0.25).

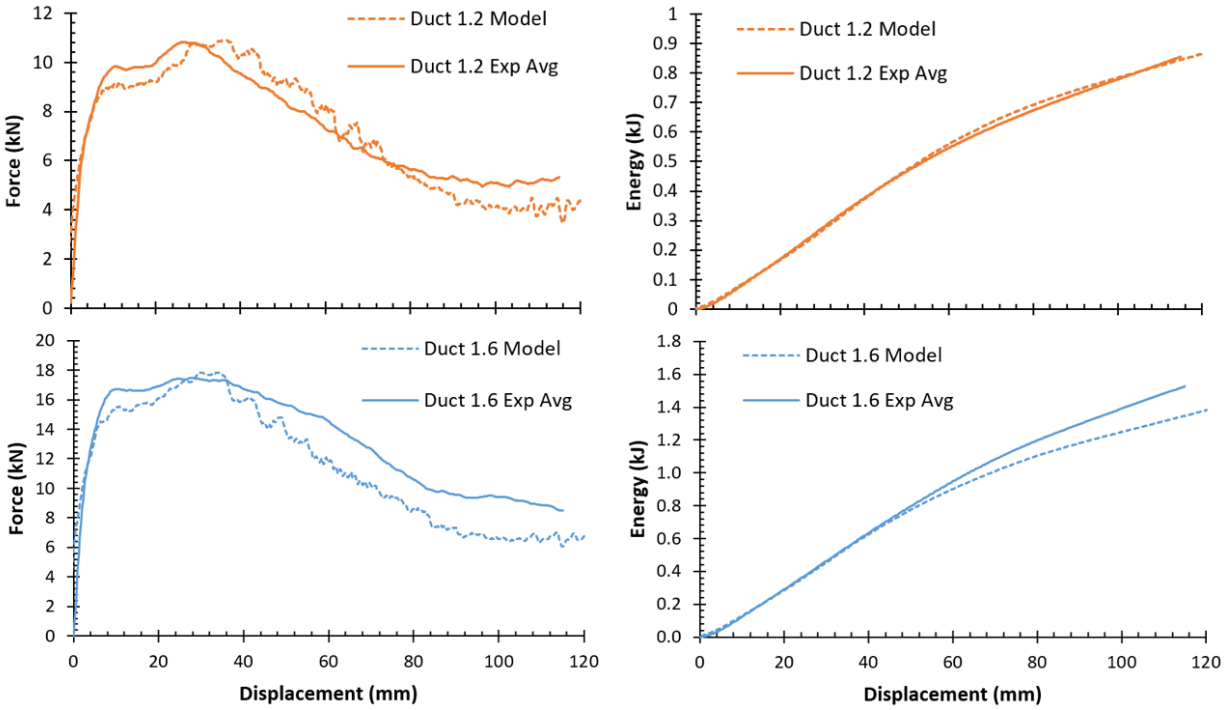

Figure 131: Comparison of experimental average with the numerical prediction for quasi-static three point bend tests.

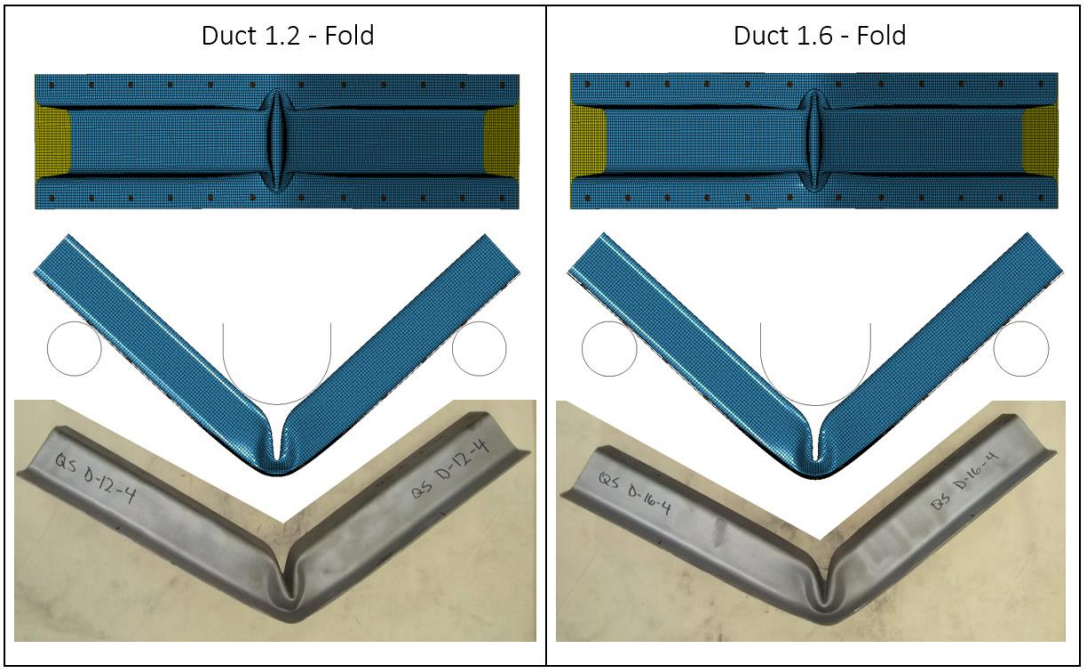

Figure 132: Comparison of experimental crush modes with the numerical prediction for quasi-static three point bend tests.

7.0 Axial Crush Experimental and Numerical Results

7.1 Axial Crush - Dynamic Experiments

7.1.1 Overview of Dynamic Axial Crush Results

For each of the material conditions, at least three dynamic crush tests were conducted. The results of these three repeat tests are summarized in Figure 133 and Figure 134. In these figures, the vertical black line at 160 mm of displacement represents the sled impacting the honeycomb arrestor blocks. The energy absorption, ranked from highest to lowest, was TWB 1.6, Duct 1.6, TWB 1.2/1.6, TWB 1.2, and Duct 1.2 (see Table 7 for specimen designations).

The TWB 1.6 specimens absorbed the highest amount of energy (31.8 kJ) over the full displacement (240 mm) to stop the sled. They also had the highest peak force (423.7 kN). The energy absorption and peak force for the different material conditions are compared in Figure 135. As crush extended into the stronger Usibor® 1500-AS section of the part, the force level increased back up to 282.3 kN.

The Duct 1.6 specimens absorbed the second most energy (28.6 kJ) in the first 240 mm of crush. They absorbed 29.9 kJ over the full displacement of 251.2 mm necessary to stop the sled. The peak force of 413.5 kJ was only slightly lower than that of the TWB 1.6 specimens. This is to be expected, as the same ductile material is undergoing the formation of the first folds. With no hard material in the back end of the part, there was not a second force peak, as was seen in the TWB 1.6 specimens.

The TWB 1.2/1.6 specimens absorbed 21.5 kJ of energy in the first 240 mm of crush. They absorbed 27.5 kJ over a full sled displacement of 260.5 mm, and had an initial peak force of 208.8 kN. With the difference in stiffness between the 1.2 mm thick ductile section and the 1.6 mm thick hard section, the load reached a second peak (321.1 kN) during crush of the hard section that exceeded the initial peak required to initiate folding in the ductile section. If the sled was run at a higher speed, it is expected that these specimens would absorb more energy than the Duct 1.6 with more crush of the hard section, albeit with a high likelihood of tearing of the Usibor® 1500-AS [21]. The force versus displacement plot in Figure 133 shows that these specimens transition from the force level of the 1.2 mm ductile section, to that of the 1.6 mm hard section. The

corresponding energy versus displacement plot (Figure 134) shows a similar increase in slope as the hard section engages.

Without the benefit of a thicker hard section, the TWB 1.2 specimens absorbed 18.9 kJ of energy in the first 240 mm of crush, and a total of 24.4 kJ over the full 289.5 mm sled displacement. They reached an initial peak force of 284.6 kN, then a second peak of 131.6 kN as folds formed in the hard section. This initial peak was quite a bit larger than that of the TWB 1.2/1.6 which was initiating in the same 1.2 mm ductile material. A possible explanation for this is a slight difference in crush initiator depth. Since the multi-gauge specimens were built and tested separately from the rest of the rails, it is also possible that something changed in the load cell setup, whether their physical mounting or in the electronic data acquisition.

Lastly, the Duct 1.2 specimens absorbed the least energy, both in the first 240 mm (15.2 kJ) and over the full crush distance of 286.5 mm (17.2 kJ). The initial peak force was similar to the TWB 1.2 specimens at 272.4 kN.

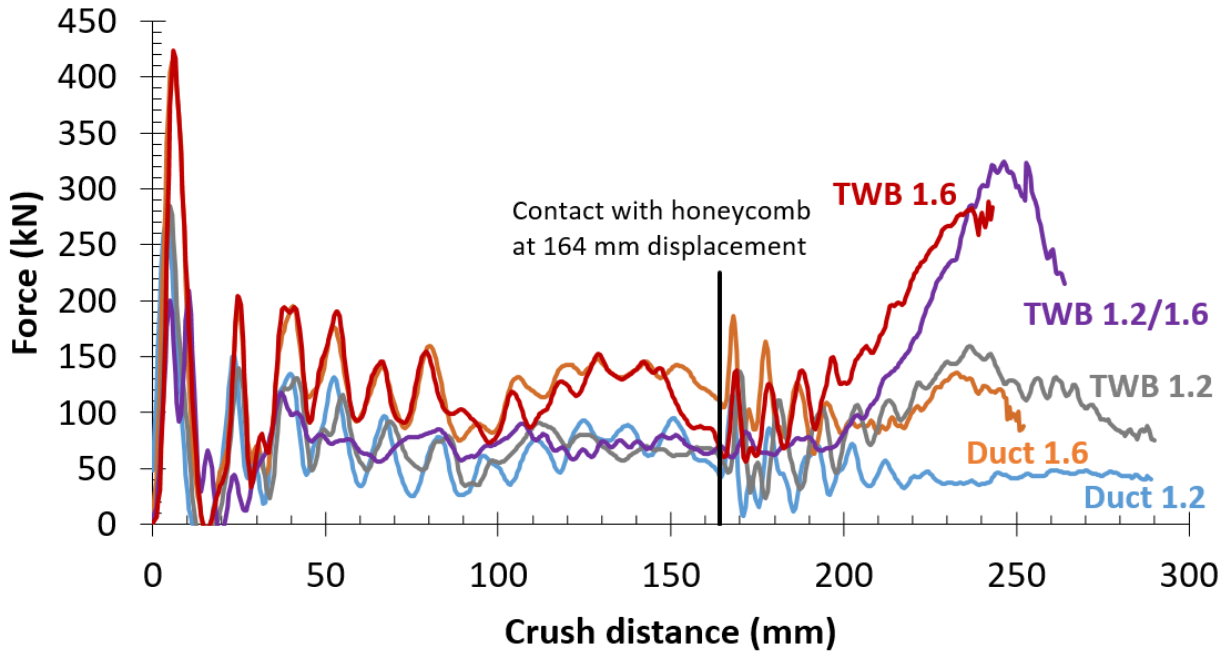

Figure 133: Force vs displacement for all dynamic axial crush conditions.

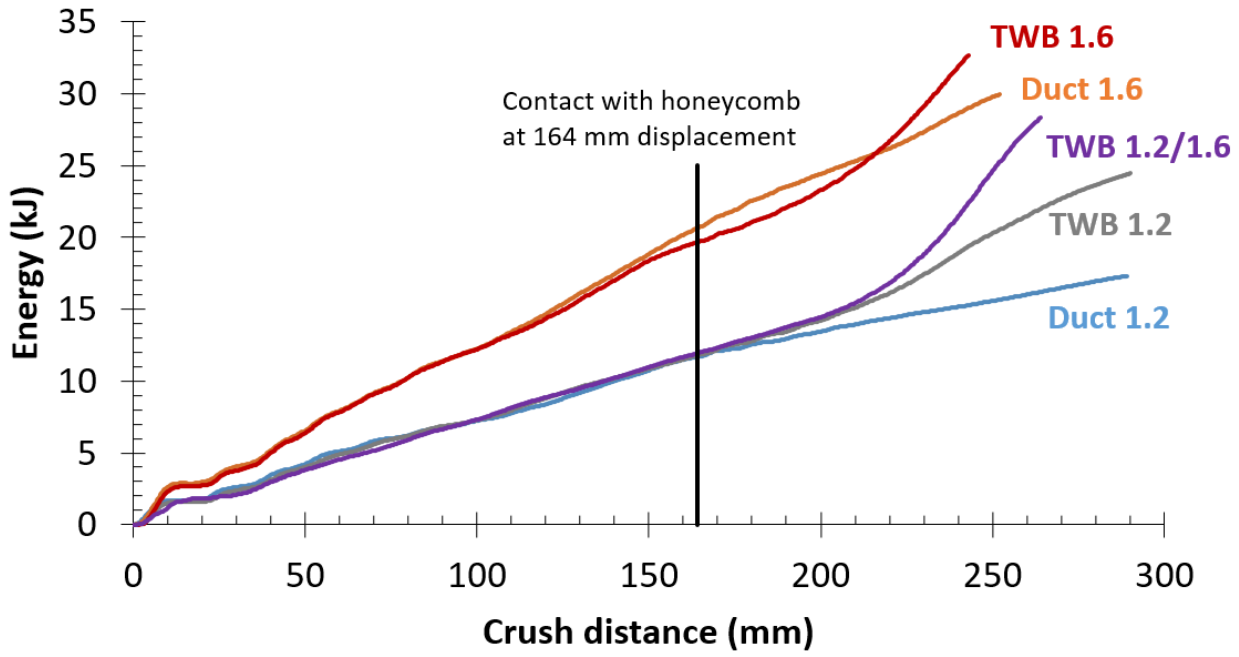

Figure 134: Energy vs displacement for all dynamic axial crush conditions.

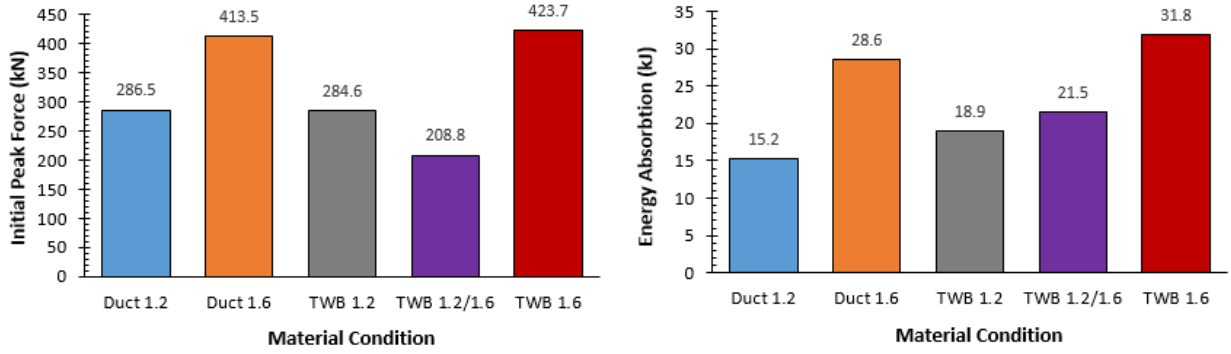

Figure 135: Summary of initial peak force and energy absorption in the first 240 mm of crush for the five material conditions of dynamic axial crush rails.

7.1.2 Dynamic Crush Response of 1.2 mm Ductibor® 500-AS Specimens

The still images in Figure 136 are taken from the high speed overhead camera video of a dynamic crush test of a monolithic 1.2 mm Ductibor® 500-AS rail. The final deformed shapes of three of these specimens are shown in Figure 137. It is shown that the specimens began folding at the initiator and initially folded well for two folds, after which the folding became unstable. In two of the three specimens, folds initiated at the fixed end of the rail and caused lateral buckling to the right. The third specimen did not buckle, but the folding was not stable, with folds initiating at both ends of the specimen.

The load-displacement and energy absorption results in Figure 138 show the three individual experiments as grey lines, and the average response as a red line. The vertical black line represents the point at 164 mm of displacement where the sled engaged with the honeycomb attenuators. The loads are very similar for the first 125 mm of crush before they diverge somewhat. The first 125 mm corresponds to the formation of the first two folds, after which the buckling behaviour is more irregular.

Ductibor® 500-AS in a 1.2 mm thickness folded well initially, but became susceptible to buckling when used in a long slender member such as this. Due to the low strength and thin gauge, the overall energy absorption was low. Parent metal failure was not observed in these tests due to its high ductility. A small amount of spot weld failure was observed in the folds, usually in the form of a partial pullout as the material bends tightly.

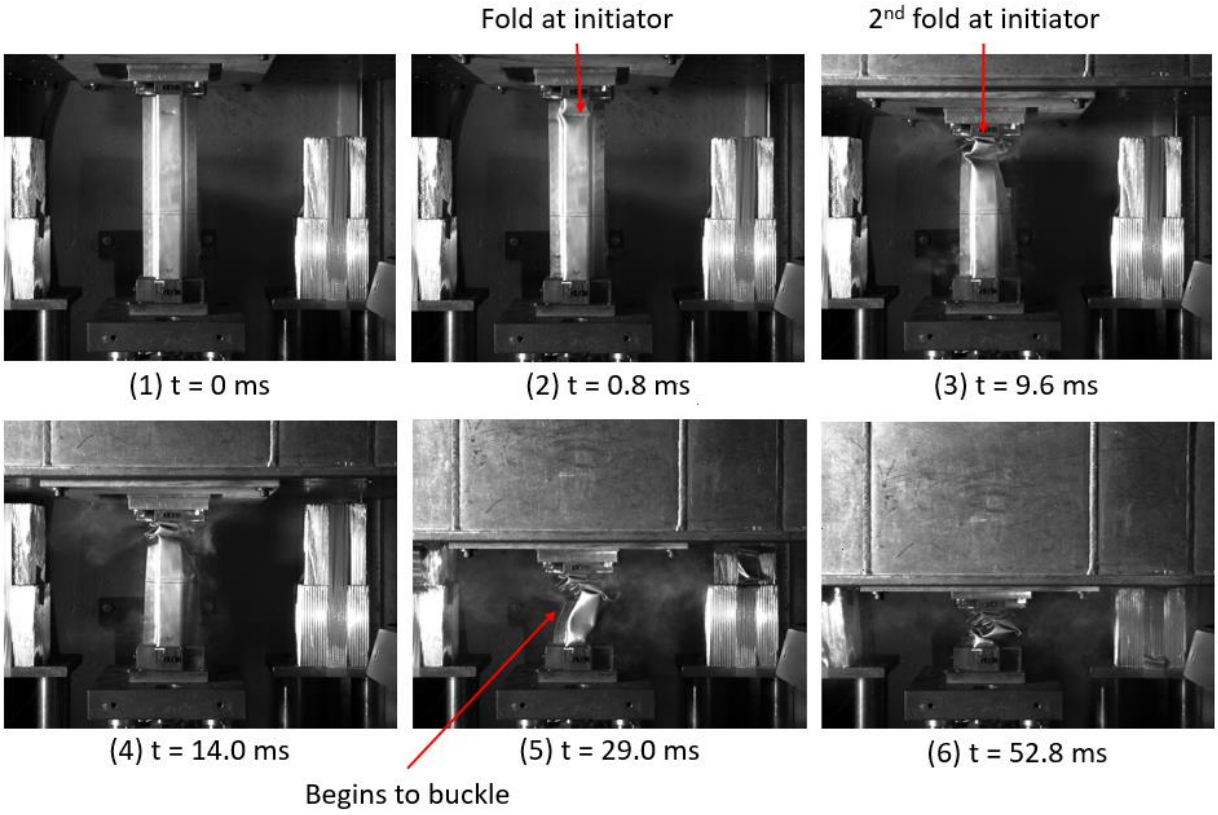

Figure 136: Dynamic crush deformation of a 1.2 mm Ductibor® 500-AS specimen.

Figure 137: Final shape of three 1.2 mm Ductibor® 500-AS specimens after dynamic crush.

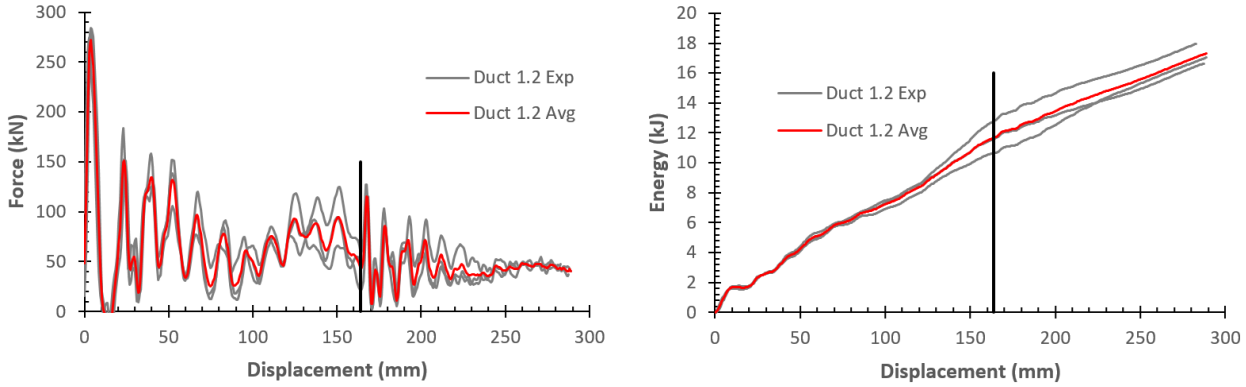

Figure 138: Dynamic force-displacement and energy absorption data for 1.2 mm Ductibor® 500-AS specimens.

7.1.3 Dynamic Crush Response of 1.6 mm Ductibor® 500-AS Specimens

The still images in Figure 139 were taken during the dynamic crush experiment of a 1.6 mm monolithic Ductibor® 500-AS rail. Figure 140 shows the final deformed shape of the three specimens that were tested. These performed similarly to the 1.2 mm specimens with the first two folds forming at the initiator, followed by unstable folding. A fold initiated at the fixed end of two of the three specimens, with one buckling slightly to the left and the other slightly to the right. In the third specimen (pictured in the center) the folds all formed progressively at the impacted end, though the last one formed on an angle.

Figure 141 shows the load displacement and energy absorption plots. The experimental curves diverge somewhat after 125 mm of repeatable displacement, but the scatter is less than in the 1.2 mm monolithic parts. The higher energy absorption of the specimen that folded progressively is shown.

These parts absorbed more energy than the 1.2 mm monolithic condition due to their thicker gauge requiring more force to form folds. The added stiffness also helped to suppress the buckling tendency of the thinner gauge, though less severe buckling was still observed. Parent metal failure was not observed, while a small amount of spot weld failure did occur.

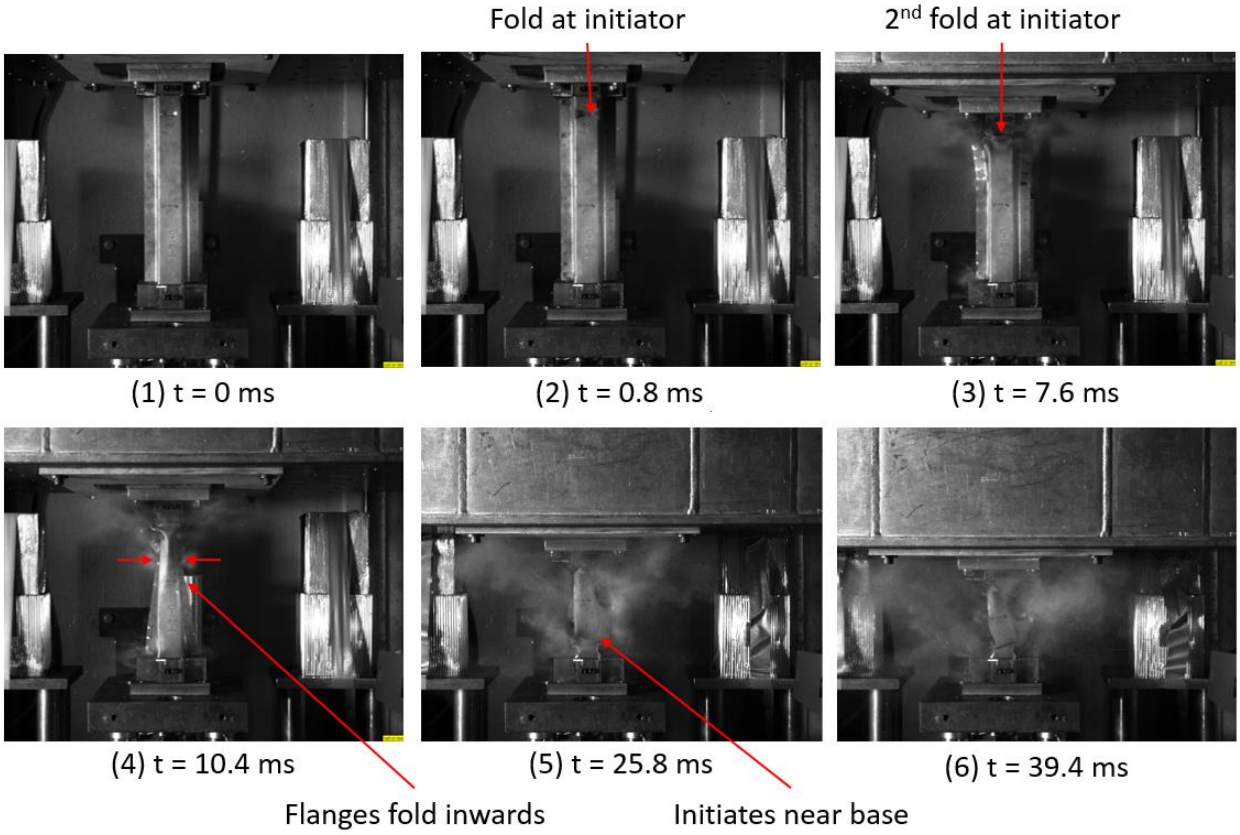

Figure 139: Dynamic crush deformation of a 1.6 mm Ductibor® 500-AS specimen.

Figure 140: Final shape of three 1.6 mm Ductibor® 500-AS specimens after dynamic crush.

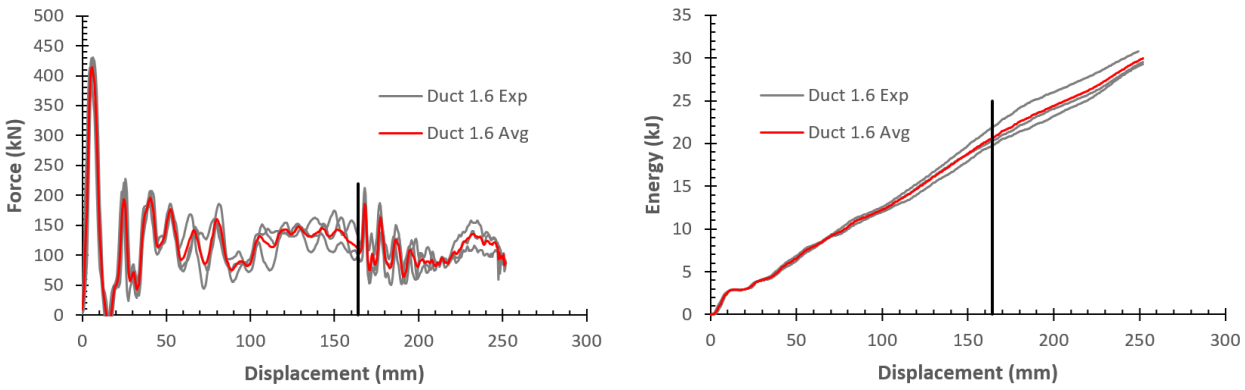

Figure 141: Dynamic force-displacement and energy absorption data for 1.6 mm Ductibor® 500-AS specimens.

7.1.4 Dynamic Crush Response of 1.2 mm TWB Specimens

The still images in Figure 142 show the dynamic crush experiment of a 1.2 mm TWB crush rail. Just after impact, the first fold formed at the initiator while a bulge was also seen in the soft material adjacent to the laser weld line. A second fold formed adjacent to the first, then the third fold formed at a second initiation site just above the weld line. As the part continued to crush, the soft Ductibor® 500-AS zone full consolidated on top of the intact Usibor® 1500-AS hard zone. As the crush continued, folds formed in this hard zone as well as fracture. Figure 143 shows the final deformed shape of the three specimens tested. All three parts experienced some degree of folding at the top of the hard zone. Two of them initiated folds near the bottom of this zone, with fracture occurring in both of these folds.

The force-displacement and energy absorption data for these specimens is shown in Figure 144. The tests were very repeatable (more so than either of the monolithic conditions), particularly during the formation of the first few folds in the soft zone. The load level increases noticeably as the hard zone begins to crush, which is also reflected in the energy absorption.

The use of a hard Usibor® 1500-AS zone in the latter section of these TWB rails stabilized the crush mode by preventing buckling. Having the hard zone clamped to the wall pushed the site of second fold initiation from the base of the rail up to the transition zone, shortening the effective column length from 500 mm to 290 mm. The sharp gradient in strength level created a discontinuity at this transition that caused the development of a fold during the tests. The hard zone did not deform significantly until the soft zone had completely collapsed on itself and absorbed as much energy as possible. When the hard zone did collapse, some cracking was observed in the

tight folds. Some spot weld failure was also observed in the hard zone. This failure was more significant than in the monolithic soft parts, with one or more welds completely releasing and changing the folding mode.

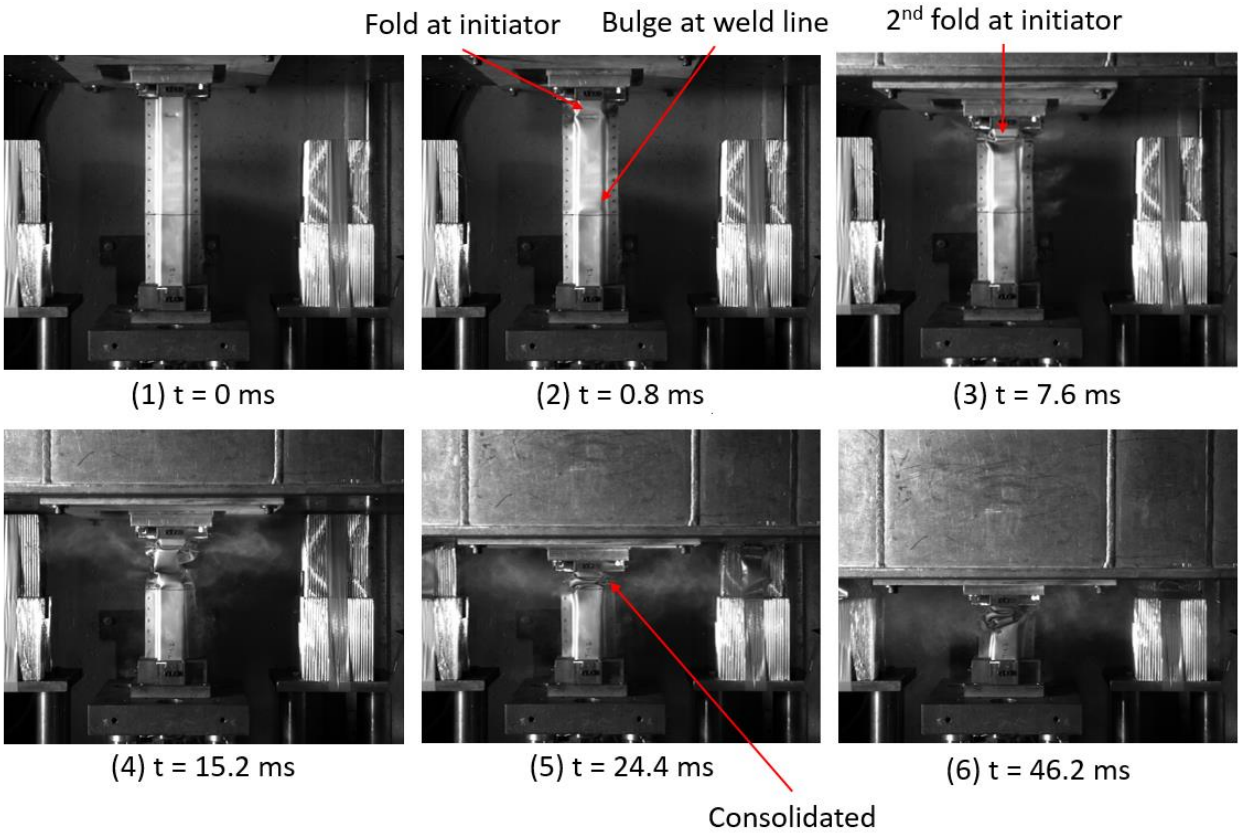

Figure 142: Dynamic crush deformation of a 1.2 mm TWB specimen.

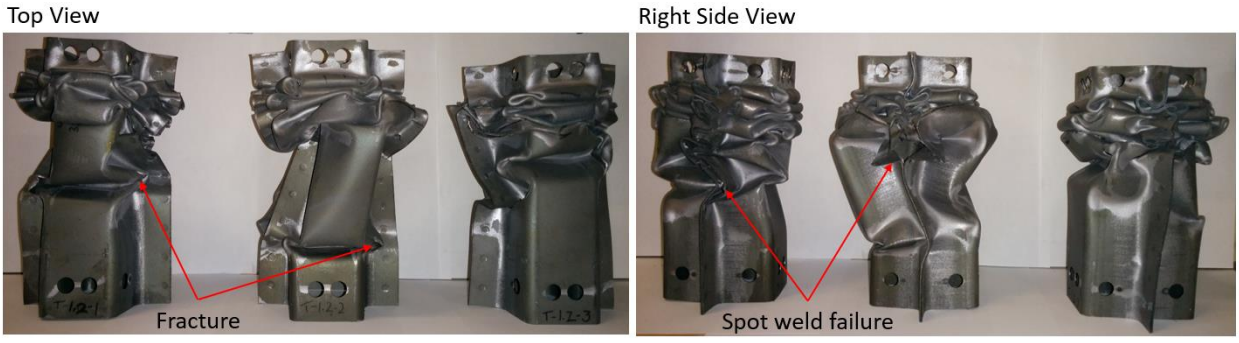

Figure 143: Final shape of three 1.2 mm TWB specimens after dynamic crush.

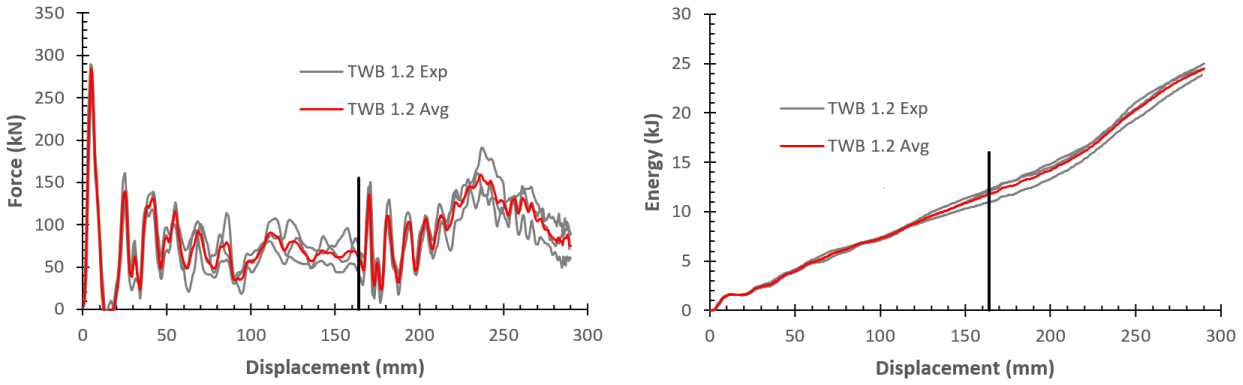

Figure 144: Dynamic force-displacement and energy absorption data for 1.2 mm TWB specimens.

To better investigate the folding behaviour in these 1.2 mm TWBs, the impacted end of one rail was sectioned using a band saw through two different planes of the part. The cut faces were ground and filed flat, and then sanded to a smooth finish. Figure 145 shows these cross sections cut from front to back and at a 45 degree angle through the corner of the rail. The Ductibor® 500-AS forms very tight folds as it consolidates, and no cracks were observed in any of these tight folds due to the material's high ductility.

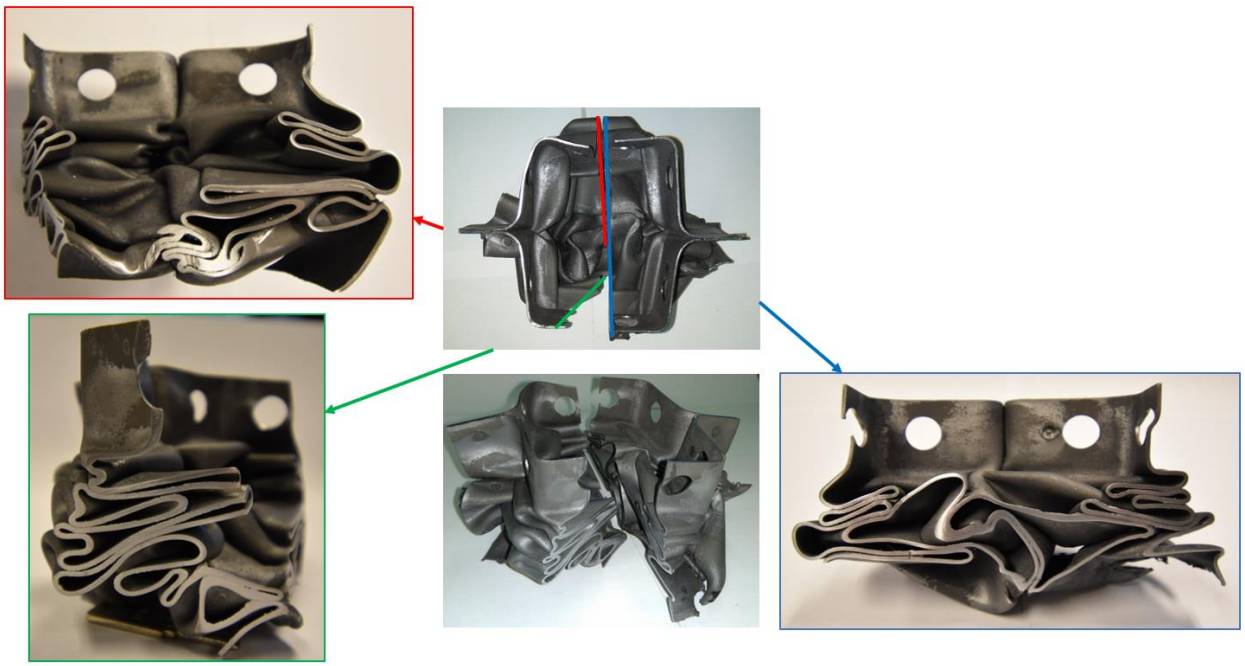

Figure 145: Cross section of the folds in a crushed 1.2 mm TWB.

7.1.5 Dynamic Crush Response of 1.2/1.6 mm TWB Specimens

Figure 146 shows still images of the dynamic crush response of a 1.2/1.6 mm multi-gauge TWB rail. This rail folded in a desirable progressive crush fashion. The first fold formed at the initiator, and each subsequent fold formed behind the previous one. Similar to the 1.2 mm TWBs, the soft zone fully consolidated before the hard zone began to deform. The deformed shape of the three multi-gauge specimens is shown in Figure 147. The three specimens all performed similarly, with no secondary fold initiation sites as observed in the other conditions thus far. The first and third parts show the flanges are folding inward somewhat, while the second part had the most stable folding behaviour.

Figure 148 shows the force-displacement and energy absorption data for these multi-gauge specimens. The repeatability is extremely good, better than the monolithic soft rails and the 1.2 mm TWBs. These tests were performed last, after taking down the test setup used for the other four conditions and re-installing it. It appears that there was far less oscillation in the measured force data in this setup, but the reason for this is not known. The force increases sharply after 200 mm of crush when the hard zone begins to deform, which also is evident in the energy absorption.

The thicker 1.6 mm Usibor® 1500-AS hard section in the back part of these rails specimens stabilized the crush mode better than the 1.2 mm hard section used in the 1.2 mm TWBs. The very stiff section clamped to the wall was very stable, leading to progressive folding all the way through the crush, preventing any secondary fold initiation from occurring. The difference in strength led to a large increase in force once the soft zone had fully consolidated. Interestingly, parent metal failure was not observed in the harder Usibor® 1500-AS zone in these experiments. Minor spot weld failure occurred in the folds of the soft zone.

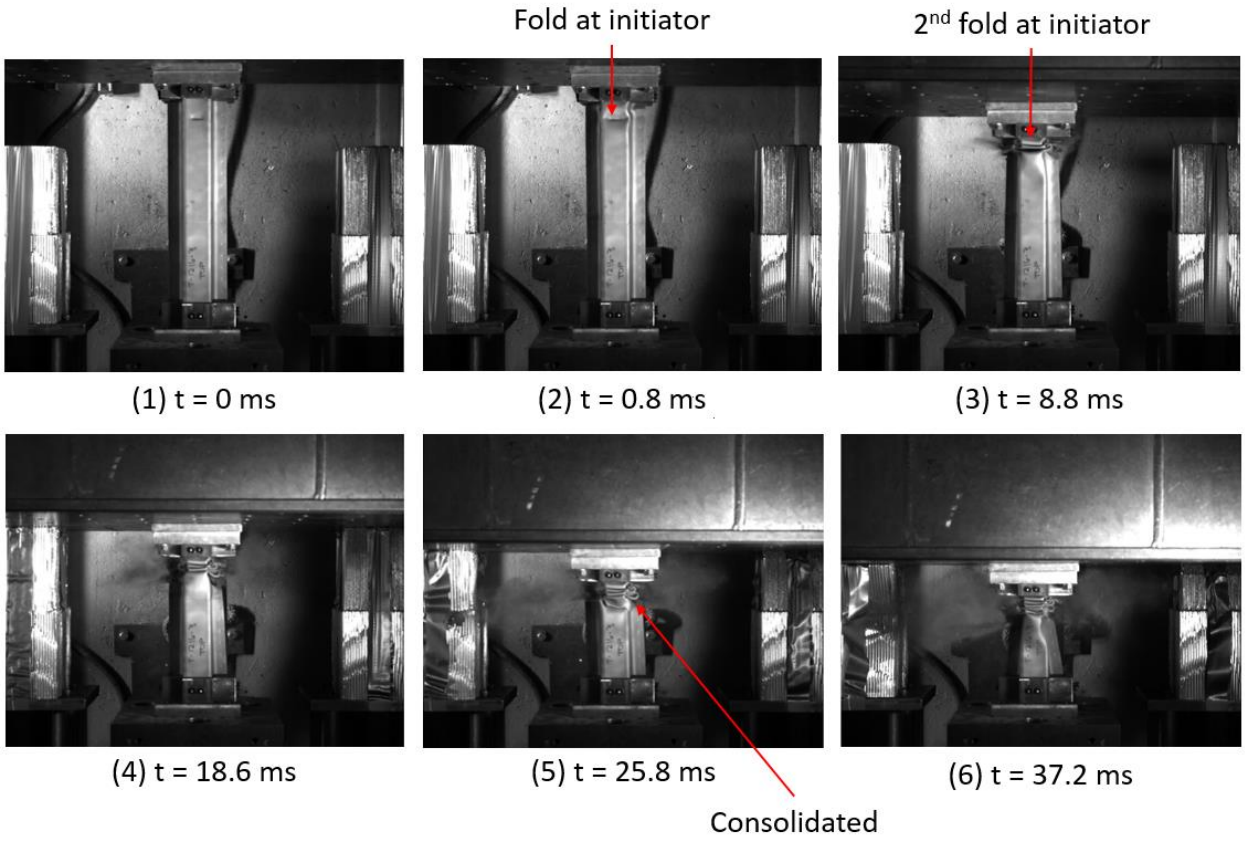

Figure 146: Dynamic crush deformation of a 1.2/1.6 mm TWB specimen.

Figure 147: Final shape of three 1.2/1.6 mm TWB specimens after dynamic crush.

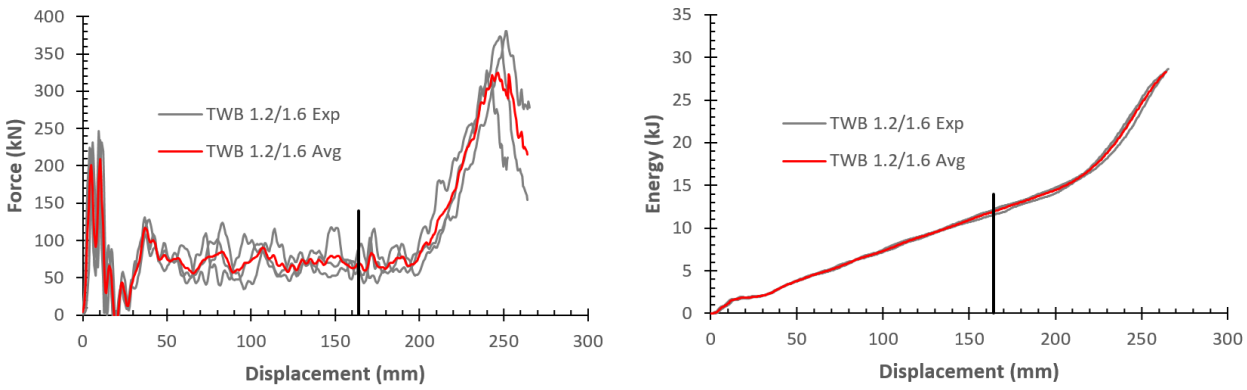

Figure 148: Dynamic force-displacement and energy absorption data for 1.2/1.6 mm TWB specimens.

7.1.6 Dynamic Crush Response of 1.6 mm TWB Specimens

Figure 149 shows still images of a dynamic crush test of a 1.6 mm common gauge TWB crush rail specimen. These performed similarly to the 1.2 mm common gauge TWBs with the first two folds forming cleanly at the initiator, then a third fold forming further down in the soft zone near the transition at the weld line. The soft zone consolidated fully on top of the intact hard zone, absorbing most of the sled's energy. The hard zone then deforms slightly to absorb the remaining energy. With the thicker 1.6 mm soft zone in these rails, there is little energy remaining for the hard zone to absorb. The deformed shapes of the three specimens tested are shown in Figure 150. The first part, and to a lesser degree the second part, had some unstable folding in the soft zone that resulted in an irregular folded shape. The third part had failure occur in the laser weld line. All of the parts had only a small amount of crush into the hard zone with only a partial fold forming. This is the result of the thicker soft zone absorbing the majority of the sled energy.

The force-displacement and energy absorption data is shown in Figure 151. With these tests being performed on the initial setup of the fixtures, the oscillation in the force data has returned. The results are very repeatable through the first two folds (125 mm) of crush, after which the curves diverge. The force increases as the hard zone begins to crush, reaching similar levels to the multi-gauge TWBs. At the end of the crush they converge again with the force level at the peak displacement being very similar for each of the tests before the sled rebounds.

As was the case with the other TWB conditions, the hard Usibor® 1500-AS section prevented buckling and promoted excellent energy absorption in the soft zone. Deformation was focused in the soft zone until it consolidated, after which the small amount of remaining energy was absorbed

in the hard zone. Partial failure of the laser weld was observed in one of the specimens. Minor spot weld failure also occurred in the Usibor® 1500-AS zone. The initial peak load of 423.7 kN in these specimens was well in excess of the 360 kN rated load of the load cell pack (3 x 120 kN). These loads cells are capable of handling a moderate overload for a short term peak load, however the strength of these rails is approaching their limit.

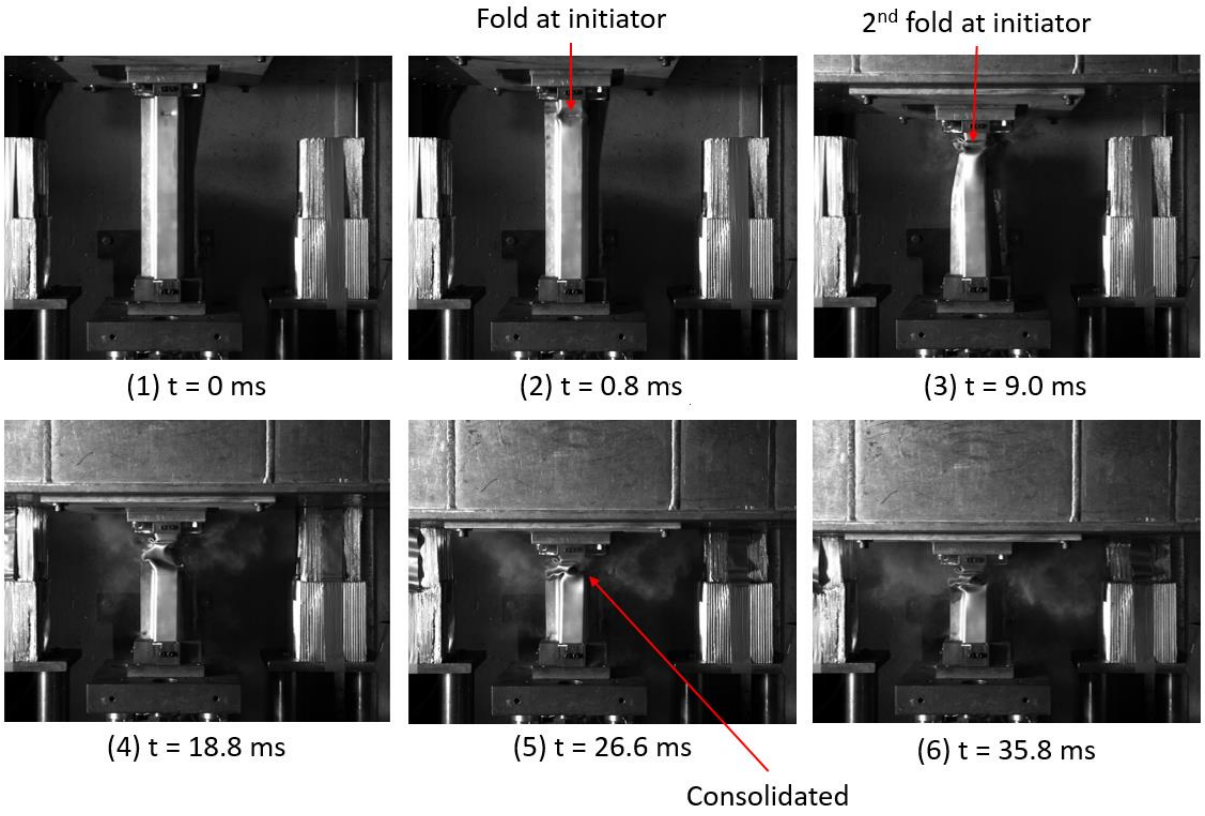

Figure 149: Dynamic crush deformation of a 1.6 mm TWB specimen.

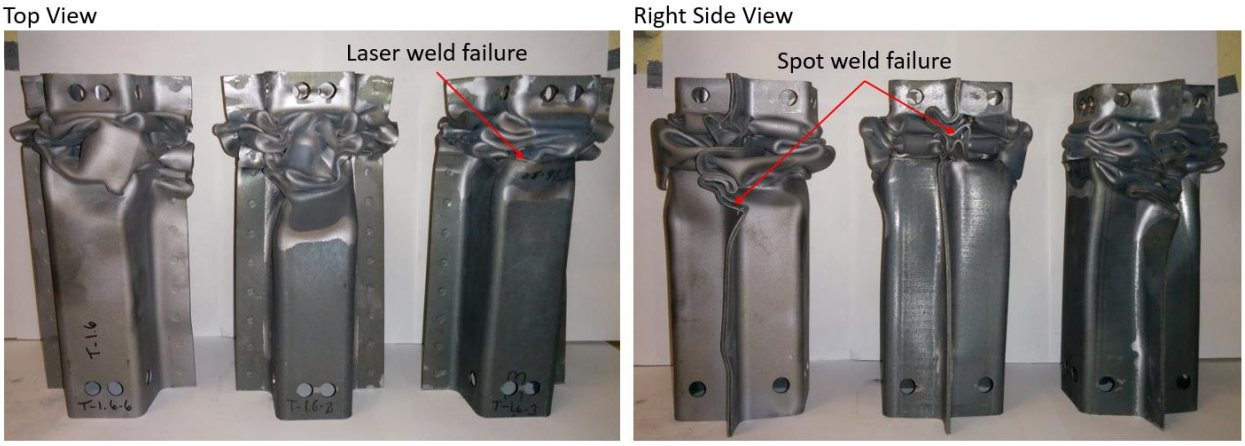

Figure 150: Final shape of three 1.6 mm TWB specimens after dynamic crush.

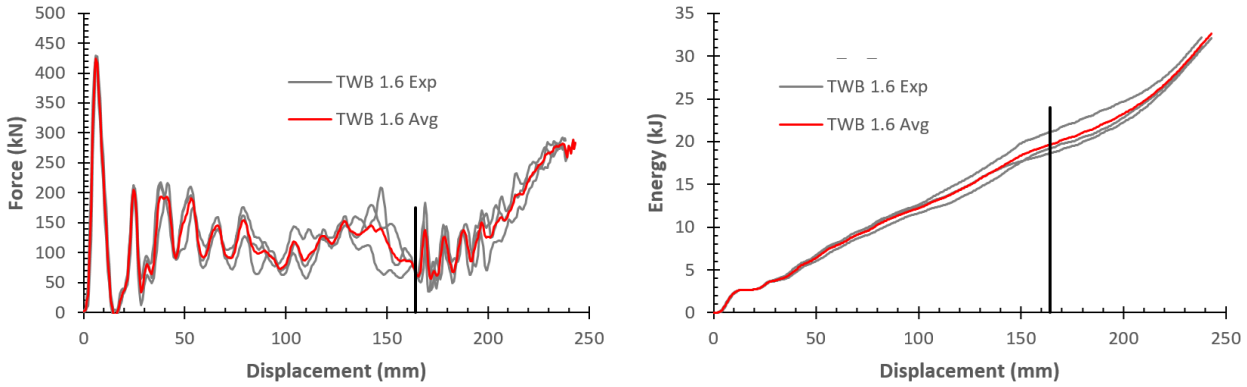

Figure 151: Dynamic force-displacement and energy absorption data for 1.6 mm TWB specimens.

As was done with a 1.2 mm TWB, one of the 1.6 mm TWBs was sectioned on a band saw through three planes. Figure 152 shows one plane cut through the front and back sides of the rail, another went through the left side of the part, and the third went through the corner on a 45 degree angle. As with the 1.2 mm, tight folds are formed with no evidence of cracking or fracture.

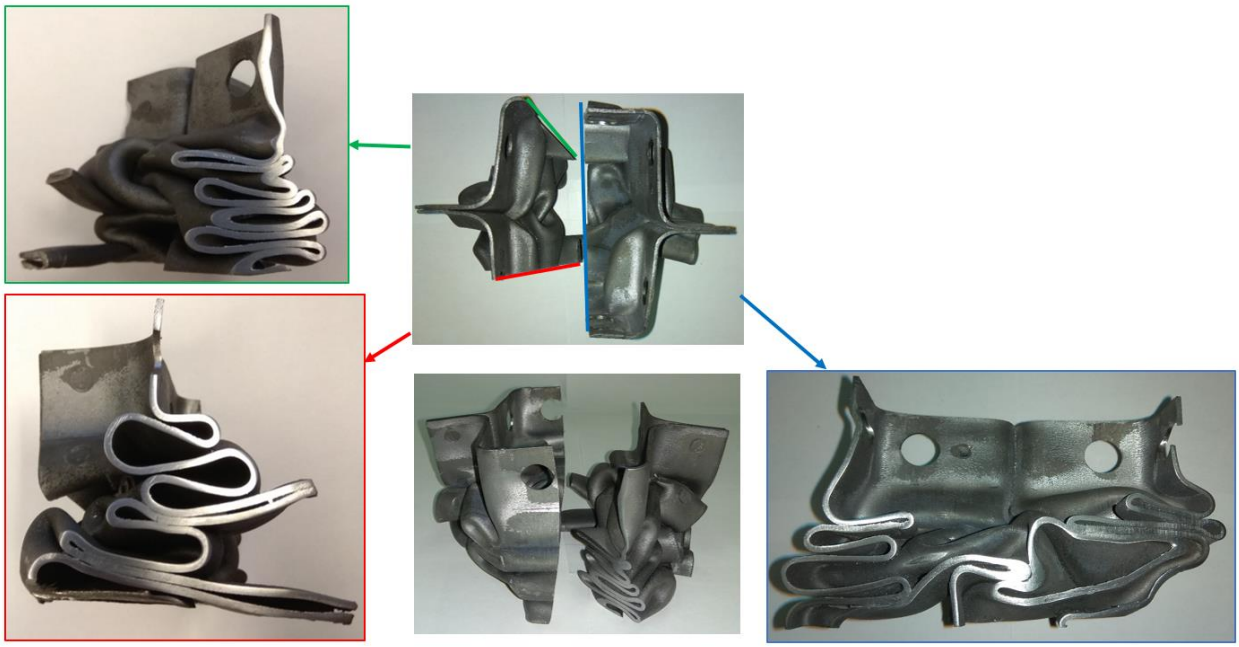

Figure 152: Cross section of the folds in a crushed 1.6 mm TWB.

7.2 Axial Crush - Quasi-Static Experiments

7.2.1 Overview of Quasi-Static Axial Crush Results

As in the dynamic crush tests, at least three tests were successfully performed for each material condition, and the average results are summarized in Figure 153 and Figure 154. The order of most to least energy absorbed is identical in the static tests to that in the dynamic tests, with the TWB 1.6 absorbing the most, followed by the Duct 1.6, TWB 1.2/1.6, TWB 1.2, and lastly Duct 1.2.

The TWB 1.6 specimens absorbed the highest amount of energy (29.8 kJ) over the full 250 mm displacement of the press platen. They also had the highest initial peak force of 241.5 kN, significantly lower than what was recorded in the dynamic tests. As crush extended into the hard section of the part, the force level increased back up to a later peak of 272.3 kN. The initial peak force, and the total energy absorbed over the 250 mm crush are compared for the different material conditions in Figure 155.

The Duct 1.6 specimens absorbed the second most energy (24.3 kJ) in the 250 mm of displacement used in these tests. As was the case in dynamic tests, the peak force (240.7 kJ) was only slightly lower than that of the TWB 1.6 specimens. As with the previous specimens, the initial peak force has reduced significantly from the 413.5 kN that was measured dynamically.

The TWB 1.2/1.6 specimens absorbed 21.0 kJ of energy in the 250 mm crush, and had an initial peak force of 131.0 kN. At this lower strain rate, the second load peak (271.8 kN) measured during crush of the hard section was more than double the initial peak. As was the case dynamically, these specimens transition from the force level of the 1.2 mm ductile section, to that of the 1.6 mm hard section. Interestingly, the peak force for the quasi-static TWB 1.2/1.6 was similar to that of the other 1.2 mm Ductibor® 500-AS specimens and did not show the drop in peak force observed in the dynamic tests. This comparison suggests that some aspect of the dynamic tests of the TWB 1.2/1.6 specimens led to the observed drop in initial peak load.

The TWB 1.2 specimens absorbed 17.4 kJ of energy in their 250 mm crush. They reached an initial peak force of 139.0 kN, then a second peak of 143.8 kN. At this lower rate there was a much smaller difference between the initial peak forces of the multi-gauge and 1.2 mm common gauge specimens.

The Duct 1.2 specimens absorbed the least energy (13.5 kJ) over the 250 mm quasi-static crush. The initial peak force of 137.8 kN was similar to the TWB 1.2 and TWB 1.2/1.6 specimens.

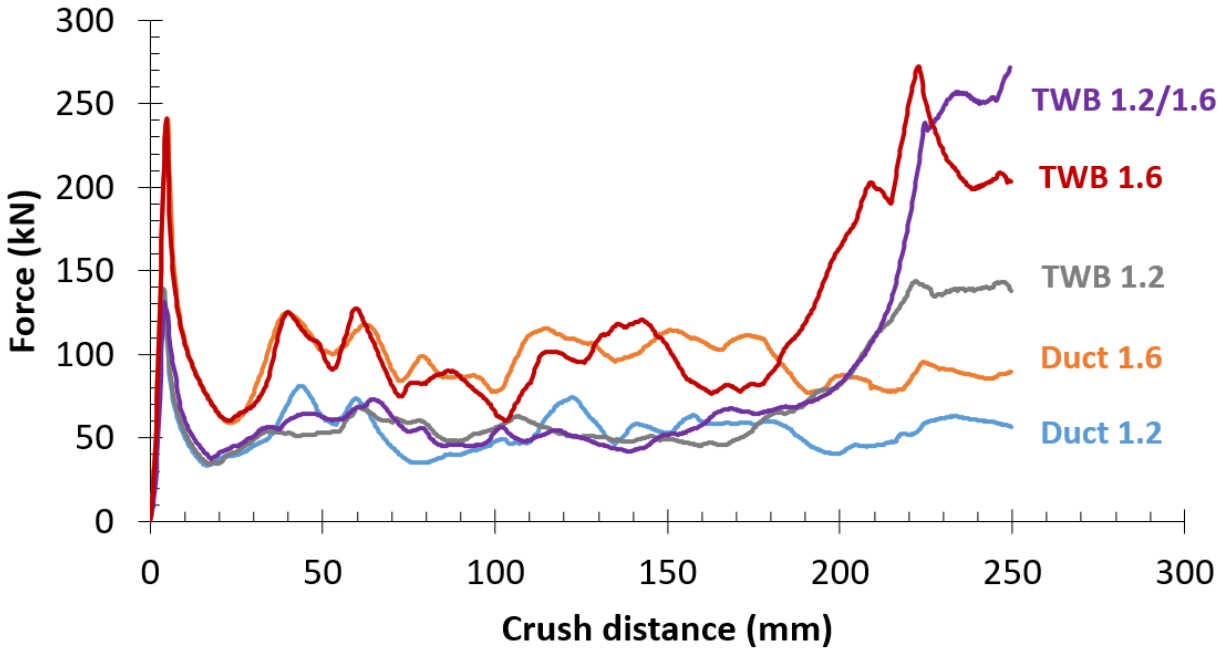

Figure 153: Average force vs displacement for all quasi-static axial crush conditions.

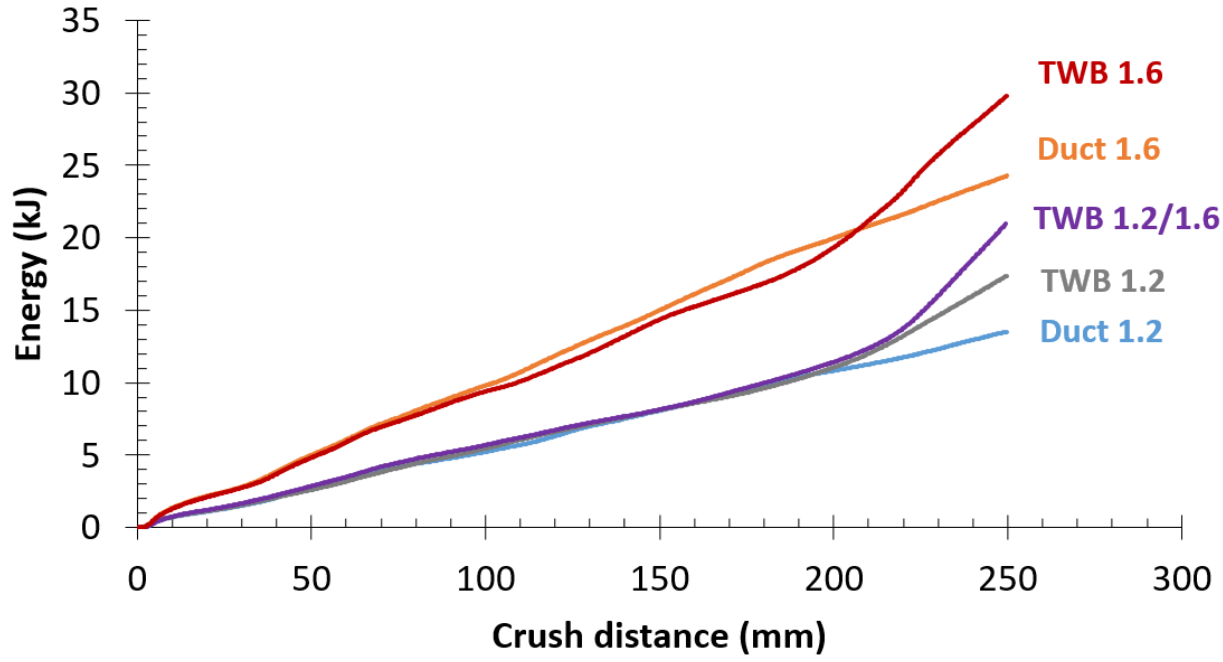

Figure 154: Average energy absorption vs displacement for all quasi-static axial crush conditions.

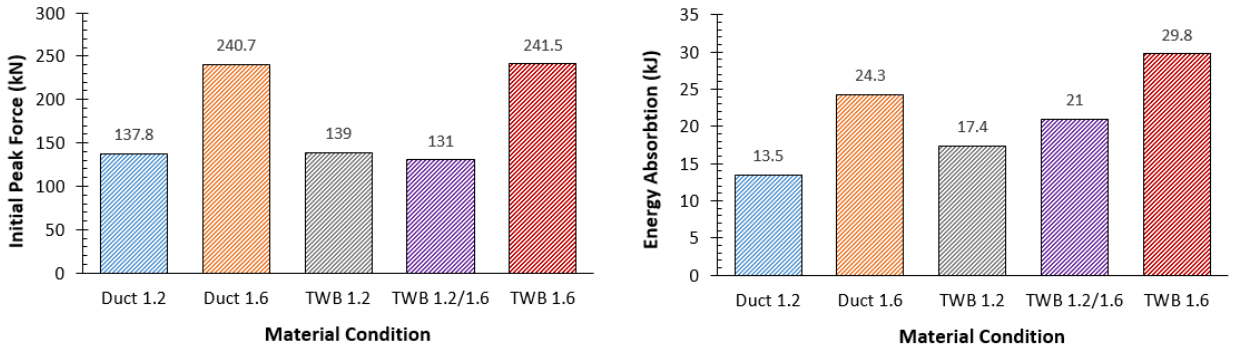

Figure 155: Summary of initial peak force and energy absorption in the full 250 mm crush distance for the five material conditions of quasi-static axial crush rails.

7.2.2 Quasi-Static Crush Response of 1.2 mm Ductibor® 500-AS Specimens

Figure 156 shows still images of the quasi-static crush of a 1.2 mm monolithic Ductibor® 500-AS crush rail. As the press platen slowly advanced onto the crush rail, the first fold initiated at the crush initiator dimple. As it continued to advance, a second fold formed below the first, then a third fold formed further down the rail, and another on top of the bottom clamps. Unlike in the dynamic tests, severe buckling did not occur, with the rail continuing with a primarily axial collapse until the full 250 mm of displacement had completed. The final shape of the three specimens tested is shown in Figure 157. It shows that all of the specimens had some degree of folding near the bottom clamps, with one of the specimens buckling slightly towards the camera.

The force-displacement and energy absorption data logged by the press computer and DAQ system is shown in Figure 158. The repeatability was very good for the first 100 mm before diverging slightly, though there was far less scatter than in the dynamic experiments. The oscillation in force seen in the dynamic results was also not observed.

These specimens folded well initially before becoming rather unstable. The forces and energy absorption were low due to the low strength and thin gauge of material. Parent metal failure was not observed, nor was spot weld failure.

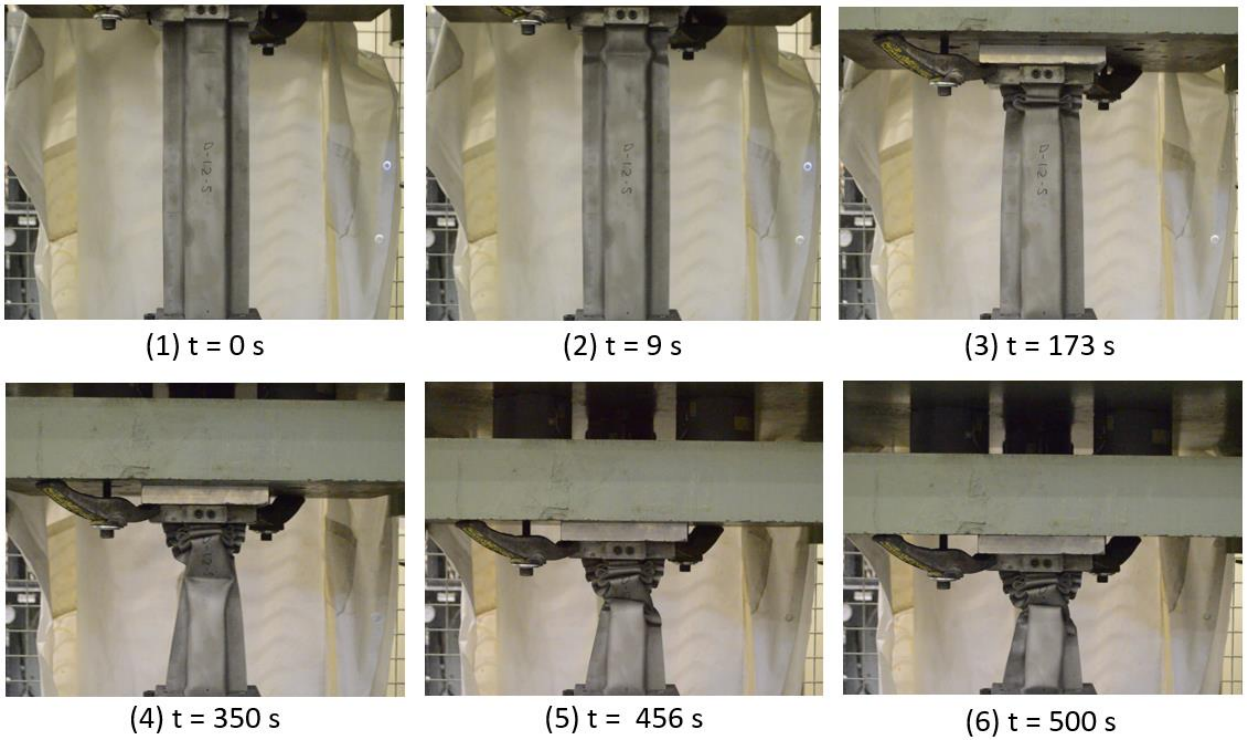

Figure 156: Quasi-static crush deformation of a 1.2 mm Ductibor® 500-AS specimen.

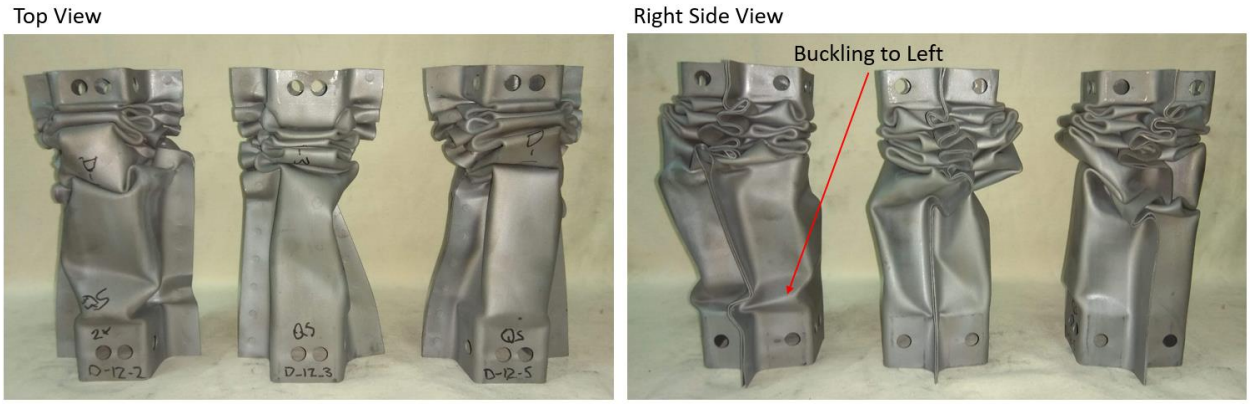

Figure 157: Final shape of three 1.2 mm Ductibor® 500-AS specimens after quasi-static crush.

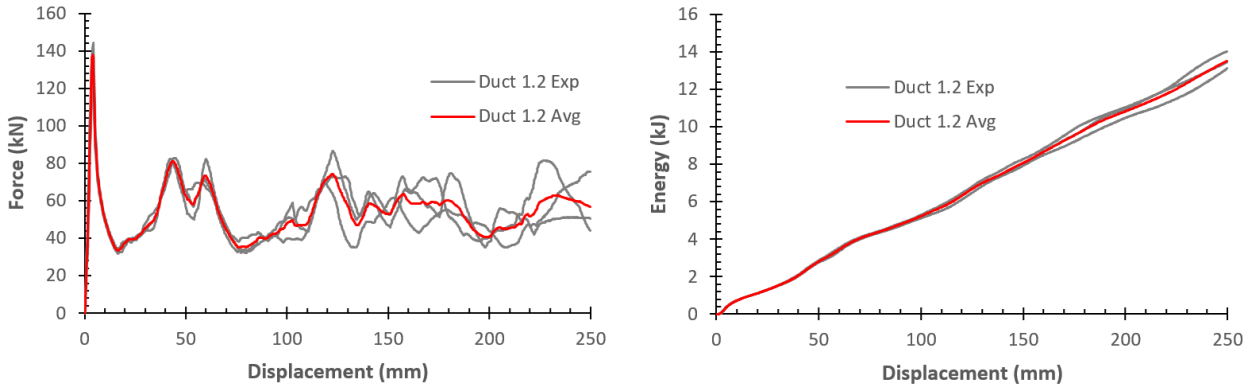

Figure 158: Quasi-static force-displacement and energy absorption data for 1.2 mm Ductibor® 500-AS specimens.

7.2.3 Quasi-Static Crush Response of 1.6 mm Ductibor® 500-AS Specimens

The quasi-static crush of a 1.6 mm monolithic crush rail specimen is shown in the still images of Figure 159. This rail initiated folding at the initiator and formed several successive folds in that location. Later in the test a fold also initiated at the top of the lower clamp. The deformed shape of the three specimens tested is shown in Figure 160. The first two specimens behaved similarly with progressive axial folding. The third specimen started out this way, but began forming unstable folds partway through the test and began to buckle to the side.

Figure 161 shows the load-displacement and energy absorption for these three parts. Once again, the first 125 mm of displacement is extremely repeatable as the first folds are formed. Afterwards, the load levels are still quite repeatable but there is more scatter than initially. There is far less scatter in the energy absorption curves than in the force-displacement curves. It appears that the specimens can get out of phase with each other and reach a certain force level at different displacements, but overall these forces average out to a similar energy absorption.

These specimens folded well and remained relatively stable throughout the experiment. With the thicker gauge material, the sustained crush force was higher than in the 1.2 mm monolithic specimens. Spot weld and parent metal failure were not observed.

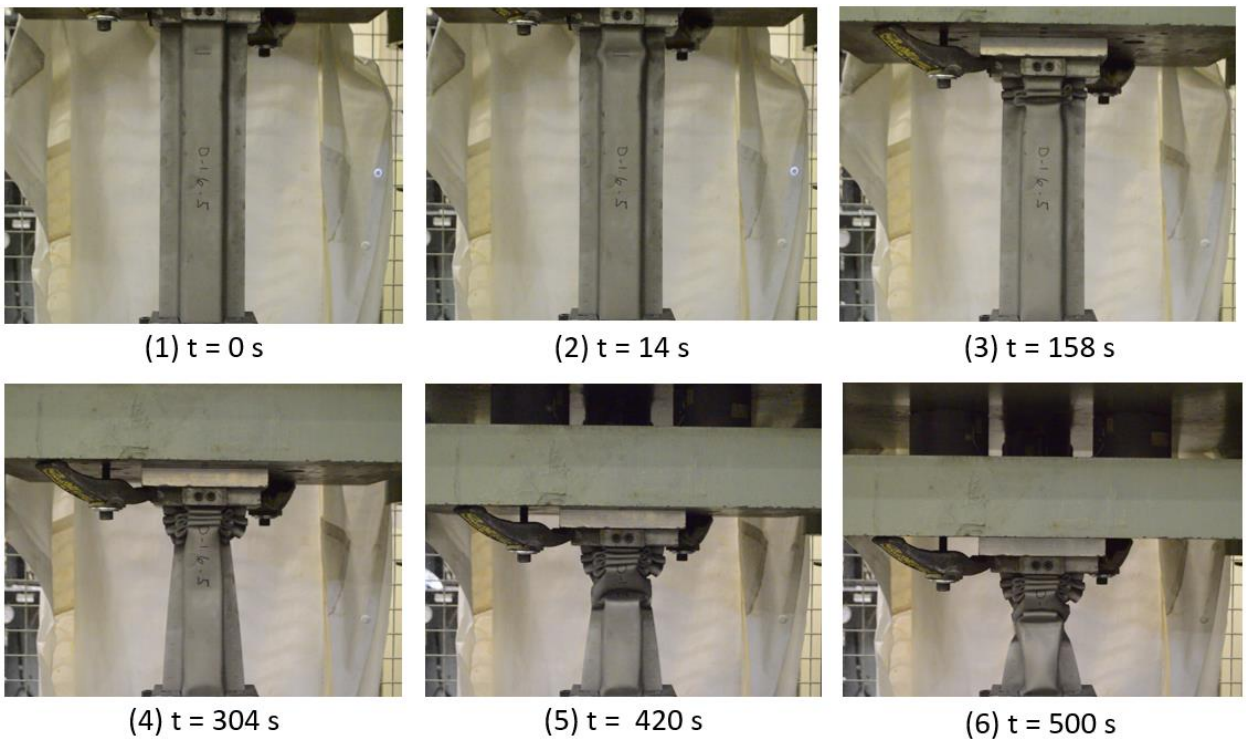

Figure 159: Quasi-static crush deformation of a 1.6 mm Ductibor® 500-AS specimen.

Figure 160: Final shape of three 1.6 mm Ductibor® 500-AS specimens after quasi-static crush.

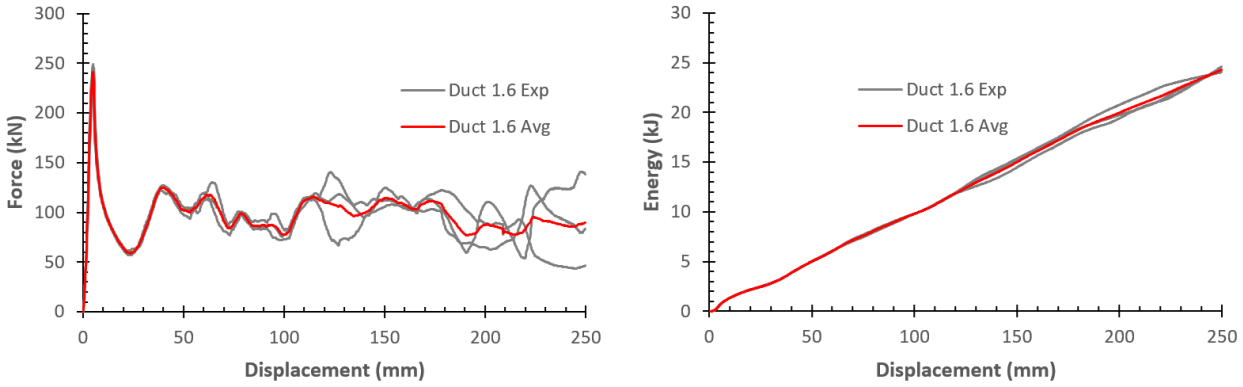

Figure 161: Quasi-static force-displacement and energy absorption data for 1.6 mm Ductibor® 500-AS specimens.

7.2.4 Quasi-Static Crush Response of 1.2 mm TWB Specimens

The still images in Figure 162 show the quasi-static crush test of a 1.2 mm TWB crush rail specimen. Folding initiated at the initiator dimple and formed several progressive folds in the soft zone. As the soft zone neared consolidation, an angled fold formed that pushed the hard zone over to the left, with one of the flanges buckling near the bottom. The remainder of the displacement caused folding and fracture in the top of the hard zone. Figure 163 shows the final deformed shape of the three specimens that were tested. Of these, the first one folded mostly axially, while the other two deflected slightly to the left and right respectively.

Figure 164 shows the load-displacement and energy absorption data from these tests. With the differing folding modes and the onset of fracture in the hard base material, there is a reasonable amount of scatter in the results beyond the first 50 mm of displacement.

As was observed dynamically, the hard section at the base of the rail prevented severe buckling and promoted full consolidation of the soft zone. After full consolidation of this soft zone, some folding occurred at the top of the hard zone. Fracture of the Usibor® 1500-AS parent metal occurred in these folds. Additionally in the second specimen the laser weld failed as the flange folded over. Minor spot weld failure was seen.

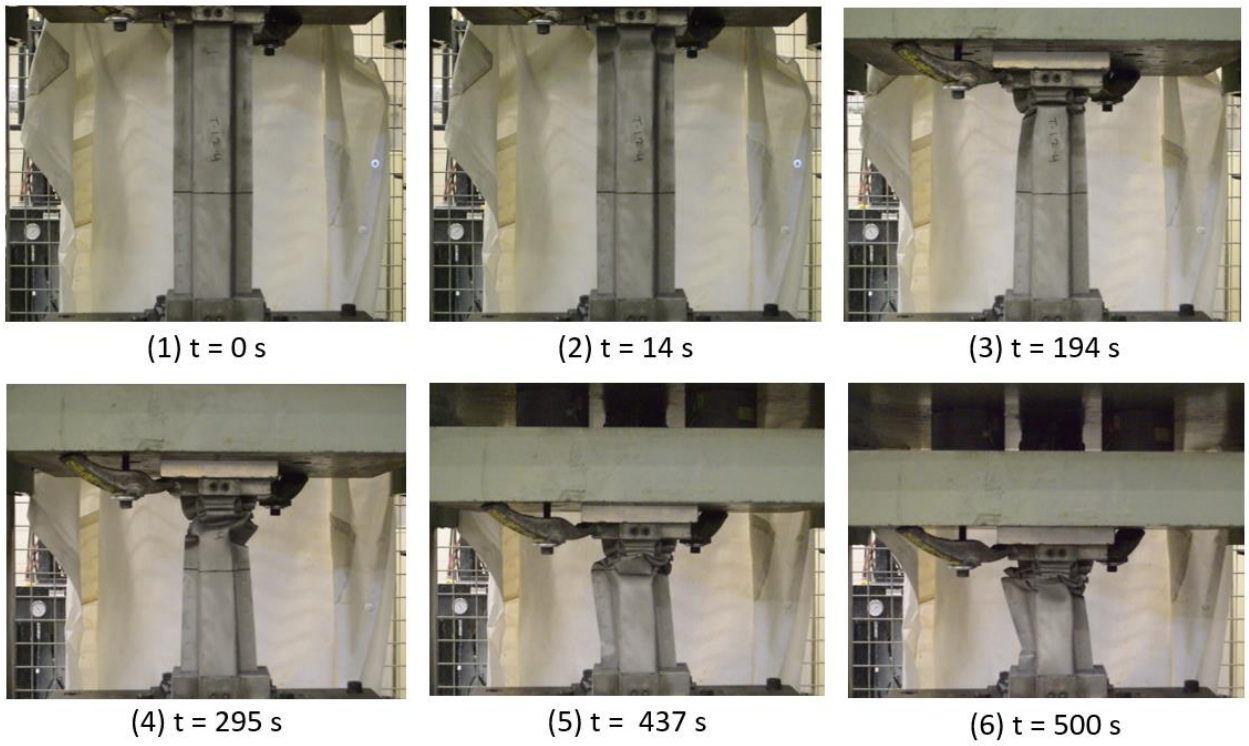

Figure 162: Quasi-static crush deformation of a 1.2 mm TWB specimen.

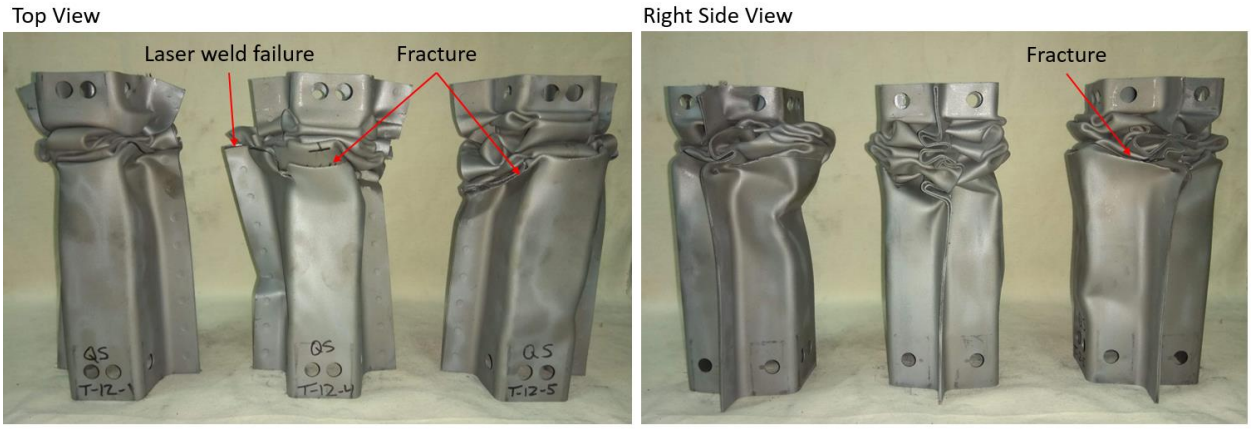

Figure 163: Final shape of three 1.2 mm TWB specimens after quasi-static crush.

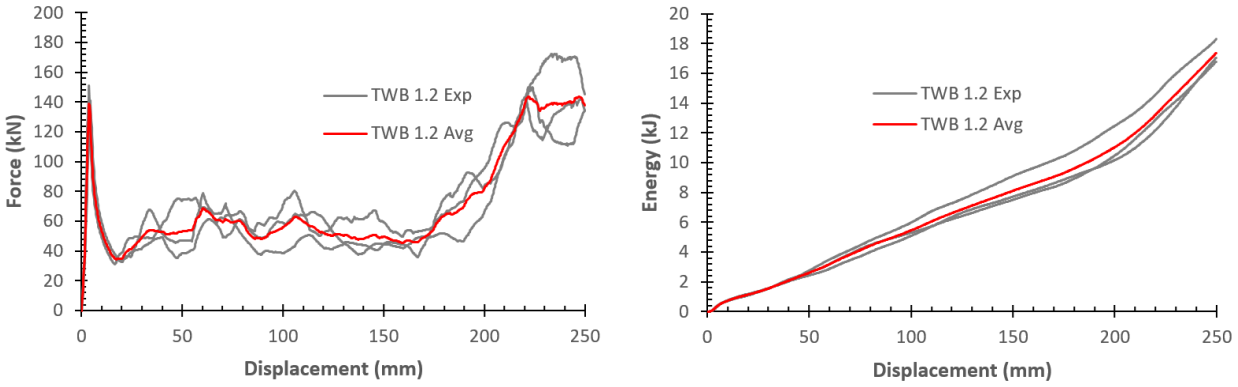

Figure 164: Quasi-static force-displacement and energy absorption data for 1.2 mm TWB specimens.

7.2.5 Quasi-Static Crush Response of 1.2/1.6 mm TWB Specimens

Figure 165 shows a multi-gauge 1.2/1.6 mm TWB undergoing quasi-static axial crush. In each of these specimens, the first fold initiated just above the transition between the hard and soft zones. This was in spite of forming fold initiators at the top of the soft zone as was done for all of the other conditions. Despite this different initiation location, the part still folded progressively, with each fold forming above the previous. When the soft zone had fully consolidated, it was forced into the top of the hard section, with more of it being pushed in between the two hard sides than was seen previously. This caused tight folds to form with some parent metal fracture. The deformed shape of the three specimens is shown in Figure 166. All three folded very similarly, with the same point of initiation and fold progression.

The load-displacement and energy absorption for the three tests is shown in Figure 167. The responses are extremely close for the first 100 mm, after which they diverge slightly. As loading of the hard zone initiates after soft zone consolidation, the curves converge again to virtually identical load paths before diverging again as the hard zone deforms and fractures. There is a relatively sudden increase of force as the soft zone runs into the top of the much stiffer hard zone, which may not be desirable in a crash event.

These multi-gauge TWBs have the largest difference in strength and stiffness between the hard and soft zones, which may be the reason for the fold initiation at the weld line. The offset between the mid plane of the two sheets of differing thickness will also induce a bending moment that may lower the initiation force at this weld line transition. The initiators were formed at the same time

as those used for dynamic tests, so they are not thought to be the cause. Fracture of the hard parent metal was observed, but spot weld failure was not.

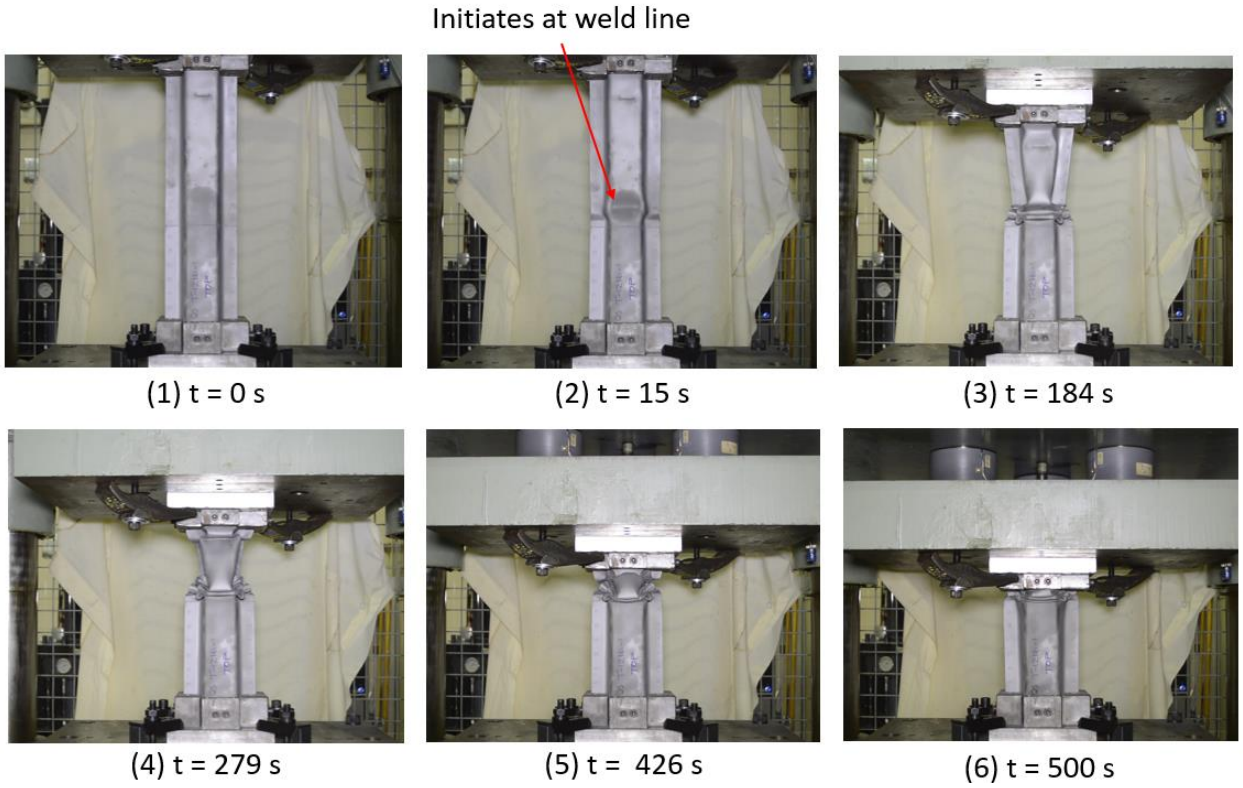

Figure 165: Quasi-static crush deformation of a 1.2/1.6 mm TWB specimen.

Figure 166: Final shape of three 1.2/1.6 mm TWB specimens after quasi-static crush.

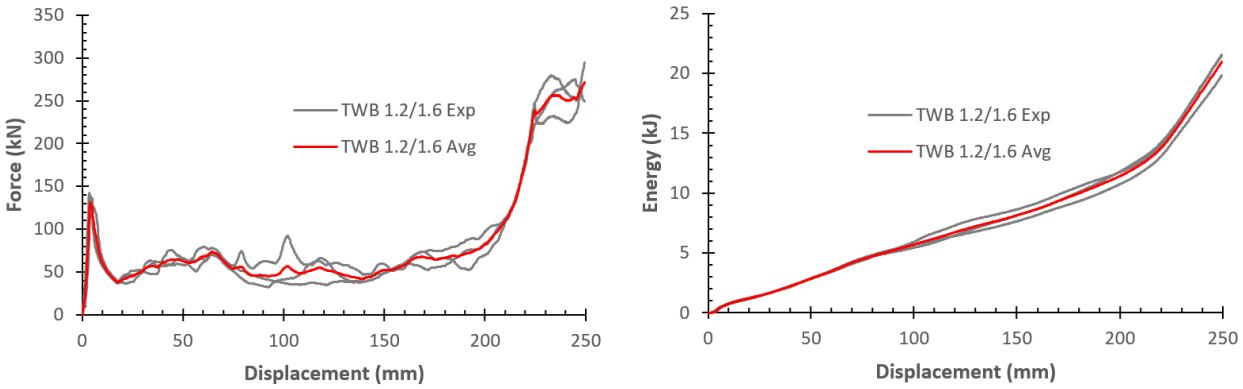

Figure 167: Quasi-static force-displacement and energy absorption data for 1.2/1.6 mm TWB specimens.

7.2.6 Quasi-Static Crush Response of 1.6 mm TWB Specimens

The still images in Figure 168 show the quasi-static axial crush progression of a 1.6 mm common gauge TWB. These rails folded well with folding initiating at the crush initiator and progressively moving down the length of the soft zone. When the soft zone had consolidated, an additional fold formed in the hard zone. Figure 169 shows that the three specimens tested behaved very similarly, with only one unusual fold in the first specimen.

Figure 170 shows the force-displacement and energy absorption data from these three specimens. The repeatability was excellent across these tests due to the very similar folding modes. When the hard zone begins to crush the force level increases dramatically, but the increase is not as sudden as for the multi-gauge TWBs.

The 250 mm displacement used in these tests pushed the specimens to a higher displacement than occurred in the dynamic tests, resulting in some fracture as the hard Usibor® 1500-AS formed a fold. Spot weld and laser weld failure were not observed.

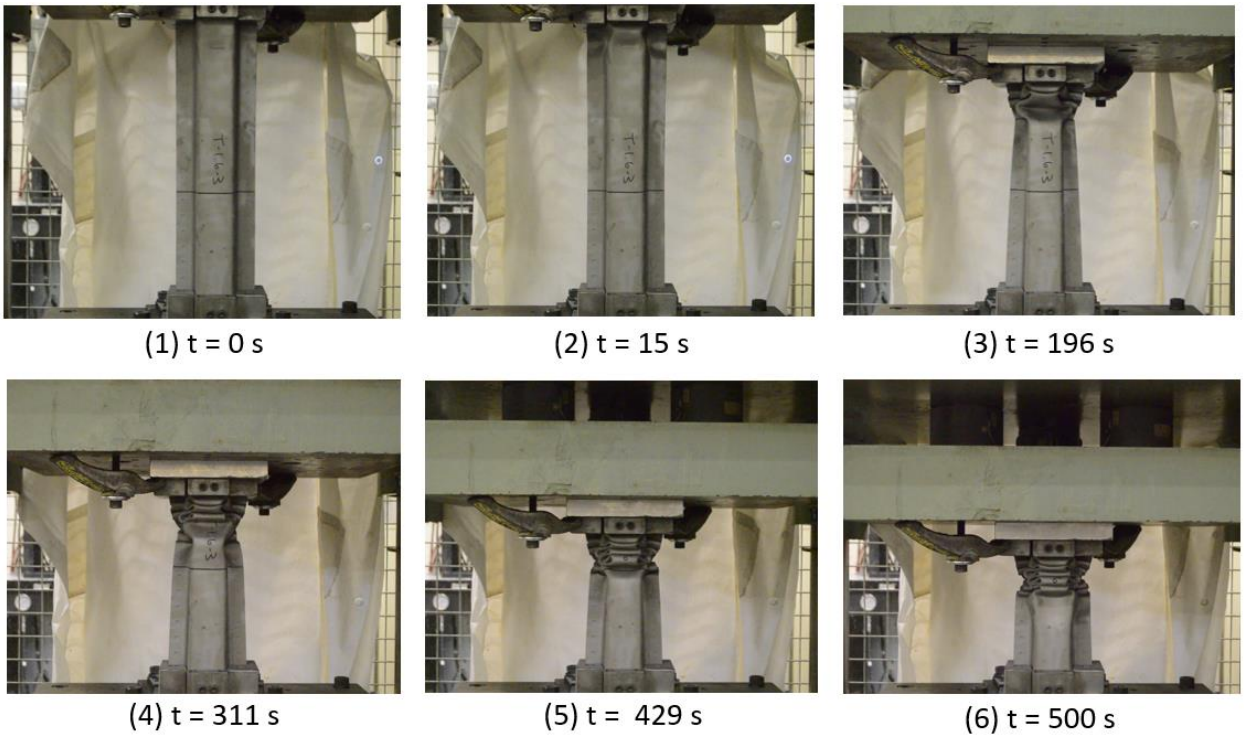

Figure 168: Quasi-static crush deformation of a 1.6 mm TWB specimen.

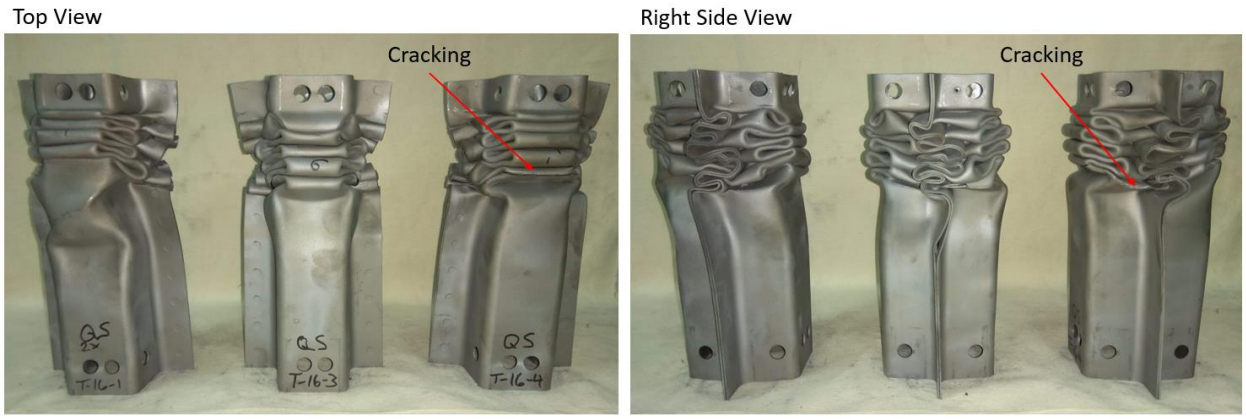

Figure 169: Final shape of three 1.6 mm TWB specimens after quasi-static crush.

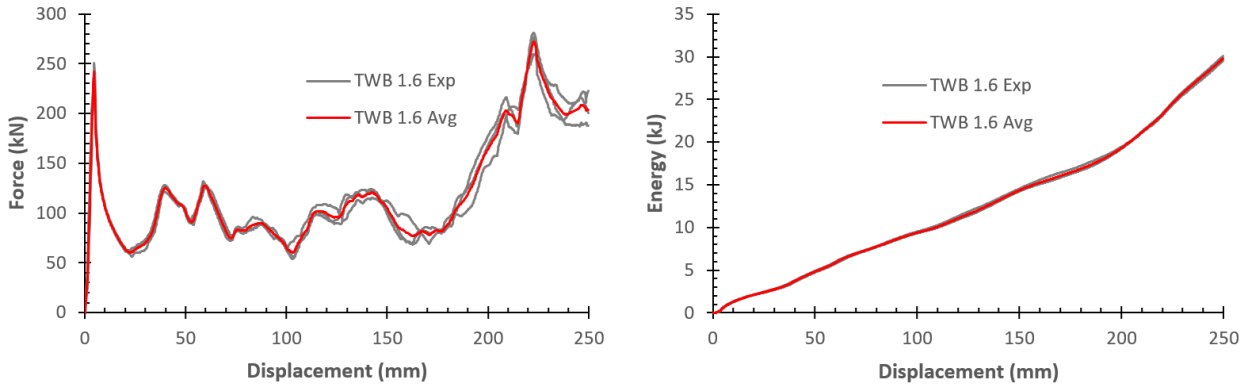

Figure 170: Quasi-static force-displacement and energy absorption data for 1.6 mm TWB specimens.

7.3 Axial Crush - Dynamic vs. Quasi-Static Comparison

The average force-displacement and energy absorption curves for each of the five material conditions tested dynamically and quasi-statically are compared in Figure 171. The dynamic tests are represented by solid lines, and the quasi-static tests by dashed lines. The initial peak forces and overall energy absorption of the different conditions are compared in Figure 172, and summarized in Table 9.

The initial peak forces are much lower in the quasi-static tests than dynamic. Generally the peak quasi-static load is about 50-60% of the dynamic peak. There is a great deal of oscillation in the dynamic data for the monolithic and common gauge TWB conditions, but it can still be seen that the load levels are lower in the quasi-static tests. This is shown more clearly in the plots of energy absorption, which shows that the dynamic tests consistently absorbed more energy. This can be largely attributed to the positive strain rate sensitivity that both Ductibor® 500-AS and Usibor® 1500-AS exhibit, as characterized by Abedini *et al.* [60] and Bardelcik *et al.* [64] and shown in Figure 94 and Figure 91.

The quasi-static specimens exhibited much more stable folding, with less buckling and spurious fold initiation. This is due in part to having the bosses at both ends of the specimen clamped in place. In dynamic tests that buckled, sometimes the top boss would slide across the face of the sled. A significant difference in folding behaviour was observed between the dynamic and quasi-static tests of TWB 1.2/1.6 specimens. In the dynamic tests these rails began folding at the crush initiators, whereas in the quasi-static tests the folding began in the soft zone just above the laser weld line. This was the only specimen type that exhibited this folding behaviour.

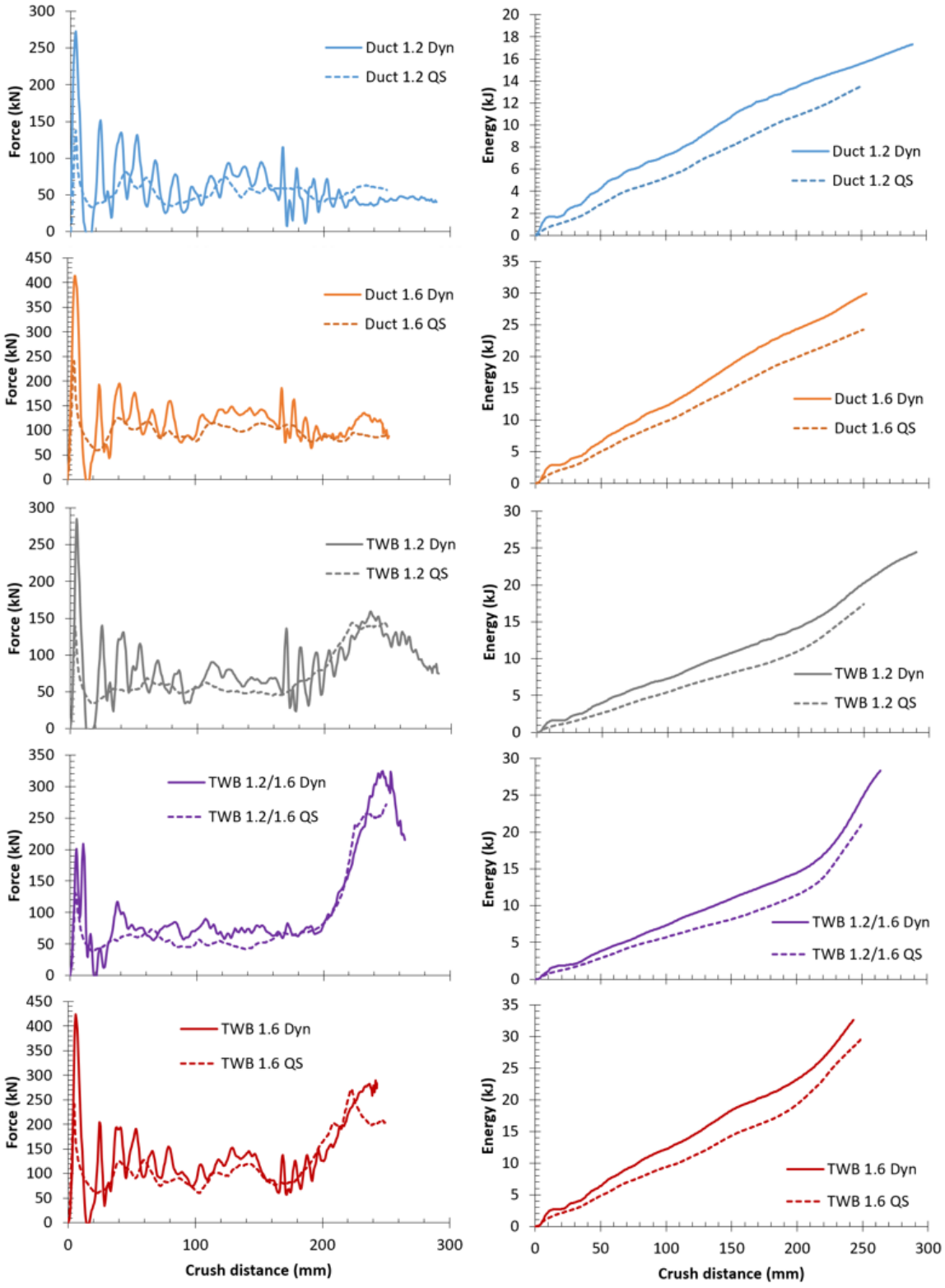

Figure 171: Comparison between dynamic and quasi-static force and energy absorption for each material condition.

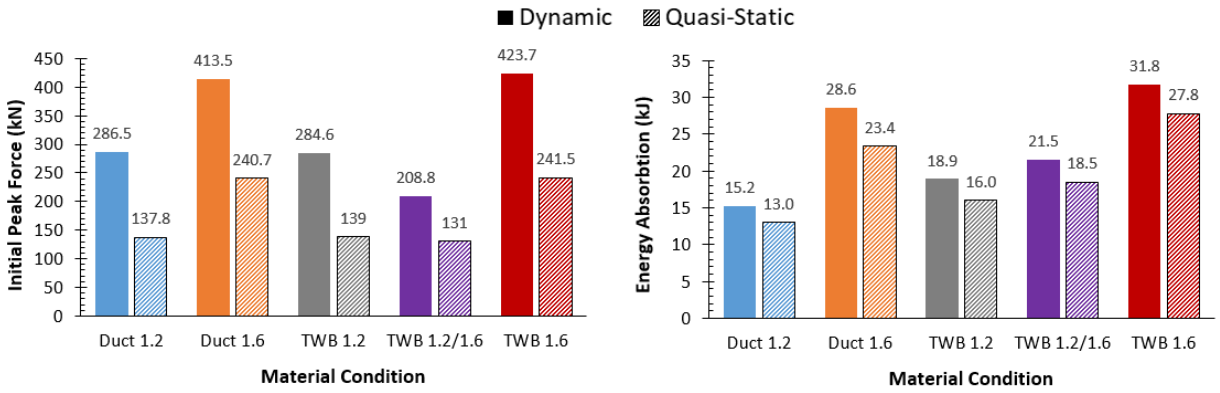

Figure 172: Comparison of initial peak force and energy absorption over the first 240 mm for the five material conditions of axial crush rails tested dynamically and quasi-statically.

Table 9: Summary of loads and energy absorption over the full crush distance in axial crush rails tested dynamically and quasi-statically.

Test Designation	Velocity	Initial Peak Force (kN)	Absorbed Energy (kJ)	Final Crush Distance (mm)	Average Crush Force (kN)
Duct 1.2	10.6 m/s	286.5	15.2	289	59.9
	0.5 mm/s	137.8	13.0	250	54.1
Duct 1.6	10.6 m/s	413.5	28.6	252	84.3
	0.5 mm/s	240.7	23.4	250	97.1
TWB 1.2	10.6 m/s	284.6	18.9	290	107.3
	0.5 mm/s	139.0	16.0	250	69.6
TWB 1.2/1.6	10.6 m/s	208.8	21.5	264	118.7
	0.5 mm/s	131.0	18.5	250	84.1
TWB 1.6	10.6 m/s	423.7	31.8	243	134.5
	0.5 mm/s	241.5	27.8	250	119.3

7.4 Axial Crush - Dynamic Models - Results and Comparison with Experiments

Figure 173 shows that the deformation behaviour predicted in the dynamic models is similar to what occurs in the experiments. The buckling tendency for the Duct 1.2 specimens is captured, as well as the asymmetric folding in the Duct 1.6 case. In the TWB parts it is more difficult to match the fold behaviour due to the prevalence of fracture in both the model and the experiment, although the extent of fracture is predicted relatively well. There is no fracture predicted in the Ductibor® 500-AS material, but some cracking occurs in the tight folds of the Usibor® 1500-AS. The model

also accurately predicts the failure of some spot weld elements in the Usibor® 1500-AS zone. The partial erosion in the model is analogous to the partial weld nugget pullout that is observed in some of the folds.

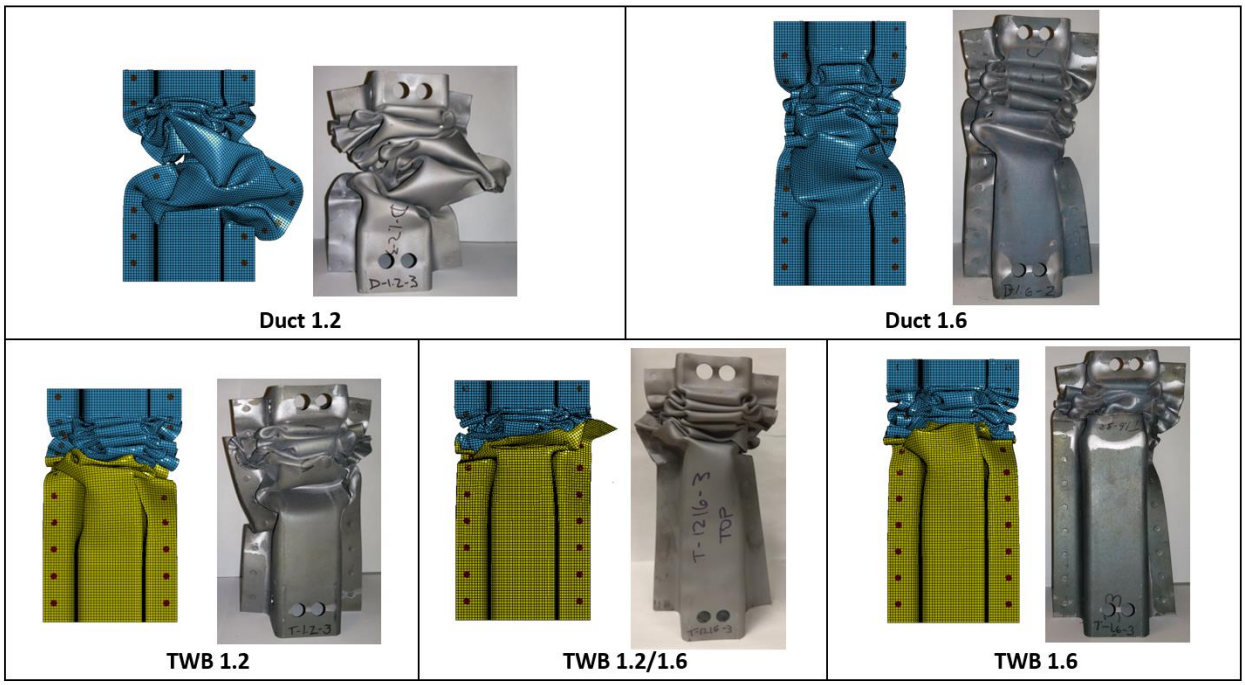

Figure 173: Comparison of deformation modes in dynamic axial crush experiments and models for each material condition.

The predicted force-displacement and energy absorption curves from the dynamic axial crush model are compared to the average experimental results in Figure 174 below. The initial peak forces are under-predicted by the model, and the oscillation measured in the experiments is not predicted numerically. This oscillation may be ringing associated with the barrier wall load cell pack mass that is not captured in the model. The overall force profile is predicted reasonably well, and the predicted and measured energy absorptions are very close.

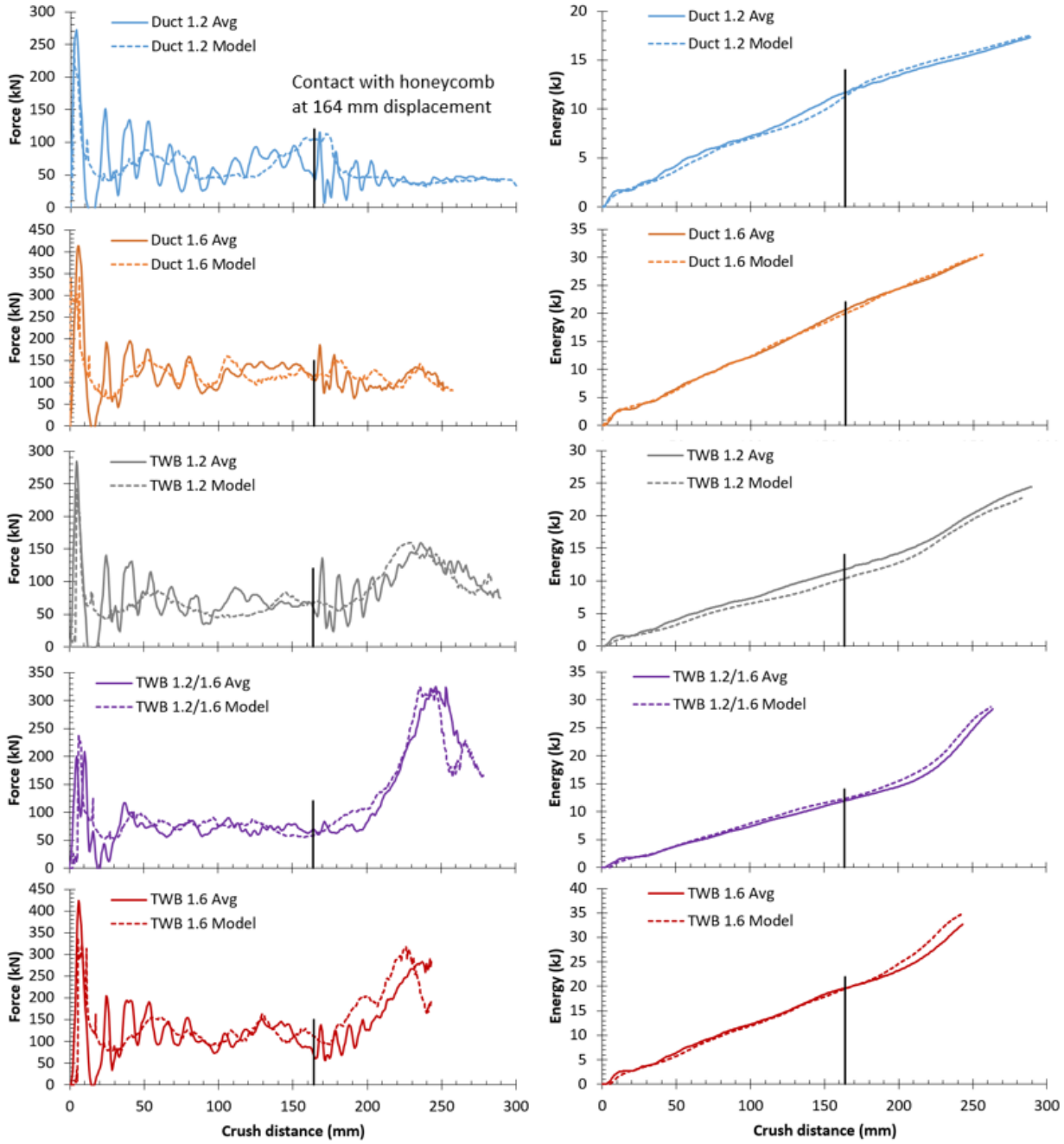

Figure 174: Comparison between dynamic axial crush experiments and models for force-displacement and energy absorption.

7.5 Axial Crush - Quasi-Static Models - Results and Comparison with Experiments

Figure 175 compares the deformation behaviour in the quasi-static models to the experiments. The model over predicts buckling in the Duct 1.2 specimens, but otherwise predicts the general folding a fracture behaviour quite well. In the model, the TWB 1.2/1.6 specimen began folding at the crush initiator, whereas in the quasi-static experiments the folds initiated near the laser weld line. As was discussed in Section 7.3, the quasi-static TWB 1.2/1.6 tests were the only material condition in which fold initiation occurred at the weld line.

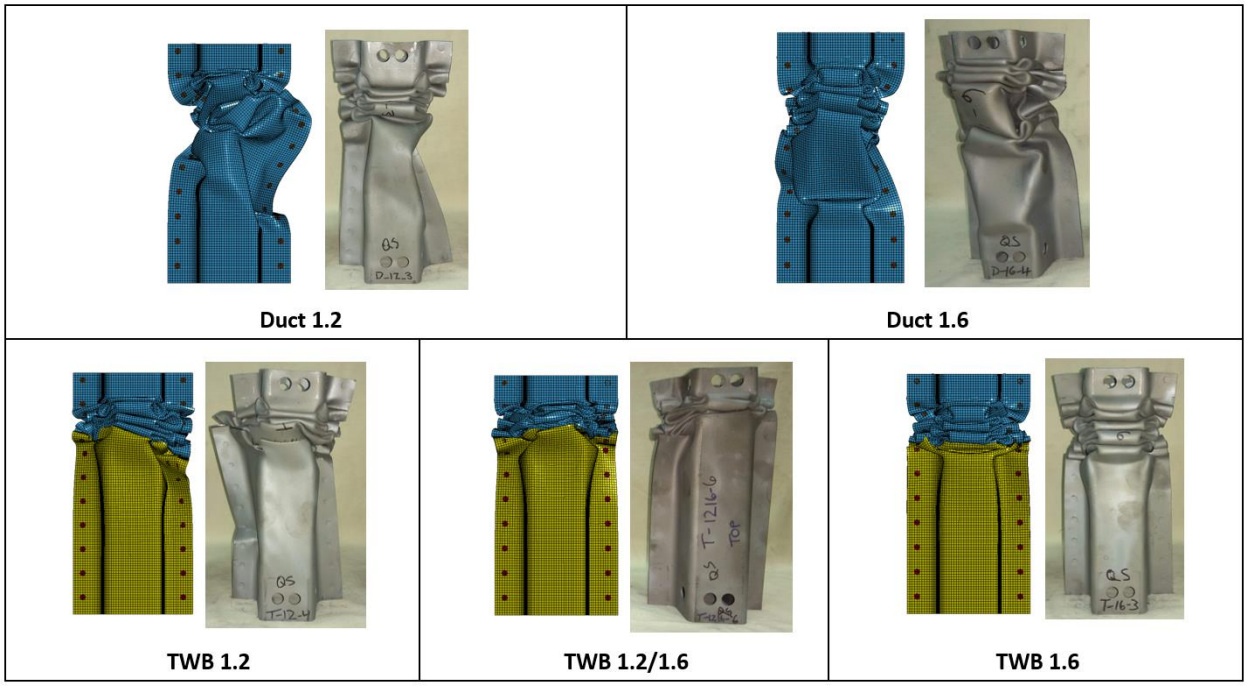

Figure 175: Comparison of deformation modes in quasi-static axial crush experiments and models for each material condition.

The force-displacement and energy absorption curves in Figure 176 show that the initial peak force is over predicted by the model. After this initial peak, the agreement between the model and experiment is very good for all of the material conditions.

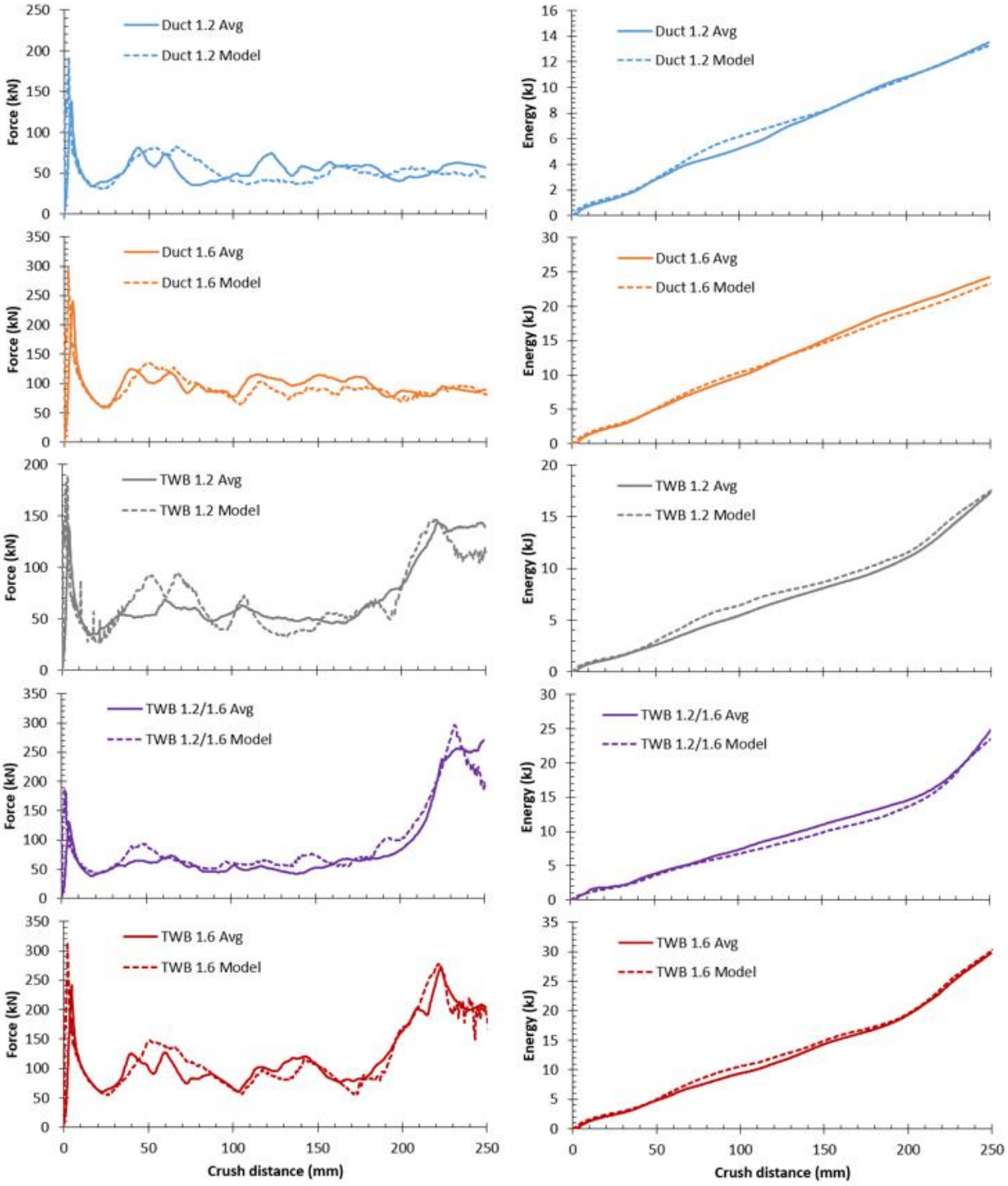

Figure 176: Comparison between quasi-static experimental force and energy absorption compared to predictions from the numerical model.

8.0 Substitution of Ductibor® 500-AS within the Demonstrator Structure Crush Tip

As a first step towards implementing hot stamped TWBs in a lightweight demonstrator of the SUV front side frame, the substitution of hot stamped Ductibor® 500-AS into the frontal crush region of the SUV side frame was examined as part of the current thesis. This chapter presents the results of that substitution study which was comprised primarily of a numerical study of the impact behavior of the crush tip of the side frame when fabricated using hot stamped Ductibor® 500-AS. Prior to showing the simulation results, a series of baseline experiments and models of the impact behavior of the current JAC590R crush tip are presented.

8.1 Dynamic Crush Experiment Results

In the baseline side frame structure (Figure 19), three distinct crash responses or behaviors can be observed, corresponding to: (i) progressive folding and energy absorption within the axial crush zone (referred to herein as the crush tip); (ii) buckling and energy absorption within the mid-section (axial buckling zone); and (iii) almost rigid response of the intrusion resistant s-rail zone. In order to decouple these three behaviors, the current work focuses exclusively on the response of the crush tip region. For these tests, a total of six left hand (LH) and six right hand (RH) crush tip specimens were extracted from front side frame assemblies and tested, as described in Section 4.3. Figure 177 shows the deformation of a LH crush tip specimen. The first frame shows the point at which the plywood sheet on the face of the crash sled touches the end of the specimen, denoted as time zero. The second frame is taken 3.2 ms later, showing the beginning of the first fold forming in the impacted part. The third and fourth frames show that the crush tip continues to progressively fold and collapse onto itself as it absorbs energy. The fifth frame shows the maximum crush displacement at 54.6 ms, at which point the specimen has absorbed all of the sled energy and has brought it to a stop. This occurred prior to the sled contacting the honeycomb arrestors, so all of the sled energy was absorbed by the crush tip. The sled has just 24 kJ of kinetic energy in these tests conducted at 7.5 m/s, half as much energy as the 48 kJ in the axial crush tests of TWBs described in Chapter 7.0 that were conducted at 10.6 m/s.

The deformed shape of the six LH specimens is shown in Figure 178. All of the specimens deformed in a very repeatable manner, which was expected since these are mass production parts.

The impacted end of the crush tips cut into the plywood, transferring some of the wood to the end of the specimen when the sled rebounded after the test. All of the specimens folded in a controlled manner, absorbing the crash energy in a repeatable fashion. The occasional spot weld failure was observed, but there was no unzipping of multiple welds.

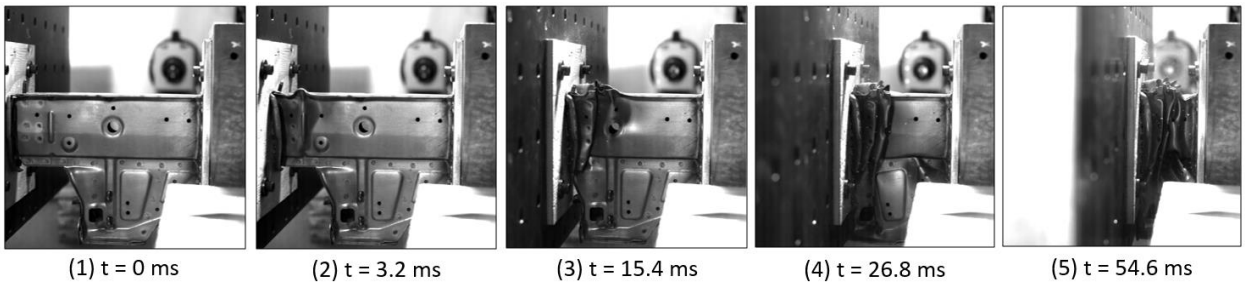

Figure 177: Deformation of the left hand (LH) baseline commercial crush tip in dynamic crush.

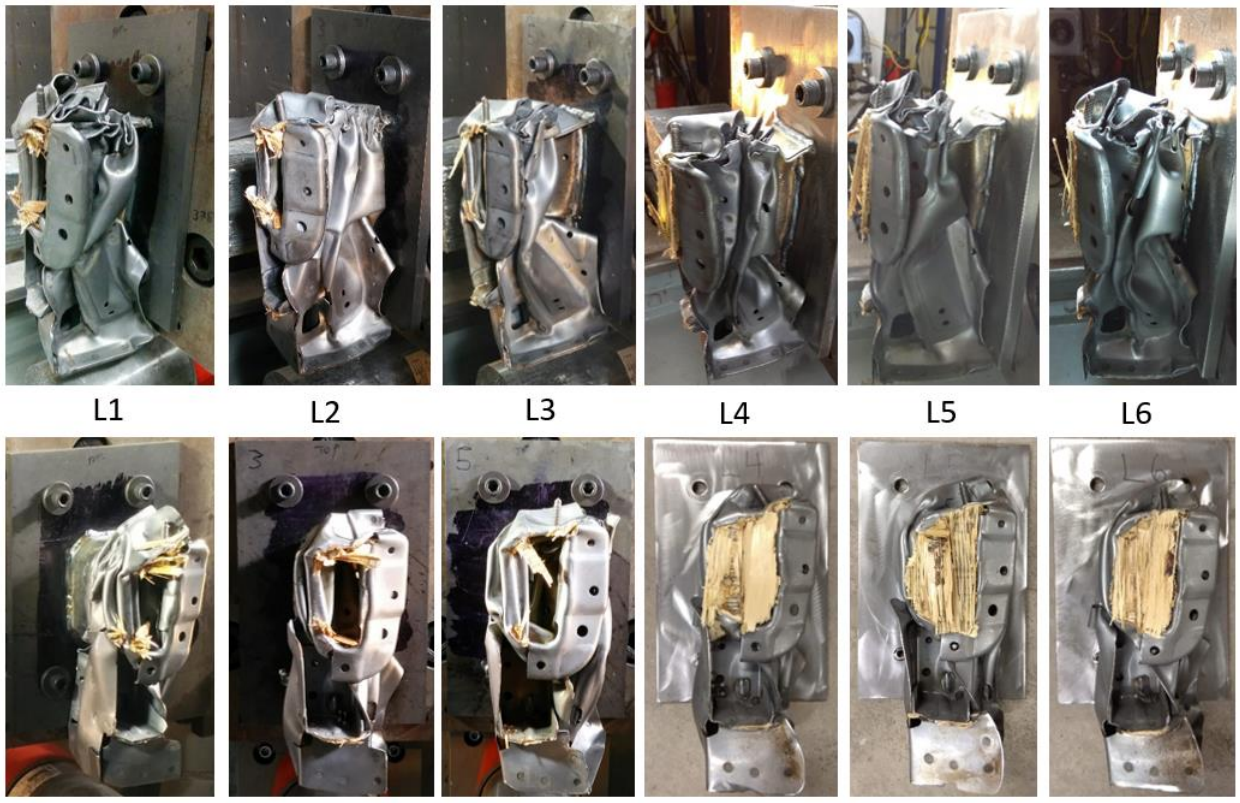

Figure 178: Deformed left hand (LH) baseline commercial crush tips after dynamic crush.

The load-displacement and energy absorption results from five of these six tests are shown in Figure 179. The data from the L3 test was not recorded due to a data acquisition error. In these plots, the five grey lines represent the recorded data from each experiment, and the red line is the

average of these experiments. The scatter is shown to be very low, which was expected based on the similar folding performance that was observed. The force reaches an initial peak of 119.5 kN, then reduces to below 50 kN before increasing again and oscillating between 80 and 100 kN as folds form. After 200 mm of displacement, the part begins to consolidate as it fully collapses towards the welded base plate. With this consolidation, the force increases to a peak of 176 kN, however this is the result of the consolidation and not indicative of the true crush performance in the full rail. With the sled being stopped by the specimen prior to honeycomb contact, it absorbed the full sled energy of 23.74 kJ.

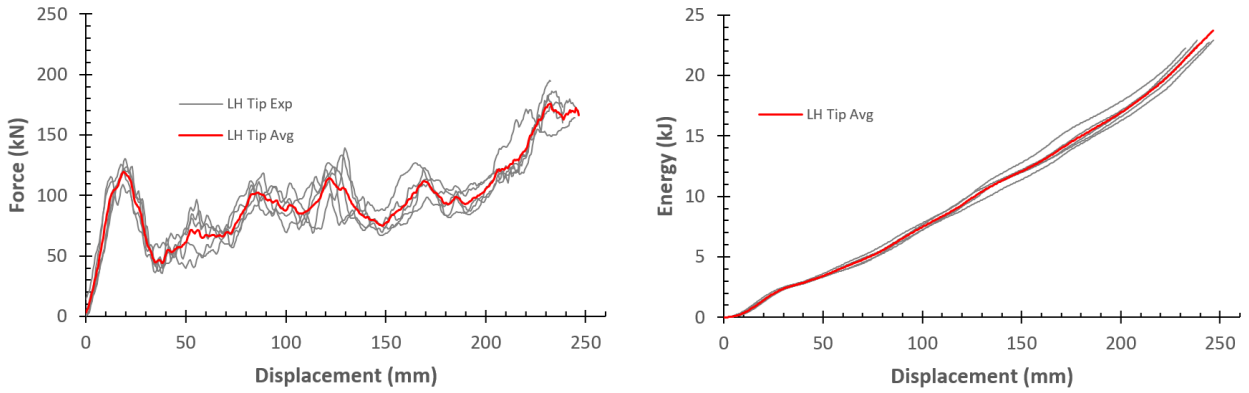

Figure 179: Force-displacement and energy absorption results from five dynamic crush experiments on LH baseline commercial crush tips.

High speed video frames from a RH crush tip specimen are shown in Figure 180. This video is shot from the opposite side compared to the LH parts, thereby showing the same features on the mirror image part. These parts folded in the same way as the LH parts, resulting in the deformed parts shown in Figure 181. These were also very repeatable with a similar fold pattern in each of the specimens, and plywood embedded in the end of the rail.

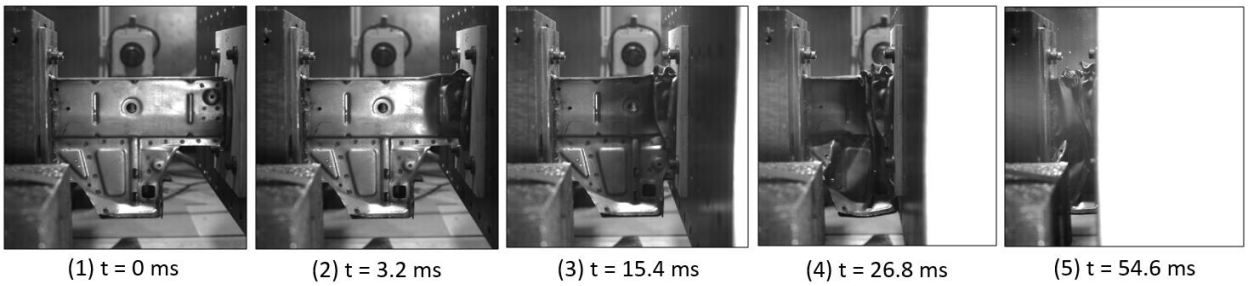

Figure 180: Deformation of the right hand (RH) baseline commercial crush tip in dynamic crush.

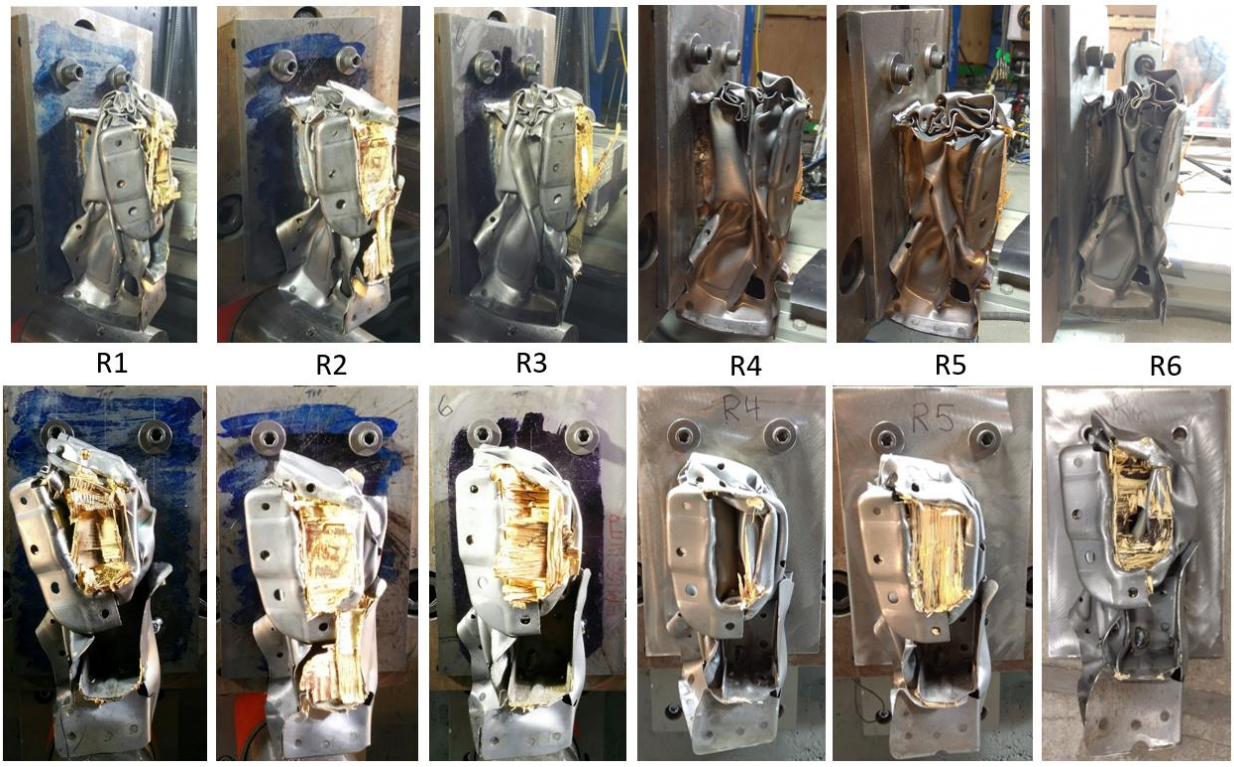

Figure 181: Deformed right hand (RH) baseline commercial crush tips after dynamic crush.

The load-displacement and energy absorption results for the six RH parts is shown in Figure 182. The performance is very similar to the LH rails, with an initial peak of 110.0 kN, reduction to 50 kN, and oscillation between 80 and 100 kN. Like the LH specimens, there is very little scatter in this data. As the rail consolidates it reaches an eventual peak of 171.5 kN, and absorbs 23.75 kJ of energy as it stops the sled. The slight discrepancy in energy absorption despite both tests stopping the sled can be attributed to the sled having slightly different speeds in each of the tests due to the nature of the firing mechanism.

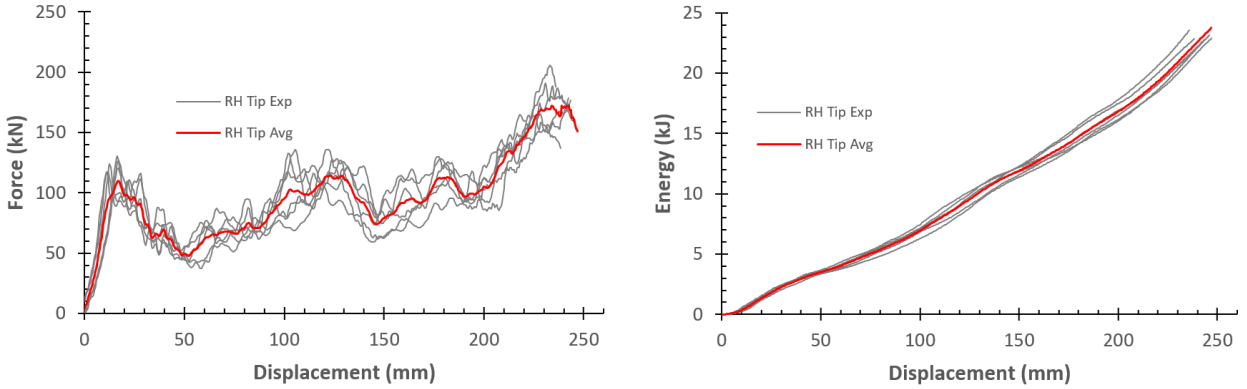

Figure 182: Force-displacement and energy absorption results from six dynamic crush experiments on RH baseline commercial crush tips.

Figure 183 compares the average experimental force-displacement and energy absorption of the LH and RH crush tips. As was discussed previously, these parts performed very similarly as they are largely a mirror image of each other. The force profile is quite close together, and the energy absorption curves lie on top of each other. The energy absorption and loads are summarized in Table 10.

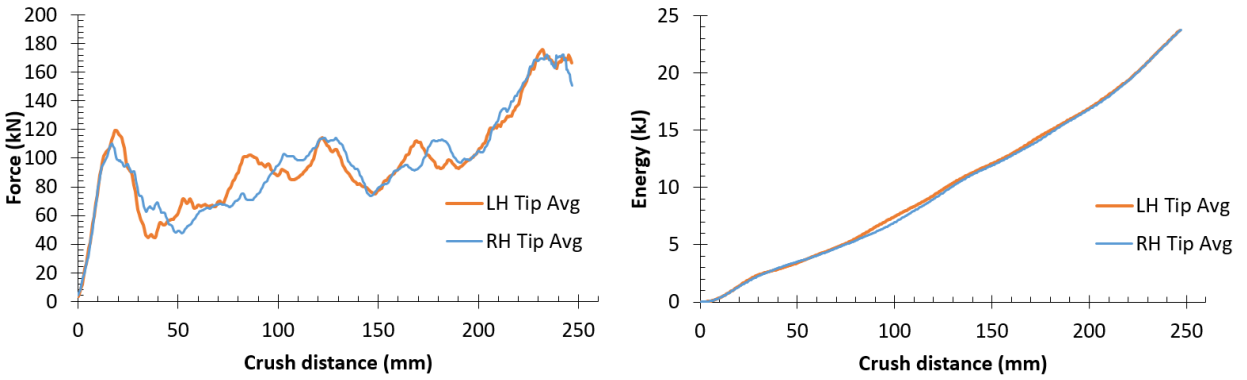

Figure 183: Experimental force-displacement and energy absorption comparison between LH and RH baseline crush tips.

Table 10: Summary of loads and energy absorption over the first 175 mm of crush in the baseline crush tip experiments.

Test Designation	Velocity (m/s)	Initial Peak Force (kN)	Absorbed Energy (kJ)	Final Crush Distance (mm)	Average Crush Force (kN)
LH Crush Tip	7.5	119.5	14.5	246.5	82.8
RH Crush Tip		110.0	14.2	247.0	81.1

In Figure 184 the average experimental force and energy absorption of the LH crush tip are compared to those of the baseline demonstrator structure discussed in Chapter 2.0. The results are similar for the formation of the first fold, after which they follow similar profiles but differ somewhat in magnitude. The average crush force over the first 100 mm of displacement in the LH crush tip was 74.6 kN, 17.7% lower than the 90.6 kN average found over the same displacement in the baseline demonstrator structure tests (Table 2). The divergence in crush force beyond this displacement is expected due to the large difference in boundary conditions between the two tests. In the baseline demonstrator structure experiments, lateral buckling occurs that changes the folding mode, whereas in the baseline crush tip experiments the crush is mostly axial. There may also be a strain rate effect, with the crush tips being tested at about half the speed of the baseline demonstrator structures.

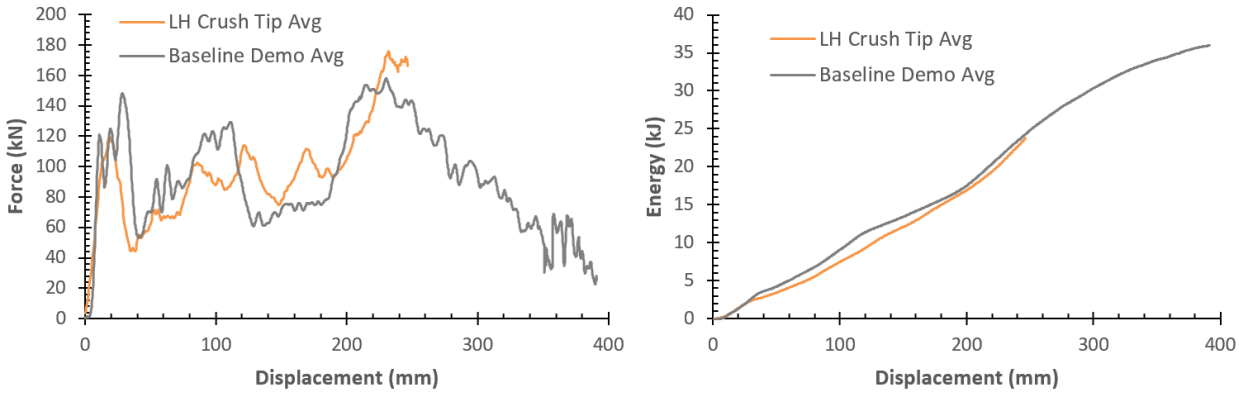

Figure 184: Comparison of force-displacement and energy absorption between baseline crush tip experiments and the larger baseline demonstrator structures tested in Section 0.

8.2 Numerical Model Results of Baseline Commercial Crush Tip

The force versus displacement and energy absorption predictions are compared to the experimental results in Figure 185. The model matches very closely with the experiments both for force-displacement and energy absorption in the first 175 mm of deformation. Beyond this point, the forces predicted in the model are higher than what occurred experimentally as the crush tip consolidated against the backing plate.

Since the backing plate is only used to facilitate testing of this short section, the loads that are of real interest occur in the first 175 mm, before there is any interaction with the backing plate. At this 175 mm displacement point, the LH rail had absorbed 14.5 kJ of energy, compared to the

model prediction of 14.8 kJ. At the same point the RH rail had absorbed 14.2 kJ, with a prediction of 14.4 kJ.

Figure 186 compares the folding behaviour predicted by the LH crush tip model to the folds that formed in the dynamic axial crush tip experiments. The video recorded by the high speed cameras was stepped through and six frames were extracted at the same times as the model. The initiation and formation of the first fold is predicted well by the model. The subsequent folds form somewhat more tightly in the experiment than was predicted by the model, but the general folding mode is similar. This result validates that the numerical model is an accurate predictor of the folding performance of the axial crush tip of the baseline front side frames.

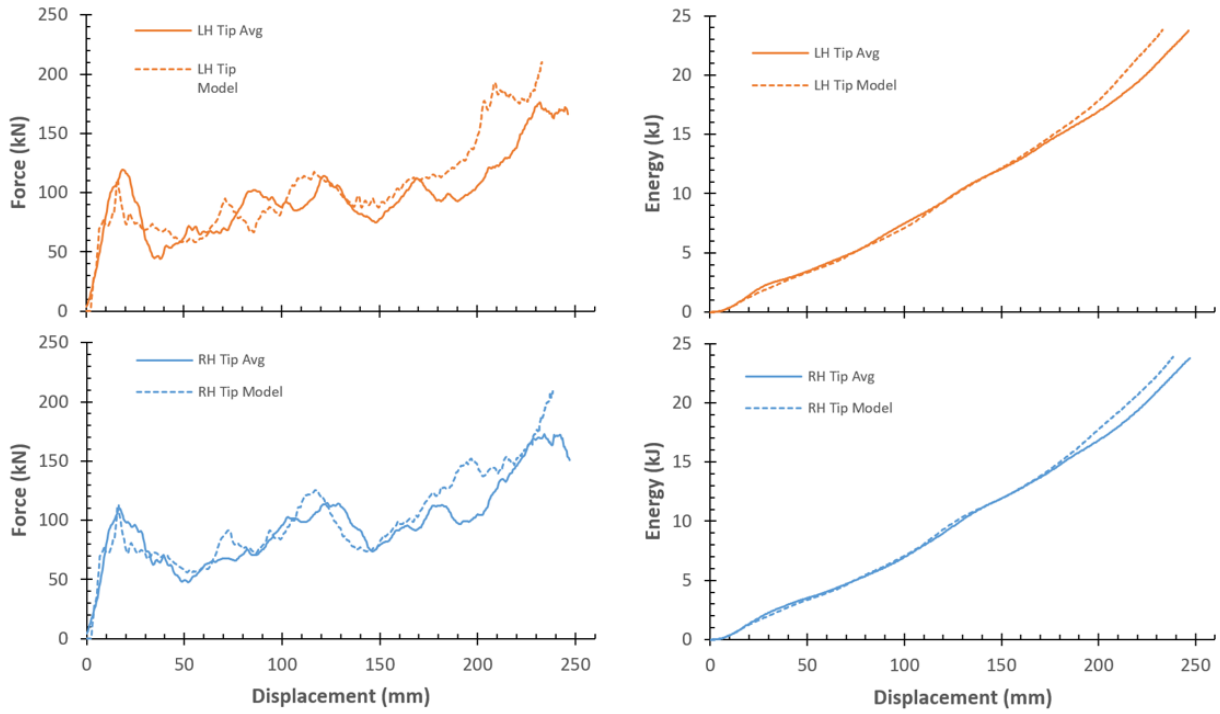

Figure 185: Comparison of experimental and numerical force-displacement and energy absorption for LH and RH baseline crush tips.

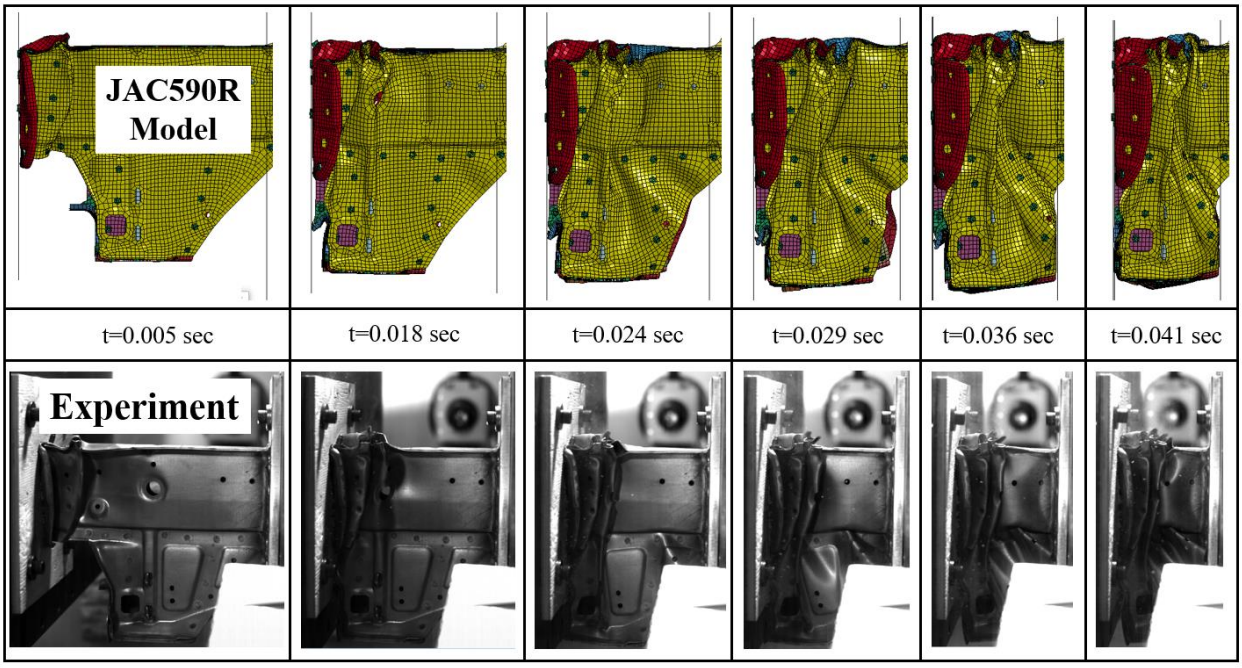

Figure 186: Comparison of folding behaviour predicted by the numerical model to the high speed video from the experiment in a LH baseline crush tip.

8.3 Simulation of Ductibor® 500-AS Crush Tip

The previous section has served to validate that the numerical model of the JAC590R crush tip, based on the full vehicle model provided by Honda, matched very closely to the experimentally measured forces and energy absorption. This section presents the application of this model to investigate the substitution of hot stamped materials to replace the lower strength steels used in current production.

Both the experiments and the model showed that the crush tip is designed to fold and collapse on itself in an axial crush mode; therefore a high degree of ductility is required. It was shown in Chapter 7.0 that Ductibor® 500-AS performs well in axial crush applications, so it was believed to be an ideal candidate as a ductile hot stamped substitute for JAC590R. With the existing JAC590R steel having a strength similar to that of Ductibor® 500-AS, this substitution will not allow for weight savings through reduced gauge thickness. What it does enable is the potential use of a larger hot stamped TWB that also incorporates Usibor® 1500-AS, for example in the anti-intrusion s-rail region of the side frame, that would allow for gauge reduction and mass savings.

To investigate the performance of Ductibor® 500-AS in this crush tip, the validated JAC590R crush tip numerical model was used. The Ductibor® 500-AS was substituted into the three main

parts of the crush tip on each side of the rail, as shown in Figure 187. As described in Section 5.2, to account for the 25 micron thick coating on each side of the Ductibor® 500-AS sheet, the 1.4 mm and 1.6 mm section thicknesses in the material model were reduced by 50 microns to 1.35 mm and 1.55 mm respectively. The smaller brackets and reinforcements were left as JAC590R since the high cost of hot stamping tools and processing made it unlikely that such small parts would be hot stamped.

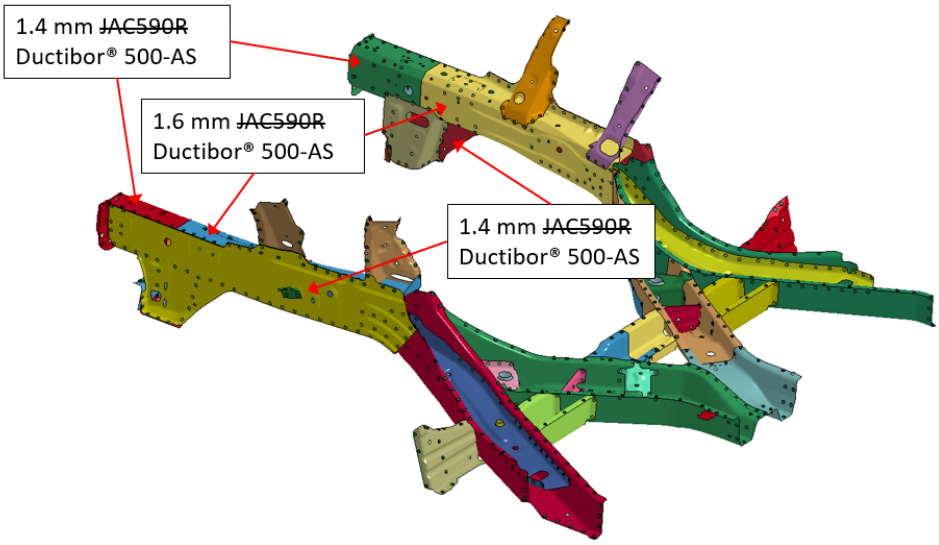

Figure 187: Front side frames with Ductibor® 500-AS substituted for JAC590R in axial crush tip.

The predicted force-displacement and energy absorption for the Ductibor® 500-AS crush tip are compared to the baseline crush tip simulation and the baseline crush tip experiments in Figure 188. The two simulation results are very similar, following almost identical load profiles and energy absorptions as they crush. Figure 189 compares the folding behaviour of the two materials in simulation at six intervals through the crush of the LH crush tip. The folding is very similar in the two simulations, with the main folds forming in the same places and at the same times. One difference is that the red bracket on the front of the rail does not fold over as far in the Ductibor® 500-AS model. The RH crush tip exhibits almost identical folding behavior between the JAC590R and Ductibor® 500-AS simulations, so its folding behaviour is not shown here for brevity.

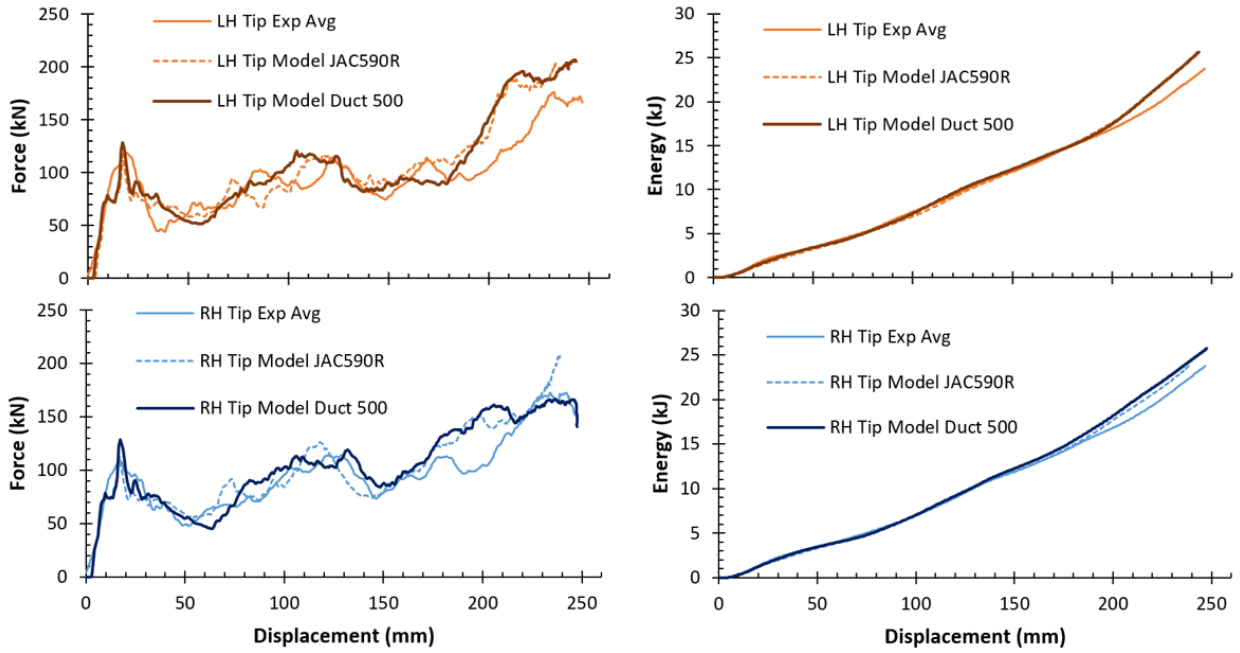

Figure 188: Numerical prediction for force-displacement and energy absorption with Ductibor® 500-AS substituted for the baseline JAC590R in the crush tip.

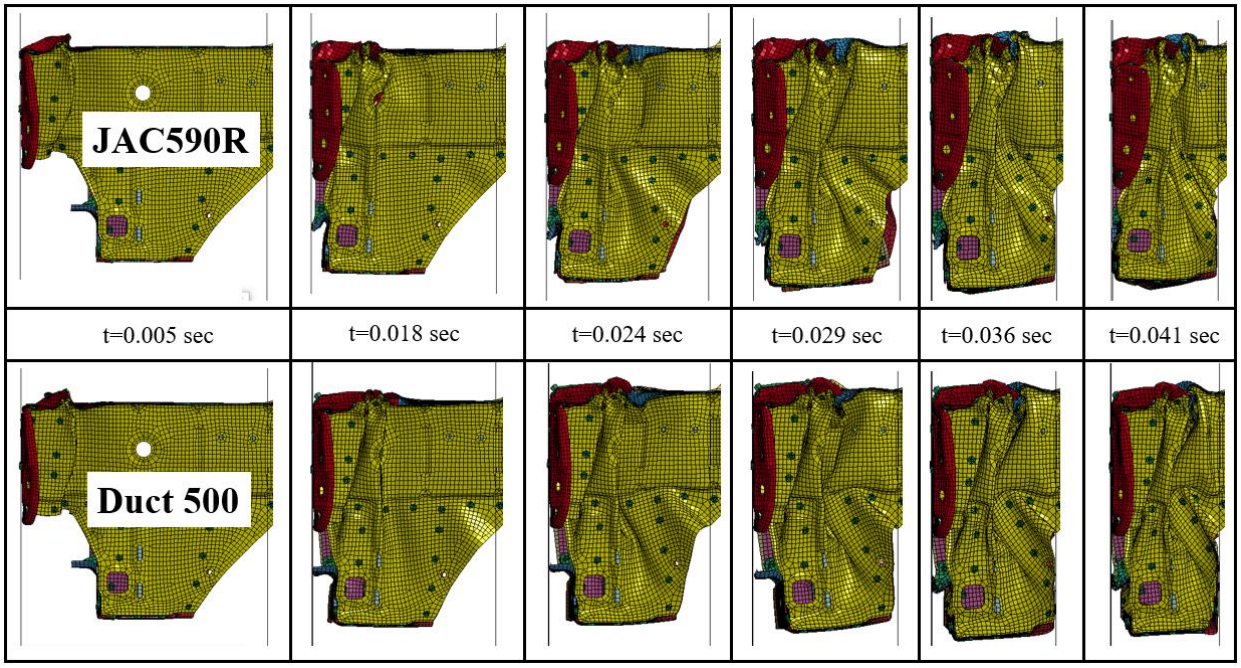

Figure 189: Comparison of folding modes predicted for the baseline JAC590R and the hot stamped Ductibor® 500-AS in the LH crush tip.

These results indicate that Ductibor® 500-AS can be successfully substituted into an existing crush structure made from JAC590R with matching folding and energy absorption performance. This creates the opportunity for use of hot stamped tailor-welded blanks in frontal crush structures, with the ductile Ductibor® 500-AS in the crush zone, and ultra-high strength Usibor® 1500-AS in the intrusion resistance zone. No weight savings are anticipated with a transition from JAC590R to Ductibor® 500-AS, but the ultra-high strength Usibor® 1500-AS has significant lightweighting potential. In this manner, the use of high ductility Ductibor® 500-AS serves to enable the use of higher strength Usibor® 1500-AS within TWBs to fabricate frontal crash structural components. The use of TWBs also has a potential part consolidation benefit, reducing the number of spot welds needed in the assembly.

9.0 Discussion, Conclusions, Recommendations

9.1 Discussion

9.1.1 Axial Crush Response of Ductibor® 500-AS and TWBs

Through this work, the crash performance of crush members made from monolithic Ductibor® 500-AS and from TWBs comprising Ductibor® 500-AS and Usibor® 1500-AS were investigated. In general, Ductibor® 500-AS exhibits good fracture resistance during axial crush and side impact for the sheet thickness and structural geometries considered in the current work.

The initial peak force for the five TWB crush rail conditions are compared to the baseline crush tip in Figure 190. The many crush initiators formed into the baseline crush tip contributed to it having a much lower initial peak force of just 119.5 kN, compared to 208.8 kN for the TWB 1.2/1.6 condition, the lowest of the TWB conditions.

The average crush load over the full crush distance (ranging from 243 mm to 290 mm) for the five TWB crush rail conditions are compared to the baseline crush tip in Figure 191. The baseline crush tip has a cross-sectional area of 537 mm^2 at its impacted end, while the TWB rails have cross-sectional areas of 483 mm^2 and 648 mm^2 in the 1.2 mm and 1.6 mm thicknesses, respectively. The baseline crush tip's average crush load of 82.8 kN over the first 175 mm of crush was similar to that of the TWB 1.2 (84.3 kN) condition over its full crush distance. The laboratory scale TWB crush rail specimens exhibit folding conditions similar to that of the baseline crush tip specimens.

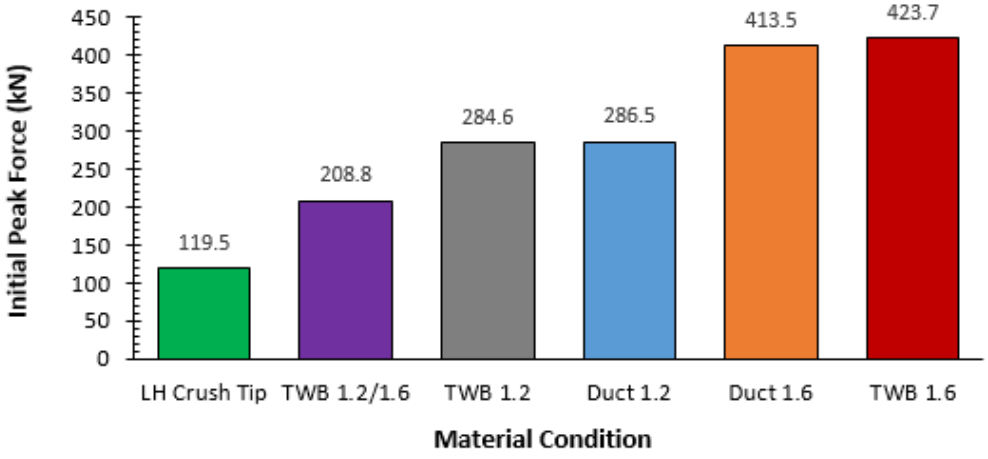

Figure 190: Initial peak force of the five TWB dynamic axial crush conditions compared to the LH baseline crush tip experiments.

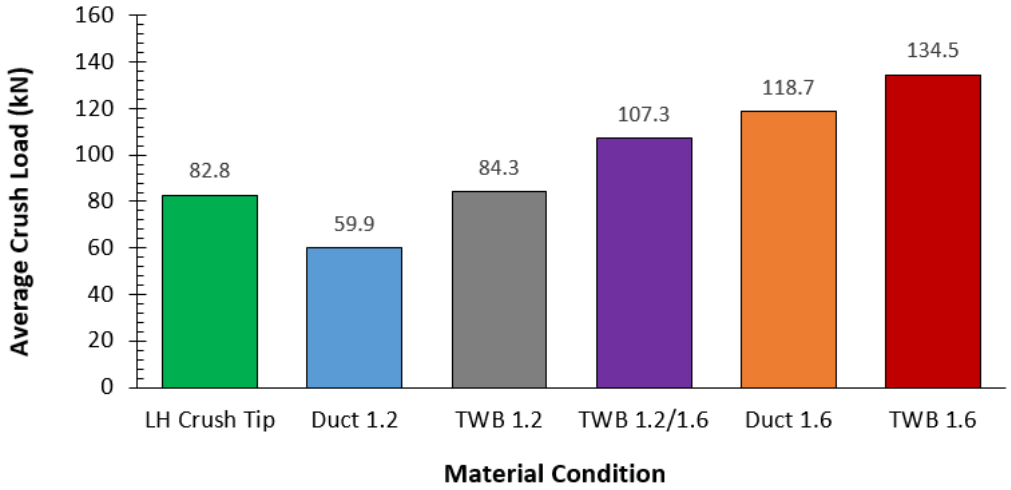

Figure 191: Average crush load for the five TWB axial crush rail conditions and the LH baseline crush tip experiments.

9.1.2 Comparison of Current TWB Axial Crush Results with Prior IDH Results

It is of interest to compare the performance of the current tailor-welded grades based on Ductibor® 500-AS to crush members that were tailored using the in-die heating (IDH) process applied to monolithic Usibor® 1500-AS channel sections.

Previous work by Omer *et al.* [20, 21] was introduced in Section 1.5. They used IDH to achieve axial tailoring of properties in Usibor® 1500-AS top hat channels, and conducted axial crush testing using the same experimental conditions that were used in the current TWB study. In Figure 192 the results from axial crush testing of two IDH grades are compared to the Duct 1.2 and TWB 1.2 results. The IDH 400 and IDH 700 curves are from rails in which the impacted end was formed in a die heated to 400°C and 700°C, respectively. The IDH 400 condition has a strength of 876 MPa, while the IDH 700 condition has a strength of 655 MPa. The two IDH grades exhibit force and energy absorption histories that are similar to that of the TWB 1.2 specimen. The Duct 1.2 is similar to these grades initially, but diverges later in the crush once the higher strength zones of the tailored parts begin to deform. The initial peak forces and overall energy absorptions are also compared in Figure 193. Fully quenched Usibor® 1500-AS was also tested by Omer *et al.* [20, 21] and found to exhibit heavy tearing as it crushed due to its low ductility. This makes fully quenched, martensitic Usibor® 1500-AS unsuitable for applications such as a crush tip where extensive folding is required.

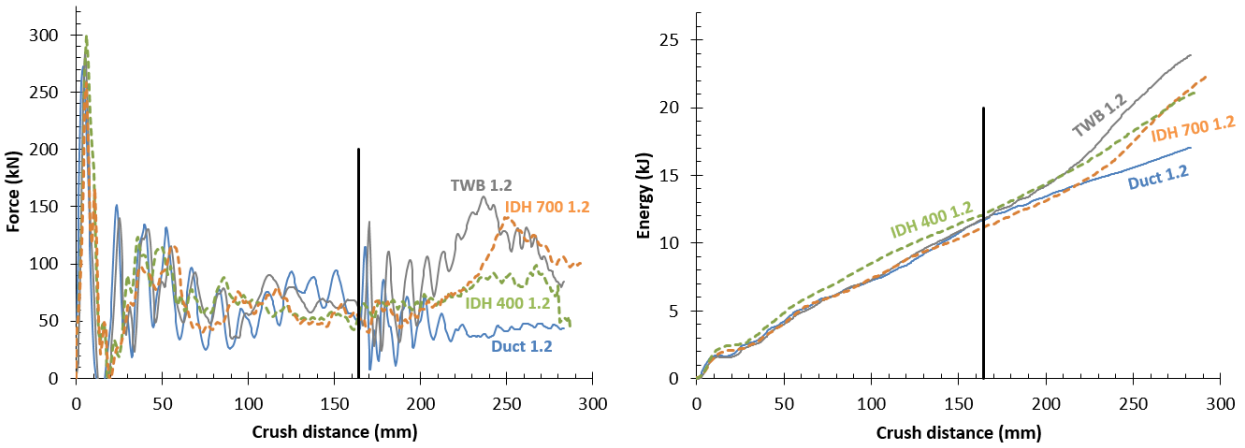

Figure 192: Comparison of force and energy absorption recorded in dynamic axial crush testing of Duct 1.2 and TWB 1.2 (solid lines) to tests performed by Omer [20] on different grades of 1.2 mm IDH Usibor® 1500-AS (dashed lines).

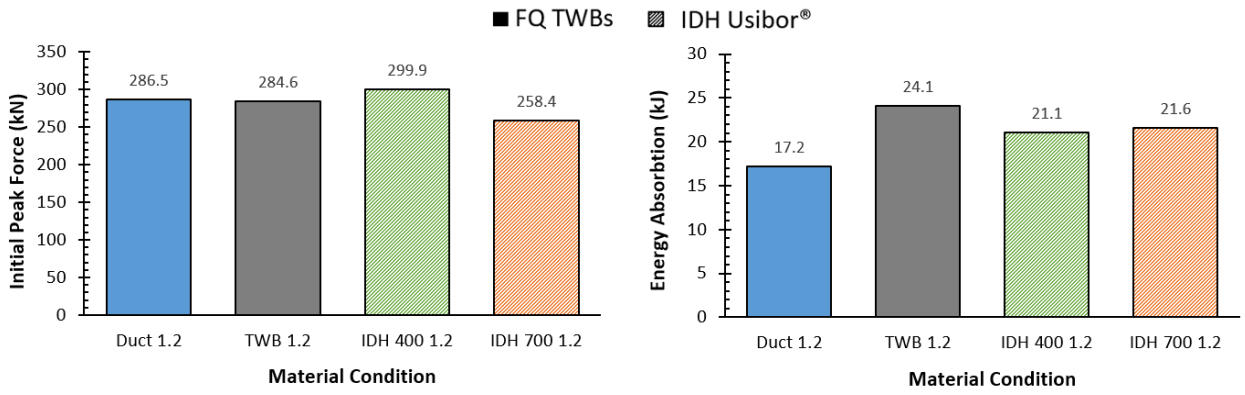

Figure 193: Bar chart showing initial peak force and the total energy absorption over the first 285 mm of crush distance, comparing Duct 1.2 and TWB 1.2 to IDH dynamic crush testing by Omer [20].

Omer *et al.* [20, 21] also conducted quasi-static axial crush tests of the same two IDH grades using similar testing conditions to the current experiments on TWBs. Figure 194 compares the results for the first 190 mm of crush. Similar to the dynamic results, the two IDH grades and the TWB 1.2 had similar force profiles. There was a larger difference between the IDH 400 and IDH 700 grades at the quasi-static rate, with the IDH 700 having lower loads and energy absorption than the TWB 1.2 and Duct 1.2, while the IDH 400 had higher loads. With the displacement distance being only 190 mm in the quasi-static experiments, the Duct 1.2 case did not diverge from the TWB 1.2 results so it had a very similar result. The initial peak forces and energy absorption over 190 mm are summarized in Figure 195.

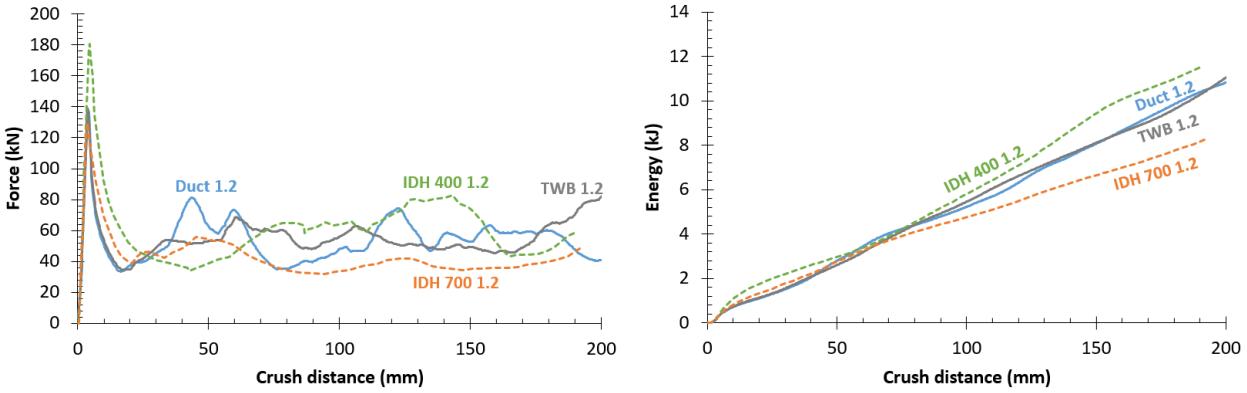

Figure 194: Comparison of force and energy absorption recorded in quasi-static axial crush testing of Duct 1.2 and TWB 1.2 (solid lines) to tests performed by Omer [20] on different grades of 1.2 mm IDH Usibor® 1500-AS (dashed lines).

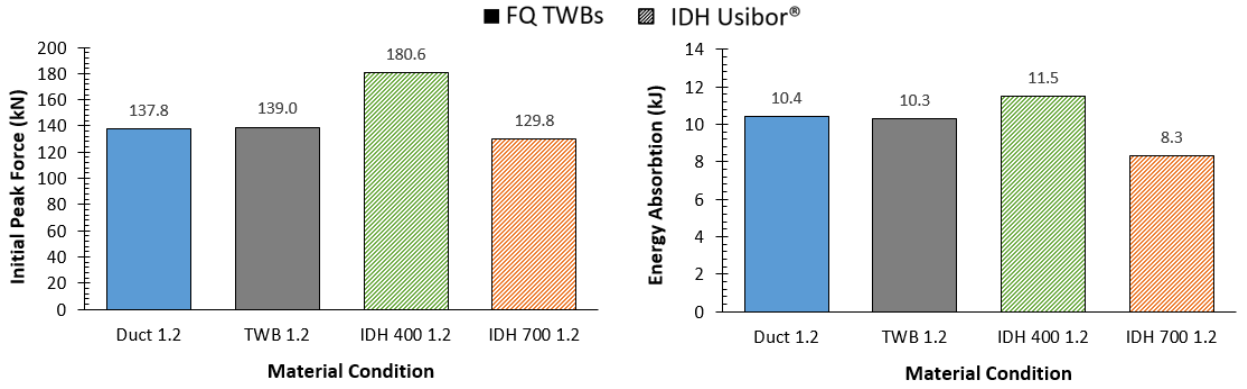

Figure 195: Bar chart showing initial peak force and the total energy absorption over the first 190 mm of crush distance, comparing Duct 1.2 and TWB 1.2 to IDH quasi-static crush testing by Omer [20].

9.1.3 Comparison of Ductibor® 500-AS Three Point Bend Results with Prior Usibor® 1500-AS Results

Work by Prajogo [19] (introduced in Section 1.5) considered hot stamped top hat channels made from Usibor® 1500-AS (fully quenched) that were subjected to three point bending tests using similar experimental conditions as were used in the current Ductibor® 500-AS work. In Figure 196 the dynamic three point bend results from fully quenched Usibor® 1500-AS considered by Prajogo are compared to the current Ductibor® 500-AS results (Duct 1.2). The dashed red curve corresponds to the fully quenched Usibor® 1500-AS condition, while the solid orange and brown curves are for the Ductibor® 500-AS conditions. The Usibor® 1500-AS data is heavily filtered but still shows that the initial peak force achieved is much higher than in the Duct 1.2 case. This

is also reflected in the energy absorption, however the Duct 1.2 specimen that exhibited the wrapping mode ultimately absorbed more energy than the fully quenched Usibor® 1500-AS grade.

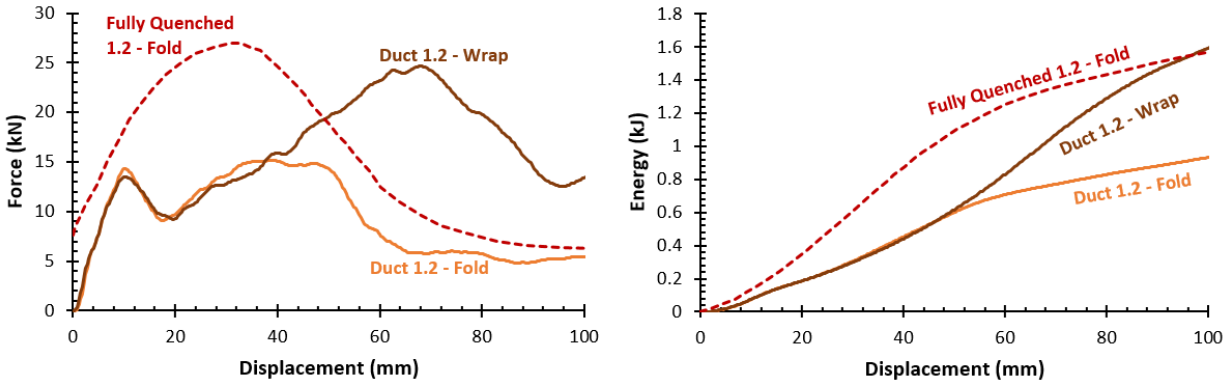

Figure 196: Comparison of force and energy absorption recorded in dynamic three point bend testing of Duct 1.2 (solid lines) to tests performed by Prajogo [19] on fully quenched 1.2 mm Usibor® 1500-AS (dashed line).

Prajogo [19] also conducted quasi-static three point bend tests, again using the same experimental parameters that were used for the Ductibor® 500-AS. Figure 197 compares the results from fully quenched Usibor® 1500-AS to those of Duct 1.2. The fully quenched Usibor® 1500-AS condition experienced a wrapping mode of deformation, while the Duct 1.2 experienced the folding mode and had a much lower force and energy absorption.

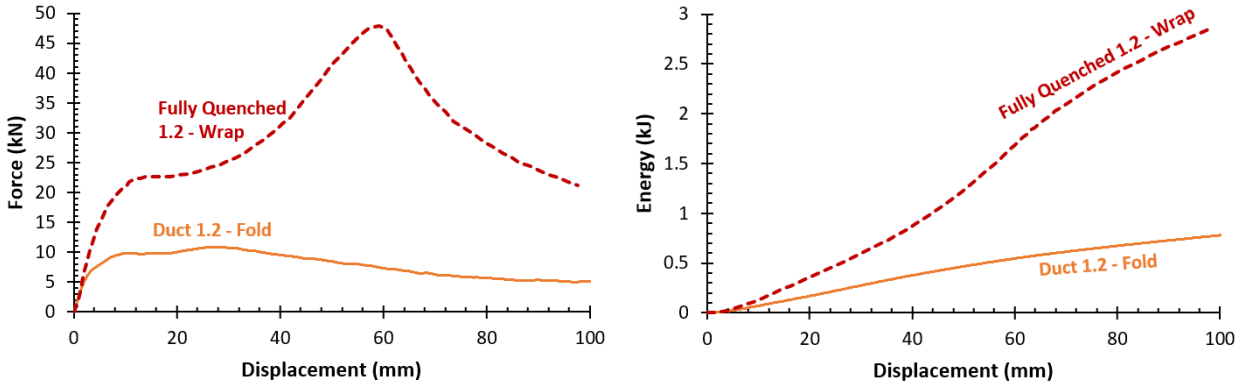

Figure 197: Comparison of force and energy absorption recorded in quasi-static three point bend testing of Duct 1.2 (solid line) to tests performed by Prajogo [19] on fully quenched 1.2 mm Usibor® 1500-AS (dashed line).

In general, the higher bending loads and energy absorption afforded by the higher strength Usibor® 1500-AS allows for better performance than Ductibor® 500-AS in an intrusion-resistant type loading for which there is limited deformation and folding. Nonetheless, the current work has

served to demonstrate the important potential role of multi-alloy TWBs for frontal (and rear) axial crush applications for which progressive folding is required. The introduction of Ductibor® 500-AS within a tailor welded blank affords the opportunity to fabricate a multi-functional tailored component with an energy absorbing Ductibor® 500-AS crush tip, for example, welded to a higher strength Usibor® 1500-AS anti-intrusion zone. Such a tailoring strategy also enables significant part consolidation opportunity.

9.2 Conclusions

This study has addressed the axial crush and three-point bending performance of hot stamped TWBs. The following conclusions can be drawn:

1. The baseline crush performance of a driver's side front side frame demonstrator structure was tested and the collapse mode of the structure was characterized. The demonstrator structure exhibited an initial peak force of 123.9 kN at the start of crushing, and absorbed about 30 kJ of energy after 300 mm of crush (23.4 kJ after 240 mm of crush).
2. Dynamic axial crush tests of the isolated left and right tips of the baseline crush rails showed excellent repeatability and good agreement with the numerical model. The crush tip initial peak load was 119.5 kN and absorbed energy after 240 mm of crush was 22.6 kJ. These values were within 3.6% and 3.5% of corresponding initial peak load and energy absorption (240 mm) for the full demonstrator structure.
3. Forming a laser-welded blank of Usibor® 1500-AS and Ductibor® 500-AS on a fully cooled die created a part with relatively uniform hardnesses of about 490 HV and 220 HV, respectively, in the two sections. The hardness transition across the weld line was just 2 mm wide. A new die with freshly machined surfaces produced for the 1.2:1.6 mm TWBs resulted in slightly higher hardness levels of 540 HV and 250 HV, respectively.
4. In three point bending tests of monolithic Ductibor® 500-AS, no material fracture occurred in the tight folds that were produced. The samples displayed positive rate sensitivity with the dynamic experiments reaching 55% higher peak loads and absorbing 15% more energy than in the quasi-static tests. The 1.2 mm specimens displayed two deformation modes when tested dynamically, with the level of friction controlling whether the part folded or wrapped around the impactor. In all other test conditions, the folding mode occurred exclusively.

5. Axial crush tests of monolithic Ductibor® 500-AS and TWBs showed that hot stamped TWBs have performance advantages over monolithic parts. The monolithic Duct 1.2 specimens and to a lesser extent the Duct 1.6 specimens had a tendency to buckle globally due to their low stiffness and long length. The introduction of a fully quenched section of Usibor® 1500-AS in the fixed end of the crush rail served to stabilize the TWB, allowing for progressive axial crush of the Ductibor® 500-AS energy absorption section. After full consolidation of this soft zone, the harder fully quenched Usibor® 1500-AS zone increased the crush load significantly, with some isolated tearing of the parent metal and/or weld failures. The dynamic and quasi-static results followed similar trends, with the higher loads and energy absorption of the dynamic results indicating the presence of positive rate sensitivity. The Ductibor® 500-AS did not exhibit fracture despite forming very tight folds.

6. The numerical simulations, incorporating rate-sensitive constitutive behaviour, the GISSMO fracture model, and a spot weld failure model, agreed well with experiments in terms of the predicted force *versus* displacement response of both the three point bend and axial crush experiments at dynamic and quasi-static rates.

7. Substitution of Ductibor® 500-AS into the baseline crush tip model showed that the folding modes and load-displacement response were very similar to those of the baseline JAC590R material. This outcome supports the use of Ductibor® 500-AS as a hot stamped substitute for 600 MPa conventional steels. There exists an opportunity for substitution of a Ductibor® 500-AS to Usibor® 1500-AS TWB into a lightweight front side frame demonstrator structure. A soft zone would be used in the crush tip to absorb energy, while a fully quenched Usibor® 1500-AS zone would resist intrusion into the passenger compartment and allow for weight savings through gauge reduction, primarily in the Usibor® 1500-AS zone. The consolidation of multiple parts into a single TWB reduces the complexity of the assembly by eliminating many spot welds.

9.3 Recommendations

1. The shock tower mounting system used for testing of the baseline demonstrator structures should be modified prior to testing of additional baseline and lightweight demonstrator structures.

   At a minimum, larger diameter bolts with stronger threads should be used to attach the bracket to the end of the support on the wall. In the tests, this bracket could rotate slightly within the clearance of the M12 bolt holes, and the threads were not strong enough to increase the preload on the bolts. Alignment pins could be used to resist the shear load at the expense of some of the adjustability. A sheet of material with a high friction coefficient and some compliance such as rubber or urethane could be sandwiched between the bracket and the wall support to help prevent sliding.

   The bolted connection between the bar on the shock tower and the bracket also experiences sliding during the tests despite being torqued to 380 Nm. A rubber material may also help here, or some of the adjustability will need to be removed.

2. LED lights or IR filtering should be used to illuminate heating of surfaces being recorded with an IR camera. The mercury vapour lights reflect heat off of the shiny galvanized surface of the baseline demonstrator structures, inflating the measured temperatures.

3. The Usibor® 1500-AS to Ductibor® 500-AS TWBs and the monolithic Ductibor® 500-AS should be ordered in large sheets from which several top hat channel forming blanks can be cut. This would reduce the cost of water jet cutting or laser cutting of blanks. Having an individual sheet for each blank required more setup time to do the cutting, rather than one setup to cut ten or more blanks out of a large sheet.

4. Laser cutting should not be used to extract samples for hardness testing. It was found that the laser cutting can leave a HAZ in the samples that must be ground away before testing, otherwise it will affect the hardness results. The thickness of the HAZ varied, making it difficult to reliably polish it away.

5. The clamping bosses used for top hat channel axial crush rail testing should be retired. These bosses have been used for several years and are in poor condition from all of the impacts. Their design requires 16 bolts to be removed and re-installed, and a further 16

bolts to be loosened and re-tightened in order to remove a tested specimen and install the next one. This is very time consuming and is no longer necessary. New bosses were designed and built that require just 6 bolts to be removed and installed, and 12 more bolts to be loosened and tightened, greatly reducing the time required to remove and install specimens. These new bosses should be used for all top-hat channel axial crush rails going forward.

6. Spot weld failure criteria should be added to the models for Ductibor® 500-AS. Although there is not a great deal of failure in these welds, it will make the models more complete and may improve the agreement with experiments. This characterization work is ongoing as part of the larger scope of this project.

7. A coupled thermo-mechanical hot stamping forming model should be built to predict the hardness distribution in the TWB channels after forming. This should use the Åkerström model calibrated for Usibor® 1500-AS and Ductibor® 500-AS. The hardness distribution and strains predicted by the forming model should be mapped into the crash model to improve its prediction accuracy over the current assumption of uniform hardness.

8. The crush performance of higher strength Ductibor® 1000-AS should be investigated through a similar study. It has significant lightweighting potential if it is able to fold and absorb energy without fracture.

9. TWBs comprising Ductibor® 500-AS and Usibor® 1500-AS (and possibly Ductibor® 1000-AS) should be implemented into a lightweight front side frame demonstrator structure to be compared to the performance of the baseline demonstrator structure. Ductibor® 500-AS has shown that it will fold extensively to absorb energy without fracture, and Usibor® 1500-AS has the ultra-high strength to resist intrusion and reduce weight through gauge reduction. Newer alloys such as Usibor® 2000-AS should also be considered in the anti-intrusion s-rail section of the demonstrator structure.

10.0 References

[1] National Highway Traffic Safety Administration, "NHTSA and EPA Set Standards to Improve Fuel Economy and Reduce Greenhouse Gases for Passenger Cars and Light Trucks for Model Years 2017 and Beyond," 1 12 2011. [Online]. Available: https://www.nhtsa.gov/staticfiles/rulemaking/pdf/cafe/CAFE_2017-25_Fact_Sheet.pdf. [Accessed 22 12 2018].

[2] H. Karbasian and A. Tekkaya, "A review on hot stamping," *Journal of Materials Processing Technology*, vol. 210, no. 15, pp. 2103-2118, 2010.

[3] K. Mori, P. Bariani, B. Behrens, A. Brosius, S. Bruschi, T. Maeno, M. Merklein and J. Yanagimoto, "Hot stamping of ultra-high strength steel parts," *CIRP Annals - Manufacturing Technology*, vol. 66, pp. 755-777, 2017.

[4] ArcelorMittal, "ArcelorMittal Product Catalog," 5 March 2018. [Online]. Available: https://automotive.arcelormittal.com/saturnus/sheets/ArcelorMittal%20Automotive%20product%20offer%20EN.pdf. [Accessed 31 October 2018].

[5] ArcelorMittal, "Steels for hot stamping - Usibor® and Ductibor®," 31 August 2018. [Online]. Available: https://fce.arcelormittal.com/saturnus/tmp/E_EN.utf8.pdf.html. [Accessed 31 Oct 2018].

[6] D. Munera, A. Pic, D. Abou-Khalil, F. Shmit and F. Pinard, "Innovative Press Hardened Steel Based Laser Welded Blanks Solutions for Weight Savings and Crash Safety Improvements," *SAE Int J Mater Manuf*, vol. 1, pp. 472-479, 2008.

[7] American Honda Motor Co., "2016 Pilot: New Model Body Repair Information," June 2015. [Online]. Available: https://techinfo.honda.com/rjanisis/pubs/web/ABN01970.PDF. [Accessed 31 October 2018].

[8] R. George, M. Worswick, D. Detwiler and J. Kang, "Impact Testing of a Hot-Formed B-Pillar with Tailored Properties - Experiments and Simulation," *SAE International*, Vols. 10.4271/2013-01-0608, 2013.

[9] P. Belanger, "Gestamp R&D North America GDIS Presentation," 2016. [Online]. Available: https://www.autosteel.org/-/media/files/autosteel/great-designs-in-steel/gdis-2016/track-3---belanger.ashx. [Accessed 31 October 2018].

[10] K. Omer, R. George, A. Bardelcik, M. Worswick, S. Malcolm and D. Detwiler, "Development of a hot stamped channel section with axially tailored properties - experiments and models," *Int J Mater Form*, vol. Online, pp. 1-16, 2017.

[11] R. George, A. Bardelcik and M. Worswick, "Hot forming of boron steels using heated and cooled tooling for tailored properties," 2012.

[12] C. Peister, R. George, K. Omer, M. Worswick, S. Malcolm, J. Dykeman, C. Yau, R. Soldaat and W. Bernert, "Forming of an axially tailored automotive channel section through hot stamping of tailor-welded blanks," in *36th International Deep Drawing Research Group Conference*, Munich, Germany, 2017.

[13] C. Peister, C. O'Keeffe, M. Nemcko, J. Imbert, C. Butcher, M. Worswick, R. Soldaat, W. Bernert, C. Yau, E. deNijs, S. Malcolm and J. Dykeman, "Tailor Welded Hot Stamped Automotive Axial Crush Structures: Crash Experiments and Modelling," in *International Auto Body Congress*, Dearborn, Michigan, USA, 2017.

[14] C. Peister, C. O'Keeffe, J. Imbert, C. Butcher, M. Worswick, S. Malcolm, J. Dykeman, C. Yau, E. deNijs, R. Soldaat and W. Bernert, "Crash Testing and Modelling of Hot Stamped Multi-Gauge Tailor-Welded Automotive Axial Crush Structures," in *2nd International Conference on Impact Loading of Lightweight Structures*, Xi'an, China, 2018.

[15] C. Peister, C. O'Keeffe, J. Imbert, C. Butcher, M. Worswick, S. Malcolm, J. Dykeman, C. Yau, R. Soldaat and W. Bernert, "Dynamic and Quasi-Static Testing and Modeling of Hot Stamped Tailor-Welded Axial Crush Rails," in *18th International Conference on Experimental Mechanics*, Brussels, Belgium, 2018.

[16] R. George, "Hot Forming of Boron Steels with Tailored Mechanical Properties: Experiments and Numerical Simulations," *Master's Thesis*, 2011.

[17] J. Banik, F. Lenze, S. Sikora and R. Laurenz, "Tailored Properties - A Pivotal Question for Hot Forming," in *3rd International Conference on Hot Sheet Metal Forming of High Performance Steel*, Kassel, Germany, 2011.

[18] J. Wilsius, B. Tavernier and D. Abou-Khalil, "Experimental and Numerical Investigation of Hot Stamped B-Pillar Concepts Based on Usibor(R) 1500P," in *3rd International Conference on Hot Sheet Metal Forming of High Performance Steel*, Kassel, Germany, 2011.

[19] J. Prajogo, "Hot Stamping of a Boron Steel Side Impact Beam with Tailored Flange Properties - Experiments and Numerical Simulations," *Master's Thesis*, 2015.

[20] K. Omer, "Development and Testing of a Hot Stamped Axial Crush Member with Tailored Properties," *Master's Thesis,* 2014.

[21] K. Omer, L. ten Kortenaar, C. Butcher, M. Worswick, S. Malcolm and D. Detwiler, "Testing of a hot stamped axial crush member with tailored properties - Experiments and models," *Int J Impact Eng*, vol. 103, pp. 12-28, 2017.

[22] T. Eller, L. Greve, M. Andres, M. Medricky, A. Hatscher, V. Meinders and A. van den Boogard, "Plasticity and fracture modeling of quench-hardenable boron steel with tailored properties," *Journal of Materials Processing Technology,* 2014.

[23] M. Merklein, M. Johannes, M. Lechner and A. Kuppert, "A review on tailored blanks-Production, applications and evaluation," *Journal of Materials Processing Technology,* vol. 214, pp. 151-164, 2014.

[24] ArcelorMittal, "Innovative process dedicated to Usibor® 1500P and Ductibor® 500P," [Online]. Available: http://automotive.arcelormittal.com/tailoredblanks/1864/1868. [Accessed 1 October 2018].

[25] M. Kang and C. Kim, "Laser welding for hot-stamped tailor-welded blanks with high-strength steel/high-energy absorption steel," *J of Laser Applications,* vol. 26, pp. 1-6, 2014.

[26] M. Merklein, M. Wieland, M. Lechner, S. Bruschi and A. Ghiotti, "Hot stamping of boron steel sheets with tailored properties: a review," *J Mat Proc Tech,* vol. 228, pp. 11-24, 2016.

[27] American Honda Motor Co., "2016 Civic: New Model Body Repair Information," September 2016. [Online]. Available: https://techinfo.honda.com/rjanisis/pubs/web/ABN02539.PDF. [Accessed 31 October 2018].

[28] N. Adebrabbo, R. Mayer, A. Thompson, C. Salisbury, M. Worswick and I. van Riemsdijk, "Crash response of advanced high-strength steel tubes: Experiment and model," *Int J Impact Eng,* vol. 36, pp. 1044-1057, 2009.

[29] T. Wierzbicki and W. Abramowicz, "On the crushing mechanics of thin-walled structures," *J of Applied Mechanics,* vol. 50, pp. 727-734, 1983.

[30] R. Hayduk and T. Wierzbicki, "Extensional collapse modes of structural members," *Computers and Structures,* vol. 18, pp. 447-458, 1984.

[31] W. Abramowicz and T. Wierzbicki, "Axial crushing of multicorner sheet metal columns," *J of Applied Mechanics,* vol. 56, pp. 113-120, 1989.

[32] W. Abramowicz and N. Jones, "Transition from initial global bending to progressive buckling of tubes loaded statically and dynamically," *Int J Impact Eng,* vol. 19, pp. 415-437, 1997.

[33] S. Hsu and N. Jones, "Quasi-static and dynamic axial crushing of thin-walled circular stainless steel, mild steel and aluminium alloy tubes," *Int J Crash,* vol. 9, no. 2, pp. 195-217, 2004.

[34] F. Schneider and N. Jones, "Impact of thin-walled high strength steel structural sections," *Proc Instn Mech Engrs Vol 218 Part D: Automobile Engineering,* 2004.

[35] V. Tarigopula, M. Langseth, O. Hopperstad and A. Clausen, "Axial crushing of thin-walled high-strength steel sections," *Int J Impact Eng,* vol. 32, pp. 847-882, 2005.

[36] B. Williams, D. Oliveira, C. Simha, M. Worswick and R. Mayer, "Crashworthiness of straight section hydroformed aluminum tubes," *Int J Impact Eng,* vol. 34, pp. 1451-1464, 2006.

[37] R. Grantab, D. Oliveira, B. W. Williams, M. J. Worswick and R. Mayer, "Numerical modelling of a dual crush mode welded aluminum crash structure," *Int J Crashworthiness,* vol. 11, no. 2, pp. 165-175, 2005.

[38] K. Sato, T. Inazumi, A. Yoshitake and S. Liu, "Effect of material properties of advanced high strength steels on bending crash performance of hat-shaped structure," *Int J Impact Eng,* vol. 54, pp. 1-10, 2013.

[39] C. O'Keeffe, J. Imbert-Boyd, M. Worswick, C. Butcher, S. Malcolm, J. Dykeman, P. Penner, C. Yau, R. Soldaat and W. Bernert, "Examination of Mode I loading on resistance spot weld groups in tailored hot stampings," in *DYMAT's 23rd Technical Meeting,* Trondheim, Norway, 2017.

[40] O'Keeffe, "Investigation of Resistance Spot Weld Failure in Tailored Hot Stamped Assemblies," *Master's Thesis,* 2018.

[41] T. Eller, "Modeling of tailor hardened boron steel for crash simulation," *PhD Thesis,* 2016.

[42] C. Peister, M. Worswick, K. Omer, S. Malcolm, J. Dykeman, C. Yau, R. Soldaat and W. Bernert, "Numerical Modelling of the Crash Performance of Tailored Hot Stamped Crush Rails," in *6th International Conference on Hot Sheet Metal Forming of High Performance Steel,* Atlanta, Georgia, 2017.

[43] P. Akerstrom, "Numerical implementation of a constitutive model for simulation of hot stamping," *Modelling and Simulation in Materials Science and Engineering,* vol. 15, pp. 105-119, 2007.

[44] T. Olsson, "An LS-DYNA Material Model for Simulations of Hot Stamping Processes of Ultra High Strength Steels," in *7th European LS-DYNA Conference,* Salzburg, Austria, 2009.

[45] A. Bardelcik, M. Worswick, S. Winkler and M. Wells, "A strain rate sensitive constitutive model for quenched boron steel with tailored properties," *Int J Impact Eng,* vol. 50, pp. 49-62, 2012.

[46] A. Bardelcik, M. Worswick and M. Wells, "The influence of martensite, bainite and ferrite on the as-quenched constitutive response of simultaneously quenched and deformed boron steel - Experiments and model," *Materials and Design,* vol. 55, pp. 509-525, 2014.

[47] A. Haufe, F. Neukamm, M. Feucht, P. DuBois and T. Borvall, "A comparison of recent damage and failure models for steel materials in crashworthiness application in LS-DYNA," in *11th International LS-DYNA Users Conference*, Detroit, Michigan, 2010.

[48] L. ten Kortenaar, "Failure Characterization of Hot Formed Boron Steels with Tailored Mechanical Properties," *Master's Thesis,* 2016.

[49] J. Prajogo, K. Omer, A. Bardelcik, R. George, M. Worswick, N. Adam and D. Detwiler, "Development of a Hot Stamped Side Impact Beam and Axial Crush Member with Tailored Properties - Numerical Models," in *4th International Conference on Hot Sheet Metal Forming of High-Performance Steel*, Lulea, Sweden, 2013.

[50] A. Bardelcik, K. Ghavam, R. George and M. Worswick, "An Impact Model of a Hot Stamped Lab-Scale B-Pillar with Tailored Properties," in *3rd International Conference on Hot Sheet Metal Forming of High Performance Steel*, Kassel, Germany, 2011.

[51] N. Ma, P. Hu and Z. Zhang, "Research on Tailored Microstructure Material in Hot Forming and its Application," in *3rd International Conference on Hot Sheet Metal Forming of High Performance Steel*, Kassel, Germany, 2011.

[52] S. Kim, "Dynamic and Quasi-Static Response of Warm and Hot Formed Aluminum Beams Under Three-Point Bending," *Master's Thesis,* 2018.

[53] M. Tummers, *Personal Communication: Demonstrator Structure Design,* 2018.

[54] S. Malcolm, *Personal Communication: SUV Front Rail Crush Model,* 2017.

[55] National Highway Traffic Safety Administration, "Laboratory Test Procedure for New Car Assessment Program Frontal Impact Testing," 09 2012. [Online]. Available: https://www.safercar.gov/staticfiles/safercar/NCAP/Frontal_TP_NCAP.pdf. [Accessed 23 12 2018].

[56] Seattle Safety, "Decelerator Sled Systems," [Online]. Available: http://www.seattlesafety.com/wp-content/uploads/2014/03/Decel_brochure_10.06.pdf. [Accessed 4 Oct 2018].

[57] Plascore Inc., "Plascore Crushlite: Lightweight, Constant Force Energy Absorber," 2 April 2018. [Online]. Available: https://www.plascore.com/download/datasheets/energy_absorption_documentation/Plascore_CrushLite.pdf. [Accessed 4 Oct 2018].

[58] E. Famchon, *Personal Communication: Welding of TWBs.*

[59] DADCO, "Dadco Ultra Force Nitrogen Gas Springs Catalog," 2016. [Online]. Available: http://www.dadco.net/wp-content/uploads/2013/02/u_catalog.pdf. [Accessed 20 12 2018].

[60] A. Abedini, C. Butcher, J. Imbert, A. Zhumagulov, M. Nemcko and P. Samadian, *Personal Communication: Material Model for Ductibor 500-AS*, 2018.

[61] Steel Market Development Institute, "DP600 - High Strain Rate Data," 2012. [Online]. Available: https://www.autosteel.org/research/ahss-data-utilization/dp600. [Accessed 20 12 2018].

[62] Livermore Software Technology Corporation (LSTC), LS-DYNA Keyword User's Manual, Livermore, California: LSTC, 2015.

[63] MathWorks, "smooth - Smooth response data," [Online]. Available: https://www.mathworks.com/help/curvefit/smooth.html. [Accessed 24 11 2018].

[64] A. Bardelcik, C. Salisbury, S. Winkler, M. Wells and M. Worswick, "The effect of cooling rate on the high strain rate properties of boron steel," *Int J Impact Eng*, vol. 37, pp. 694-702, 2010.